ScuDo

Scuola di Dottorato ◡ Doctoral School

WHAT YOU ARE, TAKES YOU FAR

Doctoral Dissertation
Doctoral Program in Environmental Engineering (30th cycle)

Debris flow interaction with open rigid barriers

A DEM-LBM approach for trapping efficiency and impact force analysis

By

Maddalena Marchelli

******

Supervisor(s):
Prof. M. Pirulli, Supervisor
Dr. A. Leonardi, Co-Supervisor

Doctoral Examination Committee:
Prof. E. Bowmann, Referee, University of Sheffield
Prof. P. Villard, Referee, Université Grenoble Alpes UGA
Prof. M. Barbero, Politecnico di Torino
Prof. S. Cola, Università degli Studi di Padova
Prof. A. Segalini, Università degli Studi di Parma

Politecnico di Torino
2018

Declaration

I hereby declare that, the contents and organization of this dissertation constitute my own original work and does not compromise in any way the rights of third parties, including those relating to the security of personal data.

Maddalena Marchelli
2018

Acknowledgements

Abstract

Debris flow is a dangerous landslide phenomenon occurring after intense rainfall in mountainous regions. It can be defined as a very rapid flow of heterogeneous material of different grain sizes with high water content. Due to its multi-phase nature, in which solid, fluid and air continuously interact, debris flow is a complex phenomenon, difficult both to analyze and to simulate. Because of its rapidity and unpredictability, it can cause loss of lives and extended damages to environment and structures. Thus, efficient mitigation measures are often desirable. Due to the complexity of the phenomenon, the design of barriers is still a challenging problem. Since a proper regulation does not exist, several of them have been designed only by imitating previously built barriers that have exhibited the proper functions during past events. Moreover, different types exist. The present thesis focuses on structural mitigation measures, with particular reference to open rigid barriers. Several Authors suggested that these barriers have to lower the kinetic energy of the flowing mass and to retain coarse sediments, allowing water and fine particles to pass.

The main aspects to consider in the design of such barriers are: (1) the filter size problem, i.e. the size of the outlets, (2) the forces exerted on the barrier by the flowing mass during and after its impact. Thus, the present thesis addresses such two problems through a novel numerical method. An existing DEM-LBM code (Leonardi et al., 2015) has been enhanced with a complete friction model, which allows the creation of stable structures among grains. The result, a 3D continuum-discrete two-phase code, is able to consider the three-dimensional behaviour of the granular mass, the influence of the fluid phase, and their effects when they impact on the barrier. The new code has been validated and adopted to study the clogging mechanisms and the outlet geometry that promotes a retention of coarse grains.

First, a monosized dry granular mass has been released under the effect of gravity in an inclined channel, at end of which the barrier is set. A complete parametric study on a single outlet barrier has been performed to provide the bases for further

simulations on multiple-outlets barriers. The influence of the impact angle, of the channel slope, and of the normalized outlet width on both the trapping efficiency and the impact force has been evaluated and critically discussed. Then, progressively weakening the assumption of dry monosized mass, more realistic configurations have been analyzed. On one hand, bidisized dry granular simulations have been performed accounting for the presence of fine particles. On the other hand, a fluid phase, representing water and fine particles, has been added to the monosized dry granular mass. Interesting outcomes have been obtained on both trapping efficiency and impact forces.

Starting from the dry monosized material and a single outlet barrier, a geometrical setting which provides a complete clogging of the barrier has been found. For opening width lower than 5 times the mean particle radius, the trapping efficiency is almost 100%. This result can be extended to the multiple-outlets barrier case if the width of the barrier piles is at least 6 times the mean particle radius. Moreover, introducing a bidispersion in grain size, the efficiency of the retaining function of the barrier is preserved up to a 70% in volume of small particles. The addition of a fluid phase, for solid volume fraction greater than 5%, does not affect the results. Considering the impact forces, high stresses are localized in the outlet neighbourhood, and their intensity increases by increasing the outlet width. The presence of bidispersion lowers the global impact forces, almost independently from the fraction of fine particles. Comparing the dry cases with those in which the fluid is added, it is noted that, in the first seconds after the impact, the presence of the fluid slightly lowers the impact forces due to the solid phase. Then, the fluid phase mainly transfers its momentum to the clogged solid phase, rather than directly to the barrier.

Contents

List of Figures

List of Tables

Nomenclature

In the present thesis, whenever not differently specified, the vector notation is adopted with the common typographic convention: vectors and tensors are denoted with boldface upright type, while scalars with plain symbols. In both cases, there is no difference between the upper case and the lower-case symbols. Whenever a vector quantity is referred using both italic plain and upright bold symbols, the former represents the magnitude of the vector. In case of a bold symbol representing a tensor (e.g. the stress tensor $\boldsymbol{\sigma}$ and the shear rate tensor $\dot{\boldsymbol{\gamma}}$), the plain italic symbol denotes the second invariant of the tensor. Dots above the symbols denote time derivatives. The cartesian coordinate system is denoted using the axis x, y and z (in lower and upper cases). The local reference system is defined by n, t, b, namely the normal, tangential and binormal axes. Symbols, superscripts, subscripts, and acronyms used are listed hereafter.

Roman symbols

Symbol	Unit	Description
D	m	Grain diameter
$\mathbf{F}$	N	Force
Fr	-	Froude number
$\mathbf{g}$	m/s^2	Gravity
h	m	Height
$\mathbf{J}$	kg m^2	Moment of inertia
k	N/m	Contact stiffness
m	kg	Mass
p	Pa	Pressure
P	m	Width of the pile of the barrier

Q	m³/s	Flow discharge
r	m	Radius
R	m	Radial distance
S	m	Width of the barrier outlet
t	s	Time
v	m/s	Velocity

Greek symbols

Symbol	Unit	Description
α	-	Damping coefficient
γ	N/m³	Bulk density
δ	m	Particle overlap
Δl	m	Lattice size
Δt	s	Time step
$\dot{\gamma}$	1/s	Shear rate tensor
ζ	-	Coefficient of restitution
η	Pa·s	Viscosity
θ	°	Slope angle
μ_s	-	Static sliding friction coefficient
μ_d	-	Dynamic sliding friction coefficient
μ_r	-	Rolling friction coefficient
ν	-	Poisson ratio
ξ	m	Elongation of the tangential spring
ρ	kg/m³	Mass density
σ	Pa	Stress tensor
τ	Pa	Shear component of the stress tensor
ϕ	°	Friction angle
ω	1/s	Rotational velocity

Superscripts

n	Normal component
r	Rolling
t	Tangential component

Subscripts

b	Quantity inherent to the barrier
B	Quantity inherent to the boulder
d	Quantity inherent to the fluid debris mass (if continuum approach)
f	Quantity inherent to the fluid
n	Normal component
o	Quantity inherent to the outlet of the barrier
p	Quantity inherent to the particles
r	Rolling
s	Sliding
t	Tangential component
w	Quantity inherent to the wall
W	Quantity inherent to the water

Acronyms/Abbreviations

BB	Bounce-back
CFD	Computational Fluid Dynamics
DEM	Discrete Element Method
FEM	Finite Element Method
LBM	Lattice-Boltzmann Method
DEM-LBM	Coupled DEM-LBM Method
SPH	Smoothed-Particle Hydrodynamics

Chapter 1

Introduction

1.1 Overview and motivation

Debris flow is a very rapid flow of heterogeneous material and water that occurs in mountain regions. The material involved in the phenomenon comprises debris of different sizes, even boulders, as well as organic material entrained by the flow. For the variability of the conditions at which the phenomenon occurs, a unique definition of debris flow is rather difficult to be found. Debris flow generally occurs when, after a period of intense rainfalls, sediments on a steep area are mobilized by water and begin moving, resulting in a multiphase flow. During their motion, the largest grains tend to move to the flow surface and to the front, originating a longitudinal sorting combined with an inverse grading. As a consequence, debris flow is a very complex phenomenon, involving phase-interaction effects at different observation scales. Due to the high velocities involved and its unpredictability, it constitutes one of the most dangerous landslide phenomenon, in terms of both loss of lives, and of damage to environment and structures.

To protect hazardous areas, efficient mitigation measures are often required. The present research work focuses on structural mitigation measures, with particular reference to open rigid barriers. Due to the nature of debris flow, its evolution can involve different effects, e.g. collisions among grains, solid-fluid interaction, segregation, and inverse grading phenomena. Different types of stresses, e.g. collisional, frictional, and viscous, can arise, also depending on the involved material composition. In the perspective of guaranteeing an effective performance of debris-flow

mitigation measures, all these aspects need to be considered. Transported material and water interact with the barrier, resulting in high impact forces. The capacity of granular material to form force chains among grains results in arch formation on the barrier face and its outlets, possibly jamming the flow.

As a result of this complexity, different design approaches emerged in the last decades. Being inspired by the solution adopted in solid transport problems, several researchers (e.g. Armanini et al., 1991; Larcher and Armanini, 2000) suggested to create a temporal retention of sediment and water, combined with an energy dissipation function. Considering the high velocities involved in a multi-phase flow, higher than in a streamflow, other Authors proposed to design barriers with a filtering function, i.e. promoting a selective mechanical sieving of the coarse material, filtering water and fine grains (e.g. Hübl and Holzinger, 2003; Suda et al., 2009). This action is combined with an energy dissipation function. The design of such barriers requires an accurate evaluation of both impact forces and filter size, i.e. outlet geometry.

In the last decade, the design of such structures has been based on the designer's experience, by imitating previously built barriers that have exhibited the proper functions during events. Designing these structures and verifying their efficiency is a very difficult task since a specific regulation does not exist. On the international stage, the Austrian Code Series (ONR 24800, 2009; ONR 24801, 2013; ONR 24802, 2010; ONR 24803, 2008), the Technical Reports for the Hong-Kong area (Kwan, 2012; Lo, 2000), for China (MLR, 2004), and for Taiwan (SWCB (Soil and Water Conservation Bureau), 2005), the European Commission Scientific Reports (Johannesson et al., 2009), and the US codes (FEMA P-259, 2012; FEMA P-55, 2011) only propose simplified models to calculate the impact forces, often neglecting the filter size problem. Thus, due to this uncertainty, a remarkable variety of open barrier types exist, with different geometries and construction materials.

The filter size problem, i.e. the size of the outlets, has traditionally been addressed prescribing the outlet width. This is evaluated as a function of the minimum grain size that has to be entrapped, by following empirical or semi-empirical relationships based on on-site measurements, past-event observations or small-scale laboratory experiments. Consequently, verifying the real retaining capability, i.e. the trapping efficiency of the barrier, is difficult. Similarly, impact forces are often evaluated through empirical formulations, derived from classical hydraulic theories, whose coefficients have to be calibrated through back-analyses.

Numerical modeling has been adopted in literature to study this problem, with

particular reference to the impact forces. Among the existing models, the 2D depth-averaged equations are frequently employed for simulating two-phase debris flow events, describing the flow either as a single-phase or a two-phase medium. Nevertheless, they do not allow to consider different flow-depth velocity profiles, the possibility of collisions and the raise of force chains among grains. Besides, 3D continuum models, generally monophase, cannot study the interactions among grains and segregation phenomena, i.e. the sorting effects produced by the presence of different grain sizes. On the contrary, although discrete element modelling reveals to be very effective for investigating the three-dimensional processes among grains, it lacks the capacity of dealing with solid-fluid interaction problems. A method for realistically simulating the complex interaction of debris flow and structures is, therefore, still missing.

1.2   Problem and objectives

The present research work aims at proposing an accurate numerical approach able to better represent and consider the interaction between debris flow and an open rigid barrier. Evaluating the dynamics of the phenomenon, the study aims to answer the major design problems: filter size and impact forces evaluation. To achieve these goals, the desiderata of the numerical approach for investigating the problem are:

- *Full 3D modelling*: to correctly represents the granular material, catching the three-dimensionality of the phenomenon.

- *Two-phase*: to deal with the contemporary presence of a solid and a fluid phases.

In addition, the numerical code has to correctly reproduce the following aspects:

- *Arching*: capability of the grains to create stable structures;

- *Friction*: as it sustains the stable structures and promotes the halt of the particle motion;

- *Different grain shapes*: as the grain shape differs from a perfect sphere, which is generally adopted in numerical simulations.

Among the existing numerical codes, the DEM-LBM code developed by Leonardi et al. (2015) satisfies the three-dimensional and two-phase required targets. The particles are discrete elements moving in a three-dimensional space. The fluid, which is a continuum phase, is simulated through the Lattice Boltzmann Method. The interaction effects arising between the phases are considered. However, the code had a few deficiencies in simulating the capacity of the grains to create stable structures, and the dissipating effects of friction. Also, it does not account for grain shapes different from perfect spheres. Thus, in the present research work, the code has been enhanced to overcome the highlighted shortcomings. The new version is validated and, consequently, adopted to study the interaction with rigid open barriers.

Several numerical simulations are performed, considering both the trapping efficiency and the impact forces. Firstly, the discharge of a monosized dry granular material inside a channel and the interaction with a single-outlet barrier are simulated, using only the DEM part of the code. This simple case allows to investigate the geometrical setting that guarantees an efficient trapping of the material. The influence of the impact angle, of the channel slope, and of the opening width are investigated. Then, the multiple-outlet geometry is considered, evaluating the mutual influence of two neighbouring outlets. Finally, a more realistic configuration is simulated, attempting to consider also the presence of water and fine grains. With this aim, two different strategies are investigated to simulate two-phase debris flows: (1) through a bisized dry granular mass; (2) including the fluid phase in the model, by activating the LBM part of the code. These simulations are a first step in the direction of a more realistic modeling of debris flow events, and their interaction with open barriers.

1.3   Outline

The present thesis is organized as follows. Chapter 2 relates to the definition and classification of debris flow phenomena. The main characteristics of the flow, from triggering to deposition, are given. Chapter 3 describes the most frequently employed criteria for open rigid barrier design. The barrier functions are presented in the perspective of debris flow event management. Further analyzing the barrier design strategies, Chapter 4 reports the state of the art on both the evaluation of impact forces and the filter sizing, highlighting the need of further investigation. Chapter 5 presents the DEM-LBM original version of the adopted code. As mentioned, this

code is improved in the present work to properly consider friction, arching and shape effects. The performed enhancements and their validation are explained in Chapter 6. Chapter 7 reports the performed simulations on monosized dry granular flows and the respective geometrical parametric analyses on single and multiple outlets barriers. Chapter 8 deals with the simulations of a two-phases flow, both with a grain size bidispersion method and the introduction of the fluid phase. For the former method both single and multiple outlets barriers are considered, while for the latter the only single outlet barrier configuration is investigated. Finally, in Chapter 9 the conclusions are drawn, providing an outlook on possible future developments of the carried out research.

Chapter 2

Debris flow: definition and mechanisms

Due to the complexity of debris-flow type phenomena, a remarkable variety of definitions exist in literature, thus creating ambiguities and uncertainties. This chapter gives the main characteristics of what is intended as debris flow in the present work. As a general concept, debris flow is ascribed among landslides of flow type, i.e. the rearrangement of grain contacts is pervasive during the motion, promoting significant internal distortion of the moving mass (Iverson, 2014; Varnes, 1978). Nevertheless, a clear distinction among the flow-type phenomena is a problematic issue and comparing the definitions given by different Authors is often misleading.

To overcome this problem, in Sec. 2.1, different references are evaluated and compared, trying to draw conclusions and find a unique definition, able to distinguish debris flow from other flow-like landslide phenomena. Then, Sec. 2.2 classifies and describes the several debris flow types reported in literature, outlining some clearly separated typologies. Finally, in Sec. 2.3 the main characteristics of the phenomenon are introduced. These aspects are very important for an accurate modelling of the phenomenon and for the choice of the input parameters.

2.1 Definition and characterisation

Debris flow is a complex phenomenon (Fig. 2.1), involving different materials and high water content. Stini (1910) firstly defined debris flow as "a viscous mass,

Fig. 2.1 The Kedarnath debris flow in Uttarakhand, India (June, 2013). Courtesy and copyright of Vaibhav Kaul.

consisting of water, soil, sand, gravel, rocks and wood mixed together". Then, Sharpe (1938) focused on the characteristic rapid velocity of the phenomenon, which is channelized, and defined the material of which it is composed as debris. Cruden and Varnes (1996); Varnes (1954, 1978) firstly included debris flow in the flow type landslide, providing a definition of debris as a material containing a percentage of material larger than 2 mm ranging from 20% to 80% (Varnes, 1954). They individuated the range of the characteristic velocity from 0.5 to 20 m/s. Hutchinson (1988), for the first time, focused also on the morphology, the kinematics, failure and propagation mechanisms, besides materials and rate of movement. The Author highlighted the important role of water supply and increasing pore pressure for the mobilisation of the flow mass.

Hungr et al. (2001) based their definition on genetic and morphological aspects, avoiding a taxonomic hierarchical description, that considers either movements mechanism, material properties, or movement velocity. Considering landslides of flow-type only, the material involved can be characterised by its origin, its degree of cohesion, and pore pressure conditions (Fig. 2.2). The Authors gave one of the most famous definition of debris flow, as "a rapid to extremely rapid flow of saturated non-plastic debris in a steep channel (Plasticity Index <5% in sand and finer fraction. [...] Materials involved in debris flow range from clay to boulder of several meters.". This statement was later modified by (Hungr et al., 2014) adding the adjective "surging" to highlight the transient nature of this phenomenon, which generally occurs in a

Origin	Character	Condition[1]	Name
SORTED (marine, lacustrine, fluvial, eolian, volcanic, anthropogenic)	Non-cohesive (Plastic Limit < 5%)	Dry or Saturated	- Gravel - Sand - Silt
	Cohesive (Plastic Limit > 5%)	- Plastic ($I_L < 0.5$) - Liquid ($I_L > 0.5$)	- Clay - Sensitive Clay
UNSORTED (residual, colluvial, glacial, volcanic, anthropogenic)	Non-cohesive (Plastic Limit < 5%)	Dry or Saturated	- Debris[2]
	Cohesive (Plastic Limit < 5%)	- Plastic ($I_L < 0.5$) - Liquid ($I_L > 0.5$)	- Earth - Mud
PEAT	Organic	Saturated	- Peat
ROCK	Fragmented	Dry or Saturated	- Rock

[1] Related to the material found in the vicinity of the rupture surface at the time of failure, if it can be determined. In many cases, the material condition must be deduced from the behavior of the landslide, especially velocity.
[2] Debris may contain a considerable proportion of organic material.

Fig. 2.2 Characteristics of the materials involved in landslide of the flow type (Hungr et al., 2001).

series of multiple surges. Furthermore, it is characterised by a strong entrainment capability of both material and water, thus increasing debris flow size up to 10^9 m^3. The Authors also underlined the importance of the lateral confinement; that is, the flow occurs on an established channel, thus enhancing rapidity and water content. Furthermore, they also identified a degree of sorting in the longitudinal and transversal flow profile as a distinguishing feature.

In the present research work, the definition provided by Hungr et al. (2001) is adopted, even if some other aspects have to be considered. For example, Coussot and Meunier (1996) pointed out the importance of the solid fraction, besides the material type. In fact, debris flow is characterised by a sufficiently high solid particle concentration (exceeding 40% according to (Iverson, 2014), and ranging from 50% to 90% according to Ancey (2001)) to allow large deformations inside the mass, without changing the mechanical properties.

2.1.1   Differences with other flow like landslides

In the perspective of clarifying the major features of debris flows, it is worth comparing this phenomenon with other landslides of the flow type, to which debris flow is sometimes equated. Distinguishing among flow-like phenomena is often complicated, and for this reason several Authors have either unified different typologies under the unique name of debris flow or differentiated it in various ways. Figure 2.3 shows the most important characteristics through which a debris flow can be

Rate of movement	Bedrock	Debris (<80% sand and finer)	Earth (>80% sand and finer)
Rapid and higher (>1.5 m/day)	Rock flow (creep, slope sagging)	Debris flow Debris avalanche	Wet sand and silt flow Rapid earth flow Loess flow Dry sand flow
Less than rapid (<1.5 m/day)		Solifluction Soil creep Block stream	Earth flow

(a)

Material	Water content[1]	Special condition	Velocity	Name
Silt, sand, gravel, and debris (talus)	Dry, moist, or saturated	No excess pore-pressure Limited volume	Various	*Non-liquefied sand (silt, gravel, debris) flow*
Silt, sand, debris, and weak rock[2]	Saturated at rupture surface	Liquefiable material[3] Constant water content	Extremely rapid	*Sand (silt, debris, rock) flow slide*
Sensitive clay	At or above liquid limit	Liquefaction *in situ*[3] Constant water content[4]	Extremely rapid	*Clay flow slide*
Peat	Saturated	Excess pore-pressure	Slow to very rapid	*Peat flow*
Clay or earth	Near plastic limit	Slow movements Plug flow (sliding)	Less than rapid	*Earth flow*
Debris	Saturated	Established channel[5] Increased water content[4]	Extremely rapid	*Debris flow*
Mud	At or above liquid limit	Fine-grained debris flow	Greater than, very rapid	*Mud flow*
Debris	Free water present	Flood[6]	Extremely rapid	*Debris flood*
Debris	Partly or fully saturated	No established channel[5] Relatively shallow, steep source	Extremely rapid	*Debris avalanche*
Fragmented rock	Various, mainly dry	Intact rock at source Large volume[7]	Extremely rapid	*Rock avalanche*

[1] Water content of material in the vicinity of the rupture surface at the time of failure.
[2] Highly porous, weak rock (examples: weak chalk, weathered tuff, pumice).
[3] The presence of full or partial *in situ* liquefaction of the source material of the flow slide may be observed or implied.
[4] Relative to *in situ* source material.
[5] Presence or absence of a defined channel over a large part of the path, and an established deposition landform (fan). *Debris flow* is a recurrent phenomenon within its path, while *debris avalanche* is not.
[6] Peak discharge of the same order as that of a major flood or an accidental flood. Significant tractive forces of free flowing water. Presence of floating debris.
[7] Volume greater than 10,000 m^3 approximately. Mass flow, contrasting with fragmental rock fall.

(b)

Fig. 2.3 Main characters of the landslides of the flow type, according to (a) Varnes (1978), and (b) Hungr et al. (2001).

recognised among other landslides of the flow type, according to Varnes (1978) and Hungr et al. (2001).

One of the most comprehensive classification of sediment flows has been performed by Pierson and Costa (1987) (Fig. 2.4), who considered the sediment concentration and grain-size distribution as fundamental parameters to rheologically subdivide debris flow phenomena from others. Also the mean velocity plays an important role. Figure 2.4 shows how debris flow is associated with a rapid increase in yield strength, that allows the static suspension of gravel and the onset of a liquefaction behaviour. The left boundary B (Fig. 2.4) marks the rapid increase of yield strength. Before this limit, the phenomenon is called *hyperconcentrated streamflow*. This is an apparently liquid flow, that is a flowing mixture of water

and sediments (20%-60% solid fraction in volume) which, despite possessing a measurable but low yield strength, still appears to flow like a liquid. The sediment concentration of the hyperconcentrated streamflow is intermediate between normal sediment-laden stream flow and debris flow concentration. On the contrary, the right boundary C (Fig. 2.4) marks the cessation of liquefaction behavior. After this threshold the phenomenon is called *earth flow*, *grain flow*, or *debris avalanche* depending from its velocity. However, in the present research it is assumed valid also the distinction made by Hungr et al. (2001), according to whom debris avalanche is a non-channelized phenomenon.

Similarly to the hyperconcentrated streamflow, Hungr et al. (2001) considered also the *debris flood*, which is a very rapid surging flow of water, but whose sediments concentration is comparable with the one of debris flow. Another phenomenon similar to debris flow is called *mud flow*, whose difference lies in the plasticity of the debris and water mixture, with a plastic index >5% (Hungr et al., 2001). This feature gives cohesion to the material, while debris flow is, in general, considered as a non-cohesive material flow. Finally, the *debris avalanche* is similar to the debris flow for materials type, velocity involved, but it is not confined in an established channel, thus resulting in a saturation of the debris.

2.2   Classification of debris-flow types

In this section the mechanical classification of debris flow type made by Takahashi (2007) is introduced, as well as the rheological one proposed by Coussot and Meunier (1996). Finally, the rheological-mechanical classification presented by Ancey (2001) and Bardou et al. (2003) is shown as it considers both aspects and is considered one of the most complete. Finally, the different classes of nomenclature are compared. The aim of this section is to evaluate the different types of debris flow generally observed. This is important in the perspective to correctly simulate the flow dynamics and to accurately choose the input rheological parameters in the frame of a numerical modeling of the flow.

Takahashi (1978, 2007) based his classification according to the prevalence within the flow of one (or more) of the following types of stresses, as defined by Iverson et al. (1997):

SEDIMENT CONCENTRATION (VOL.%)
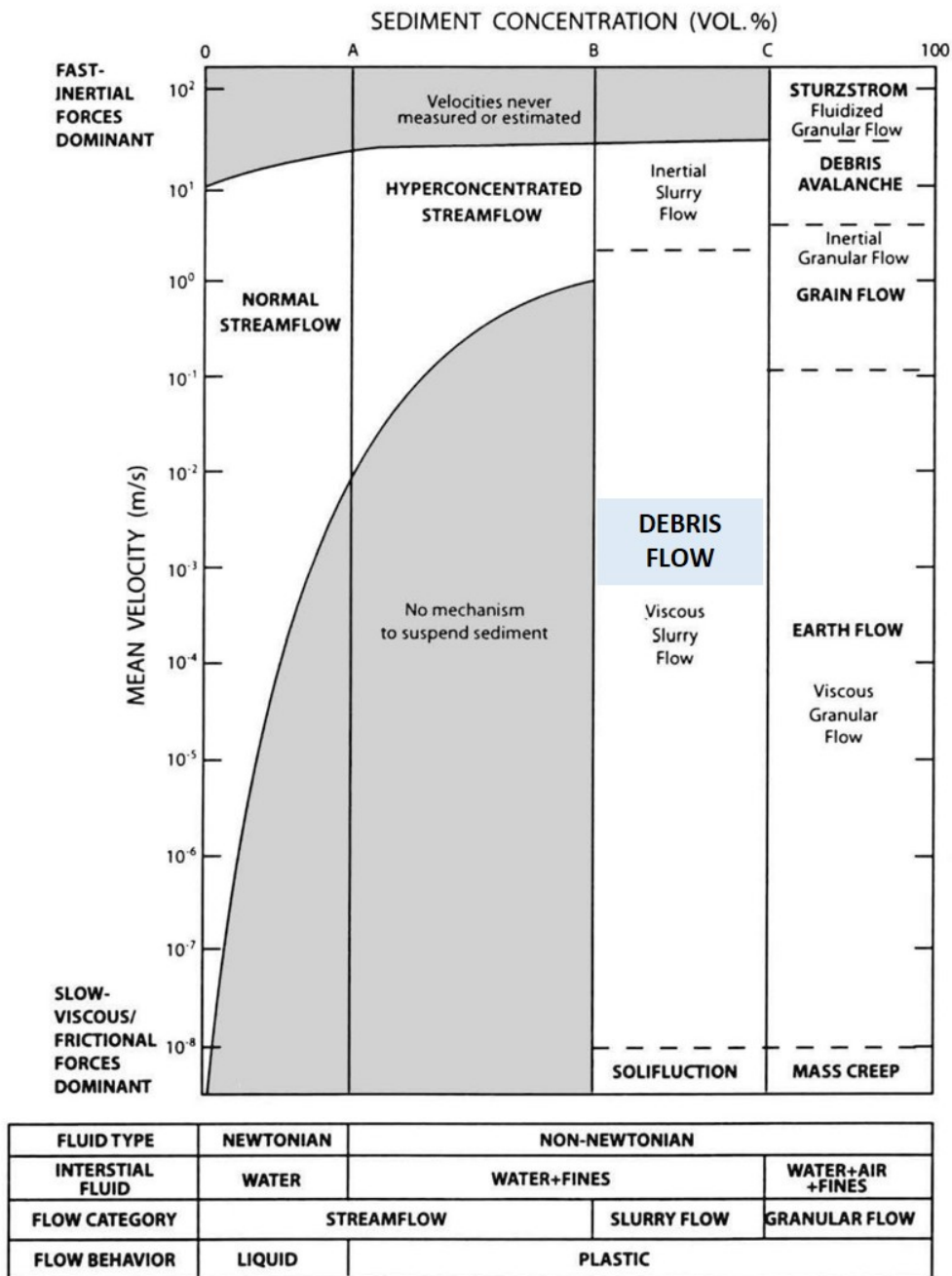
Fig. 2.4 Rheologic classification of sediment flows. Unified version of two schemes proposed by Pierson and Costa (1987). Exact values of the boundaries of sediments volume concentration can not be defined, as they depend also on grain-size distribution and physical-chemical composition of the material.

- *Inertial grain stress* $\mathbf{T}_c$: this stress is due to collisions among the coarser particles of the debris flow mass.

- *Inertial fluid or turbulent stress* $\mathbf{T}_t$: this stress is due to the macro turbulent mixing of the fluid body comprising the fluid and the finer particles of the mass.

- *Quasi-static Coulomb friction stress* $\mathbf{T}_{sq}$: this quasi-static solid stress is due to the frictional forces between particles.

- *Quasi-static Newtonian or viscous stress* $\mathbf{T}_{fq}$: this quasi-static fluid stress is due to the deformation of the viscous mixture composed by fluid and finer particles.

- *Solid fluid interaction stress*: this stress is the one that arises between solid and fluid phase.

Some useful ratios between these stresses have been defined to identify the preponderance of one of these stresses among the others. The transition values provided, although studied for debris flow Iverson (1997), are not to be considered as strict limits:

- *Bagnold number* Ba: $\mathbf{T}_c/\mathbf{T}_{fq}$. If Ba>200, collisional stresses prevail on viscous ones.

- *Reynolds number* Re: $\mathbf{T}_t/\mathbf{T}_{fq}$. This number allows to define if the flow is turbulent or laminar, even though the fluid within the pore space of a debris flow is always laminar (since Darcian flow applies), except at the head of the flow. There, the particles are often too large and the fluid phase separates, desaturating the front. The pore pressure developed between moving grains tends to buffer grain interactions (Iverson, 1997).

- *Savage number* Sa: $\mathbf{T}_c/\mathbf{T}_{sq}$. If the quasi-static Coulomb friction stress $\mathbf{T}_{sq}$ prevails, Sa<0.1. This is possible only for solid concentration $C_s > 0.51$ (Takahashi, 2007), as particles must be in contact. This solid concentration refers to an average mass and assumes uniform grain distribution.

- *Mass Number* Ma: $\mathbf{T}_c/\mathbf{T}_t$. This number is equal to the ratio between the depth of the flow h_d and the representative particle diameter d_p.

Figure 2.5 represents the mechanical classification introduced by Takahashi (1978, 2007), which highlights the prevalence of one stress over the others, making use of the previously mentioned ratios. Furthermore, the Author stated that a complete dynamic development of debris flow also depends on the solid concentration C_s, which has to be $0.2 \leq C_s \leq 0.56$. If $C_s \geq 0.56$ neither dynamic nor quasi-static debris flow is possible and the material becomes rigid. This corresponds to the definition of debris flow made by Pierson (1986). Three different types of debris flow have thus been identified:

- *Stony type*: when the inertial grain stresses $\mathbf{T}_c$ prevail.

- *Turbulent muddy type*: when the inertial fluid stresses $\mathbf{T}_t$ prevail.

- *Viscous type*: when the viscous stresses $\mathbf{T}_{fq}$ prevail.

Furthermore, Takahashi (2007) grouped the stony and the turbulent types in a unique category called *inertial debris flow*. Nevertheless, this classification does not consider the rheological aspects, due to the solid-fraction and the ratio between fine content and total solid fraction. According to the Authors, fine particles refers to clay and sand, i.e. particles whose main size is ≤ 0.04 mm. This distinction was first made by Coussot and Meunier (1996). The Authors subdivided in:

- *Muddy debris flow*: in this case, the fine fraction is large enough (>10%) to lubricates the grain and imposes its behavior on the whole mass.

- *Granular debris flow*: in this case, the fine fraction is so low that the coarse grain contacts play the major role on the mass behavior.

As mentioned before, firstly Ancey (2001) and further Bardou et al. (2003) developed a complete classification of debris flows, accounting for both the mechanical and the rheological aspects. This classification is considered in the present research work as one of the most comprehensive. In particular, they distinguished three types (Fig. 2.6):

- *Muddy debris flow*: this type is characterized by a viscoplastic behavior, due to the high content of fine material, containing clay. The liquid and fine particles lubricate the contacts between the coarse particles. As the matrix is more dilute, this kind of debris flow generally reaches longer runout distance and
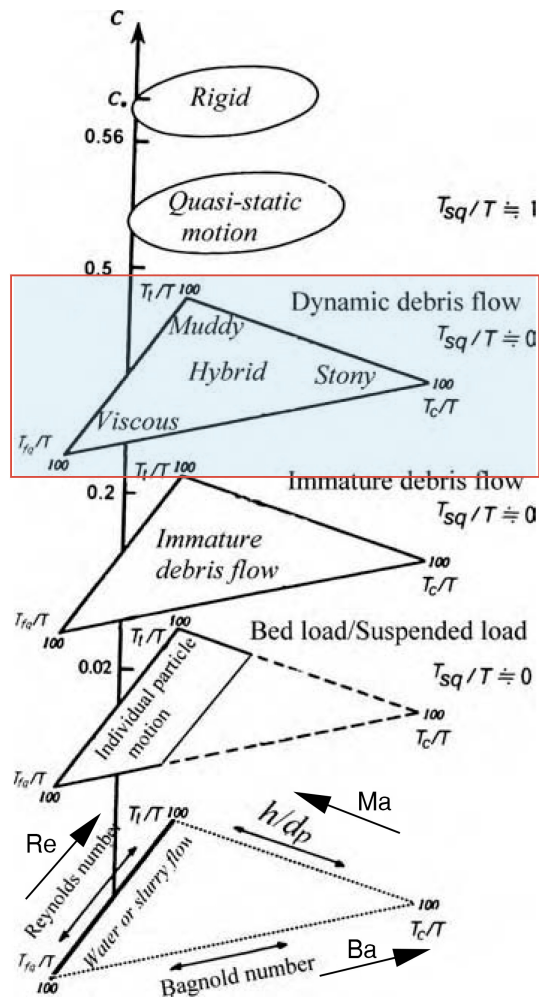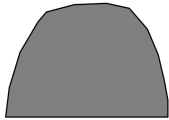
Fig. 2.5 Mechanical criterion to classify the debris flow types (Takahashi, 2007). The total stresses are represented with the symbol **T**. The immature debris flow corresponds to the hyperconcentrated streamflow, while the quasi-static motion corresponds to the earth flow, as as defined in Sec. 2.1.1.

	Scientific name	viscoplastic	collisional-frictional	frictional-viscous
Mechanics	**Appropriate rheophysical model**	Herschel-Bulkley Bingham	Coulomb-like, collisional-frictional constitutive equation	Coulomb-like at low speed Newton-like (or power-law) at high speed
	Common name	muddy	granular	fluid
Field observation	**Deposit appearance**	smooth with clear limits in the field, very cohesive once dry	rough with no clear deposits limits in the field, non cohesive once dry	terrace-like deposit, very cohesive once dry
		levee cross-section	levee cross-section	whole body cross-section (not the same scale as levee cross-section sketch)
	Stopping slope	< 2°	< 10°	< 1°
	Grain size	grains + + matrix + + clays +	grains + + matrix- clays - -	grains - / + matrix + + silts + clays -

The following notation is adopted :
− − very little content
−   little content
+   high content
+ + very high content

Fig. 2.6 Rheological-mechanical classification of debris flow types according to Bardou et al. (2003).

presents a deposit where the coarser grains are randomly distributed in a finer matrix. According to the fine content, either turbulent stress (T_t) or viscous stresses (T_{fq}) are involved. In particular, the more dilute the fluid is, the more the turbulent stress prevails.

- *Granular debris flow*: in this case the mechanical behavior is collisional (T_c) and frictional (T_{sq}). The prevalence of inertial grain stress to the frictional one depends on different factors, such as the internal frictional coefficient, the solid concentration, and the steepness of the slope.

- *Fluid or lahar-like debris flow*: this type has a frictional-viscous behaviour, due to a high fine content. This kind of flow is typical of volcanic soil areas. The clay content is small, but the matrix is rich with silt.

Finally, Table 2.1 constitutes an attempt to correlate the different nomenclature proposed by different Authors, subdividing in the above mentioned three categories.

Authors	Muddy debris flow	Granular debris flow	Fluid debris flow
Varnes (1954)		Debris flow	
Hutchinson (1988)	Debris flow involved weathered rock debris (except on volcanoes)	Channelized debris flow	Associated with volcanoes, lahars
Takahashi (1978)	Viscous type debris flow	Stony type debris flow	Turbulent muddy debris flow
Coussot & Meunier (1996)	Muddy debris flow	Granular debris flow	-
Hungr *et al.* (2001)	Mudflow	Debris flow	-
Ancey (2001)	Muddy debris flow	Granular debris flow	Lahar debris flow
Bardou *et al.* (2003)	Muddy debris flow	Granular debris flow	Fluid debris flow

Table 2.1 Correlation among the different nomenclature given from several Authors.

It emerges that providing a unique classification is still difficult and some debris-flow type can be associated to other landslide of flow type.

2.3 Debris-flow dynamics

In this section, the main characteristics of the debris flows during all their path are introduced. In fact, as recognized by Iverson (2014), debris flows typically involve a sequence of events, explained in the following paragraphs.

2.3.1   Triggering conditions and mobilization

In is widely recognized (e.g. Ancey, 2001; Costa, 1984; Hutchinson, 1988; Varnes, 1978) that the principal prerequisite conditions to mobilize debris flow can be ascribed in:

- *Abundant source of unconsolidated materials*: both in the initiating zone and along the channel a large amount of fine-grained rocks or soil debris is required, promoting an high weathering.

- *Steep slope*: this characteristic promotes the instability of the marginal stable debris, especially when saturated. Furthermore, the steeper the channel is, the higher the velocity of the flowing mass will be.

- *Large source of moisture and excess of pore pressure*: a large but intermittent source of moisture is required for the saturation of the sediments. This can be produced by rainfall, snowmelt, glacial outburst floods and rapid drainage of volcanic crater lakes. In general, the most common situation occurs when a continuous rainfall occurs for a period and, after it ceases, the soil remains partially saturated, with negative pore pressure. Then, a subsequent high-intensity rainfall provokes the saturation and consequently an abrupt positive pore-pressure situation occurs in the debris.

- *Sparse vegetation*: a slope denude of vegetation intensifies the susceptibility to debris flow. This condition, according to Varnes (1978) can be enhanced by wildfires.

Iverson (1997) defined the mobilization as "the process by which a debris flow develops from an initially static, apparently rigid mass of water-laden soil, sediment and rock". Several Authors (e.g. Armanini, 1997; Coussot and Meunier, 1996; Iverson et al., 1997) have investigated the main types of initiation processes, which can be ascribed as:

- *Erosion of the surface of the initiating zone and mobilization of sediments*: the marginally stable debris mantle becomes saturated by an intense rainfall or thawing processes and begins its motion.

- *Progressive transition of a sliding phenomenon into a debris flow*: sliding type landslides generally differ from debris flow as the latter allows internal

deformations during its motion. This transition requires a sufficient conversion of gravitational potential energy into internal kinetic energy. This conversion can derive from a slope increase or from a supply of water. Nevertheless, Iverson et al. (1997) highlighted also that the required amount of water to generate this transition does not necessarily cause a complete saturation of the mass. In fact, the spatial distribution of pore pressure can alone determine the Coulomb failure potential. Furthermore, the transition can occur also by a partial or complete liquefaction due to an abrupt increase of pore pressure originated by an earthquake. Finally, the grain collision with a rough bed can cause an increase in the granular temperature and thus some translational kinetic energy is transformed into internal kinetic energy (Iverson et al., 1997).

- *Collapse of a natural dam formed in the riverbed or of a retaining system hit by an initial debris flow:* a consistent volume of debris is abruptly released, promoting a debris flow event.

2.3.2   Path and shape evolution

It is widely recognized that a debris flow path can be clearly subdivided into an initiating, a transport, and a deposition zone, whose characteristics are quite different. In these three stages of motion, debris flow assumes different typical configurations.

Initiating zone

The initiating zone is characterized by the morphological requirements expressed in the triggering conditions (Sec. 2.3.1), that is an abundant source of debris and steepness. Nevertheless, referring to the latter, i.e. the slope required to promote debris flow initiation, different Authors propose significantly different values. This may be partly attributable to the geographic area of interest. Table 2.2 provides an overlook on the steepness suggested by different Authors, comparing also the geographic area of origin both of the Author and of observation of the phenomena. In addition, the basis of their statements is provided.

Authors	Steepness (°)	Observed area	Authors's origin area	Note
Takahashi (1978)	15°-23°	China and Japan	Japan	From infinite slope theory, inertial regime according to (Bagnold, 1971)
Costa (1984)	>15°-20°, commonly exceeding 30°	All the world	USA	From observation of real cases
Ancey (2001)	>11°	All the world	France	From laboratory experiments
Hungr *et al.* (2005)	20°-45° In steeper slope the required amount of debris is not in general sufficient.	Not specified, examples from Canada and Nepal	Canada and Spain	From field observations.
Iverson (2014)	>25° (generally 25°-30°)	Not specified, examples from USA	USA	From observations of real cases

Table 2.2 Steepness requirement in the initiating zone according to different Authors.

Transportation zone

The transportation zone is constituted by either a bedrock channel generally covered by erodible soil or a fully erodible channel, generally steeper than $10°$. In this stage, the velocity of the flow increases, ranging from 0.5 to 20 m/s, according to the size, the concentration and the sorting of the material, and to channel geometry. During its motion, the debris flow generally entrains loose material and water from the bed and the banks, thus growing in size. The volume increase can be even tenfold or more (Iverson, 2014). Fannin and Wise (2001), from several field observation on the Queens Charlotte Islands debris flow events, observed that, along a debris flow transportation zone, entrainment dominates for slopes greater than $10°$, while deposition is not an important factor.

During the motion, an inversely graded particle-size distribution can be observed, thus creating an upward coarsening. The small particles percolate downward, and the larger particles remain on the surface. Furthermore, the debris flow mass presents a vertical velocity gradient: the velocity profile shows higher velocity on top, so that the coarser grains, positioned on the surface, are pushed towards the front (Johnson et al., 2012), as shown in Fig. 2.7. As a consequence, the flowing mass is characterized by a longitudinal sorting, which brings the largest clasts, or even boulders, towards the flow front, thus creating the so called head-and-tail morphology. This results in a bouldery front, relatively free of matrix, a main body of finer or liquefied debris, and a dilute tail (Fig. 2.8). Thus, the front is characterized by a great permeability and high frictional resistance, while the body sustains high pore pressure, due to its lower permeability. The tail is also called afterflow (Hungr et al., 2005), and it is similar to a hyperconcentrated streamflow, which pushes against the body. The differences in frictional resistance and in the pore pressure diffusion also explain the surging feature of the phenomenon. Hungr et al. (2001) underlined that the longitudinal sorting as well as the surging aspect are encouraged by the presence of a channelized path. Finally, the repeated undrained loads, due to progressive entrainement of water and sediments, promote a multiple-surge behavior.

Deposition zone

When the whole kinetic energy of the flowing mass degrades to an irreversible form, i.e. the grain vibrational energy progressively falls to zero, the deposition process

SIDE VIEW
(cross section
moving with flow)

Path of largest particles

Largest particles collect at
front and are pushed to sides

Velocity profile

TOP VIEW
(Moving with front of flow)

Paths of largest particles at surface

Largest particles
lag behind as
levees form

(a)

Coarse-enriched surface layer

Breaking size-segregation wave

Levee

Deposition point

(b)
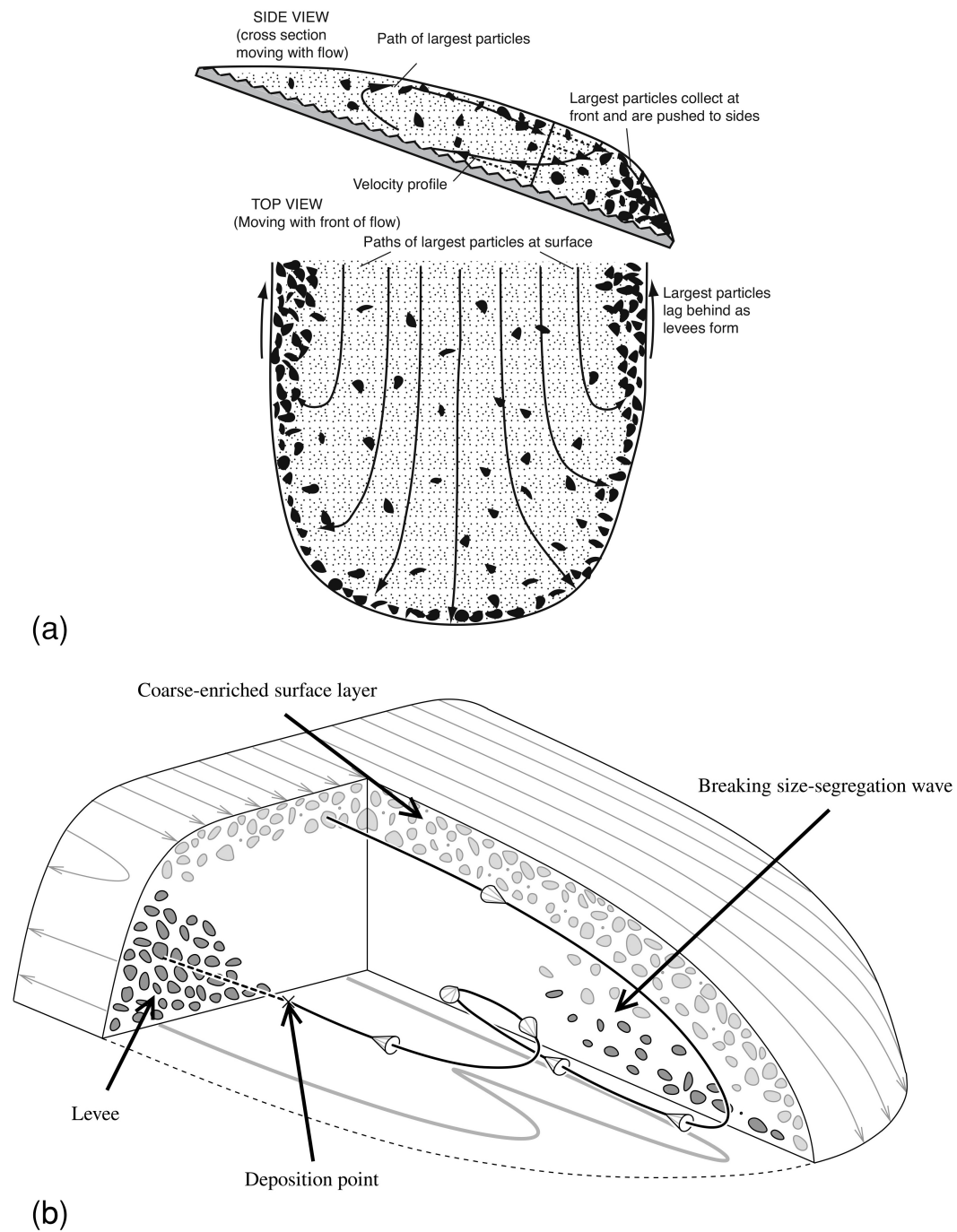
Fig. 2.7 (a) Scheme of how segregation of coarse particle on the surface of a debris flow promotes the segregation to the front and to the margins of the flow (Vallance, 2005), (b) 3D view of the recirculation of particles in the moving mass (Johnson et al., 2012).
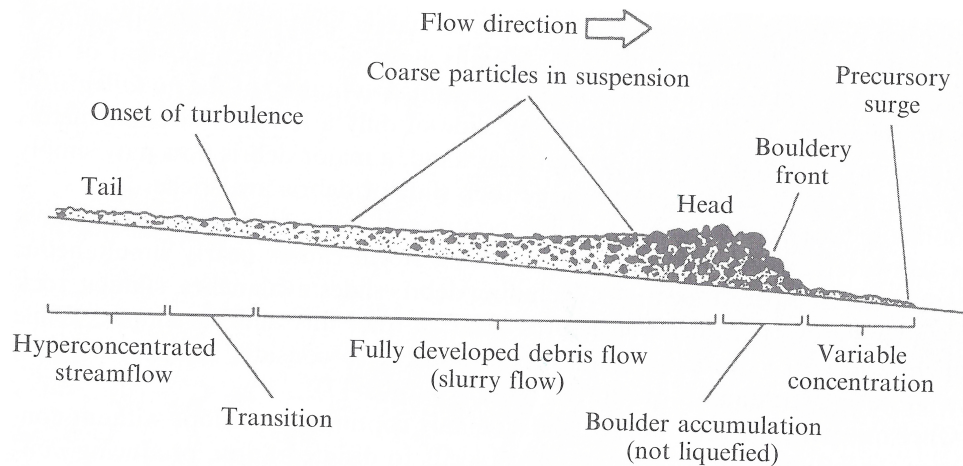
Fig. 2.8 Characteristic morphology of a debris flow during in motion (Pierson, 1986).

begins (Iverson et al., 1997). The energy decrease is generally due to a combination of a slope reduction and a loss of confinement (Ancey, 2001) and occurs on an established fan, called debris fan, colluvial fan or cone (Hungr et al., 2005). As regards the former, Ancey (2001) stated that, in Alpine regions, debris flows usually begin to decelerate when the slope is 10%-25%, and can propagate over gentle slopes (of less than 5%). Nevertheless, the slope deposition angle is a function of the the grain concentration by volume, density, size, the total volume, and the angle of the internal friction of the flowing mass (Takahashi, 2007). Hence, in fact, Hungr et al. (2001) stated also that in general fan slopes ranges from $5°$ up to even $20°$.

When the flow loses the channel confinement, the main body of the surge collapses, thus depriving the front of the hydraulic thrust that propels it forward. Then, when the frictional resistance of the coarse-grained flow front is sufficiently high to halt motion, the depositional process occurs. The front rapidly deposits in the form of levees, that are ridges of coarse material, or abandoned boulder fronts, while the finer and more dilute material in many cases continues further downslope, spreading in lobes.

Nevertheless, a constant deposition rate can occur also along the whole channel during runout, forming the levees on the lateral boundaries of the channel, which act as additional banks. In this case, the deposition process can occur also before the loss of confinement. In fact, while lateral levees arise, the advancing flow head

becomes thicker, and the progressive slope reduction causes the deposition of the granular front. Then, the sudden stop of the granular front increases the flow depth of the body, promoting its overflow over channel banks and spreading as broad lobes (Ancey, 2001). Finally, Iverson et al. (1997) highlighted that also the pore pressure distribution plays an important role in the deposition process and in the final morphology. The wetter the flowing mass is, the more the debris is mobile, preserving its momentum, thus reaching longer distances. Conversely, the less the pore pressure is, the more the frictional resistive forces halt the motion. It is worth mentioning that this aspect is function of both water supply, grain size distribution, and permeability.

Chapter 3

Structural mitigation measures for debris flow

Mitigation measures are essential for minimising the existing risk, reducing it to an acceptable residual level. Different solutions can be adopted depending on the spatial and temporal targets and on the requested degree of protection. Two types of mitigation measures can be distinguished: passive and active (Hübl and Fiebiger, 2005). Passive mitigation measures are used to reduce the potential loss of both life and buildings. They alter the spatial and temporal character of either the damage produced or the associated vulnerability (Hübl et al., 2005), i.e. the conditions which increase the susceptibility to the impacts of hazards. As an example, land-planning, as well as improved environmental policies and public awareness, promotes the reduction of potential loss. In contrast, active mitigation measures focus on lowering of the hazard. To achieve such goal, both disposition and event management can be applied, controlling the probability of occurrence or the flow itself (Hübl et al., 2005). In the former case, generally, non structural measures are adopted, while, in the latter, structural ones are employed. Non-structural measures involve policies and laws, public awareness raising, training and education to reduce disaster risk, while structural measures are especially designed constructions aimed at reducing or avoiding possible impacts, or enhancing resistance and resilience of a hazardous area.

Active debris-flow mitigation measures can be designed to either control the triggering, changing its occurrence frequency and magnitude, or the evolution of phenomenon, changing the deposition settings. Focusing on the latter desiderata,

concerning the event management, different possible engineering solutions can be undertaken. The present research focuses on those measures that can be built along the stream, i.e. check dams or rigid barriers, as being particularly effective to prevent the loss of human lives and protect settlement and infrastructures (Kwan, 2012).

The main objectives and functions that can be achieved with barriers in the frame of debris flow management are (Hübl et al., 2005; Piton and Recking, 2016; Suda et al., 2010):

- *Retention*: more or less permanent storage of sediments. These sediments have to be dredged by machinery after an event.

- *Dosing*: temporary retaining of water and/or sediment. After an event, the deposits should be released by water during the following regular streamflow.

- *Filtering or sorting*: filtration and deposition of the coarse sediments, allowing only water and a grains size below a threshold value to pass the structure. This implies a particle segregation by size.

- *Energy dissipation or debris flow breaking*: reduction of the high-energy of a debris flow by slowing or depositing the surge front of the flow.

Two kinds of barriers can be distinguished: closed and open (Fig. 3.1). The former can efficiently lower the kinetic energy of the impacting mass, but is often rapidly filled by the solid material, losing its effectiveness. The latter open barriers can be designed to either promote a temporary retention of sediments and water or to filter water and fine particles, entrapping the coarse material. As stated in the introductory chapter, this research work focuses on open barriers, and in particular with structures designed for filtering and energy dissipation.

3.1   Open barriers

Open barriers, according to the way in which they are designed, constitute an effective measure for dosing, filtering and for energy dissipation. In particular, two main complementary approaches exist in the design of open barriers, i.e. hydraulic and/or mechanical controls of the deposits (Piton and Recking, 2016). The choice of one of these typologies depends on the functions for which they are designed. In
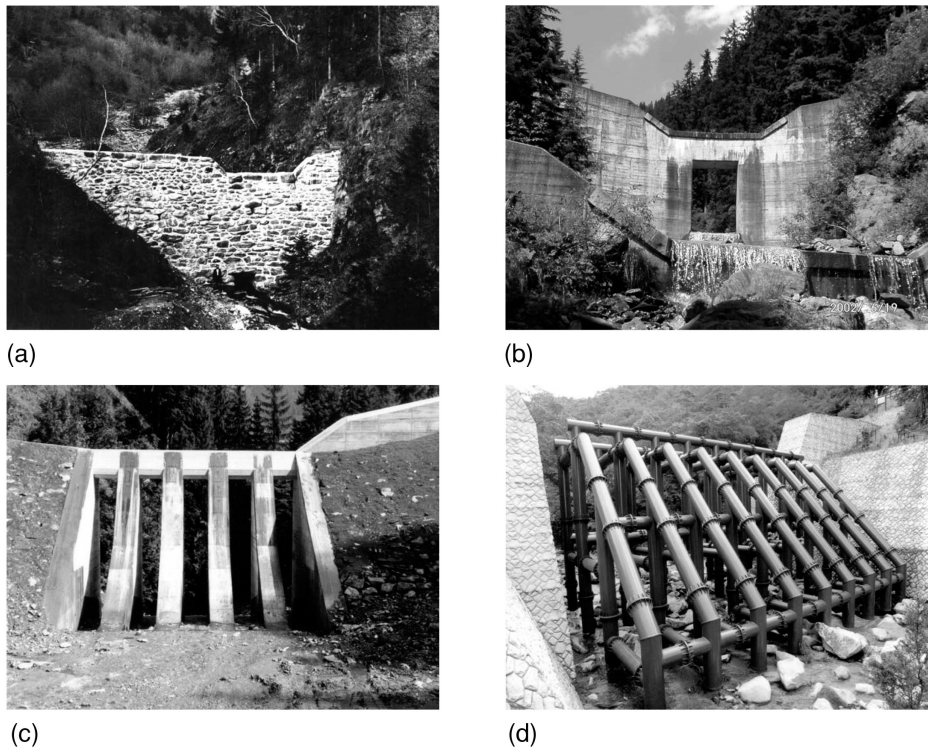
Fig. 3.1 (a) Closed barrier, Einachgraben, Austria; Open rigid barriers: (b) large slot barrier, Nieschenbach, Austria; (c) sectional barriers with fins, Luggauerbach, Austria; (d) lattice barrier, Ashiya River, Japan (Hübl et al., 2005).

particular, hydraulic control achieves the dosing and energy dissipation functions, while mechanical control the filtering and energy dissipation.

The hydraulically controlled deposits (Armanini, 1997; Armanini et al., 1991; Larcher and Armanini, 2000) relates to the deceleration of the flowing mass due to the reduction of the natural channel section created by the barrier, Fig. 3.2(a). This kind of barrier presents one, or rarely more, narrow, vertical openings, spanning the whole height of the barrier. When the flowing mass reaches the barrier, the narrowing of channel section promotes the deceleration of the flow and the creation of a calm water area, allowing most of the particles to deposit upstream the dam. This phenomenon is called "backwater effect" and the temporary deposition is also defined "hydrodynamic sorting" (Armanini et al., 1991). When a steady flow regime is re-established, the deposited sediments are released by the erosion action of the water. In this manner, water cleans the barrier, restoring its functionality. This type of structures is also defined as "self-cleaning". These barriers have traditionally

been designed for sediment transport rate control in the frame of torrent restoration (Armanini and Larcher, 2001). Only in a later stage extended to a temporary storage of the debris volume (Armanini et al., 2006). Based on the conservation of the mass of water and sediments and on the energy balance between an upstream section and the section of the barrier outlet, the height of the barrier and the opening size are calculated. Nevertheless, despite theoretical prediction, it is worth mentioning that the perfect self-cleaning of the structure does not always occur. In particular, during debris flow events, the outlets can be obstructed by large boulders that have to be mechanically removed.

Mechanically controlled deposits relate to the direct clogging of barrier outlets, whose size is comparable to the coarse sediments which have to be entrapped, Fig. 3.2(b). The openings width is the crucial parameter for the filtering. In particular, the design approach of the filter is based on the clogging probability as a function of the ratio between the shorter dimension of the opening, called S, and the relevant grain size D_{max}. This corresponds to the minimum grain size that has to be entrapped. According to D'Agostino and Bertoldi (2014), the maximum sediment diameter D_{max} to consider has to be taken in the interval $D_{75} - D_{84}$ of the armoured bed surface, where D_{75} and D_{84} are the diameters corresponding to the 74 and 84 percentile of the grain size distribution, respectively. The values of the ratio S/D_{max} found in literature mainly derive from observations of past events (Ikeya, 1989; Watanabe et al., 1980) or laboratory experiments (Han and Ou, 2006; Itoh et al., 2011; Mizuyama et al., 1995), i.e. on a small scale. A twofold difficulty emerges: the choice of the D_{max} to consider and its estimation. Another drawback is represented by the fact that, once coarse materials clog, also the fine particles suspended in the debris flow upstream the barrier can be obstructed and thus stopped, preventing the filtering function of the barrier. Considering the height of the barrier, this parameter has to be equal or higher than the necessary deposition height.

Of course, due to the variability of real events, hydraulic and mechanical control may occur also together. Moreover, despite this functional subdivision, a wide variety of rigid barrier typologies exists. This reveals how unique design criteria do not exist. Dosing and sorting effects can be pursued in the form of large slots, slits, piles, fins, beams and so on. Furthermore, no universal nomenclature exists yet. A classification can be performed according to either functions, building materials or geometrical characteristics of the main body of the structures. Wehrmann and Johannes (2006) proposed a classification of both open and closed barrier depending on the opening
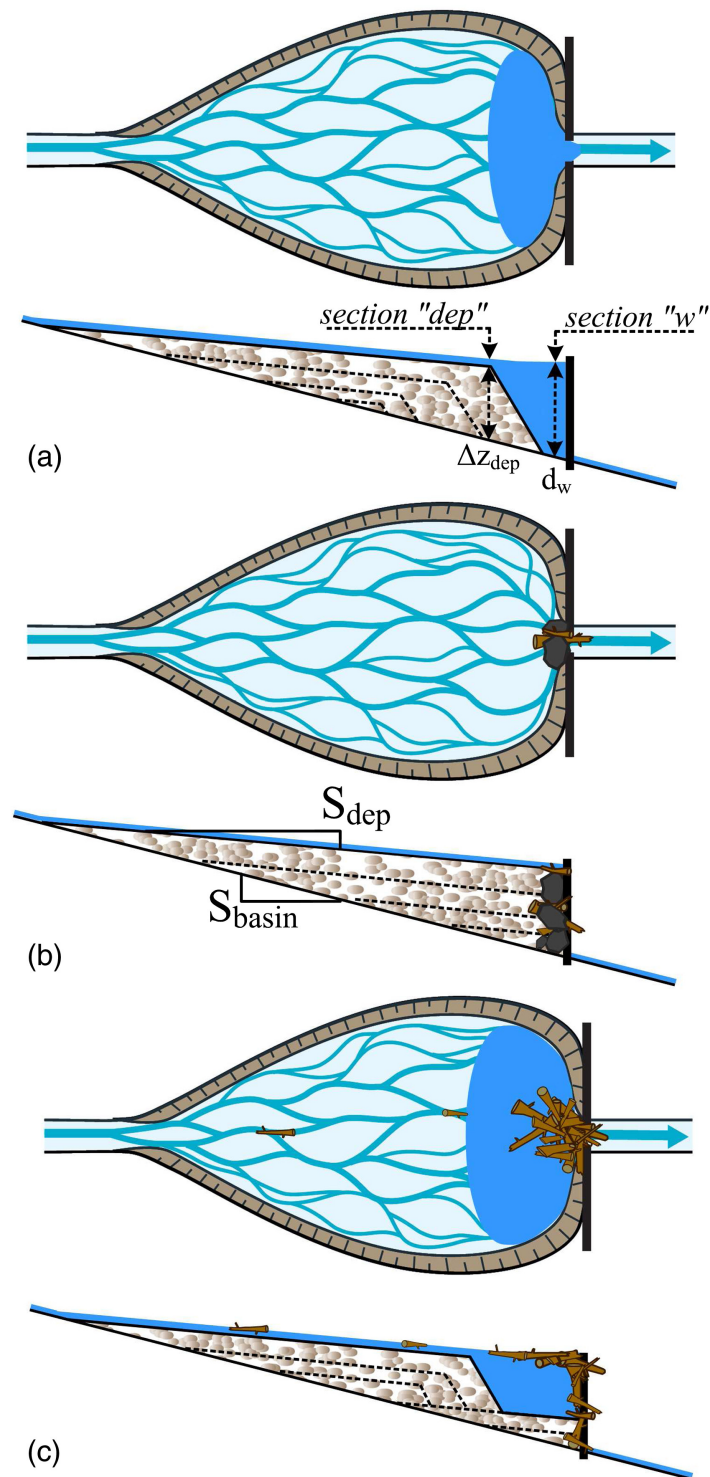
Fig. 3.2 Plan and longitudinal schemes of: (a) hydraulic control of the deposits, (b) mechanically controlled deposits, (c) mixed controlled deposits (Piton and Recking, 2016).

dimensions. With a particular focus on the open type, this classification is adopted in the present research work, but using the term "barrier" instead of "dam". According to this classification, the relevant dimension of the openings are illustrated in Fig. 3.4, where w_0 and w_s stand for the above defined S and P, respectively:

- *Height of the opening h_o*: vertical size of the outlet.

- *Width of the opening S*: horizontal size of the outlet.

- *Long side of the opening l_o*: maximum size of the opening ($l_o = max(h_o, S)$).

- *Narrow side of the opening n_o*: shortest size of the opening ($n_o = min(h_o, S)$).

Figure 3.4 shows six subclasses for the open barrier types:

- *Slot barrier*: open barrier with a continuous overflow crest that fulfills one of the following conditions: $l_o \leq 2n_o$ and $l_o > h_{bar}/2$ (with h_{bar} the height of the barrier) or $l_o \leq h_{bar}/2$. Furthermore, a slot barrier is considered large if the width of the openings is designed to let part of the sediment pass.

- *Slit barrier*: open barrier which fulfills one of the following conditions: $l_o > 2n_o$ and $l_o > h_{bar}/2$ or $l_o > h_{bar}/2$. In both cases $S < P$ (with P the width of the solid element).

- *Compound barrier*: a transitional type for which $h_o \leq h_{bar}/2$ but with no openings larger than weep holes within the lower half of the dam.

- *Sectional barrier*: in this case $h_o > h_{bar}/2$, similar to the slit dam but with $S \geq P$. The filtering part of the barrier consists in fins, narrow side charged walls, or piles, columnar bodies.

- *Lattice barrier*: the filtering part of the barrier consists of bars, that is elements with a very small cross sectional area in respect of their length. These bars are defined "rakes" if vertical, or "beams" if horizontal. If the dam body consists of both beams and rakes, the barrier is defined "plane grill barrier" in 2D and "frame barrier" in 3D (or also *Sabo dams* in Japan).

- *Net barrier*: consists of flexible elements which form a net.
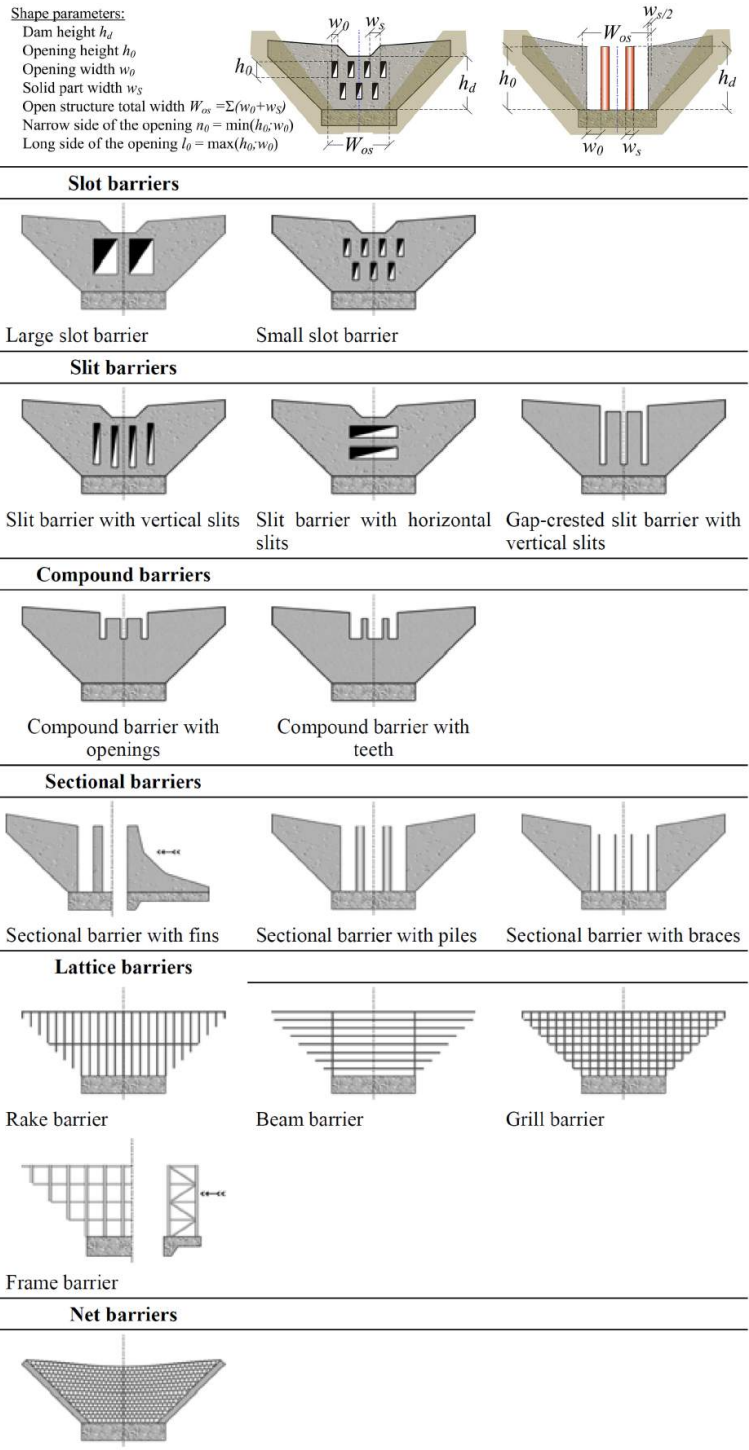
Fig. 3.3 Types of open barriers according to Wehrmann and Johannes (2006). Adapted from Piton and Recking (2016) and Hübl et al. (2005).

Among these typologies, open barriers with large slits or slots are generally adopted for dosing and energy breaking functions, while sectional, small slits, lattices, and net open barriers for filtering and energy breaking ones (Piton and Recking, 2016). Thus, with particular reference to the barriers designed with filtering purposes, as revealed by Fig. 3.4, several configurations exist. Filters can be realised by installing piles, or beams, or both, i.e. sectional barrier with piles, beam and grill barrier respectively. Generally, steel beams are used, while for piles concrete or steel is usually employed. Lattice steel barriers, also defined Sabo dams, are generally adopted in Japan, where steel structures and buildings are widely designed. However, no detailed study exists on the filtering effectiveness of one type in comparison with another and the design choice ofter derives from economic, installation or maintenance reasons or even from the tradition of the country. Only some suggestions can be provided by small-scale laboratory experiments, proving the effectiveness of horizontal beams (Itoh et al., 2011; Wang et al., 2014) to allow a through-flow, of an aligned plan layout in comparison with a V shape (Silva et al., 2016, 2015), or of fins inclined to promote the energy dissipation function. Choi et al. (2018), showed a that a V-type barrier, i.e. where the piles were placed in a V-shape, has a higher trap ratio than the P-type, in which each rectangular pile is placed in parallel, due to the smaller effective opening ratio, defined as the ratio between the flow outlet width and the total channel width. Furthermore, the trap ratio decreased increasing the piles angle for the P- and V-type arrangements. Furthermore, the Authors revealed that an angle of the barrier piles smaller than $60°$ is required to benefit from debris trap mechanisms. However, even though other laboratory tests have been performed involving the discharge of a mass in an incline channel adopting an open barrier (Choi et al., 2016; Han and Ou, 2006; Shima et al., 2016; Shrestha, Badri Bhakta Nakagawa et al., 2007, e.g.), these references do not compare different barrier typologies.

As the present research work focuses on structures designed for filtering and for energy dissipation, slit barriers and sectional barriers are considered. These are widely employed, especially in the Alpine regions. They are traditionally preferred to a lattice barrier as areless expensive and easier to install on steep slopes. In addition, the use of concrete or composite steel-concrete, rather than only steel barriers, can be justified by the Italian tradition on civil engineering structures.

The design of such structures is related to both the filter sizing and the determination of the impact forces. In the following chapter both the filter sizing and impact

(a)
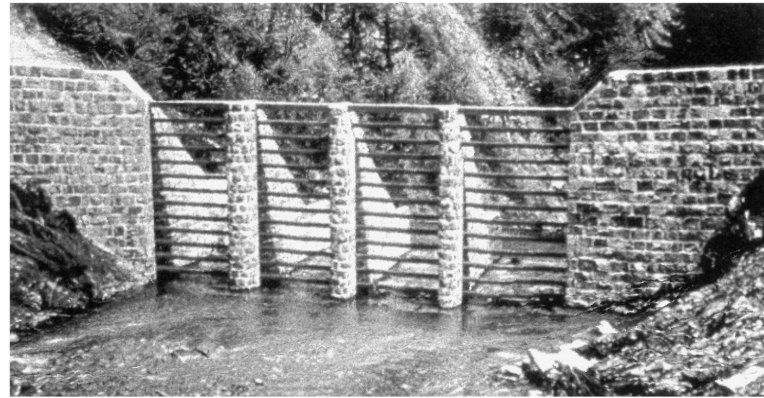
(b)

(c)

Fig. 3.4 Open rigid barriers: (a) sectional barrier with piles (Saint-Vincent, Italy), (b) beam barrier in Zillertal, Tyrol (Austria) (Armanini and Larcher, 2001), (c) sabo dams in Hokkaido (Japan) (Ishikawa et al., 2014).

forces evaluation problems are considered, presenting the state of the art. It reveals that, still nowadays, the rational design of these barrier remains an unresolved issue.

Chapter 4

Previous work on the interaction between debris flow and barriers

This chapter deals with the state of the art related to the two main features of open barrier design: the evaluation of the impact forces and sizing the filter. As a specific regulation or standardised procedures does not exist, the adoption of simplified assessment methods is not infrequent. In contrast, advanced numerical models are far from being adopted in the framework of open barrier design. Only few examples of numerical approaches exist. Considering impact forces, numerical modelling is generally used to evaluate the interaction of a closed barrier, and the flowing mass is simulated as either a monophase dry granular mass or a two-phase continuum. As regards the filter, i.e. the outlet size, general suggestions derive from observations of past-events or on small-scale laboratory experiments. Moreover, as this issue is strictly connected with the outlet clogging probability, several studies have been performed on the discharge dry granular materials from silos, which is a much more widely studied problem. These researches provide some useful results on the relationship between the outlet size-grain size ratio and the jamming of the outlet. Nevertheless, the viability of these results also for the barrier case has not been proved yet. Furthermore, a combined study of both impact force and filtering is almost completely lacking. As further explained, in the present thesis the debris flow-open barrier interaction issues are addressed with a fully 3D numerical approach that considers both a solid granular and a fluid phases.

This chapter first provides a general overview of the existing procedures and assessment methods related to study the interaction problems related to debris flow

encountering a rigid barrier (Sec. 4.1). Section 4.2 relates to the assessment and estimation of the impact forces, while Section 4.3 deals with the filtering problem and, thus, the trapping efficiency of the barrier. Being useful to understand clogging mechanisms related to filtering function, numerical studies on similar problems are considered (Sec. 4.3.1). Finally, Section 4.3.2 includes the existing suggestions on the filter sizing problem, i.e. the outlets size.

4.1   Physical and numerical modelling, an overview

Debris flow are still frequently modelled adopting simple approaches and methods derived from the classic theory of hydraulic. Debris flow are water-sediments mixtures flowing through a channel that can be compared, in some aspects, with a streamflow, involving higher solid concentration and higher velocities. This similarity justifies the traditional adoption of formulations originally developed for clear-water, to which one or more corrective factors are applied. These coefficients, which are empirical, correct the clear water formulas accounting for the presence of a solid phase inside the flow. The estimation of these coefficients derives by either observation of past events or from small-scale laboratory experiments. However, the knowledge on past-events is often incomplete, missing some interesting and relevant details. Moreover, experimental studies are generally conducted at the laboratory-scale, rather than the real-scale, because of the costs and execution difficulties. As often occurs in experimental modelling, but notably in representing multi-phase real natural events, they are affected by scaling problems and the choice of the materials simulating the debris flow can be unrealistic, or unsatisfactory for representing a multiphase phenomenon. Due to their cost, experiments are often unrepeatable or reduced in number, limiting the representative sample for results comparison and complete parametric studies.

At the end of the Nineties, the rise of numerical modelling provided important progresses to the study of debris flows (Turnbull et al., 2015). In the perspective of risk mitigation, debris flow problem has grown in popularity and a considerable number of investigations have been carried out. In addition, over the years, limitations due to costs and computational efforts progressively decreased. Different dynamics approaches, able to describe the flow during each stage of the motion through the integration of analytical expressions, have arisen, as briefly summarised in the

following. They differ for the considered number of phases, the initial conditions, the assumptions and simplifications, and, above all, the constitutive equation used to represent material behaviour.

Largely adopted, the continuum approach is one of the methods adopted in the study of debris flows (Pirulli, 2010; Pirulli et al., 2015; Savage and Hutter, 1989). It considers the flowing material as a continuous mass, modelling the real heterogeneous mass, made of water, air and solid materials. According to the considered number of phases, neglecting the air, continuum models can be subdivided into single-phase (Hungr, 1995; Hutter et al., 1996; Iverson, 1997) and two-phase (Armanini et al., 2009; Pailha and Pouliquen, 2009; Pitman and Le, 2005; Pudasaini, 2012). The solving equations are mass and momentum conservation, and the depth averaged shallow water approximation is done - according to the Saint-Venant theory (Hungr, 1995; Iverson, 1997). However, this approach, although very effective for simulating debris flow along its path, does not allow to consider some important aspects, related to the flowing mass and the interaction with a structure. Collisions and creation of stable structures among grains cannot be evaluated, as well as different velocity profiles along the depth. Moreover, even the two-phase model lacks in considering some important aspects of the solid-fluid interaction, e.g. segregation phenomena (Hill and Tan, 2014; Iverson, 2003; Leonardi et al., 2014).

In the perspective of studying the interaction between a debris-flow and a rigid barrier, the three-dimensionality of the problem is a crucial aspect that has to be considered. Several 3D continuum approaches (Wu et al., 2016b), e.g. Smoothed Particle Hydrodynamic (SPH), Lattice Boltzmann Method (LBM), Material Point Method (MPM), have been recently introduced to simulate debris flow as a single-phase flow (Gracia et al., 2017). Nevertheless, although different velocity profiles can be obtained, continuum methods lack in accounting for discrete grains, colliding and interacting with each other. With discrete elements approaches (Pöschel, 2005), e.g. Discrete Element Methods (DEM) (Cundall and Strack, 1979), Event-Driven Molecular Dynamic (ED) (Brilliantov and Pöschel, 2003), Rigid body dynamics (Lötstedt, 1981), every single grain is treated separately as a Lagrangian point, with mass and moment of inertia. This preserves the three-dimensional characteristics of the problem. Particles can collide and exchange forces, and force chains can arise, thus creating stable structures, promoting the halt of the motion. Nevertheless, the discrete element approach, alone, cannot represent the solid-fluid interaction, i.e. a discrete-continuum interaction.

As a consequence, it emerges that an ideal numerical model of the phenomenon has to be three-dimensional and two-phase, discrete for the solid materials and continuum for the fluid phase. All the interaction effects, i.e. among grains, between solid and fluid, and with a structure have to be correctly represented. If such an approach is applied, a combined study of both impact forces and trapping efficiency, i.e. filtering issue, can be performed. Since these aspects have been treated separately, the impact forces and trapping efficiency are treated in two separate sections.

4.2   Impact forces

The evaluation of the impact forces is a central problem for the structural design of barriers. The maximum impact force and its location are generally the reference parameters for the design. However, the knowledge of the force time-history and the complete spatial distribution is greatly desired for an efficient design procedure. As briefly discussed in the overview section, simplified empirical approaches derived from the clear-water theory are often applied to evaluate the impact force of a debris flow against a rigid barrier. In this sense, the international codes and standards, e.g. the Austrian Code Series (ONR 24800, 2009; ONR 24801, 2013; ONR 24802, 2010; ONR 24803, 2008), or the Hong-Kong Technical Reports (Kwan, 2012; Lo, 2000), refer to such empirical approaches as "commonly adopted" methods. Here are two of the simplified approaches traditionally adopted to calculate debris flow impact forces, sometimes even combined together:

- *Hydrostatic approach* (Armanini, 1997; Lichtenhahn, 1973): this considers a triangular load distribution along the barrier height, with a load increase factor to consider the dynamic component, according to:

$$p_\mathrm{d} = k_\mathrm{d,a} \rho_\mathrm{d} g h_\mathrm{d}, \tag{4.1}$$

  where p_d is the flow pressure, ρ_d the density of the mixture of the debris flow, g the gravity factor, h_d the height of the flow mixture (assumed equal to the height of the barrier), and $k_\mathrm{d,a}$ the dimensionless coefficient. Different values for $k_\mathrm{d,a}$ are proposed in the literature, ranging from 3 to 11 (Lichtenhahn, 1973).

- *Hydrodynamic approach*: this considers a constant load distribution, with intensity proportional to the flow velocity according to:

$$p_\mathrm{d} = k_\mathrm{d,b}\rho_\mathrm{d}v_\mathrm{d}^2, \tag{4.2}$$

where v_d is the velocity of the mixture, and $k_\mathrm{d,b}$ the dimensionless coefficient. The adopted value of the empirical factor $k_\mathrm{d,b}$ generally ranges from 2 to 5 (Armanini, 1997; Hübl et al., 2009; Lo, 2000; Wendeler et al., 2007; Zhang et al., 1996), increasing with the expected amount of coarse material and impact velocities.

However, during an event, both static and dynamic forces occurs in the same instant. Thus, for both the approaches,the dimensionless coefficients consider only the static or the dynamic contribution.

Table 4.1 summarises the empirical equations and coefficients suggested by various scholars, revealing that the hydrostatic and hydrodynamic approach are sometimes combined in a unique formulation.

Similarly, the simple elastic theory is chosen to consider the possible impacts of a boulder on the barrier, adding some corrective coefficients. The Hertz equation is generally adopted (Zhang et al., 1996), that is:

$$F_\mathrm{B} = K_\mathrm{c}n\alpha^{1.5}, \tag{4.3}$$

where F_B is the magnitude of the boulder impact force, K_c is the dimensionless load reduction factor, n and α are coefficients calculated as a function of the barrier and boulders characteristics:

$$n = \frac{4r_\mathrm{B}^{0.5}}{3\pi(k_\mathrm{B}+k_\mathrm{b})}, \tag{4.4}$$

with r_B the radius of the boulder, $k_\mathrm{B} = \left(1 - v_\mathrm{B}^2\right)/(\pi E_\mathrm{B})$ the coefficient related to the boulder mechanical properties and $k_\mathrm{b} = \left(1 - v_\mathrm{b}^2\right)/(\pi E_\mathrm{b})$ the coefficient related to the barrier materials, where $v_\mathrm{B,b}$ is the Poisson's ratio and E_B, E_b the Young's moduli of the boulder and the barrier, respectively. The coefficient α, that is the indentation, is equal to:

$$\alpha = \left(5m_\mathrm{B}v_\mathrm{B}^2/4n\right)^{0.4}, \tag{4.5}$$

with m_B the mass of the boulder and v_B the component of the boulder velocity normal to the barrier. Both the boulder mass and its radius are empirically evaluated

Authors	Model	Formula	Note
Kherkheulidze (1967)	Mixed	$F_{\rm d} = 0.1\gamma_{\rm d}(5h_{\rm d} + v_{\rm d}^2)$	-
Lichtenhahn (1973)	HS	$F_{\rm d} = \frac{1}{2}k_{\rm d,a}\rho_{\rm w}gh_{\rm w}^2$ $k_{\rm d,a} = 7 - 11$	For small flow velocity, based on recalculations
Mizuyama (1979)	HD	$F_{\rm d} = \frac{\gamma_{\rm d}}{g}qv$ q is the peak discharge	Considering momentum change
Watanabe and Ikeya (1981)	HD	$F_{\rm d} = 2\frac{\gamma_{\rm d}v_{\rm d}^2}{g}$	Field measurement
Hungr et al. (1984)	HD	$F_{\rm d} = \frac{\gamma_{\rm d}v_{\rm d}^2}{g}$	Load area should be distributed over an area as wide as the design debris flow reach, but 1.5 greater height to account for the formation of a stagnant wedge in front of the toe of the barrier
Yamaguchi (1985)	HD	$F_{\rm d} = k_{\rm d,b}\frac{\gamma_{\rm w}}{g}v_{\rm d}^2h_{\rm d}\sin\theta$; θ is the slope incline	Considering momentum change
Nakano and Ukon (1986)	HD	$F_{\rm d} = k_{\rm d,b}\frac{\gamma_{\rm d}v_{\rm d}^2}{g}$	Considering momentum change
Du et al. (1987)	HD	$F_{\rm d} = 3\frac{\gamma_{\rm d}v_{\rm d}^2}{g}$	-
Song (1994)	HS	$F_{\rm d} = (0.067 + 0.004D_{50}) + (0.85 + 0.07D_{50})\rho_{\rm d}\frac{v_{\rm d}^2}{g}$ D_{50} is the mean grain diameter	Considering momentum change
Yu (1992)	HD	$F_{\rm d} = \sqrt{D_{\rm max}}\rho_{\rm d}\frac{v_{\rm d}^2}{2g}$ $D_{\rm max}$ is the maximum grain diameter	Considering momentum change
Armanini and Scotton (1993)	HS	$F_{\rm d} = 9\rho_{\rm w}g\frac{h_{\rm d}^2}{2}$	For small velocity
	HD	$F_{\rm d} = k_{\rm d,b}\rho_{\rm d}h_{\rm d}v_{\rm d}^2; k_{\rm d,b} = 0.7 - 2$	Considering momentum change
Daido (1993)	HD	$F_{\rm d} = k_{\rm d,b}\rho_{\rm d}h_{\rm d}v_{\rm d}^2$ $k_{\rm d,b} = 5 - 12$	Considering momentum change
Zhang (1993)	HD	$F_{\rm d} = k_{\rm d,b}\frac{\gamma_{\rm w}v_{\rm d}^2}{g}$ $k_{\rm d,b} = 3 - 5$	From real scale events in the Jiangjia Ravine (China)
Lin (1994)	Mixed	$F_{\rm d} = 2\frac{\rho_{\rm d}}{g}v_{\rm d}^2 + K_{\rm a}rh_{\rm d}$ r is the mean grain radius	Considering momentum change and active soil pressure
Van Dine (1996)	HD	$F_{\rm d} = \frac{\gamma_{\rm d}v_{\rm d}^2}{g}$	According to Hungr et al. (1984)
Scotton and Deganutti (1997)	HS	$F_{\rm d} = k_{\rm d,a}\rho_{\rm w}gh_{\rm w}^2$ $k_{\rm d,a} = 2.5 - 7.5$	Small scale debris flow model test
Armanini (1997)	HS	$F_{\rm d} = 5\rho_{\rm w}g\frac{h_{\rm d}^2}{2}$	From experimental investigation
Egli (2000)	HD	$F_{\rm d} = k_{\rm d,b}\frac{\gamma_{\rm d}v_{\rm d}^2}{g}$ $k_{\rm d,b} = 2 - 4$	-
Lo (2000)	HD	$F_{\rm d} = 3\frac{\gamma_{\rm d}v_{\rm d}^2}{g}$	-
Lien (2002)	HD	$F_{\rm d} = k_{\rm d,b}\frac{\rho_{\rm d}}{g}h_{\rm d}v_{\rm d}^2$	Considering momentum change
Hübl and Holzinger (2003)	Modified HD	$p_{\rm d,b} = 4.5\rho_{\rm d}v_{\rm d}^{0.8}(gh_{\rm d})^{0.6}$ equivalent to $F_{\rm d,b} = 4.5\rho_{\rm d}gh_{\rm d}^2$ or $F_{\rm d,b} = k_{\rm d,b}\rho_{\rm d}gh_{\rm d}^2$ $k_{\rm d,b} = 0.5 - 2.2$	Small scale experiments, studying Fr and pressure
Arattano and Franzi (2003)	Mixed	$F_{\rm d} = \rho_{\rm d}qv_{\rm d} + \rho_{\rm d}g\frac{h_{\rm d}^2}{2}$	Mathematical model
Zanuttigh and Lamberti (2006)	Mixed	$F_{\rm d} = k_{\rm d,b}\frac{(1+{\rm Fr}_{\rm d}/2)^2}{2}\rho_{\rm d}gh_{\rm d}^2$	Integrate model
Wendeler (2008)	HD	$F_{\rm d} = k_{\rm d}\frac{\gamma_{\rm d}v_{\rm d}^2}{g}$ $k_{\rm d} = 0.7 - 2$	Full scale test at the Illgraben (CH)
Bugnion et al. (2012)	HD	$F_{\rm d} = k_{\rm d,b}\frac{\gamma_{\rm w}v_{\rm d}^2}{g}$ $k_{\rm d,b} = 0.4 - 2$	Real scale test

Table 4.1 Modified and integrated version of the summarising tables of dynamic impact formulations proposed by Huang et al. (2007) and Hübl et al. (2017). The abbreviations *HS* and *HD* stand for the hydrostatic and the hydrodinamic approaches, respectively

imposing $r_B = h_d/2$. The Eq. (4.3) can be rewritten as:

$$F_B = \hat{K}_c v_B^{1.2} r_B^2, \tag{4.6}$$

where $\hat{K}_c$ considers both boulder and barrier properties, and the load reduction factor K_c. In this regards, considering the design of inflexible structures, in which contact deformation is very important, Hungr et al. (1984) stated that the impact forces estimated through the Hertz equation of the elastic contact theory (Eq. (4.3)) are conservative. The Authors suggested, hence, to apply a load reduction factor K_c of 0.1, standing for plastic deformation and associated energy loss. In agreement with what stated by Hungr et al. (1984), different Authors proposed different values for the load reduction coefficient (Tab. 4.2).

Authors	Formula	K_c	Note
Mizuyama (1979)	$F_B = 241 v_B^{1.2} r_B^2$	–	Based on elastic collision theory
	$F_B = 48.2 v_B^{1.2} r_B^2$	0.2	Modified by Mt. Yakedake's field data
Yamaguchi (1985)	$F_B = 426 v_B^{1.2} r_B^2$	–	Based on elastic collision theory
	$F_B = 50 v_B^{1.2} r_B^2$	0.1	Modified by Myoukou Plateau's field data
Lien (2002)	$F_B = 80.8 v_B^{1.2} r_B^2$	0.2	Based on elastic collision theory
Huang et al. (2007)	$F_B = 30.8_B^{1.2} r_B^2$	0.06	Based on flume experimental data on open barrier

Table 4.2 Modified and integrated version of the summarising tables of the boulder impact formulations proposed by Huang et al. (2007).

As soon as numerical methods were developed, computational modelling, sometimes combined with results from laboratory experiments, has been adopted to determine less simplified formulations for evaluating the maximum impact force. These formulae aim to consider more realistic scenarios, either evaluating the evolution in time of the force, or determining a three-dimensional velocity profile, but they still remain incomplete (Calvetti et al., 2017; Vagnon and Segalini, 2016). Even though the height and the velocity of the flow included in almost all these formulae can be derived from a complex numerical model, in fact, also these expressions include corrective coefficients that are difficult to calibrate. These coefficients account for various aspects for which a closed-form solution cannot be found. As an example, Zanuttigh and Lamberti (2006), through a 1D continuum approach, proposed a formula that considers a possible total reflection of the flow and the presence of

boulders. Koo et al. (2017), through a new momentum-based model, tried to consider the attenuation of momentum flux during the flow and the progressive formation of a stationary zone of deposited material behind the barrier. Calvetti et al. (2017), adopting a discrete element approach, combined static and dynamic contributions, defining the latter as function of the velocity of propagation of compression waves within the impact medium.

Recently, due to increasing computational resources, numerical simulations have also been adopted to perform parametric analyses, evaluating the influence of geometrical, mechanical and rheological parameters on both magnitude and spatial distribution of forces on the barrier. These analyses are in an early stage and generally consider only closed barriers impacted by a mono-phase flow. Several Authors performed DEM analyses, considering a dry granular flow discharged just in front of a rigid wall. Observing the behaviour of the moving mass, i.e. impact and deposition dynamics, Calvetti et al. (2015) and Calvetti et al. (2016, 2017); Calvetti and Vairaktaris (2016) noted that the inter-particle friction is the most influencing factor. For large friction values, the soil mass seems to behave like a solid, while for small values, like a fluid. With intermediate inter-particle friction values, the fluid-like behaviour is limited to the zone close to the top surface. They observed that three zones develop at the very impact instant: a lower layer in which material is approximately still, an intermediate one in which part of the material is solid-like and force chains arise, and a top layer of fluidised material in which energy is dissipated by the collisions among grains. The middle layer disappears when a static situation is reached. The Authors reported that the maximum impact force rapidly decreases for large porosity since the granular mass, no more compacted, becomes similar to a granular gas. They showed that the force magnitude is not affected by the variation of the velocity profile of the impacting mass. Instead, the maximum impact force increases by increasing either the flow height, the impact velocity, or the front inclination just before the impact. With a similar initial configuration, Ceccato and Simonini (2016) and Ceccato et al. (2017) observed that the front inclination influences the forces exerted on the barrier as well as their evolution with time. In case of a mass whose front is parallel to the barrier, the force increases linearly with velocity.

A different initial configuration is adopted in Gabrieli and Ceccato (2016) and Teufelsbauer et al. (2011) who found that the impact force of a dry granular material against a rigid closed barrier increases as the slope angle of the channel increases.

Interesting parametric studies have been carried out by Li et al. (2010) through 2D DEM analyses, considering the influence of inter-particle friction angle, and slope inclination. Increasing the former, the impact force decreases. A nonlinear trend is observed for the latter: the maximum impact force is recorded for a slope angle of $60°$, for larger slopes lower magnitudes are found. Finally, several Authors (e.g. Albaba et al., 2015; Wu et al., 2016a) make use of experimental results related to a granular mass impacting against a rigid barrier to calibrate their DEM numerical models.

A very limited amount of scientific work has been done to estimate force magnitudes on open rigid barriers. Among them, Shima et al. (2016) analysed the response of a steel grid barrier subjected to the impact of a large rock though DEM. Several studies relate to the forces on energy breaking devices, such as, a wedge obstacle (Salciarini et al., 2010), multiple small obstacles arranged in a matrix (Teufelsbauer et al., 2011), or successive rows of debris-resisting baffles (Choi et al., 2014).

As open rigid barriers seem to be very effective for reducing damages and preventing loss of lives in debris flow events, the insufficient number of studies on the dynamics and the forces exerted by the flowing mass against them is a problem that needs urgent attention.

4.3   Trapping efficiency

The filtering function of a barrier is strictly related with the probability that granular material with grain size larger than a given dimension are retained, or trapped, behind the barrier. Thus, from here, the measure of the effectiveness of the filtering function in an open barrier is defined as "trapping efficiency". As a consequence, the design of the filter focuses on sizing the outlets of the barrier S, as function of the size of the minimum grain which has to be retained D_{max}, as previously defined in Sec. 3.1.

A typical feature of granular materials consists of the capability to organise in stable collective structures, formed by several grains that can withstand high pressure (Garcimartín et al., 2010). These structures are called arches or bridges (or even "domes", if fully 3D), and the phenomenon is called the "arch effect". In debris flow events, the granular mass encountering an obstacle (e.g. a restriction in the path or a rigid holed wall) can arrange in arches, resulting in a temporary or permanent clogging of the outlet. Due to arch formation, also grains smaller than the outlet

Fig. 4.1 Image recorded after the event on 11-07-2017 event in Saint-Vincent (AO), Italy. Also grains smaller than the outlets width of the sectional barrier clog and are retained behind the barrier. Courtesy of Valle d'Aosta Region.

width clog behind the barrier, as shown in Fig. 4.1, resulting in jamming of the flow. This phenomenon is also crucial for segregation, the nonuniform propagation of the forces.

At the field-scale, clogging is the physical phenomenon that exerts the filtering function. However, even nowadays, in the frame of debris flow events, a complete study of clogging and arching mechanisms is still lacking. The filter size problem is generally addressed prescribing a ratio S/D_{max}, generally disregarding the barrier type (sectional, beam or lattice). The values of this ratio generally derive from the observation of past-events or experiments. Only in the last decade, these studies have been combined with numerical simulations.

In contrast, clogging and arch formation have been widely investigated in the field of granular assemblies discharged by silos. This problem is very important in the industrial field. The discharge velocity of the material and the probability that the mass jams have to be properly investigated for preventing damages to machinery. Clogging probability is, among the other factors, related to the opening of the silos compared to the size of the released material. Although advanced numerical modelling has been performed, the simulations are limited to a dry granular material, generally confined inside a 2D vertical silos or, if 3D modelled, passing through a

circular outlet. Despite all these differences with debris flows, the obtained results are very useful to understand the particles-structure interaction mechanisms.

With all these premises, Section 4.3.1 illustrates the results obtained from the numerical simulations in the field of granular mass discharged from a silos/hopper. Then Section 4.3.2 provides an overview to the suggestions and analyses performed for sizing the outlets of a debris flow open barrier.

4.3.1   Related numerical studies

Although arching and clogging can be also observed in real debris flow events, the majority of the studies relates instead to the arrest of granular flow at the outlet of a silos. Investigations are both experimental and numerical. The jamming of a silo or a hopper is studied experimentally both in 2D (e.g. Cleary and Sawley, 2002; Garcimartín et al., 2010; Janda et al., 2008; To, 2005; To and Lai, 2002; To et al., 2001) and 3D systems (e.g. Ashour et al., 2017; Pournin et al., 2007; Sheldon and Durian, 2010; Thomas and Durian, 2013; Zuriguel et al., 2005, 2003). This problem is widely investigated also with numerical analyses with DEM (e.g. Arévalo and Zuriguel, 2015; Balevičius et al., 2008; Hidalgo et al., 2013; Magalhães et al., 2015; Mondal and Sharma, 2014; Pournin et al., 2007; Tsukahara, 2009), generally in a 2D frame. Tables 4.3a and 4.3b summarize some of the more recent studies on this frame, indicating if 2D or 3D (column 3) and if experimental or numerical (column 4). As a similar problem, also examples of non confined granular sandpile formation are considered (Magalhães et al., 2010, 2012).

Generally speaking, Authors relate the probability of the flow to be halted and to form arches to the ratio between the opening size S and the characteristic dimension of the grains D, considering this as the most influencing parameter. It is worth mentioning that, in general, they consider a circular outlet. As a consequence S is the diameter of the outlet. As a general rule, if the outlet width or diameter S exceeds by several times the typical size of particle, the flow is no more arrested. The maximum S/D value allowing a stable clogging is defined "critical ratio" R_{crit}. The larger the outlet is, the lower the arching probability or the higher the probability of being destabilised is. In fact, at least an arch spanning the whole outlet width is required to generate a permanent clog in the system. Thus, by increasing S, a greater number of grains is required for arching. Moreover, in this condition, also the number of collisions from particles coming from behind increases, resulting in stronger or more

numerous impacts to withstand. Column 2 of Tables 4.3a and 4.3b summarise the critical ratio R_{crit} found by Authors. In this table, only approximatively spherical or circular shapes are considered. Consequently, Tables 4.3a and 4.3b provide a comparative sample for the numerical analyses carried out in the present thesis. A common trend emerges: the studies generally agree that silos clog if $S/D < 3 - 6$, but mostly around 5.

From all these studies, other important aspects that affect the arch formation and jamming probability emerge. In particular, considering the ones that can be applied also in the debris flow case, the following features have to be evaluated:

- *Frictional properties of the materials.* Stable arches can form also in case of frictionless material since two neighbouring grains exchange only compressive forces. Nevertheless, the presence of friction enhances the possibility of jamming, as also tangential forces can arise among grains. In this condition, stable arches can occur also with concave angles formed by a particle with its neighbours, and not only if the shapes are convex. These concave conditions are called "defects " (Garcimartín et al., 2010; Pournin et al., 2007) and require also a lower number of grains, and thus larger arches.

- *Shape effect of the material.* Both numerical and experimental investigations reveal that an elliptical particle shape makes the microstructure significantly stronger and greatly slows the flow (Cleary and Sawley, 2002; Garcimartín et al., 2010; Thomas and Durian, 2013; Zuriguel et al., 2005). Moreover, also a change in the blockiness, i.e. from circular shaped to squared, increases the jamming probability, altering both the distribution of the voids and the bulk density of the mass.

- *Direction of the flow in relation with the outlet.* The angle with which the flowing mass reaches the path restriction affects the clogging probability. Sheldon and Durian (2010) and Thomas and Durian (2013), considering tilted hoppers, revealed that a direction of flow non normal to the obstruction encourages the clogging phenomenon.

- *Polydispersity of the grains.* A polydisperse system seems to improve the fluidity of the flow, thus reducing the jamming probability (Mondal et al., 2011). Magalhães et al. (2012), through 2D numerical analyses on a non-confined vertically discharged mass, considered bidispersion both in term

Authors	R_{crit}	2D-3D	E-N	Notes
To (2005); To et al. (2001)	$\sim 4\text{-}5$	2D	E	Steel disks and a hopper with inclined lateral walls have been used.
Zuriguel et al. (2005)	~ 5	3D	E	Glass, lead, derlin, steel beads has been employed. The Authors assessed that the material properties of the grains do not affect the arch formation probability.
Pournin et al. (2007)	~ 3	3D	E+N	The value is the one with 50% of $J(R)$.
Janda et al. (2008)	~ 6	2D	E	Authors asserted that a real critical value does not exist but spoke about jamming probability. For $R \leq 2.5$ $J(R) \simeq 1$. The experiments are not strictly 2D as monosized glass spheres are used but with a hopper width spanning only one diameter.
Garcimartín et al. (2010)	~ 5	2D	E+N	Steel beads are used in the experiments. The Authors found that the mean number n_b of beads forming an arch is $n_b = 1.41 + 1.15R$

Table 4.3a Summary of the critical ratio above which no clogging occurs $R_{\mathrm{crit}} = S/D$ provided in the literature, for a spherical or circular assembly discharged in a silo. E stands for experimental, while N for numerical analyses. $J(R)$ is defined as the jamming probability, that is the probability that an arch clogging the flow occurs when the $S/D = R$. Where not specified, a flat bottomed condition has been considered.

Authors	R_{crit}	2D-3D	E-N	Notes
Magalhães et al. (2010)	~ 5	2D	N	The flowing mass has no lateral contraints.
Sheldon and Durian (2010)	~ 5	3D	E	Glass beads have been employed.
Mondal et al. (2011)	~ 5	3D	N	A polydispherse system is considered.
Hidalgo et al. (2013)	~ 3	2D	N	Numerical analyses have been compared with the experimental results of Garcimartín et al. (2010).
Thomas and Durian (2013)	~ 3 for slit hole ~ 5 for circular hole	3D	E	Glass beads have been used.
Arévalo and Zuriguel (2015)	~ 5	3D	N	Numerical analyses have been compared with the experimental results of Garcimartín et al. (2010).
Ashour et al. (2017)	~ 5	3D	N	Spherical peas have been employed.

Table 4.3b Summary of the critical ratio above which no clogging occurs $R_{\mathrm{crit}} = S/D$ provided in the literature, for a spherical or circular assembly discharged in a silo. E stands for experimental, while N for numerical analyses. $J(R)$ is defined as the jamming probability, that is the probability that an arch clogging the flow occurs when the $S/D = R$. Where not specified a flat bottomed condition has been considered.

of grain size and density of the grains, separately. The Authors observed that clogging is related to a natural statistic selection among several random possibilities of realisations of arches: few large grains have slightly more probability to clog the flux rather several small grains, and the same for heavy particles, as light ones can escape more easily. However, increasing S/D, a segregation phenomenon or selective behaviour is highlighted in the arch formation. For the inverse grading phenomenon, small grains flow through the voids generated by large grains and clog small openings.

All these examples consider a vertical discharge, so that the gravitational force is direct as the main flow direction. The pressure that the grains forming an arch have to withstand is thus the maximum potential one. Arévalo and Zuriguel (2015) investigated the influence of gravity and revealed that for almost every inclinations of the silos, for $S/D \leq 2.5$ the probability that materials instantaneously clog tends to unity and the probability that arches are destabilised is almost zero. Furthermore, for $S/D \leq 5$, for each investigated slope, a permanent clog is observed, albeit non instantaneously when the mass reaches the hole. Of course, the higher the component of the gravity parallel to the main flow direction is, the lower the jamming probability will be.

In debris flow events, channel slopes do not generally exceed $45°$ and barriers are usually located in the fan apex. Differing from silos, the mass is not upper confined and can pass not only through the outlet but also over the barrier itself. However, the mechanism of arch formation and trapping efficiency in the framework of granular flow and open rigid mitigation systems has not been widely investigated.

4.3.2   Designing the filter: outlet width size

The efficiency of trapping in a filtering barrier depends on the filter design, i.e. the shape and the size of the outlets. The problem is often made dimensionless by considering the ratio between the shorter dimension of the outlet, called S, and the characteristic grain size d that has to be entrapped. The problems of both determining the characteristic size distribution of the flowing mass and then choosing which d value should be considered has been highlighted in Sec. 3.1.

Focusing on the S/d to adopt, an exhaustive investigation is still lacking. The majority of the design suggestions, which are provided by the international guidelines,

derive from observation of past events or from small scale laboratory studies. In particular, in China, MLR (2004) suggests to use $2.0 \le S/D_{\max} \le 4.5$, while in Taiwan SWCB (Soil and Water Conservation Bureau) (2005) $1.5 \le S/D_{\max} \le 2.0$. Finally, in Japan, Management) and Infrastructure (2007) prescribes to use $S/D_{\max} \simeq 1.5$. These examples provide an S/d value disregarding the shape of the outlets and, thus, are considered valid for each open barrier type.

Trapping efficiency can, in the first instance, be estimated from the clogging probability, thus, evaluating the amount of non-retained material. This aspect is difficult to consider during real debris flow events. Thus, some experimental investigations have been performed, considering a granular assembly released under the effect of gravity into a confined channel, ending with an open barrier. Considering experiments on plane grill barriers, Watanabe et al. (1980) revealed that, for $S/D_{\max} < 2$, the volume of the debris flow downstream the barrier can be reduced by at least 50%. With similar experiments, Mizuyama et al. (1995) found that trapping occurs if $S/D_{\max} < 1.5 - 2$ and that, for these values, the peak sediment discharge is reduced by a percentage, experimentally deduced, equal to:

$$0.11 \left(\frac{S}{D_{\max}} - 1 \right)^{0.36} C_{\mathrm{s}}^{-0.96} \quad \times \quad 100\%. \tag{4.7}$$

Han and Ou (2006) carried out an experimental work on sectional barriers and compared their results with the one of Watanabe et al. (1980) and Mizuyama et al. (1995). According to the Authors, a total blocking condition is reached for $S/D_{\max} < 0.739$, while no blocking occurs for $S/D_{\max} > 1.478$. The major density reduction of the debris occurs for $0.739 \le S/D_{\max} \le 1.232$ and for an outlet density $0.2 \le \sum S/W_{\mathrm{ch}} \le 0.5$, where W_{ch} is the width of the channel. Similar experiments have been carried out by Itoh et al. (2011). The Authors studied the influence of the initial channel slope observing that, for values of $S/d \le 1.5$, the bed slope has no significant influence on the trapping efficiency, whereas an opposite trend is shown for $S/d \ge 2$. Still in the frame of plane grill barrier experiments, Shima et al. (2016), considering a steel lattice barrier (defined in Sec. 3.1), studied real cases and performed physical model tests on four different types of debris flow: wooden debris + rocks + sediment, wooden debris + sediment, rocks + sediment, and wooden debris only. Even if the presence of wooden debris and rock enhances the trapping probability, the Authors observed that, in all these four scenarios, a permanent clog occurs for $S/D_{95} \le 1.5 - 2.0$, where D_{95} is the grain size with only

Opening[a]	Relative opening[b]	Clogging probability	Sources
w_0	1.5	100%	Watanabe et al. (1980)
—	2	0%	—
w_0	1.6	High	Zollinger (1983)
h_0	1.2	High	—
w_0	1.5	High	Ikeya (1989)
w_0	1.5	100%	Frey and Tannou (2000)
—	2	33%	—
h_0	1.5	100%	—
—	2	0%	—
n_0	1(2)[c]	100%	Ono et al. (2004)
—	—	—	Osanai et al. (2010)
—	—	—	Itoh et al. (2011)

[a]w_0, h_0 and n_0, the horizontal, vertical, and minimum size of the opening, respectively.
[b]Opening dimension/material dimenson $= w_0$ or h_0/D_{MAX}.
[c]See comments in the text.
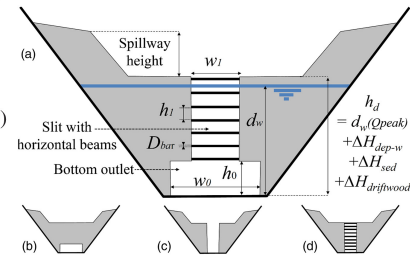
Table 4.4 Relative opening clogging probability as function of the opening width, according to different Authors, source Piton and Recking (2016).

the 5% of probability of being exceeded. The performed tests did not include water. Piton and Recking (2016) provided a table (Tab. 4.4) that summaries the principal suggestions given by several Authors in order to define a relationship between S and the trapping efficiency.

Only recently, in comparison with laboratory experiments, the first numerical analyses have been carried out. Fukawa et al. (2002) conducted 2D DEM numerical analyses, considering also the drag effects induced by water, investigating the probability of clogging, and evaluating both the randomness of the granular size and outlet width of an open rigid barrier with horizontal piles. Using a polydisperse material, the Authors found that $S/D \leq 2.5$ guarantees a high trapping probability. Ishikawa et al. (2014) compared experimental and DEM numerical analyses on a sectional barrier. The effects of water are numerically treated simply giving a flow velocity distribution. The Authors, using monodisperse granular material, found a stable clogging for $S/d \leq 1.5$. They also studied the influence of the particles diameter on the stopping time, revealing that the time for reaching a stable configuration increases by decreasing the diameter. Silva et al. (2016), both with laboratory tests and numerical simulations on a sectional barrier, considering a dry material and assuming $d = D_{95}$, showed that the trapping efficiency mainly depends on S/d, on the slit density $\sum S/W_{\text{ch}}$ and on the debris characteristics. This study demonstrates that sectional barriers are effective in mitigating stony-type debris flow if $1.18 \leq S/D_{\text{max}} \leq 1.36$, for a peak discharge Q_{peak} up to about 6 m³/s, i.e. within the limits of the performed

laboratory tests and numerical studies. The trapping efficiency E_{tr} is evaluated with an empirical formula, derived from the experimental results:

$$E_{\mathrm{tr}} = \frac{1.55\left(1 - \sum S/W_{\mathrm{ch}}\right)}{\left(S/D_{95}\right)^{1.40} e^{v_{\mathrm{d}}^{0.7}}} \tag{4.8}$$

where $v_{\mathrm{d}} = 2.1 Q_{\mathrm{peak}}^{0.33} \theta^{0.33}$. The Authors confirmed also the founding of Itoh et al. (2011) related to channel slope influence.

Summarising these results, it emerges that the trapping efficiency depends mainly on the ratio S/d, but it is influenced also by the outlet density and by the debris characteristics. However, for $S/d \leq 2$ a complete trapping seems to be guaranteed. Further investigations have to be performed, to evaluate all these parameters and consider also the presence of a fluid phase.

Chapter 5

The DEM-LBM method. A multi-phase approach to debris flow

This chapter illustrates in detail the original version of the DEM-LBM code developed by Leonardi et al. (2015). The code couples the Discrete Element Method (DEM) for the solid phase, and the Lattice-Boltzmann Method (LBM) for the fluid, providing an efficient tool to simulate debris flow as a mixed continuum-discrete medium. The two methods are outlined separately. Section 5.1 describes the DEM, illustrating both the normal and tangential contact models. Section 5.2 describes the LBM, outlining the algorithm for the implementation of the rheology of the fluid phase (Sec. 5.2.1), the free surface (Sec. 5.2.2), the interaction with walls and rigid obstacles (Sec. 5.2.3), and the fluid-particle coupling (Sec. 5.2.4). For both methods, the numerical arrangements for improving the computational performance and efficiency are briefly shown, in Sec. 5.1.4 and 5.2.5, for DEM and LBM, respectively.

5.1 The Discrete Element Method for the solid phase

This numerical method treats every single grain separately as a Lagrangian point, with a mass m_p and a moment of inertia $\mathbf{J}_\mathrm{p}$. Its translational and rotational degrees of freedom are tracked continuously. The DEM numerical model, known also with the name of Soft-Particle approach, has been firstly developed by Cundall and Strack (1979). In this method, the particles are allowed to suffer small deformations, namely the overlap δ between particles (Fig. 5.1), through which, the forces between

particles are calculated. Their motion is described by the time-dependent numerical solution of Newton's equation of motion:

$$m_{\mathrm{p}} \frac{\mathrm{d}^2 \mathbf{v}_{\mathrm{p}}}{\mathrm{d}t^2} = \mathbf{F}_{\mathrm{p}}, \tag{5.1}$$

$$\mathbf{J}_{\mathrm{p}} \frac{\mathrm{d}^2 \boldsymbol{\theta}_{\mathrm{p}}}{\mathrm{d}t^2} = \mathbf{M}_{\mathrm{p}} - \frac{\mathrm{d}\boldsymbol{\theta}_{\mathrm{p}}}{\mathrm{d}t} \times \left(\mathbf{J}_{\mathrm{p}} \frac{\mathrm{d}\boldsymbol{\theta}_{\mathrm{p}}}{\mathrm{d}t} \right), \tag{5.2}$$

where $\mathbf{F}_{\mathrm{p}}$ and $\mathbf{M}_{\mathrm{p}}$ are the force and the momentum resulting from the interactions acting on the particles, respectively. These are the fluid-particle coupling interactions, the collisions between particles, and external force fields, e.g. gravity. The simplification, arisen by considering the overlap as a measure of particle deformation, derives from considering each individual particle small in comparison to the deformation of the whole granular assembly (Cundall and Strack, 1979).

In its simplest form, DEM considers particles as spheres with radius r_{p}. If two particles p1 and p2 are in contact, the overlap between them is (Fig. 5.1):

$$\delta = r_{\mathrm{p}1} + r_{\mathrm{p}2} - d_{\mathrm{p}1,\mathrm{p}2}, \tag{5.3}$$

where $d_{\mathrm{p}1,\mathrm{p}2}$ is the magnitude of the vector distance between the two centers $\mathbf{d}_{\mathrm{p}1,\mathrm{p}2} = \mathbf{x}_{\mathrm{p}2} - \mathbf{x}_{\mathrm{p}1}$. In particular, the collision reference system has a normal component given by:

$$\mathbf{n} = \frac{\mathbf{d}_{\mathrm{p}1,\mathrm{p}2}}{d_{\mathrm{p}1,\mathrm{p}2}}, \tag{5.4}$$

while the second and third tangential components $\mathbf{t}$ and $\mathbf{b}$, are defined according to the collision velocity $\mathbf{v}_{\mathrm{coll}}$. The normal component of $\mathbf{v}_{\mathrm{coll}}$ is proportional to the relative translational velocity of the two particles:

$$\mathbf{v}_{\mathrm{coll}}^{\mathrm{n}} = ((\mathbf{v}_{\mathrm{p}1} - \mathbf{v}_{\mathrm{p}2}) \cdot \mathbf{n})\mathbf{n}, \tag{5.5}$$

where $\mathbf{v}_{\mathrm{p}1}$ and $\mathbf{v}_{\mathrm{p}2}$ are the translational velocities of particles p1 and p2, respectively, while the tangential velocity is also function of the rotational velocity $\boldsymbol{\omega}$ of the two colliding particles, as:

$$\mathbf{v}_{\mathrm{coll}}^{\mathrm{t}} = \mathbf{v}_{\mathrm{p}2} - \mathbf{v}_{\mathrm{p}2} - \mathbf{v}_{\mathrm{coll}}^{\mathrm{n}} - r_{\mathrm{p}1}\boldsymbol{\omega}_{\mathrm{p}1} \times \mathbf{n} - r_{\mathrm{p}2}\boldsymbol{\omega}_{\mathrm{p}2} \times \mathbf{n}. \tag{5.6}$$
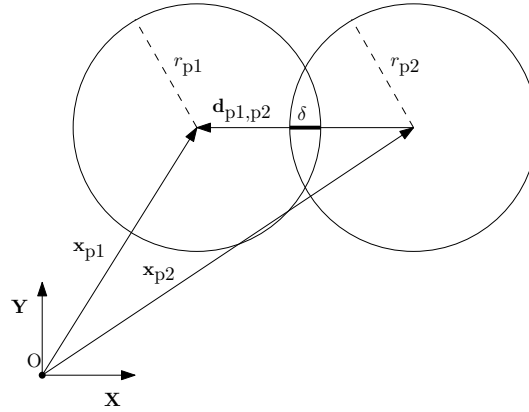
Fig. 5.1 Geometrical representation of the contact law of two particles in collision in the DEM model.

From this, the remaining components of the collision reference system are:

$$\begin{aligned} \mathbf{t} &= \mathbf{v}_{\text{coll}}^{\text{t}}/v_{\text{coll}}^{\text{t}}, \\ \mathbf{b} &= \mathbf{n} \times \mathbf{t}. \end{aligned} \tag{5.7}$$

The overlap δ represents the elastic deformation of the colliding particles. The two particles exchange a force only if the overlap is positive. The force is repulsive and its expression depends on the adopted contact model. This force can be subdivided in a normal and a tangential component. The final system, when two particles collide, is:

$$\begin{aligned} \mathbf{F}_{\text{p1}} &= -F_{\text{coll}}^{\text{n}}\mathbf{n} + F_{\text{coll}}^{\text{t}}\mathbf{t}, \\ \mathbf{M}_{\text{coll,p1}} &= r_{\text{p1}}F_{\text{coll}}^{\text{t}}\mathbf{b}, \\ \mathbf{F}_{\text{p2}} &= F_{\text{coll}}^{\text{n}}\mathbf{n} - F_{\text{coll}}^{\text{t}}\mathbf{t}, \\ \mathbf{M}_{\text{coll,p2}} &= r_{\text{p2}}F_{\text{coll}}^{\text{t}}\mathbf{b}. \end{aligned} \tag{5.8}$$

The movements of individual particles are traced during every time step, assuming that, in this small interval time, the disturbances propagate through the medium only to its immediate neighbors (Cundall and Strack, 1979). At all times, the resultant force on one particle derives from the interactions with the neighboring particles. The check for collisions, that is the computation of the distance vectors and Eq. (5.3), is optimized using a linked-cell algorithm, which makes the neighborhood search more efficient. The simulation area is subdivided in identical rectangular boxes to
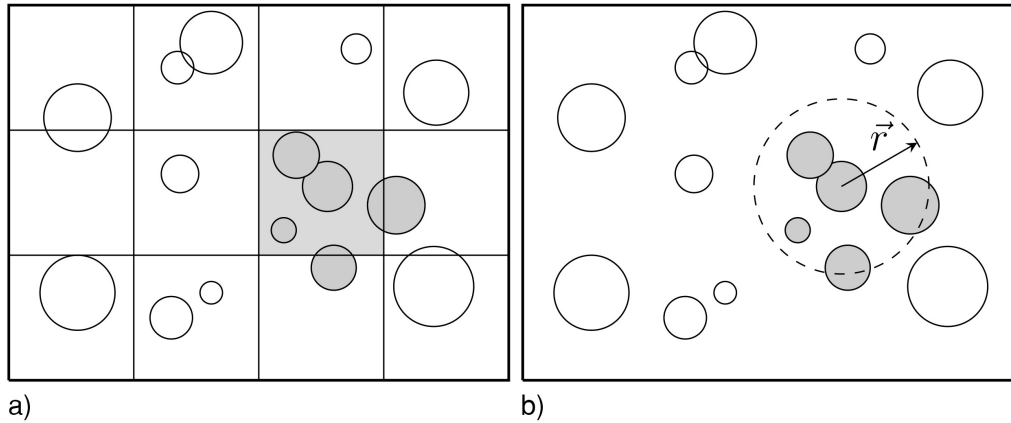
Fig. 5.2 (a) Linked cell algorithm, and (b) Verlet radius algorithm (Jakob and Konietzky, 2005).

each of which a list of residing particles is assigned. These lists are used to reduce the number of force evaluations. The check for possible collisions is performed only between particles belonging to two contiguous boxes (Pöschel, 2005). The size of each box is a multiple of the maximum radius of the particles. Furthermore, to reduce even more the computation complexity, the linked-cell algorithm is coupled with a Verlet list algorithm (Jakob and Konietzky, 2005). This considers, inside each list of contiguous boxes, only the particles within a given radius, chosen as function of the maximum particles radius and the size of the boxes (Fig. 5.2). Once checked if two particles are in contact, that is if they overlap, a spring-dashpot model is the assumed impact model for computing the force in the normal direction. The spring simulates the elastic response and the dashpot accounts for the viscous dissipations. The spring is characterized by a stiffness k_n, while the dashpot by a damping coefficient α_n. The spring-dashpot models implemented in the code are the linear model (Cundall and Strack, 1979) and the Hertzian model (Hertz, 1882). Figure 5.3 shows the conceptual model adopted in the original version of the code.

5.1.1   Normal contact: the linear model

In this contact model, Hooke's law $F(\delta) = k_n \delta_n$ describes the elastic force. This contributes, for the normal force, as:

$$\mathbf{F}_{el}^n = k_n \delta \mathbf{n}, \tag{5.9}$$
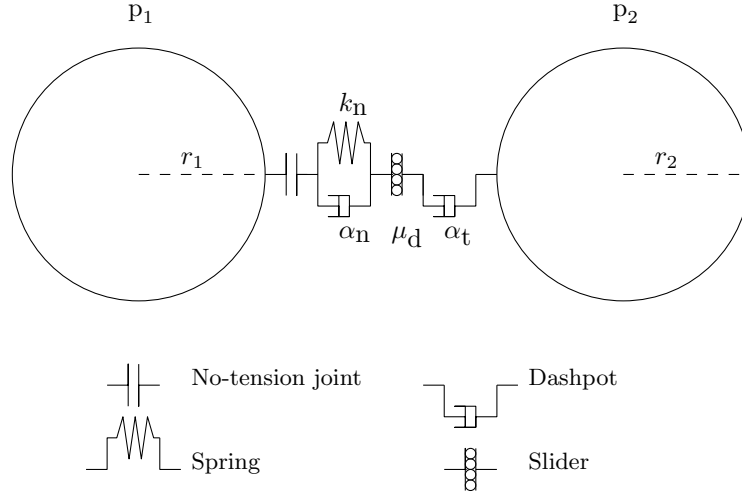
Fig. 5.3 Representation of the model adopted in the original version of the code for the contact forces (Leonardi et al., 2015, 2014, 2016).

where k_n is the normal contact stiffness. The dashpot contributes as:

$$\mathbf{F}^\mathrm{n}_\mathrm{visc} = -2\alpha_\mathrm{n}\sqrt{k_\mathrm{n}\tilde{m}}\dot{\delta}\mathbf{n}, \tag{5.10}$$

where α_n is the normal damping coefficient, $\tilde{m} = m_\mathrm{p1}m_\mathrm{p2}/(m_\mathrm{p1}+m_\mathrm{p2})$ is the effective mass. This results in:

$$\mathbf{F}^\mathrm{n} = k_\mathrm{n}\delta\mathbf{n} - 2\alpha_\mathrm{n}\sqrt{k_\mathrm{n}\tilde{m}}\mathbf{v}^\mathrm{n}_\mathrm{coll}. \tag{5.11}$$

The overlap follows Newton's law of a harmonic oscillator:

$$\ddot{\delta} + 2\alpha_\mathrm{n}\sqrt{\frac{k_\mathrm{n}}{\tilde{m}}}\dot{\delta} + \omega^2\delta = 0, \tag{5.12}$$

where $\sqrt{k_\mathrm{n}/\tilde{m}}$ is the angular frequency of the undamped oscillator. This is valid only for a half period, that is, the contact duration. In this model, considering the initial condition of $\delta = 0$ and $\mathbf{v}^\mathrm{n}_\mathrm{p2} - \mathbf{v}^\mathrm{n}_\mathrm{p1} = \mathbf{v}_0$, the analytical solution for the overlap allows the normal restitution coefficient ζ and the collision duration $t_\mathrm{c,n}$ to be determined as:

$$\zeta = \exp\left(-\alpha_\mathrm{n}\sqrt{\frac{k_\mathrm{n}}{\tilde{m}}}t_\mathrm{c,n}\right), \tag{5.13}$$

$$t_\mathrm{c,n} = \pi\left(\frac{k_\mathrm{n}}{\tilde{m}} - \frac{\alpha_\mathrm{n}^2 k_\mathrm{n}}{\tilde{m}}\right)^{-0.5}. \tag{5.14}$$

From Eqs. (5.13) and (5.14) it is worth noting that ζ and $t_{c,n}$ are independent of the impact velocity. The restitution coefficient represents the ratio between the final and initial relative velocities between two particles after they collide. Considering the restitution coefficient as constant is unphysical. Experiments (Kuwabara and Kono, 1987) showed that it changes with the impact velocity, but not dramatically. Furthermore, from Eqs. (5.13) and (5.14), it follows that the spring stiffness and damping coefficients can be set by adjusting ζ and $t_{c,n}$ to corresponding experimental values exhibited by a given material in a proper velocity range (Navarro and Braun, 2013). In general only the value of ζ is given and, thus, only the damping coefficient can be analytically derived:

$$\alpha_n = -\frac{\ln \zeta}{\sqrt{\ln^2 \zeta + \pi^2}}. \tag{5.15}$$

The value of the normal stiffness coefficient needs thus a proper choice, also depending on numerical considerations. Further details for a proper choice of k_n will be given in Sec. 5.1.4.

5.1.2 Normal contact: the Herztian model

Hertz (1882) proposed a theory to describe the elastic contact between two spheres in the normal direction, considering that the relationship between the normal force and normal displacement is nonlinear, and thus it can be modeled through a normal spring with non constant stiffness. The stiffness depends on material properties and the shape of the contact surfaces. In particular, for two spheres in contact, the model expresses the spring stiffness and the damping coefficient as functions of material mechanical parameters, that is Young's modulus E_p and Poisson's ratio ν_p, and of the particles radii. The model was slightly modified by Tsuji et al. (1992) to consider a constant coefficient of restitution:

$$
\begin{aligned}
k_n &= \frac{2E_p\sqrt{\bar{r}}}{3(1-\nu_p^2)}\delta^{0.5}, \\
\alpha_n &= -\frac{\sqrt{5}\ln \zeta}{\sqrt{\ln^2 \zeta + \pi^2}},
\end{aligned}
\tag{5.16}
$$

where $\tilde{r} = r_{p1}r_{p2}/(r_{p1} + r_{p2})$ is the effective radius.

The Hertzian model does not provide an analytical way to estimate the duration of collision, which can be approximated as (Antypov and Elliott, 2011):

$$t_{c,n} \simeq 2.214 \left(\frac{\rho_p}{E_p} \right)^{2/5} \frac{2d_{min}}{(v^n_{coll})^{1/5}}, \tag{5.17}$$

where ρ_p is the mass density of the particles. The computation of the maximum velocity is done at the beginning, assuming its maximum magnitude to be governed by the acceleration field, that is, velocity is scaled by gravity.

Regardless of the model adopted, estimating the collision time, even roughly, is important for an accurate choice of the numerical time step to adopt, as explained in Sec. 5.1.4.

5.1.3   Tangential contact: the viscous model

The viscous tangential contact force model represents only the viscous behavior for the shearing force, according to:

$$\mathbf{F}^t = -\min \left(2\alpha_t \sqrt{k_t \tilde{m}} v^t_{coll}, \mu_d F^n \right) \mathbf{t}, \tag{5.18}$$

where α_t is the tangential damping coefficient, and μ_d is the dynamic friction coefficient. The tangential component is proportional to the relative tangential velocity (Eq. (5.6)) of the two particles in contact, and the maximum force is given by the Coulomb friction criterion.

As this model does not allow a complete stop of the particles to be simulated, the applied friction coefficient μ_d is a dynamic one, according to the model proposed by Haff and Werner (1986). The tangential stiffness, to be inserted in Eq. (5.18), is assumed equal to:

$$k_t = \begin{cases} k_n, & \text{if the normal contact model is linear,} \\ \frac{E_p \sqrt{\tilde{r}(F^n)^{1/3}}}{(2-v_p)(1+v_p)}, & \text{if the normal contact model is Hertzian .} \end{cases} \tag{5.19}$$

This model simplifies the frictional behavior by neglecting the static component of friction, and thus stable forces among particles cannot be simulated. The tangential

contact model implemented in Secs. 6.2 and 6.2 accounts for both the static and the dynamic components.

5.1.4   Numerical arrangement for the simulations

The DEM simulation time step Δt^{DEM} is a crucial parameter for the stability of the simulations. It has to be chosen small enough to represent contacts with an acceptable degree of accuracy. For this it has to be:

$$\Delta t^{\text{DEM}} = \frac{1}{n}\, t_{\text{c,n}} < \frac{1}{10} t_{\text{c,n}}. \tag{5.20}$$

For guaranteeing numerical stability, it is not uncommon to find also a factor of proportion n up to 1000. However, the smaller the time step is, the higher the required computational time is.

   Another important choice concerns the stiffness of the normal spring. This value is associated with the maximum normal overlap between two particles in contact and the collision time. The contact time increases by reducing the spring stiffness, or the Young's modulus in case of the Herztian model. Consequently, by lowering the stiffness, and thus increasing the time step with lower computational load, the possible overlap between particles increases. However, the soft-spheres method adopted is based on geometrically rigid particle assumption, that is, the allowed deformations or overlaps are limited. Hence, reducing the stiffness in such a way that the overlap is large makes the simulations less accurate (Navarro and Braun, 2013). In addition, as a soft-sphere model, it has to be noted that the maximum value of normal stiffness is also upperly capped by the hard-particle limit and cannot tend to infinity, that is the contact duration time cannot diverge to an infinitesimal value.

   For this, and because of numerical difficulty (Mitarai and Nakanishi, 2003; Yuu et al., 1995), the adopted values of stiffness are usually much smaller than the one appropriate for simulating very stiff material, such as glass or steel. Norouzi et al. (2016) suggests to use a value for the spring stiffness between 10^6 and 10^8 N/m, even if some Authors (e.g. Li et al., 2007) applied also $k_{\text{n}} = 8000$ N/m. Furthermore, Norouzi et al. (2016) and Hidalgo et al. (2013) also state that the maximum overlap should not exceed $\sim 2\%$ of the particle diameter and provide a table (reported in Fig. 5.4) with the relationship for evaluating the collision time, the maximum normal overlap and the maximum normal force for an undamped elastic contact between

Parameter	Linear model	Non-linear model
t_{col}	$\pi\sqrt{\dfrac{m_{eff}}{k_n}}$	$2.86\left(\dfrac{m_{eff}^2}{R_{eff}E_{eff}^2 v_{rn,imp}}\right)^{1/5}$
$\delta_{n,max}$	$v_{rn,imp}\sqrt{\dfrac{m_{eff}}{k_n}}$	$\left(\dfrac{225}{256}\dfrac{m_{eff}^2 v_{rn,imp}^4}{E_{eff}^2 R_{eff}}\right)^{1/5}$
$f_{n,max}$	$v_{rn,imp}\sqrt{m_{eff}k_n}$	$\left(\dfrac{500}{144}m_{eff}^3 E_{eff}^2 R_{eff} v_{rn,imp}^6\right)^{1/5}$

Fig. 5.4 Relationship for evaluating collision time, maximum normal overlap and maximum normal force for an undamped elastic contact between two particles (Hidalgo et al., 2013; Norouzi et al., 2016).

two particles. Also Navarro and Braun (2013), considering the linear model, dealt with the problem of a proper choice of ζ and k_n. Defining $\beta = \pi/\ln\zeta$ and considering the non-dimensional parameter for the collision time $t_c^* = \pi\sqrt{1 + \frac{1}{\beta^2}}$ and the mean overlap $\delta^* = \exp\left(-\frac{\arctan\beta}{\beta}\right)$ the Authors provided a graph that can be used to properly calibrate the choice of the parameters (Fig. 5.5). It can be observed that the maximum overlap increases as ζ increases.

5.2 The Lattice-Boltzmann Method for the fluid phase

The fluid phase in the code is solved using the LBM method, which works with particle distribution functions at a mesoscopic scale, i.e. an intermediate scale between the microscale of atoms and molecules and the macroscopic scale of the fluid properties. LBM bridges the gap between micro-scale and macro-scale by considering the behaviour of a collection of fluid molecules as a unit rather than the behaviour of each single fluid molecule. The properties of the collection of fluid molecules are represented by a distribution function $f(\mathbf{x}, \mathbf{v}, t)$ (Mohamad, 2011).

In this context, LBM is very effective for complex domains, and for treating multi-phase flows. Nevertheless, although it is suitable for parallel processes computing, the main drawback is given by the need of more computer memory. The model takes origin from the idea of Maxwell, according to which the knowledge of velocity
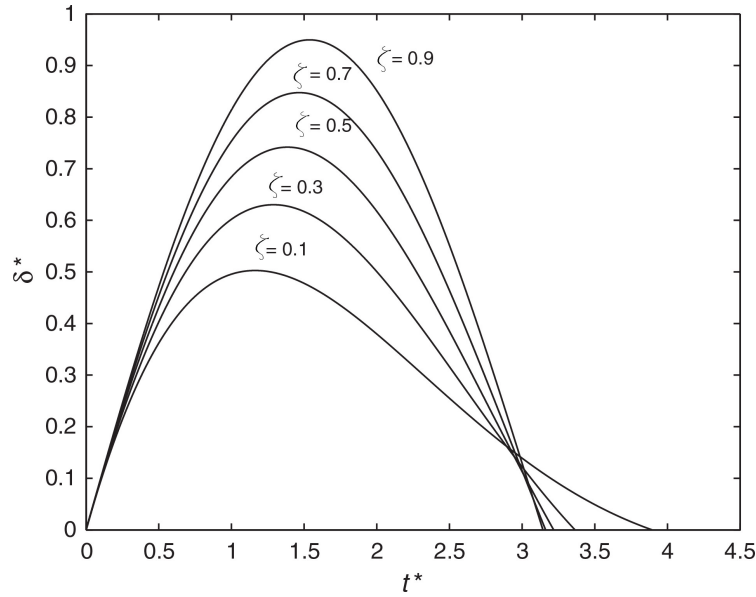
Fig. 5.5 Dimensionless overlap as function of the dimensionless contact time for different restitution coefficients ζ. This graph is obtained while the contact lasts (Navarro and Braun, 2013).

and position of each molecule at every instant of time is not important. At a given time, in a certain location of a container, the distribution function of the percentage of molecules with velocities within a certain range represents the main variable (Mohamad, 2011). Considering a molecular system with colliding molecules, the fast molecules transfer momentum to the slow molecules, conserving the global momentum. For an isothermal system, the distribution function does not depends on time but on velocity $\mathbf{v}$, resulting in:

$$f(\mathbf{v}) = 4\pi \left(\frac{m}{2\pi RT} \right)^{3/2} \mathbf{v}^2 \mathrm{e}^{-\frac{m\mathbf{v}^2}{2RT}},\tag{5.21}$$

where R is the universal gas constant and T the temperature. Therefore, Eq. (5.21) needs to be integrated in the range of velocity. Boltzmann generalised it to arbitrary large systems, integrating its probability function for all values of velocity, obtaining:

$$f(\mathbf{v}) = \left(\frac{m}{2\pi RT} \right)^{3/2} \mathrm{e}^{-\frac{m\mathbf{v}^2}{2RT}},\tag{5.22}$$

The statistical description of a system can be described by the distribution function $f(\mathbf{x}, \mathbf{v}, t)$, where $f(\mathbf{x}, \mathbf{v}, t)$ is the number of molecules at time t, with velocity $\mathbf{v}$ and position $\mathbf{x}$. Considering an external force $\mathbf{F}$, acting on the system, in absence of

collision, it leads to:

$$\frac{\mathrm{d}f}{\mathrm{d}t} = f(\mathbf{x}+\mathbf{v}\mathrm{d}t, \mathbf{v}+\mathbf{F}\mathrm{d}t, t+\mathrm{d}t)\mathrm{d}\mathbf{x}\mathrm{d}\mathbf{v} - f(\mathbf{x},\mathbf{v},t)\mathrm{d}\mathbf{x}\mathrm{d}\mathbf{v} = 0. \qquad (5.23)$$

If collisions take place between two molecules, a change between final and initial status of the distribution function occurs. Its rate is called the collision operator, Ω_{coll}. The solving equation can be written as:

$$\frac{\mathrm{d}f}{\mathrm{d}t} = \Omega_{\mathrm{coll}} \qquad (5.24)$$

that is:

$$\frac{\partial f}{\partial t} + \frac{\partial f}{\partial \mathbf{x}}\mathbf{v} + \frac{\mathbf{F}}{m}\frac{\partial f}{\partial \mathbf{v}} = \Omega_{\mathrm{coll}}, \qquad (5.25)$$

and, in the absence of an external force:

$$\frac{\partial f}{\partial t} + \mathbf{v}\nabla f = \Omega_{\mathrm{coll}}. \qquad (5.26)$$

The Boltzmann collision term is very complicated to solve, as it is function of the momentum of any two particles before and after the collision, so Bhatnagar et al. (1954) introduced an approximate collision term, simple to use, called BGK approximation:

$$\Omega_{\mathrm{coll}} = \frac{1}{\tau_{\mathrm{coll}}}(f^{\mathrm{eq}} - f), \qquad (5.27)$$

where τ_{coll} is the inverse of the collision frequency and is called the relaxation time, while f^{eq} is the Maxwell-Boltzmann distribution function in a thermodynamic equilibrium state. The basic idea is that a thermodynamic system not in a state of equilibrium tends to restore to equilibrium through molecular collisions. The relaxation time is theoretically related to the rate of deformation of the particle distribution towards the equilibrium, and is a function of the local macroscopic kinematic viscosity (Succi et al., 1991).

In LBM, Eq. (5.27) is discretised and is assumed valid along specific directions or linkages. That is:

$$\frac{\partial f_i}{\partial t} + \mathbf{v}_i\nabla f_i = \frac{1}{\tau_{\mathrm{coll}}}(f_i^{\mathrm{eq}} - f_i), \qquad (5.28)$$

or:

$$f_i(\mathbf{x}+\mathbf{v}_i\mathrm{d}t, t+\mathrm{d}t) = f_i(\mathbf{x},t) + \Omega_{\mathrm{coll},i}, \qquad (5.29)$$

or, with an external force $\mathbf{F}$:

$$f_i(\mathbf{x} + \mathbf{v}_i \mathrm{d}t, t + \mathrm{d}t) = f_i(\mathbf{x}, t) + \Omega_{\mathrm{coll},i} + \Omega_{\mathrm{force},i}, \tag{5.30}$$

where the force operator $\Omega_{\mathrm{force},i}$ will be later detailed. The adopted local equilibrium distribution function, as well as the relaxation time, determines the type of problem to be solved (Mohamad, 2011).

In LBM the solution domain is discretised as a lattice. At each node, the fictitious molecules reside, i.e. the distribution function. The velocity, which originally has infinite possible directions, is also discretised and only some directions are possible, according to the lattice shape. At each time step Δt, some of these molecules at each node, e.g. $\mathbf{x}_0$, stream (move) along pre-specified directions to the neighbouring nodes $\mathbf{x}_i$. LBM limits the eligible neighbours to a fixed set, that is the number of possible directions. Every movement corresponds to a specific velocity:

$$\mathbf{c}_i = \frac{\mathbf{x}_i - \mathbf{x}_0}{\delta t}, \tag{5.31}$$

where $\mathbf{x}_0$ is the position of the node considered, and $\mathbf{x}_i$ the position of its i neighbour node.

The D3Q19 lattice model has been adopted (Leonardi, 2015), with D and Q representing the dimension of the problem and the number of lattice velocities, respectively. The correspondent set of velocity is (Fig. 5.6):

$$\mathbf{c}_i = \frac{\Delta x}{\Delta t} \cdot \begin{cases} (0,0,0) & \text{for } i = 0, \\ (\pm 1, 0, 0) & \text{for } i = 1,2, \\ (0, \pm 1, 0) & \text{for } i = 3,4, \\ (0, 0, \pm 1) & \text{for } i = 5,6, \\ (\pm 1, \pm 1, 0) & \text{for } i = 7..10, \\ (0, \pm 1, \pm 1) & \text{for } i = 11..14, \\ (\pm 1, 0, \pm 1) & \text{for } i = 15..18. \end{cases} \tag{5.32}$$

As a consequence, 19 probability functions f_i are defined at each node $\mathbf{x}$ and time t, each corresponding to one of the discrete possible velocities: $f_i(\mathbf{x}, t) = f(\mathbf{x}, t, \mathbf{c}_i)$. Time and space discretisations, Δx and Δt, are considered unitary (i.e. $\Delta x = 1$ and $\Delta t = 1$) and thus also the lattice speed $c = \Delta x / \Delta t$ is equal to unity. This greatly
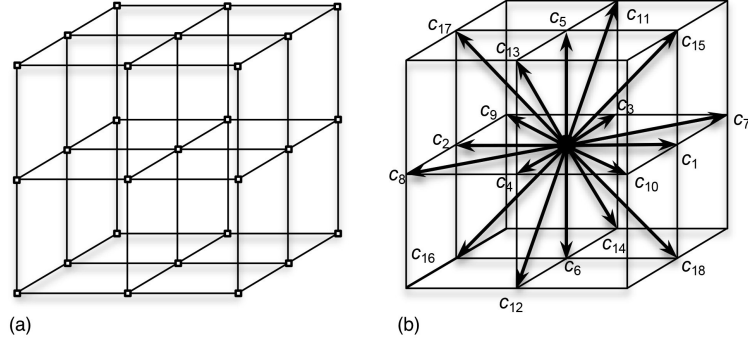
Fig. 5.6 (a) The LBM cubic lattice D3Q19 employed and (b) the set of discrete velocities (Leonardi, 2015).

simplifies the notation, and in the simulations, equations are indeed solved with unit discretisation. The discretised form of f^{eq} is obtained as a Taylor expansion up to the second order of $\mathbf{v}$, from here called $\mathbf{v}_{\mathrm{f}}$ to specifically refer to fluid phase, as:

$$f_i^{\mathrm{eq}}(\mathbf{v}_{\mathrm{f}}, \rho_{\mathrm{f}}) = \rho_{\mathrm{f}} w_i \left(1 + 3\mathbf{c}_i \cdot \mathbf{v}_{\mathrm{f}} + \frac{9}{2}(\mathbf{c}_i \cdot \mathbf{v}_{\mathrm{f}})^2 - \frac{3}{2}\mathbf{v}_{\mathrm{f}} \cdot \mathbf{v}_{\mathrm{f}} \right), \qquad (5.33)$$

where $\mathbf{c}_i$ are the possible set of velocities of the lattice, ρ_{f} is the density (defined later in Eq. (5.36)) and w_i are a set of weight chosen in such a way that the mass and momentum conservations are guaranteed:

$$w_i = \begin{cases} 1/3 & \text{for } i = 1, \\ 1/18 & \text{for } i = 2..7, \\ 1/36 & \text{for } i = 8..19. \end{cases} \qquad (5.34)$$

In the presence of a uniform force field $\mathbf{F}$, an additional operator $\Omega_{\mathrm{force},i}$ has to be adopted:

$$\Omega_{\mathrm{force},i} = w_i \left(1 - \frac{1}{2\tau_{\mathrm{coll}}} \right) [3(\mathbf{c}_i - \mathbf{v}_{\mathrm{f}}) + \mathbf{c}_i(\mathbf{c}_i \cdot \mathbf{v}_{\mathrm{f}})]\mathbf{F}. \qquad (5.35)$$

Once the lattice and the equilibrium density function are defined, under the hypothesis of a limited compressibility, the macroscopic variables of density ρ_{f} and velocity $\mathbf{v}_{\mathrm{f}}$ are reconstructed at each node by summation:

$$\rho_{\mathrm{f}} = \sum_i f_i(\mathbf{x}, t), \qquad (5.36)$$

$$\mathbf{v}_f = \frac{1}{\rho_f(\mathbf{x},t)} \left(\sum_i f_i(\mathbf{x},t)\mathbf{c}_i + \mathbf{F}/2 \right),$$ (5.37)

and also the pressure p_f:

$$p_f(\mathbf{x},t) = c_s^2 \rho_f(\mathbf{x},t),$$ (5.38)

where c_s is the speed of sound of the lattice, defined as:

$$c_s = \frac{c}{\sqrt{3}} = \frac{1}{\sqrt{3}}.$$ (5.39)

The evolution of the particle distribution in space and time is thus expressed by Eq. (5.30). It consists of a streaming part, $f_i(\mathbf{x}+\mathbf{v}_i dt, t+dt) = f_i(\mathbf{x},t)$, a collision part, $\Omega_{\text{coll},i}$, evaluated by Eq. (5.27), and a forcing term $\Omega_{\text{force},i}$. The streaming part represents the propagation of the molecules distributions from one node to a neighbouring one, along the lattice direction as shown in Fig. 5.7 (Körner et al., 2005; Succi et al., 1991). Each time step Eq. (5.30) is solved and the macroscopic variable ρ_f, $\mathbf{v}_f$, and p_f reconstructed through Eqs. (5.36)–(5.38). However, the proposed model is so far not sufficient to simulate all the aspects of a debris-flow fluid phase. The interaction between fluid and the solid phases as well as between fluid and gas phases has to be properly simulated. Moreover, also the interaction between the fluid and an obstacle has to be considered. Finally, as the fluid phase can combine both water and fine material, also a non-Newtonian rheology has to be evaluated.

Thus, in the following section the algorithms for the rheology of the fluid phase, the free surface, the interaction with walls or obstacles, and with particles are presented.

5.2.1   The rheology of the fluid phase

Fluids can be divided into Newtonian and non-Newtonian. In the present research work the fluid phase represents both water and fine grained materials. Thus, its behaviour is, in general, non-Newtonian, that is, its viscosity η is not constant but depends on the shear rate $\dot{\gamma}$ (Zhang et al., 2016), and it is named apparent viscosity η_{app}. It follows that the simple Newtonian formulation does not consider the viscoplastic behaviour of the fluid phase of a debris flow.

In the LBM context, the spatial variability of the apparent viscosity of a non Newtonian fluid is taken into account through the relaxation time τ_{coll}, which varies
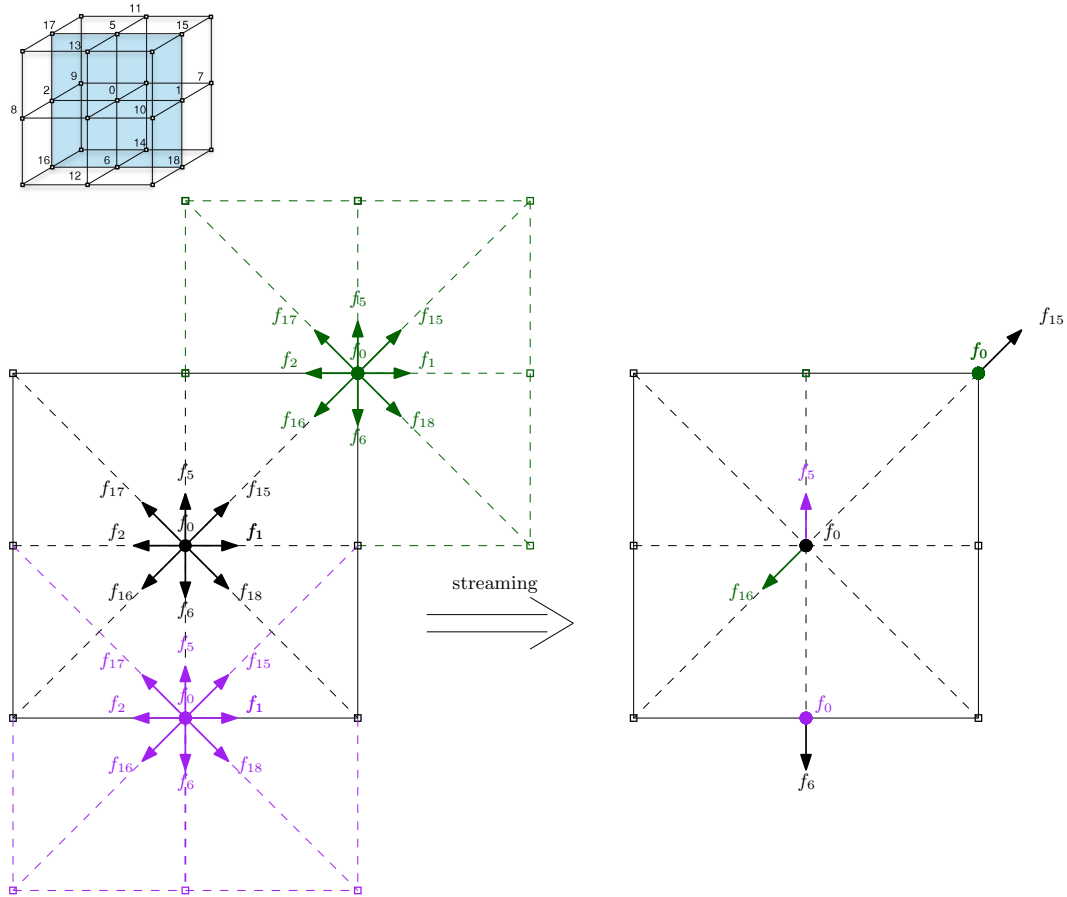
Fig. 5.7 Representation of the streaming phase.

in time and space. As the relaxation time is theoretically function of the rate of deformation of the molecule distribution towards the equilibrium, depending on the local macroscopic kinematic viscosity (Succi et al., 1991), it follows:

$$\eta_{\text{app}}(\mathbf{x},t) = \frac{\tau_{\text{coll}}(\mathbf{x},t) - 1/2}{c_{\text{s}}^2} = \frac{\tau_{\text{coll}}(\mathbf{x},t) - 1/2}{3}. \tag{5.40}$$

This expression derives from the mass conservation equation for a nearly-incompressible fluid, considering the low-Mach number approximation (Leonardi et al., 2011; Vikhansky, 2008), as further explained in Sec.5.2.5.

Among the several mathematical models describing a viscoplastic fluid, several scholars (e.g. Nikitin et al., 2012; Švec et al., 2012; Zhang et al., 2016) suggest to

apply a Bingham plastic model, expressed by:

$$\begin{cases} \tau = \tau_0 + \eta_0 \dot{\gamma} & \text{for } |\tau| \geq \tau_0, \\ \dot{\gamma} = 0 & \text{for } |\tau| < \tau_0, \end{cases} \tag{5.41}$$

where τ is the shear stress, $\dot{\gamma}$ the second invariant of the shear rate, τ_0 the yield stress, and η_0 is the plastic viscosity. The last two parameters are material constants. It follows that:

$$\eta_{\text{app}}(\mathbf{x}, t) = \frac{\tau}{\dot{\gamma}} = \eta_0 + \frac{\tau_0}{\dot{\gamma}(\mathbf{x}, t)}. \tag{5.42}$$

The computation of $\dot{\gamma}$ needs the reconstruction of the spatial derivatives, which in LBM can be computed locally from the distribution function as (Leonardi, 2015; Leonardi et al., 2011):

$$\dot{\gamma}_{ab}(\mathbf{x}, t) = \frac{3}{2\tau_{\text{coll}}(\mathbf{x}, t)} \sum_i \mathbf{c}_{i,ab} \left(f_i(\mathbf{x}, t) - f_i^{\text{eq}}(\mathbf{x}, t) \right), \tag{5.43}$$

where the Einstein notation has been used for the indices a and b. At each time step $\dot{\gamma}(\mathbf{x}, t)$ is computed as a function of the relaxation time $\tau_{\text{coll}}(t-1)$. Then, with Eq. (5.42), $\eta(\mathbf{x}, t)$ is calculated and, finally, substituting in Eq. (5.40), τ_{coll} is evaluated.

It must be noticed that Eq. (5.41) is discontinuous at shear rate $\dot{\gamma} \to 0$ and this brings difficulties in numerical simulations. The simplest solution is to limit the relaxation time $\tau_{\text{coll,min}} \leq \tau_{\text{coll}} \leq \tau_{\text{coll,max}}$, where $\tau_{\text{coll,max}}$ is the maximum allowed with respect to accuracy and stability, assumed equal to 1.8 (Leonardi, 2015). The higher the relaxation time is, the fewer the collisions among molecules are and, thus, the lower the damping of information is (Švec et al., 2012). The requirement of positive viscosity (Eq. (5.40)) mandates instead $\tau_{\text{coll,min}} > 1/2$. It is assumed $\tau_{\text{coll,min}} = 0.501$ (Švec et al., 2012). The more $\tau_{\text{coll}} \to \tau_{\text{coll,min}}$, the more the simulation requires time. An optimum can be given by $\tau_{\text{coll}} \to 1$. The limitation of the relaxation time brings a change in Eq. (5.42), which becomes (Fig. 5.8):

$$\eta(\mathbf{x}, t) = \begin{cases} \frac{1}{3} \left(\tau_{\text{coll,max}} - \frac{1}{2} \right) & \text{if } \tau_{\text{coll}} \geq \tau_{\text{coll,max}}, \\ \frac{1}{3} \left(\tau_{\text{coll,min}} - \frac{1}{2} \right) & \text{if } \tau_{\text{coll}} \leq \tau_{\text{coll,min}}, \\ \eta_0 + \frac{\tau_0}{\dot{\gamma}(\mathbf{x}, t)} & \text{otherwise .} \end{cases} \tag{5.44}$$
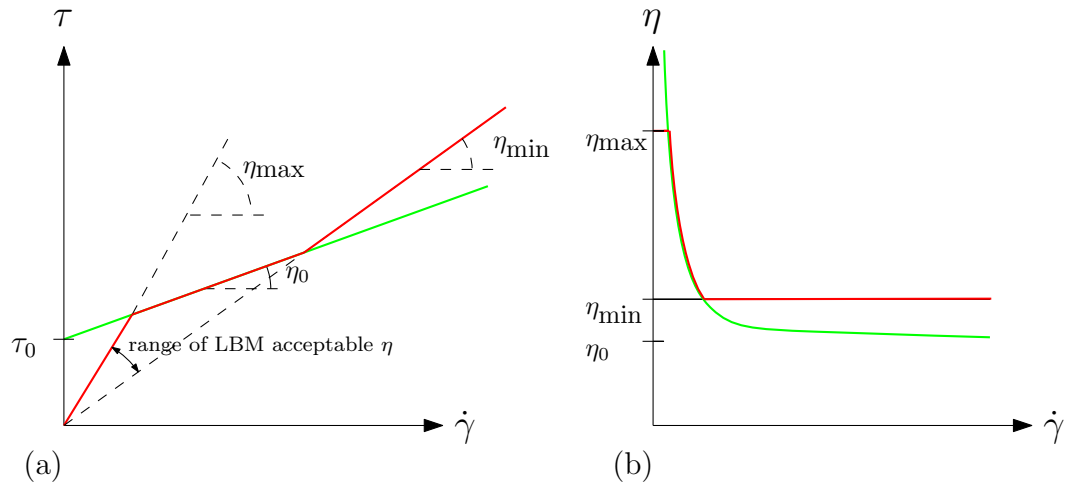
Fig. 5.8 Trilinear model obtained by approximating the Bingham plastic rheology, (a) for the shear stress τ, and (b) for the viscosity η.

5.2.2 The mass tracking algorithm for the free surface

The adopted LBM model accounts for free-surface flows by adopting the mass tracking algorithms (Körner et al., 2005), considered as one of the simplest and fastest algorithm conserving the mass (Švec et al., 2012; Thürey and Rüde, 2009). The lattice cells are subdivided into fluid, gas and interface cells (Fig. 5.9). Gas cells do not contain any particle distributions, and thus the LBM is not solved in those cells, while fluid cells behave as ordinary LBM cells as introduced in Sec. 5.2. Between a gas cell and a fluid cell an interface cell has always to be placed. The interface cells are treated as fluid cells, but require additional information, that is the local mass of the fluid m_f in the cell, as function of the liquid fraction λ:

$$
\begin{cases}
\lambda = 1 & \text{if the node is liquid,} \\
0 < \lambda < 1 & \text{if the node is interface,} \\
\lambda = 0 & \text{if the node is gas.}
\end{cases}
\tag{5.45}
$$

Consequently, the mass per unit volume becomes $m_f = \lambda \rho_f$, where ρ_f is the density of the fluid. During the streaming phase, the difference between the inflow of particle distributions coming from the neighboring fluid cells and the outflow of particle distributions leaving from the interface cells leads to a change of the mass in the
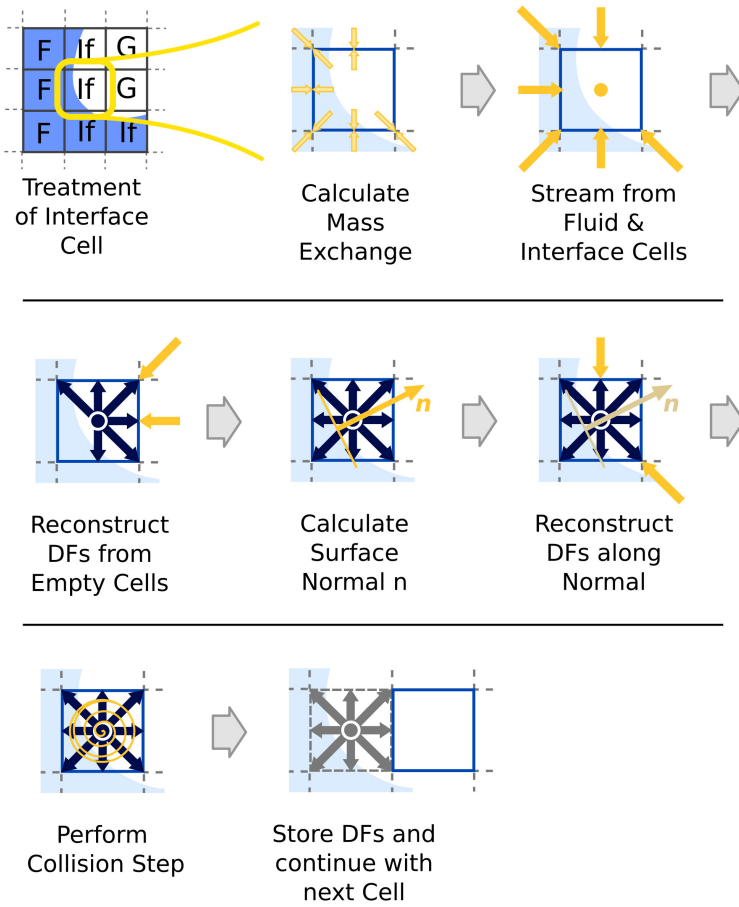
Fig. 5.9 Steps for the treatment of the interface between fluid and gas (Thürey and Rüde, 2009). The abbreviation DF stands for particles distribution function.

current interface cells, resulting in:

$$m_f(\mathbf{x}, t+1) = m_f(\mathbf{x}, t) + \sum_i \alpha_i \left[f_{i'}(\mathbf{x} + \mathbf{c}_i, t) - f_i(\mathbf{x}, t) \right], \tag{5.46}$$

where i' is the direction opposite to i and α_i is a parameter that guarantees the conservation of mass, according to:

$$\alpha_i = \begin{cases} \frac{1}{2} \left[\lambda(\mathbf{x}, t) + \lambda(\mathbf{x} + \mathbf{c}_i, t) \right] & \text{if the neighbor node is interface,} \\ 1 & \text{if the neighbor node is liquid,} \\ 0 & \text{if the neighbor node is gas.} \end{cases} \tag{5.47}$$
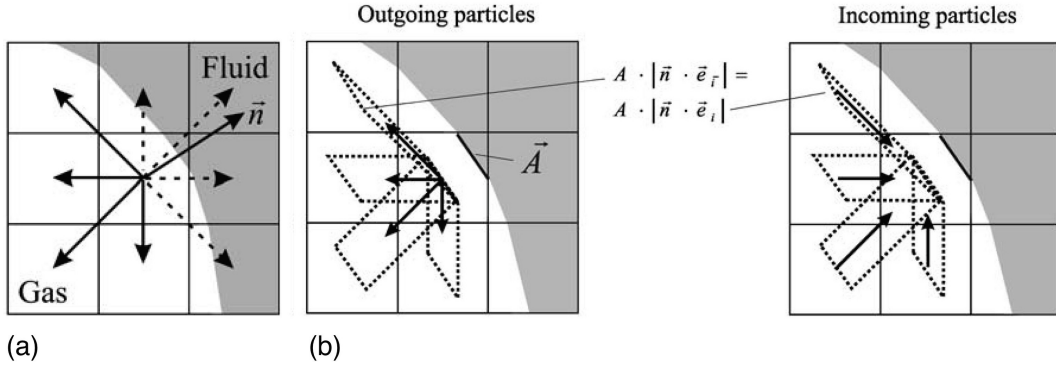
Fig. 5.10 (a) Set of distribution functions at the interface cells after streaming. Dashed lines represent the distribution functions with $\mathbf{n} \cdot \mathbf{c}_i \geq 0$. (b) Momentum transferred to the interface area of outgoing particles and incoming particles (Körner et al., 2005).

The interface cell becomes a fluid cell when the mass reaches its density, i.e. when $m_f(\mathbf{x},t) \geq \rho_f(\mathbf{x},t)$, and becomes a gas cell when the mass drops down to zero, i.e. when $m_f(\mathbf{x},t) \leq 0$. When this transformation occurs, some of the surrounding cells are converted into interface cells in order to guarantee the consistency, avoiding the direct contact between fluid and gas cells. Furthermore, in order to conserve of mass, the surplus (or shortfall) of mass is computed each time step and is corrected by distributing an opposite amount of mass among all the interface nodes.

During the streaming phase, some of the particle distributions should arrive at the current interface cell from gas cells (Fig. 5.9). Gas cells do not have information inside, that is the particle distributions do not exist and need to be reconstructed. According to Körner et al. (2005), using a momentum exchange method, the velocity of the fluid and the velocity of the gas are equal at the free surface, in the hypothesis of no-slip boundary condition (Fig. 5.10). It follows that the velocity of the gas $\mathbf{v}_{gas}$ is equal to the velocity at the interface $\mathbf{v}_{int}$. Furthermore, the density of the gas is assumed equal to unity $\rho_{gas} = \rho_{atm} = 1 < \rho_f$, and the pressure of the gas is supposed known and therefore the force exerted by the gas on the fluid. This implies that the boundary conditions are fulfilled if the force exerted by the liquid is equal to the gas force. Expressing the pressure in terms of forces acting between gas and fluid, i.e. applying a fixed-pressure boundary condition at the interface, it follows:

$$f_{i'}(\mathbf{x}+\mathbf{c}_{i'},t+1) = f_i^{eq}(\mathbf{v}_{int},\rho_{atm}) + f_{i'}^{eq}(\mathbf{v}_{int},\rho_{atm}) - f_i(\mathbf{x},t). \qquad (5.48)$$

5.2.3 Interaction with walls: dry coupling scheme

The treatment of the no-slip boundary condition in case of solid rigid obstacle (i.e. the walls of the channel or a barrier in case of debris flow), is implemented with the bounce-back scheme, also defined as dry coupling scheme (Ladd, 1994). In this scheme, when a population is streaming toward a wall, it is reflected and bounced back in the opposite direction (Fig. 5.11). In the LBM frame, this implies:

$$f_{i'}(\mathbf{x}, t+1) = f_i(\mathbf{x}, t), \tag{5.49}$$

where $\mathbf{x}$ is the position of the fluid node close to the wall, i the streaming direction pointing at the wall, and i' the opposite direction. The bounce-back location is located halfway between the solid node of the obstacle and the fluid node and this allows second-order accuracy. The resultant force given by momentum exchange is:

$$\mathbf{F}_{\text{hydro}} = \sum \left(2 f_i(\mathbf{x}, t)\right) \mathbf{c}_i. \tag{5.50}$$

In the hypothesis of rigid obstacle, the obstacle is considered rigid enough not to be affected by momentum transfer due to the collisions with fluid particles.

5.2.4 Interaction with particles: wet coupling scheme

The Immersed Boundary Method (IBM) (Feng and Michaelides, 2004) is employed to solve interaction between particles and fluid. In contrast to the bounce-back boundary conditions, this approach solves the problems of fluctuation of the forces and velocities on the particles. In the frame of moving-particles simulations, the
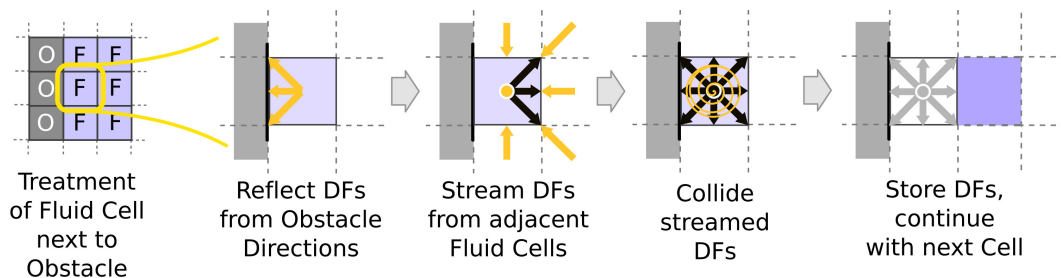
Fig. 5.11 Step for the treatment of the interactions between fluid and walls or rigid obstacles (Thürey and Rüde, 2009).The abbreviation DF stands for particles distribution function.

boundaries of solid particles evolve at each time step, thus modifying forces and velocities. In the bounce-back method, the boundary nodes have to be defined, and a finer grid has to be adopted to minimise these fluctuations. This is computationally non convenient (Fig. 5.12). Thus, the basic concept of IBM proposed by Feng and Michaelides (2004) is to represent boundaries by a set of independent Lagrangian nodes, advected by the fluid, ignoring the Eulerian nodes set for the fluid domain. This allows for a more precise resolution of particle shape without a small lattice spacing. In the original model proposed by Feng and Michaelides (2004), the interaction force field reproduces the no-slip boundary condition and is evaluated at these Lagrangian nodes, whose velocity $\mathbf{v}_\mathrm{p}$ should be equal to the velocity of the fluid in case of no-slip. Nevertheless, as differences in the velocities occur as the system evolves in discrete time steps, the interaction force is calculated from these differences as:

$$\mathbf{F}_\mathrm{hydro}(\mathbf{x}_\mathrm{p},t) = \rho_\mathrm{f}(\mathbf{x},t)\left[\mathbf{v}_\mathrm{f}(\mathbf{x}_\mathrm{p},t) - \mathbf{v}_\mathrm{p}(\mathbf{x}_\mathrm{p},t)\right]V_\mathrm{p}, \tag{5.51}$$

where V_p is the volume associated with the Lagrangian node, $\mathbf{v}_\mathrm{f}(\mathbf{x}_\mathrm{p},t)$ is the velocity of the fluid calculated at the position $\mathbf{x}_\mathrm{p}$, computed by an interpolating function $\mathscr{F}$ over every lattice node n in the neighbourhood:

$$\mathbf{v}_\mathrm{f}(\mathbf{x}_\mathrm{p},t) = \sum_n \mathscr{F}(\mathbf{v}_\mathrm{cell}(\mathbf{x}_\mathrm{p},t))V_\mathrm{p}, \tag{5.52}$$

The force transmitted to the fluid from the m cells in the proximity of a lattice node centered in $\mathbf{x}$ is:

$$\Omega_\mathrm{force}(\mathbf{x},t) = -\sum_m \mathscr{F}\left(\mathbf{F}_\mathrm{hydro,cell}(\mathbf{x}_\mathrm{cell,m},t)\right). \tag{5.53}$$

In contrast, Leonardi et al. (2016) applied a simplified version, considering as boundaries the cubic cells of the lattice rather than the Lagrangian nodes, and thus $\mathbf{x}_\mathrm{p} = \mathbf{x}$ (Fig. 5.13). If the center of the cubic cell is inside the particle, all the cell is set solid, if not is fluid. In this way no interpolation from LBM nodes is necessary to compute the correspondent velocity of the fluid $\mathbf{v}_\mathrm{f}$ required to evaluate the forces (as $\mathbf{x}_\mathrm{p} = \mathbf{x}$). Furthermore, the volume of the cubic cell is unitary. The hypothesis of no-slip boundary condition is not assumed, fluid and particles can have different velocities, and in fact, if solid and fluid have the same velocity, no interaction force
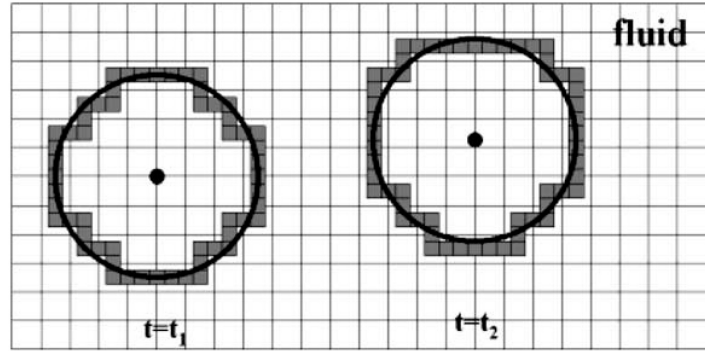
Fig. 5.12 Discretization for particles boundaries at two time step t_1 and t_2 (Feng and Michaelides, 2004).

arises. The interaction force mimics the drag and tends to relax the velocity of the fluid to the one of the solid and vice-versa. The force for every lattice cell $\mathbf{F}_{\text{hydro,cell}}(\mathbf{x}_{\text{cell}}, t) = \mathbf{F}_{\text{hydro}}(\mathbf{x}, t)$ becomes:

$$\mathbf{F}_{\text{hydro}}(\mathbf{x}, t) = \rho_f(\mathbf{x}, t) \left[v_f(\mathbf{x}, t) - v_p(\mathbf{x}, t) \right], \tag{5.54}$$

and for the fluid as:

$$\Omega_{\text{force}}(\mathbf{x}, t) = -\mathbf{F}_{\text{hydro}}(\mathbf{x}, t). \tag{5.55}$$

The resultant force on the particle (to insert in Eq. (5.2)) is then computed by simple summation of each of the l nodes covered by a particle, as:

$$\mathbf{F}_{\text{hydro}} = -\sum_{\text{cell}=1}^{l} \mathbf{F}_{\text{hydro,cell}}, \tag{5.56}$$

and the resultant moment (to insert in Eq. (5.2)):

$$\mathbf{M}_{\text{hydro}} = \sum_{\text{cell}=1}^{l} \mathbf{F}_{\text{hydro,cell}} \times \mathbf{r}_{\text{DF,cell}}, \tag{5.57}$$

where $\mathbf{r}_{\text{DF,cell}}$ is the vector connecting the center of mass of the particle and the node location $\mathbf{x}_{\text{cell}}$. It is worth mentioning that, in order to compute v_f, all the lattice cells in which solid particles lie are solved as fluid cells, i.e. inside the particle the node is active.
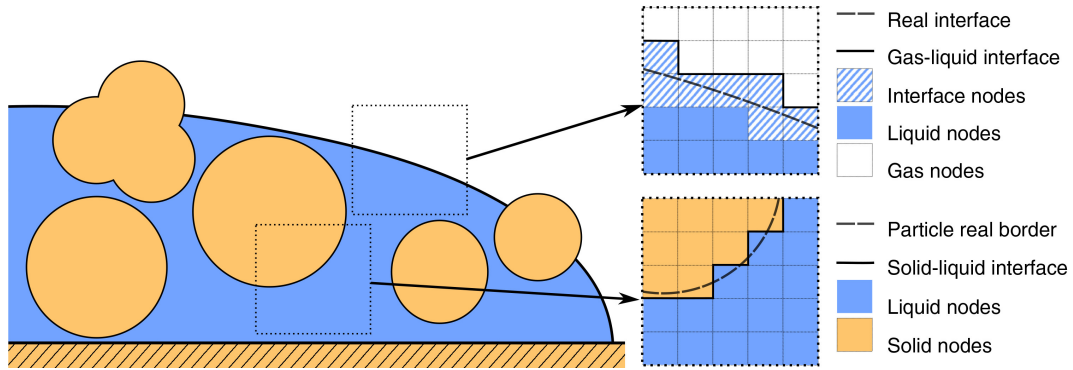
Fig. 5.13 Discretisation for interface, gas, fluid and particles cells (Leonardi et al., 2014).

Variable	LBM value	Real value
Cubic lattice length Δx	1	L (m)
Cubic lattice time step Δt	1	T (s)
Initial density ρ_0	1	D (kg/m^3)
Characteristic velocity of the actual fluid $\mathbf{V}_c$	1	L/T (m/s)
Plastic viscosity η_0	$\eta_{LBM} = \frac{\eta_0 T}{DL^2}$	η_0

Table 5.1 LBM and real parameters values.

5.2.5 Numerical arrangement for the simulations

In this subsection the numerical conditions which have to be applied are illustrated. The LBM domain is solved in a scaled reference system, different from the real physical one, as in Tab. 5.1:

As explained in Sec. 5.2, the relaxation time has to be limited, and thus the kinematic viscosity of the fluid (Eq. (5.44)). To partially overcome the problem of a trilinear rheology model, adapting the time step as it is $\Delta t = \Delta x^2 \frac{\eta_{LBM}}{\eta_0}$ (Feng and Michaelides, 2004), the plastic viscosity η_0 is taken $\eta_0 > \eta_{min}$. Thus, the model reduces to a bilinear one.

To limit the computational time, limiting the number of lattice nodes to $10^7 - 10^8$ is the second required condition. Nevertheless, considering the approximation done in the particle discretisation in the LBM domain for an efficient particle-fluid coupling (Sec. 5.2.4), the length of the cubic lattice edge has to be less than 1/10th of the minimum diameter of the particles.

The third required condition is that the Mach number, $Ma = v_f/c_s$, has to be less than 1 ($Ma << 1$) (Leonardi et al., 2011). Feng and Michaelides (2004) suggested taking $Ma \leq 0.1$, to ensure the hypothesis of near-incompressibility of the flow. This,

in LBM unit, implies:

$$\mathrm{Ma} = V_c \frac{\sqrt{3}\Delta t}{\Delta x} = \frac{V_c \Delta x}{\eta_{LBM}} \left(\frac{2\tau_{\mathrm{coll}} - 1}{2\sqrt{3}} \right). \tag{5.58}$$

Chapter 6

Numerical implementation of friction in the DEM-LBM code

This chapter outlines in detail the improvements introduced in the original code (see Ch. 5) and their validation. The original version of the code did not allow formation of long-term stable configurations between particles, and thus a complete stop of the motion. This aspect is, instead, very important in the perspective of studying the dynamics of interaction between a flowing mass and a barrier that should halt the flow motion, promoting jamming of the moving mass. From a numerical point of view, the introduction of static friction allows the formation of stable force chains between particles. This is sufficient in case of clustering particles adoption, standing for different particle shapes. With this, the interlocking between particles can be simulated (Szarf et al., 2011). Nevertheless, the adoption of clusters implies a high computational time and add more degree of freedom to the equations system. In order to limit the complexity and the variability of the system, as well as to perform a significant number of simulations, the adopted particles are single spherical ones. However, in the limit case of a sphere rotating along an inclined plane, this is not sufficient to stop its motion. Thus, the introduction of a rolling resistance model, representing the frictional contributions of the roughness, deformability and shape of the particles, is necessary. With these objectives, static sliding friction as well as the rolling friction models have been implemented and validated in this research. This requires also the introduction of two numerical input parameters: the sliding μ_s and the rolling μ_r friction coefficients.

From a physical point of view, the implemented friction models represent the

internal friction of a granular assembly of loose material, as explained herein below. The new numerical input parameters (μ_s and μ_r) need to be related to the measured physical quantities, in order to assure their representativeness of the real case. Thus, an empirical law that correlates simulation and real parameters has to be identified.

The concept of friction for solid bodies is explained in detail in Sec. 6.1.1. The definition is extended to granular materials (Sec. 6.1.2), a constituent of debris flows. The implementation of static sliding friction is explained in detail in Sec. 6.2, while Sec. 6.3 considers the issue of rolling friction modelling. The validation of these developments is described in Sec. 6.4. Finally, Sec. 6.5 introduces the correlation analysis between real and numerical parameters.

6.1 General concepts

6.1.1 Friction in solid bodies

Friction is a tangential force that arises when two elements are in contact, and opposes their relative motion. According to the state of motion in which the two bodies stand, friction could be classified in:

- *Static*: the static friction force F_s is the minimum force which has to be applied to a stable body in order to provoke its motion. Its magnitude can be computed as:

$$F_s = \mu_s F^n, \tag{6.1}$$

where F^n is the weight of the body, and μ_s is the dimensionless static friction coefficient. This coefficient is a function of the contact surfaces of the bodies, with particular reference to their roughness.

- *Dynamic*: the dynamic friction force F_d is the minimum force which has to be applied to maintain a body in uniform motion along a straight line (sliding or rolling). In this case, the magnitude of the force is:

$$F_d = \mu_d F^n, \tag{6.2}$$

where μ_d is the dimensionless dynamic friction coefficient, which is a function of the velocity of the bodies and the contact surfaces of the bodies. The dynamic state of motion implies that $\mu_d \leq \mu_s$.

Besides this subdivision, both in static or dynamic conditions, three different typologies of friction can be identified, as a function of the type of motion involved:

- *Sliding friction*: the sliding friction force opposes the mutual sliding of two bodies. Considering Eq. (6.1), the static friction coefficient can be computed as:

$$\mu_{s,s} = \tan \phi, \tag{6.3}$$

  where ϕ is defined as angle of friction. Considering the simple case of a solid body on an inclined plane, this can be calculated as the maximum angle of inclination in which the body stands before motion. On the contrary, the dynamic friction coefficient is function of the velocity of the motion, as high velocities cause a delay in contact formation, i.e., time lag between contact breaking and remaking (Braun and Peyrard, 2011). In the simple case of a solid body sliding on an inclined plane in uniformly accelerated linear motion, it can be physically computed through the equality between the acting force and the difference between the gravity and the friction forces parallel to the plane, as:

$$\mu_{s,d} = \tan \phi - a \sec \phi, \tag{6.4}$$

  where a is the uniform acceleration of the body. For notation simplicity, μ_s and μ_d are employed to indicate sliding static and dynamic friction coefficient.

- *Rolling friction*: the rolling friction force F_r is opposite to the mutual rolling of two bodies. This kind of friction is caused by the elastic and plastic deformation of the body, the surface irregularities and the molecular attraction or adhesion of the materials.

$$F_r = \frac{\mu_r F^n}{r} \tag{6.5}$$

  where r is the radius or characteristic dimension of the body, μ_r. This coefficient is a function of body size and shape, the contact surface regularity of the bodies, and their relative velocity. It represents the eccentricity of the normal force from the center of gravity, and, in fact, it has the dimensions of

a length. In the case of rigid bodies, the deformability of the contact surface, and, thus, the eccentricity of the normal force, is limited. In this case, the static and dynamic rolling friction coefficients are similar: $\mu_{r,s} \approx \mu_{r,d}$. For simplicity of notation, only μ_r is used for both the static and the dynamic rolling friction coefficient. Similarly as previously done for the sliding friction, in the simple case of a sphere released on an inclined plane, in uniformly accelerated linear motion, the rolling friction coefficient can be physically computed as $\mu_r = r(\tan\phi - a\sec\phi)$.

- *Viscous friction*: the viscous friction force $\mathbf{F}_v$ is opposed to the motion of a body inside a fluid.

$$\mathbf{F}_v = \begin{cases} -K_l\mathbf{v} & \text{if the flow is laminar,} \\ -K_t\mathbf{v}^2 & \text{if the flow is turbulent,} \end{cases} \tag{6.6}$$

with $\mathbf{v}$ is the relative velocity of the body in the fluid, and K_l and K_t are the resistance coefficients of the medium, in case of laminar and turbulent flow, respectively. K_l is measured in Pa·s·m, while K_t in Pa·s^2.

6.1.2   Friction in granular materials

When a dry granular assembly is in motion along a slope under the influence of gravity, a frictional force resisting to the motion arises. Dry granular materials exhibit solid-like frictional properties. However, a granular mass can be considered as an assembly of individual grains, thus differing from the solid body case of Sec. 6.1.1. For this reason, another classification of friction has to be defined. In particular, an internal and a basal friction are identified. Internal friction is the force opposed to the motion between the elements making up the assembly while it undergoes deformation, while basal friction is the force resisting motion of the whole granular material on a basal surface. In granular materials, the internal static and dynamic friction coefficients are influenced by both sliding and rolling friction, which arise between grains, and they are defined considering the Mohr-Coulomb failure criterion for soils.

However, a dry granular mass in motion starts from a packing state, more complex than a rigid block. As a consequence, the physical determination of the internal friction coefficient is not standardised. Metcalf (1966) stated that the internal friction

coefficient at loosest condition of packing can be considered equal to the tangent of the angle of repose; Miura et al. (1997) and Sadrekarimi and Olson (2011) provided some references in which this statement is considered valid. Nevertheless, other Authors (e.g Ghazavi et al., 2008; Lee and Herrmann, 1993; Miura et al., 1997; Van Burkalow, 1945) do not consider this equality valid, and the relation between the angle of repose and the angle of internal friction in a granular soil is still under discussion even now.

Angle of repose

The angle of repose or angle of rest is generally referred as the angle (with the horizontal) at which loose material will stand when piled (Van Burkalow, 1945). Considering soils, an angle of repose can be defined only for loose granular material. Differently from the internal friction angle, whose measurement requires to perform a triaxial test, the angle of repose can be easily measured. This angle can theoretically take values from $0°$ to $90°$. Several methods of measurement exist (Fig. 6.1), which mainly differ for the degree of lateral confinement (Carrigy, 1970). Moreover, Carrigy (1970) as well as Nagel (1992) and Albert et al. (1997) showed that a sandpile has two important angles of stability between which the slope oscillates. In general, a pile is stable and does not collapse until the slope reaches an upper value, defined as maximum stability angle ϕ_m. When the slope becomes greater than this maximum angle the pile is unstable and a global avalanche occurs, bringing the slope to a smaller value. If more grains are added to the system, the slope of the pile increases again until ϕ_m, and another avalanche occurs. The majority of Authors define the angle of repose as the lower of the two angles (e.g. Lee and Herrmann, 1993; Van Burkalow, 1945), while Bagnold (1971) considered the higher. Elperin and Golshtein (1997), instead, considered the angle of repose as an intermediate value among these two.

Nevertheless, Van Burkalow (1945), providing several references, revealed that there is also a confusion between the angle of repose as previously defined and the angle of slope (with the horizontal) of an inclined plane at which a granular mass resting on the plane will first begin to slide. This can instead be called "angle of sliding friction". It follows that sometimes the angle of internal friction is associated to different measured angles.

The present research work assumes the validity of the equality between the
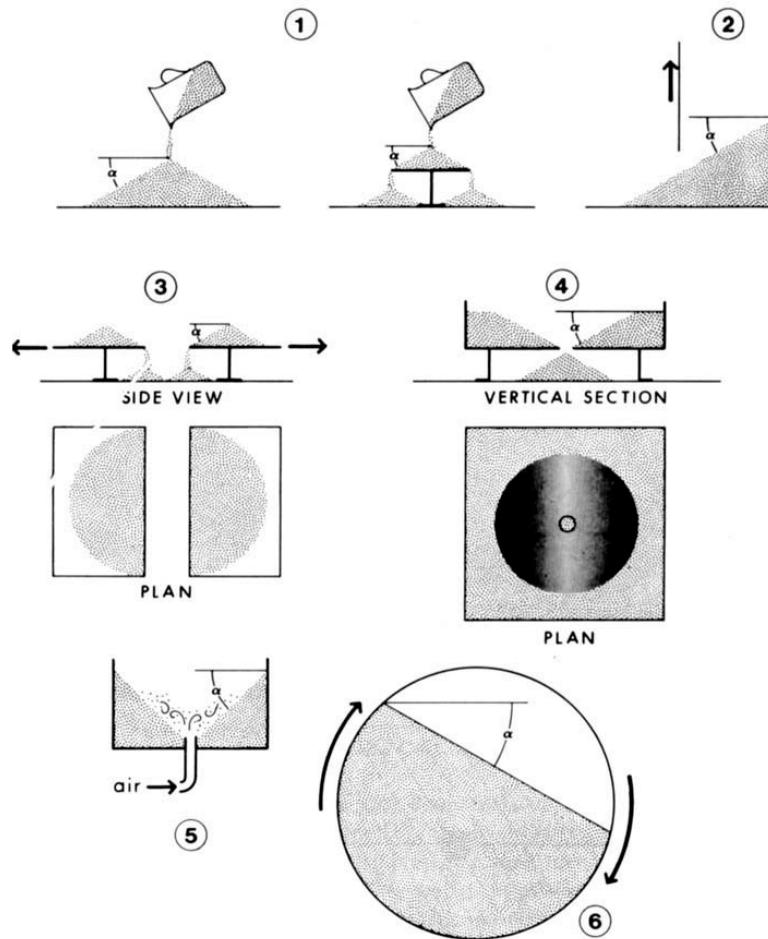
Fig. 6.1 Methods of producing angles of repose in granular materials: (1) by carefully pouring loose particles onto a cone-shaped pile, (2) by filling a container, removing one side of a container and letting the particles flow out, (3) by pulling apart the base beneath a poured cone and letting the excess material spill over the edge until movement stops, (4) by removing a plug from below a layer of loose granules and letting the particles flow through the hole until movement ceases, (5) by blowing a jet of air through loose granular material until a crater is excavated, (6) by measuring the rotation of a trough of granular material until movement begins (Carrigy, 1970).

tangent of the angle of repose and the internal friction angle of the material. However, to endorse this assumption, it is worth mentioning the dependence parameters of the repose angle. Norouzi et al. (2016) suggested that the governing mechanism for the formation of a pile is related to friction caused by surface roughness or particles shape irregularity. Other factors, like pile formation history, particle size, and polydispersity, also influence the properties of the pile (Matuttis et al., 2001). Van Burkalow (1945) showed, through controlled experiments, that the angle of repose grows:

- Inversely with fragment size in perfectly sorted materials, but directly in those imperfectly sorted; the presence of coarser grain makes the angle steeper. The experiments do not analyse the influence of the degree of imperfect sorting; however, they they have been performed with a mixture of lead shot ranging from 0.1 to 1 cm, a mixture of rhinestones ranging from 1 to 4 mm, and a mixture of wooden block ranging from 2 to 8 cm.

- Inversely with fragment density.

- Directly with fragment angularity, roughness and degree of compaction.

- Inversely with falling height on a free cone.

- Directly with the increase of moisture up to the saturation point.

El Shourbagy and Matuttis (2005) showed that the angle of repose for dry granular material crucially depends on both the particle shape and the internal friction coefficient. For no or moderately elongated particles, a strong dependence of the angle of repose on the particle roughness was found. On the contrary, for elongated particles, the effect of particle roughness on the angle of repose is suppressed, because no rolling takes place. Furthermore, the Authors observed that the influence of shape is greater than that of size. Finally, Matuttis et al. (2001) declared that the more spherical the particles are, the smaller the measured angle of repose is, if construction histories are identical.

The DEM simulation frame

In a granular material, and in particular in one made of spheres, the internal or basal friction forces are influenced by the single particle-particle or wall-particle friction

mechanisms, both sliding and rolling.

In the same way, in particle based models, e.g. the DEM models, particle-particle and wall-particle sliding and rolling friction have to be distinguished. As the inputs parameters are given for each single grain, it is appropriate to refer to inter-particle or wall-particle friction instead of internal or basal friction of the whole assembly. Considering a numerical simulation of a granular flow event, generally, the physical parameter given from the real flowing material is the angle of repose ϕ_{rep}, which is assumed equal to the internal friction angle ϕ_{i}. Thus, it is important to properly correlate ϕ_{rep} with the inter-particle or wall-particle friction coefficients, that represent the final numerical inputs.

In this perspective, Zhou et al. (2002), comparing laboratory and numerical analyses, proposed the following correlation between ϕ_{rep} and the simulation parameters:

$$\phi_{\text{rep}} = 68.61\mu_{\text{s,pp}}^{0.27}\mu_{\text{s,pw}}^{0.22}\mu_{\text{r,pp}}^{0.06}\mu_{\text{r,pw}}^{0.12}D_{\text{p}}^{-0.2},$$
$$2 \leq D_{\text{p}} \leq 10 \text{ mm}, 0 \leq \mu_{\text{s,pp}},$$
$$\mu_{\text{s,pw}} \leq 0.6, \tag{6.7}$$
$$0 \leq \mu_{\text{r,pp}},$$
$$\mu_{\text{r,pw}} \leq 0.2 \text{ mm},$$

with $\mu_{\text{s,pp}}$ and $\mu_{\text{s,pw}}$ the sliding friction coefficients between two particles and between particle and wall, respectively, $\mu_{\text{r,pp}}$ and $\mu_{\text{r,pw}}$ the rolling friction coefficient between two particles and between particle and wall, respectively, and D_{p} the mean diameter of the particles. This correlation suggests that the angle of repose is directly proportional to the friction coefficients and inversely to the particle diameter. This consideration was confirmed also by the correspondence between laboratory experiments and the numerical simulations made by Zhou et al. (1999) and of Liu and Zhou (2008). The validity of the observation was also proved through the already mentioned experiments on real granular material conducted by Van Burkalow (1945), or the laboratory experiments with glass spheres led by Frankowski and Morgeneyer (2013). In the DEM simulation frame, Zhou et al. (2001) revealed that, increasing particle size, the sliding friction force and the rolling friction torque decrease, thus producing a smaller angle of repose. However, the decreasing rate for the rolling friction torque is much more significant than that for the sliding friction force. Also Carstensen and Chan (1976) suggested that particle size affects the angle of repose mainly through its effect on rolling friction rather than on sliding friction.

Besides the size, particular attention has to be paid on the mixture of the sizes, with a specific focus on spherical assemblies. El Shourbagy and Matuttis (2005), with laboratory experiments, stressed the fact that in mono-disperse size distributions, the particles can be locally ordered in a crystal structure. This structure is absent in most tested real granular materials except, for example mono-disperse glass beads. This aspect needs thus to be properly considered in a numerical analysis, especially when monosized spheres simulate a granular flow or a debris flow event. For example, Zhou and Ooi (2009), through numerical DEM simulations, showed a crystalline packing structure for the case of monosized spheres, producing contact orientation in $60°$ and $120°$ directions, predominantly. Spheres, with their perfect symmetry, have thus the propensity for excessive particle rotation and forming crystalline structures, obscuring the phenomena pertaining to real granular solids. Pöschel and Buchholtz (1993) noticed that the slope of a pile of non-spherical grains does not depend on the number of particles, while, for spherical grains, the heap dissolves under gravity with increasing particle numbers. A different critical friction coefficient for a stable pile was analytically found as function of the different number of particles (Albert et al., 1997; Elperin and Golshtein, 1997). As regards the numerical investigation on the relation angle of repose and particle shape, Zhou et al. (2011) revealed that when the particles become more non-spherical, the angle of repose of piles generally increases. They modified the law proposed by Zhou et al. (2002), linking the angle of repose ϕ_{rep} to simulation parameters, by an additional term that is function of the aspect ratio:

$$\phi = \phi_{\text{rep}} f(\eta),$$
$$\phi_{\text{rep}} = 68.61 \mu_{\text{s,pp}}^{0.27} \mu_{\text{s,pw}}^{0.22} \mu_{\text{r,pp}}^{0.06} \mu_{\text{r,pw}}^{0.12} D_{\text{p}}^{-0.2},$$
$$f(\eta) = \begin{cases} e^{2.9\eta(1-\eta)} & \text{for } \eta \leq 1, \\ f(\eta) = 2.0 - 40 * 0.025^{\eta} & \text{for } \eta > 1. \end{cases}$$

(6.8)

If spheres are used to represent the ellipsoidal particles, the material properties of spheres (sliding and rolling friction coefficients) should be adjusted. As the sliding friction is independent of shape, only the rolling friction coefficient has to be changed, multiplying the sphere value by $f(\eta)^{5.5}$. This value derives from DEM simulations in the case of granular piles and 2D hopper flow (Zhou et al., 2011).

Thus, the correlation between ϕ_{rep} and μ_{s} and μ_{r} has to be properly calibrated. Sec. 6.5 describes the attempt to provide a law, making use of a consistent number

of numerical simulations with the modified version of the DEM code by Leonardi et al. (2015).

6.2   Numerical implementation of sliding friction

Long-term or permanent particles configurations arise if and only if stable interaction forces between particles occur. As previously explained, the original code adopted in the present research work needs developments to allow the rising of forces that can halt the motion of the flowing particles. In particular, sliding friction between particles appears as a resisting force to sliding motion between the two surfaces in contact. This force arises both in static and dynamic conditions.

When a particle-particle or particle-wall collision occurs, a normal force and a tangential force arise. The adopted liner dashpot model idealises the contact as a parallel connection of a spring of tangential stiffness k_t and a damper with tangential viscous damping coefficient α_t (for the linear dashpot model in normal direction see Sec. 5.1) (Fig. 6.2). The magnitude of the tangential force F^t is capped by the normal force F^n through Coulomb's law:

$$F^t \begin{cases} \leq \mu_s F^n & \text{in static conditions,} \\ = \mu_d F^n & \text{in dynamic conditions,} \end{cases} \tag{6.9}$$

$$\mu_d \leq \mu_s.$$

In the present case, the following relation has been assumed $\mu_d = 0.9\mu_s$, as from laboratory experiments of granular material, static and dynamic coefficients are very similar (Senetakis et al., 2013).

In the frame of DEM simulations, the static situation requires an elastic spring to allow a restoring force, that is a non-zero remaining tangential force in static equilibrium due to activated Coulomb friction. This spring stretches to a length equal to the distance between the first contact point between two particles and the actual contact point in the considered time step, as long as a contact is active. The model implemented in the code follows the solution proposed by Luding (2005, 2008). If a collision occurs, the first step is to project (rotate) the tangential spring (the initial one is a null vector) onto the actual tangential plane, because the reference system of
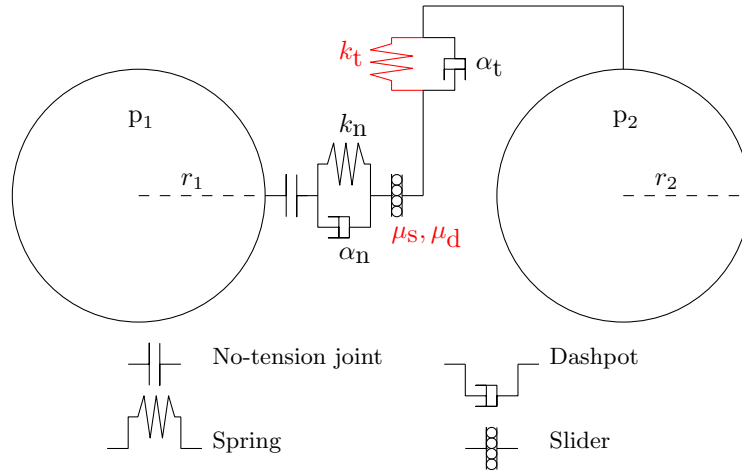
Fig. 6.2 Linear spring-dashpot model for normal and tangential forces. Symbols in red refers to the implemented static friction part.
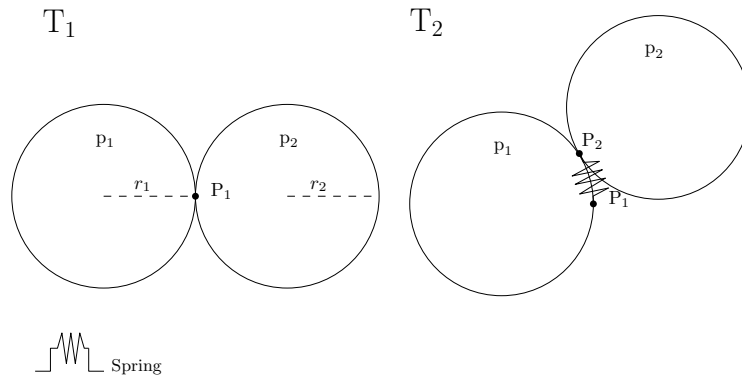
Fig. 6.3 Sliding friction model. T_1 and T_2 represent two following time steps, and P_1 and $P2$ the contact point of two particles in the considered instant.

the contact may have rotated since the last time step:

$$\xi^{P} = \xi' - \mathbf{n} \left(\mathbf{n} \cdot \xi' \right), \qquad (6.10)$$

where ξ' is the old spring length calculated at the end of the previous iteration. If the spring is new, the tangential spring length is zero, that is ξ' is a null vector, but its change is well defined after the first (initiation) step. Then, an appropriate scaling is applied:

$$\xi^{S} = \xi^{P} \frac{\xi'}{\xi^{P}}. \qquad (6.11)$$

In order to compute the changes of the spring force, a test-force $\mathbf{F}^{\text{test}}$ is first

computed as the sum of the spring force and the viscous force, as in the spring dashpot model for the normal force (Eq. (5.11)):

$$\mathbf{F}^{\text{test}} = \xi^{\text{S}} k_{\text{t}} + 2\alpha_{\text{t}} \sqrt{k_{\text{t}} \tilde{m}} \mathbf{v}_{\text{coll}}^{\text{t}}, \tag{6.12}$$

where k_{t} is the tangential spring stiffness, assumed equal to $2/7 k_{\text{n}}$, as explained in the next Sec. 6.2.1, α_{t} represents the tangential dissipation parameter, and $\tilde{m} = \frac{m_i m_j}{m_i + m_j}$ is the effective mass.

The contact remains in the initial static condition as long as:

$$F^{\text{test}} \leq \mu_s F^{\text{n}}. \tag{6.13}$$

In this case, the tangential force and the new spring length (which becomes ξ' after the Eq.(6.12)) are computed as:

$$\mathbf{F}^{\text{t}} = \mathbf{F}^{\text{test}}, \tag{6.14}$$

$$\xi' = \xi^{\text{S}} + \mathbf{v}_{\text{coll}}^{\text{t}} \Delta t. \tag{6.15}$$

If the contact between particles evolves in a dynamic condition, that is, if $F^{\text{test}} > F^{\text{n}}$ sliding friction becomes active. In this case:

$$\mathbf{F}^{\text{t}} = \mu_d F^{\text{n}} \mathbf{t}, \tag{6.16}$$

$$\xi' = \frac{\mu_d F^{\text{n}} \mathbf{t} - 2\alpha_{\text{t}} \sqrt{k_{\text{t}} \tilde{m}} \mathbf{v}_{\text{coll}}^{\text{t}}}{k_{\text{t}}}, \tag{6.17}$$

where $\mathbf{t} = \mathbf{F}^{\text{test}} / F^{\text{test}}$ is the tangential force unit vector.

Inserting Eq. (6.17) into (6.12), during the next iteration, it will lead to $\mathbf{F}^{\text{test}} \approx \mu_d F^{\text{n}} \mathbf{t}$. It is worth noting that $\mathbf{F}^{\text{test}}$ and $\mathbf{v}_{\text{coll}}^{\text{t}}$ are not necessarily parallel in space: Eq. (6.10) does not provide that ξ^{P} is parallel to $\mathbf{v}_{\text{coll}}^{\text{t}}$ but only that they both lie on the same plane. However, the mapping in Eq. (6.17) always works, rotating the new spring such that the direction of the frictional force is unchanged and, at the same time, limiting the spring in length according to Coulomb's law. If the contact between particles comes back to a static condition, that is if $F^{\text{test}} < \mu_d F^{\text{n}}$, static friction is restored so that the governing equation are again Eqs. (6.14) and (6.15).
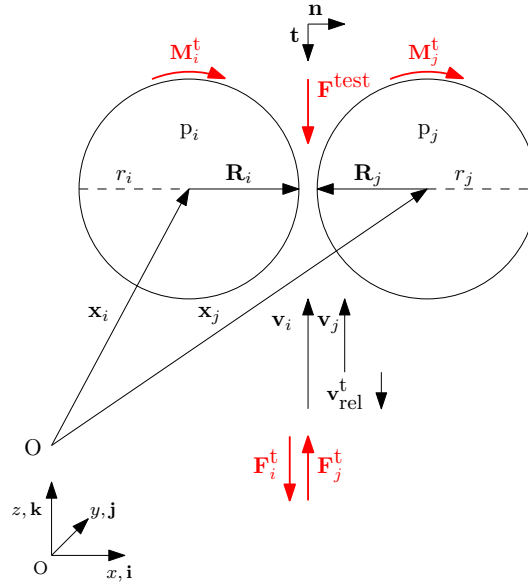
Fig. 6.4 Representation of two particles in sliding condition, in the hypothesis of null angular velocities $\boldsymbol{\omega}$. The arising tangential forces are represented in red.

At the end of each time step it results (Fig. 6.4):

$$
\begin{aligned}
\mathbf{F}_i^{\mathrm{t}} &= \mathbf{F}^{\mathrm{t}}, \\
\mathbf{M}_i^{\mathrm{t}} &= r_i \mathbf{F}^{\mathrm{t}} \mathbf{b} = r_i \mathbf{n} \times \mathbf{F}^{\mathrm{t}} = \mathbf{R}_i \times \mathbf{F}^{\mathrm{t}}, \\
\mathbf{F}_j^{\mathrm{t}} &= -\mathbf{F}^{\mathrm{t}}, \\
\mathbf{M}_j^{\mathrm{t}} &= r_j \mathbf{F}^{\mathrm{t}} \mathbf{b} = r_j \mathbf{n} \times \mathbf{F}^{\mathrm{t}} = -\mathbf{R}_j \times \mathbf{F}^{\mathrm{t}}.
\end{aligned}
\tag{6.18}
$$

The two moments are parallel but not necessarily equal in magnitude. Tangential forces and torques together conserve the total angular momentum.

The same procedure is adopted for wall-particle collisions, for which:

$$
\begin{aligned}
\tilde{m} &= m_j, \\
\mathbf{v}_{\mathrm{coll}}^{\mathrm{t}} &= \mathbf{v}_j^{\mathrm{t}} + \boldsymbol{\omega}_j \times \mathbf{R}_j, \\
\mathbf{F}_i^{\mathrm{t}} &= \mathbf{F}^{\mathrm{t}}, \\
\mathbf{F}_j^{\mathrm{t}} &= -\mathbf{F}^{\mathrm{t}}, \\
\mathbf{M}_j^{\mathrm{t}} &= r_j \mathbf{F}^{\mathrm{t}} \mathbf{b} = r_j \mathbf{n} \times \mathbf{F}^{\mathrm{t}} = -\mathbf{R}_j \times \mathbf{F}^{\mathrm{t}},
\end{aligned}
\tag{6.19}
$$

where j and i are the particle and wall indices, respectively.

6.2.1 The tangential spring stiffness

The choice of the stiffness of the tangential spring k_t differs from the original version of the code (Leonardi et al., 2014), considering that the ratio k_t/k_n results in an oblique impact, and consequently mutually dependent values of stiffness (Shafer et al., 1996). Also Cundall and Strack (1979) showed the importance of a proper choice of k_t/k_n: they observed that for $\mu_s = 0.270$, that is $\phi_s = 15°$, the adoption of either $k_t/k_n = 2/3$ or 1 does not affect the results. In contrast, depending on the adopted k_t/k_n, results differ in case of $\mu_s = 0.578$, that is $\phi_s = 30°$. From a theoretical point of view, considering the analogy with an undamped system, as in the normal contact model (Sec. 5.1.1), the duration of the contact t_c^t, that is half period of tangential oscillation, is related to k_t with:

$$t_c^t = \pi \left[\frac{k_t}{\tilde{m}} \left(1 + \frac{m_p r_p^2}{J} \right) \right]^{1/2},\qquad (6.20)$$

where, for uniform spheres, the magnitude of the rotational moment of inertia J is $J = 2/5(m_p r_p^2)$. Considering that k_n determines a half period of normal oscillation t_c^n in the normal direction, it follows that the phase of the tangential oscillation at the moment when the contact ceases is determined by the ratio t_c^t/t_c^n, which is proportional to $\sqrt{k_t/k_n}$, in the simple case of $\zeta = 1$. For uniform spheres, imposing that the periods of tangential and normal oscillations are equal, it results that $k_t/k_n = 2/7$. Also Arévalo and Zuriguel (2015) made use of this value.

Nevertheless, as this value derives from the pure elastic theory, Shafer et al. (1996) reported also other examples, in which, using different values of k_t/k_n, e.g. 1/5, the results do not differ from the case with 2/7. Di Maio and Di Renzo (2004) suggested instead to relate k_t with k_n with an expression of the mechanical properties of the involved bodies, as the Poisson ratio and the shear modulus. However, they provided also examples of Authors who have applied $k_t/k_n = 1$, obtaining good results. Finally, Luding (2008) applied $k_t/k_n = 2/10$. Even if a unique value cannot be defined, the expression $k_t/k_n = 2/7$ is adopted in the simulations carried out in this work.

6.2.2   The implementation strategy

Differently from dynamic sliding friction in the original version of the code, the adopted static friction model exhibits a significant numerical complexity. From a numerical point of view, indeed, the implementation of static sliding friction requires a considerable effort in term of computational time. In fact, according to the model proposed in Sec. 6.2, the contact between two particles (or a wall and a particle) with zero or quasi-zero relative velocity, i.e. not in motion according to the limit given by Eq. (6.13), is modelled with a tangential spring, whose elongation evolves in time, according to Eqs. (6.10) and (6.11). Thus, to update its value each time step, it is necessary to keep in memory the length of the spring, not resetting information each time step. This has to be done for each pair of particles in contact. When the contact between two particles ceases, the spring is erased. Moreover, when the contact between particles evolves from static to dynamic condition, the length of the spring is adjusted according to Eq. (6.17). Then, the contact can either cease or turn back in static condition again. Then, the storage of the state in which the two particles in contact are (static or dynamic) is required.

     The idea is to create a data container in which the value of the tangential spring as well as the condition and the point of the contact are stored for each pair of in contact particles. From a numerical point of view, the check for this information requires a loop inside the lists of the particles in contact (the list is already present in the original version of the code). This operation increases the computational time a lot. Thus, an optimisation in terms of data structures is necessary.

6.3   Numerical implementation of rolling friction

In DEM modelling, in which real grains are approximated with spheres, rolling friction, which opposes the mutual rolling of two bodies, assumes an important role. In the real case, rolling friction arises from the elastic and plastic deformation of two materials in contact: the collision between two particles creates a deformation and the contact forces no longer act on a single point, but over an area. As a result, the normal force exerts a torque that opposes the rotation (Fig. 6.5). Plastic deformation is the major source of energy dissipation during particle rolling contact. Beside this, other sources of rolling friction are (Ai et al., 2011):
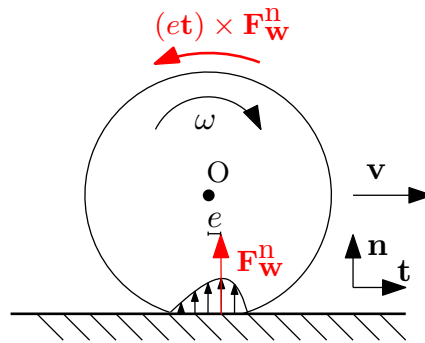
Fig. 6.5 Representation of the deformation and the torque arising when a particle is in contact with a wall w.

- *Micro-slip and friction on the contact surface*: it occurs when the rolling bodies have dissimilar elastic constants. This resistance depends on the difference between the elastic constants, the coefficient of sliding friction and the curvatures at contact.

- *Viscous hysteresis*: it is influenced by both temperature and deformation rate.

- *Surface adhesion*: the energy dissipates in breaking the adhesive bond at the separation point during the rolling motion.

- *Shape effect*: a rolling resistance arises from the effect of a non-spherical or non-circular particle shape. Even if the shape effect cannot be strictly classified as rolling friction, it influences rolling resistance. This parameter is very important, as it allows considering the lack of spherity both in real particles, and derived from large deformations of spheres. The occurrence of multiple points of contact in the real case, due to a non-spherical shape, enhances the rolling resistance.

No rolling friction exists only in case of perfectly rigid spheres. The grains constituting a real granular material have shapes that differ from perfect sphere. As a consequence, when a single sphere DEM model is chosen for representing real soils, rolling resistance has to consider also the shape effect.

6.3.1   Existing rolling friction models

In the frame of DEM simulations, several rolling resistance models exist. They can be divided into two main groups: the torque model and the angular velocity correction model. In the following, they are presented and critically evaluated, in order to show the reasons behind the choice of the rolling model chosen in this work.

Torque models

In these models, the rolling resistance is described using a torque $\mathbf{M}^r$ opposing to the rotation of the particles. The rolling resistance torque arises from the unevenness of the contact pressure distribution in the contact area. This can be explained considering a rolling spherical particle exerting a normal contact pressure on a surface (Fig. 6.5). The resulting normal force has, thus, an eccentricity e towards the rolling direction with regard to its stationary contact point. This generates a resistant moment $\mathbf{M}^r$. The eccentricity e is conventionally taken as the coefficient of rolling friction, which has the dimension of length (Zhou et al., 2003, 1999, 2001, 2002; Zhu and Yu, 2003; Zhu et al., 2007). Other researchers decompose e into two parts: a typical length parameter such as the radius of the particle and a non-dimensional parameter which is taken as the coefficient of rolling friction e/A_r (Li et al., 2005), where $A_r = (r_i r_j)/(r_i + r_j)$ is the rolling radius, function of the size of the particles in contact. Similarly to the coefficient of sliding friction, the dimensionless rolling friction coefficient can be defined as the tangent of the maximum angle of a slope on which the rolling resistance torque counterbalances the torque produced by the gravity acting on the body (Ai et al., 2011). Here below several torque models are listed and critically analysed. The models are sketched in Fig. 6.6.

a) *Constant contact-independent torque model, Fig. 6.6(a)*: in this model the value of the torque is independent of the magnitude of the angular velocity (Beer and Johnson, 1976; Zhang et al., 2004; Zhou et al., 2003, 1999, 2001, 2002):

$$\mathbf{M}_i^r = -\mu_r^a F_{el}^n \frac{\boldsymbol{\omega}_i}{|\boldsymbol{\omega}_i|},$$
$$\mathbf{M}_j^r = -\mu_r^a F_{el}^n \frac{\boldsymbol{\omega}_j}{|\boldsymbol{\omega}_j|}, \tag{6.21}$$
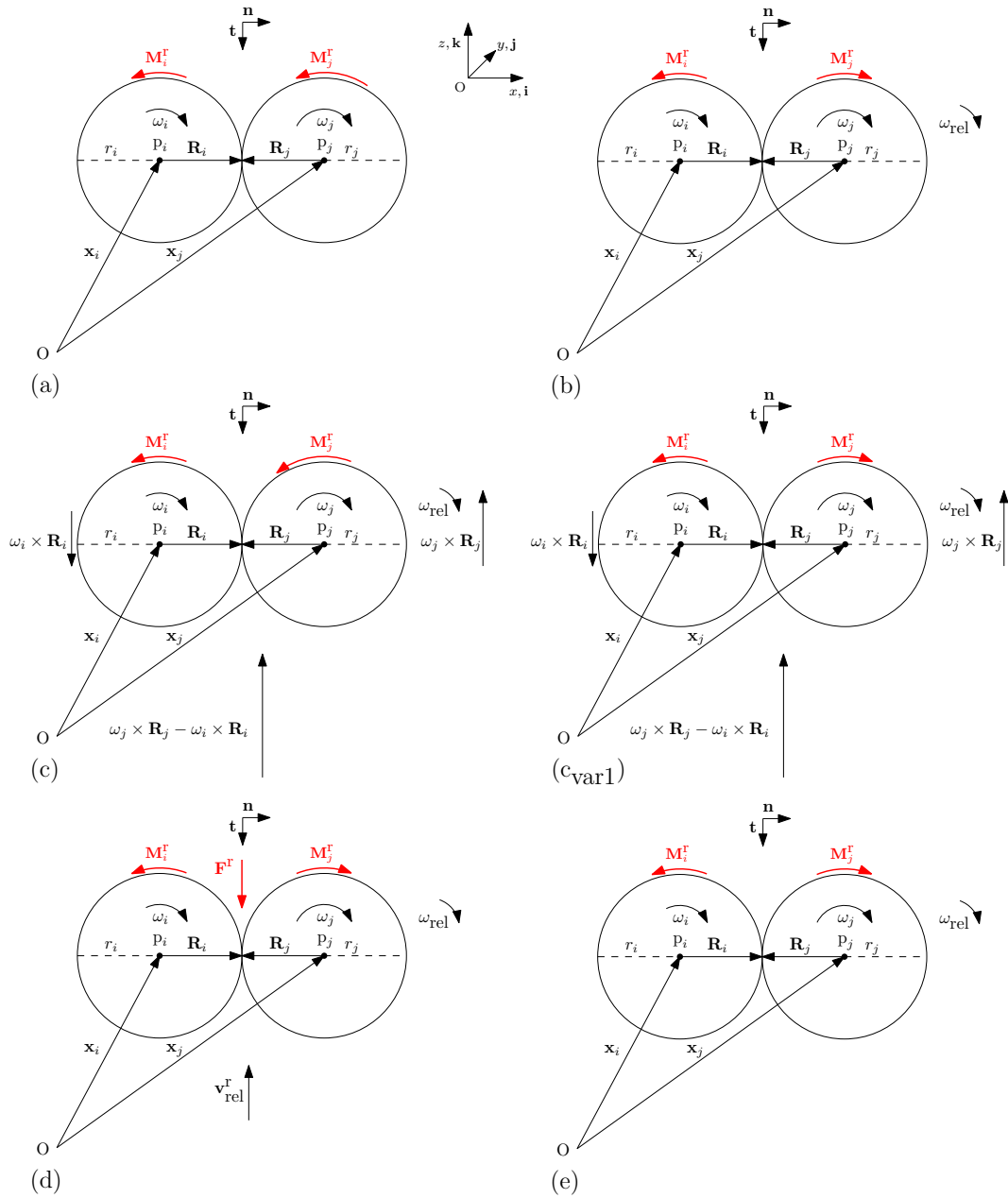
Fig. 6.6 Representation of the existing torque models: (a) the constant contact-independent torque model, (b) the directional constant torque model, (c-c$_{var1}$) the viscous model, (d) the elasto-plastic spring-dashpot model, (e) the elastic directional non-constant torque model.

where F_{el}^n is the modulus of the normal elastic component of the particle-particle force, and μ_r^a is the rolling friction coefficient, which has the dimension of length. This coefficient is function of particle size and shape, the material surface roughness, and the velocity of the movement.

As Ai et al. (2011) asserted, this model can lead to different torques applied to each particle in contact, thus violating equilibrium. In fact, the model is dependent on the rotational velocity of a particle instead of the relative velocity of a pair of particles in contact.

b) *Directional constant torque model, Fig. 6.6(b)*: a constant torque is applied, always opposing the relative rotation between the two contact entities. The torque is applied in pairs at each pair of particles in contact (Girolami et al., 2012):

$$
\begin{aligned}
\mathbf{M}_i^r &= -\mu_r^b F^n \frac{\boldsymbol{\omega}_{rel}}{|\boldsymbol{\omega}_{rel}|} A_r, \\
\mathbf{M}_j^r &= +\mu_r^b F^n \frac{\boldsymbol{\omega}_{rel}}{|\boldsymbol{\omega}_{rel}|} A_r,
\end{aligned}
\tag{6.22}
$$

where μ_r^b is the dimensionless rolling friction coefficient. Differently from μ_r^a, this last parameter is not a function of particle shape, and the relation between the two models coefficient is (Zhou et al., 2014):

$$
\mu_r^b = \frac{\mu_r^a}{A_r},
\tag{6.23}
$$

where the rolling radius A_r is equal to $A_r = (r_i r_j)/(r_i + r_j)$ for the case of two spheres and to the particle radius for a particle-wall contact This method has the shortcoming of producing a non-stop oscillating torque in a pseudo-static system, with residual kinetic energy (Ai et al., 2011). Despite this drawback, due to its simple formulation, this model is widely employed for modelling small scale systems such as a sandpile with coarse spheres, where the effect of a non-stop oscillating torque is less significant, especially if the adopted computational time step is sufficiently small.

c) *Viscous model, Fig. 6.6(c)*: the applied torque is dependent on the angular velocity (Brilliantov and Pöschel, 1998; Khan and Bushell, 2005; Li et al.,

2007; Zhou et al., 2014):

$$
\begin{aligned}
\mathbf{M}_i^{\mathrm{r}} &= -\mu_{\mathrm{r}}^{\mathrm{c}} F_{\mathrm{el}}^{\mathrm{n}} |\boldsymbol{\omega}_j \times \mathbf{R}_j - \boldsymbol{\omega}_i \times \mathbf{R}_i| \frac{\boldsymbol{\omega}_i}{|\boldsymbol{\omega}_i|}, \\
\mathbf{M}_j^{\mathrm{r}} &= -\mu_{\mathrm{r}}^{\mathrm{c}} F_{\mathrm{el}}^{\mathrm{n}} |\boldsymbol{\omega}_j \times \mathbf{R}_j - \boldsymbol{\omega}_i \times \mathbf{R}_i| \frac{\boldsymbol{\omega}_j}{|\boldsymbol{\omega}_j|},
\end{aligned}
\tag{6.24}
$$

where the rolling friction coefficient $\mu_{\mathrm{r}}^{\mathrm{c}}$ is expressed as (s/rad), and is thus independent of size and velocity. The relation with the coefficient of the directional constant torque model is:

$$
\mu_{\mathrm{r}}^{\mathrm{c}} = \frac{\mu_{\mathrm{r}}^{\mathrm{b}}}{|\boldsymbol{\omega}_j \times \mathbf{R}_j - \boldsymbol{\omega}_i \times \mathbf{R}_i|},
\tag{6.25}
$$

where $|\boldsymbol{\omega}_j \times \mathbf{R}_j - \boldsymbol{\omega}_i \times \mathbf{R}_i|$ is the relative translational velocity at the contact between two particles due to relative rotation, that is the contribution of the angular velocity to the tangential velocity.

Zhou et al. (1999) and Ai et al. (2011) found this method numerically not so efficient for simulating a sandpile formation, suggesting to use the contact independent model. In general, this method produces a pile whose height is much smaller than the one found in a real experiment. As the formulation reported can led to non-balanced torques, the viscous model has been adjusted in direction by Norouzi et al. (2016), Fig. 6.6(c_{var1}):

$$
\begin{aligned}
\mathbf{M}_i^{\mathrm{r}} &= -\mu_{\mathrm{r}}^{\mathrm{c}} F_{\mathrm{el}}^{\mathrm{n}} |\boldsymbol{\omega}_j \times \mathbf{R}_j - \boldsymbol{\omega}_i \times \mathbf{R}_i| \frac{\boldsymbol{\omega}_{\mathrm{rel}}}{|\boldsymbol{\omega}_{\mathrm{rel}}|}, \\
\mathbf{M}_j^{\mathrm{r}} &= +\mu_{\mathrm{r}}^{\mathrm{c}} F_{\mathrm{el}}^{\mathrm{n}} |\boldsymbol{\omega}_j \times \mathbf{R}_j - \boldsymbol{\omega}_i \times \mathbf{R}_i| \frac{\boldsymbol{\omega}_{\mathrm{rel}}}{|\boldsymbol{\omega}_{\mathrm{rel}}|}.
\end{aligned}
\tag{6.26}
$$

The advantage of this model over a constant model lies in its proportionality with the relative translational velocity, and $\mu_{\mathrm{r}}^{\mathrm{c}}$ is independent of velocity and size.

However, in case of two spheres of equal size in pure rolling condition with equal angular velocity, i.e. $|\boldsymbol{\omega}_j \times \mathbf{R}_j - \boldsymbol{\omega}_i \times \mathbf{R}_i| = 0$, the rolling friction torque is equal to zero, even if rolling friction is required (Khan and Bushell, 2005). Thus, as any quasi-static torque is provided, it is not effective in modelling pseudo-static systems and generates discontinuity for $\boldsymbol{\omega}_{\mathrm{rel}} = 0$.

d) *Elasto-plastic spring-dashpot model, Fig. 6.6(d)*: this method makes use of the spring-dashpot model, as expressed in Sec. 5.1, that is a sum of an elastic

spring torque and a viscous damping torque (Jiang et al., 2005, 2015; Luding, 2008). the torque consists of two components: a mechanical spring torque and a viscous damping torque. This corresponds to:

$$
\begin{aligned}
\mathbf{M}_i^{\mathrm{r}} &= \mathbf{M}_i^{\mathrm{k}} + \mathbf{M}_i^{\mathrm{d}}, \\
\mathbf{M}_i^{\mathrm{k}} &= \xi k_r, \\
\mathbf{M}_i^{\mathrm{d}} &= \alpha_{\mathrm{r}} \mathbf{v}_{\mathrm{rel}}^{\mathrm{r}},
\end{aligned}
\tag{6.27}
$$

where k_{r} is the rolling stiffness coefficient, α_{r} is the viscous damping coefficient, and $\mathbf{v}_{\mathrm{rel}}^{\mathrm{r}} = -A_{\mathrm{r}}\left(\mathbf{n} \times \boldsymbol{\omega}_i - \mathbf{n} \times \boldsymbol{\omega}_j\right)$ is the rolling relative velocity. The presence of rolling relative velocity activates these torques, acting against the rolling motion. For two particles i and j in relative rotation, the torques are then equal in magnitude and opposite in direction, i.e. $\mathbf{M}_i = -\mathbf{M}_j$. This model can be applied to many problems and successfully simulates problems of sand-pile formation (Ai et al., 2011). Nevertheless, it contains more parameters than other models and choosing appropriate values for these remains a challenge. From a numerical point of view it requires a great computational effort, since the history of the contact must be saved.

e) *Elastic directional non-constant torque model, Fig. 6.6(e)*: this model constitutes a mixture of the directional constant torque model and the elasto-plastic spring-dashpot model (Balevičius et al., 2011):

$$
\begin{aligned}
\mathbf{M}_i^{\mathrm{r}} &= -min\left(\left|k_{\mathrm{r}} \frac{\int \boldsymbol{\omega}_{\mathrm{rel}}(t)\,dt}{|\int \boldsymbol{\omega}_{\mathrm{rel}}(t)\,dt|}\right|, \mu_{\mathrm{r}}^{\mathrm{b}} F^{\mathrm{n}} \frac{\boldsymbol{\omega}_{\mathrm{rel}}}{\omega_{\mathrm{rel}}} A_{\mathrm{r}}\right), \\
\mathbf{M}_j^{\mathrm{r}} &= +min\left(\left|k_{\mathrm{r}} \frac{\int \boldsymbol{\omega}_{\mathrm{rel}}(t)\,dt}{|\int \boldsymbol{\omega}_{\mathrm{rel}}(t)\,dt|}\right|, \mu_{\mathrm{r}}^{\mathrm{b}} F^{\mathrm{n}} \frac{\boldsymbol{\omega}_{\mathrm{rel}}}{\omega_{\mathrm{rel}}} A_{\mathrm{r}}\right).
\end{aligned}
\tag{6.28}
$$

Angular velocity correction model

In this case, the rotation is controlled by applying both an empirical retarding coefficient, proportional to the number of contacts, and a retarding time to the rotational velocity. According to these parameters the angular velocity in the next time step reduces. The following proposed model has no specific name, that is why only the reference is cited (Teufelsbauer et al., 2009, 2011). The governing equation is:

$$
\boldsymbol{\omega}_i^{t+1} = k_{\lambda}^{\frac{\Delta t}{\lambda}} \boldsymbol{\omega}_i^t,
\tag{6.29}
$$

where k_λ is the retarding coefficient time, function of the number of contacts and the tangential relative velocity, and λ is the retarding time. If $\lambda \to 0$, the particle rotation is strongly constrained. However, the retarding time parameter λ is difficult to calibrate.

6.3.2   The directional constant torque model

Considering the limits and the advantages of all the methods found in the literature, the directional constant torque model, i.e. case b) in the previous list, has been chosen and implemented in the code. This method, indeed, provides a simple formula that does not generate discontinuities, and requires the calibration of a unique empirical parameter, i.e. the rolling coefficient μ_r^b, from here defined as μ_r for simplicity of notation.

In contrast, summarising the main drawbacks of the other methods, the constant contact independent torque model and the viscous model lead to a non balanced system. The additional correction of the viscous model proposed by Norouzi et al. (2016) lets the system not to be solved in case of particles of equal size with the same angular velocity. Furthermore, the elasto-plastic spring-dashpot model, the elastic directional non constant torque model and the angular velocity correction method require a lot of empirical coefficients. In the adopted method, the unique empirical coefficient, i.e. μ_r, is scaled by the rolling radius A_r, function of the size of the spheres, so that it is equivalent to a fraction of the rolling radius. It depends on the asperity, the deformability of the material, and the velocity of the motion. Multiplying this coefficient by the rolling radius, it gives the eccentricity of the normal force arisen at the contact between particles (or wall-particle).

The implementation of this method does not increase numerical complexity. The torque $\mathbf{M}^r$, indeed, is included in the the Eq. (5.2) as a contribution of $\mathbf{M}_p$, that derives from the interactions between particles. For a particle p, in the wider backdrop, it results in:

$$\mathbf{M}_p = r_{p1}F_{p\text{-}p}^t\mathbf{b} + r_{p1}F_{p\text{-}w}^t\mathbf{b} + \mathbf{M}_{hydro} + \mathbf{M}^r, \tag{6.30}$$

where $F_{p\text{-}p}^t$ and $F_{p\text{-}w}^t$ are the tangential force that arises at the contact between two particles and a particle against a wall, respectively.
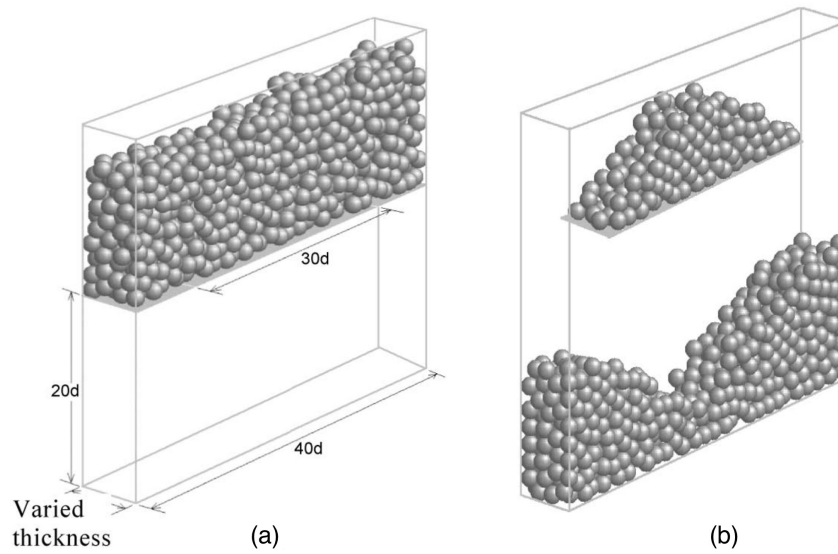
Fig. 6.7 Geometry and formation of a sandpile (a) before and (b) after discharging; *d* is the diameter of the sphere (Zhou et al., 2002)

6.4   Numerical and experimental validation of the model. Study of sandpile formation

To validate the proposed model, a comparison with real data or other numerical simulations results is required. Thus, to achieve this goal, the numerical simulations and laboratory experiments performed by Zhou et al. (1999, 2001, 2002) have been selected as the comparative sample for the validation. Zhou et al. (1999, 2001, 2002), indeed, performed numerical DEM simulations introducing rolling resistance and compared them with laboratory experiments, carried out by the Authors themselves. The simulations represent the heap formation with a discharging method ascribable to case no. 3 reported in Fig. 6.1. A monosized granular mass is discharged inside a rectangular container with a fixed middle plate and two side outlets of length of 5*d*, with *d* the diameter of the spheres. Three simulations are considered, with mean diameter of 2, 5 and 10 mm, respectively. The width of the container is 20*d* in order to avoid boundary effects. The geometrical details are shown in Fig. 6.7.

The simulation starts with the random generation of monosized spheres without overlaps in the container above the fixed middle plate with the two outlets closed, followed by a gravitational settling process to form a stable packing. Then, the instantaneous opening of the outlets starts a discharging process in which spheres drop under the effects of gravity into the bottom of the container. Some spheres

remain on the middle plate after the discharge, forming a stable stagnant zone: a heap or sandpile. The angle of repose is determined from the surface profile of the heap (Zhou et al., 2002). As a comparison, the laboratory experiments carried out by Zhou et al. (2002) were conducted under conditions comparable to those used in the numerical simulations. The container is made of wood except for the front wall, made of perspex for visual observation. The simulations were performed with monosized glass beads, whose friction coefficients are considered similar to those employed in the numerical simulation. Both the experiments and the numerical simulations carried out by Zhou et al. (2002) provided a repose angle of about 26°, 22°, and 19° for 2, 5 and 10 mm large particles, respectively, as shown in Fig. 6.8(b).

Table 6.1 lists the parameters and the adopted values in the validation simulations. It is worth mentioning that the numerical proposed model differs from the one of Zhou et al. (2002) in some characteristics:

- the rolling resistance model proposed by Zhou et al. (2002) adopted the constant contact - independent torque model as rolling resistance, where the rolling coefficient is expressed as a length. Instead, the simulations performed in the present study adopt the directional constant torque model. Thus, the rolling friction coefficient is calculated, for each simulation, through Eq. (6.23).

- Zhou et al. (2002) adopted a Hertzian normal contact model, whereas the proposed model is linear.

In the simulations performed in this thesis, the angle of repose is computed subdividing each side of the pile into 10 parts and, for each subdivision, the maximum height is evaluated. As a consequence, for each side, 10 points are detected. Thus, the angle of repose is computed for each side of the middle plate as the angular coefficient of a linear fitting of the identified points. The final angle of repose is calculated as the mean of the two obtained values. Using the parameters reported in Tab. 6.1, the obtained angles of repose for 2, 5 and 10 mm large particles are of about 27°, 24°, and 18°, respectively. These values are comparable with those identified from Fig. 6.8. The comparison of the results obtained with the proposed model in this thesis and the experimental results under the comparable conditions by Zhou et al. (2002), further confirms that the presented DEM-based simulation technique is a valid method to study the discharge of granular material.

Both experimental and numerical simulations performed by Zhou et al. (2002)

Parameters	Zhou et al. (2002)	Model proposed
Number of particles	10000	10000
Diameter (cm)	0.2-0.5-1	0.2-0.5-1
Density (kg/m^3)	2500	2500
Normal contact model	Hertzian	Linear
Young's modulus E (N/m^2)	2.16×10^6	-
Poisson ratio ν (-)	0.3	-
k_{n} (N/m)	$\frac{2}{3}\frac{E}{1-\nu^2}\sqrt{A_r}\delta^{\frac{1}{2}}$	$8.0 \cdot 10^4$-$1.25 \cdot 10^5$-$1.0 \cdot 10^6$
Restitution coef. ζ (-)	not specified	0.2
Normal damping coef. (-)	$-c_{\mathrm{n}}\left(6\tilde{m}E\sqrt{A_r}\delta\right)^{\frac{1}{2}}$ $c_{\mathrm{n}} = 0.4$ (-)	$2\alpha_{\mathrm{n}}\sqrt{k_{\mathrm{n}}\tilde{m}}$ $\alpha_{\mathrm{n}} = \frac{ln\zeta}{\sqrt{ln\zeta^2+\pi^2}}$ (-)
Tangential damping coef.	$-c_{\mathrm{t}}\left(6\tilde{m}\mu_s F_{el}^{\mathrm{n}}\frac{\sqrt{1-\delta_t\delta_{t,max}}}{\delta_{t,max}}\right)^{\frac{1}{2}}$ $c_{\mathrm{t}} = 0.4$ (-)	$2\alpha_{\mathrm{t}}\sqrt{k_{\mathrm{t}}\tilde{m}}$ $\alpha_{\mathrm{t}} = 1.0$ (-)
$\mu_{\mathrm{s,pp}}$ (-)	0.4	0.4
$\mu_{\mathrm{s,pw}}$ (-)	$1.5\mu_{\mathrm{s,pp}}$	$1.5\mu_{\mathrm{s,pp}}$
$\mu_{\mathrm{r,pp}}$	0.05 (mm)	0.10-0.04-0.02 (-)
$\mu_{\mathrm{r,pw}}$	$2\mu_{\mathrm{r,pp}}$ (mm)	$2\mu_{\mathrm{r,pp}}$ (-)

Table 6.1 Variables considered in the numerical model of Zhou et al. (2002) and the model proposed. Where the units of measurement are not the same for the two models, they are specified separately.

reveal an influence of the particle size on the angle of repose. The larger the particle size is, the lower the angle of repose. This is in line with what stated in Sec. 6.1.2. Even though the number of simulations is not high enough for a parametric study, the same trend is observed also in the performed numerical simulation in this study. Consequently, as the developed DEM model reveals to properly fit the data for three different particles sizes, in order to limit the computational time, in the following simulations a particle diameter of 10 cm is adopted.

6.4 Numerical and experimental validation of the model. Study of sandpile formation

101
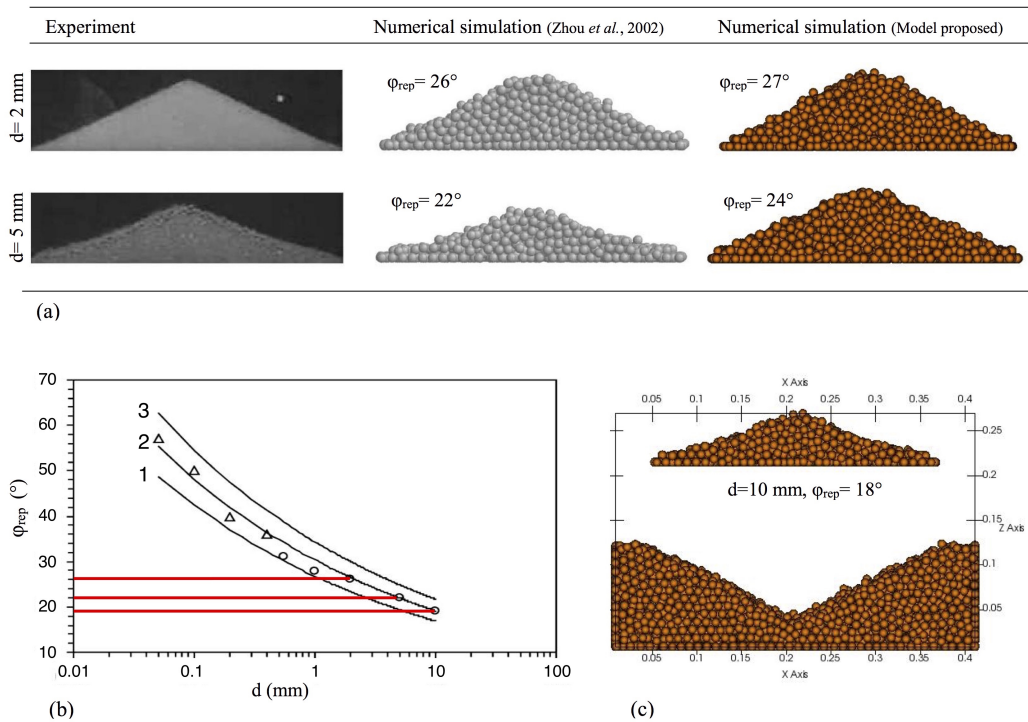
Fig. 6.8 (a) Comparison among the final configurations of the experimental results, the numerical results with the model proposed by Zhou et al. (2002), and the model proposed in the present work, for particle diameter of 2 and 5 mm. (b) Angle of repose as a function of the particle size. Circles and triangles indicate the experimental results. Line 2 represents the fitting curve of the results of the numerical simulation with the model of Zhou et al. (2002) using the inputs listed in Tab. 6.1. The red horizontal lines indicate the angle of repose for 2,5 and 10 mm large particles. (c) Final configuration of the carried out numerical simulation with the model proposed in the present work.

6.5 Correlation between physical and numerical parameters

In the frame of DEM simulations of granular flows, the frictional numerical inputs, i.e. the static sliding μ_s and rolling μ_r friction coefficients, have to be properly chosen as representative of the real material frictional properties, i.e. the internal friction angle ϕ_i (or the internal friction coefficient $\mu_i = \tan\phi_i$). Thus, the aim of this section is to find a relationship between the physical parameter of the material and the two numerical parameters governing the frictional resistance forces between particles. This represents a regression problem for the three-dimensional population (μ_i, μ_s, μ_r), in which μ_i is the dependent parameter and μ_s and μ_r are the independent parameters. As already mentioned, μ_s stands for the static sliding friction coefficient and $\mu_d = 0.9\mu_s$. Furthermore, as the physical measured parameter is the angle of repose ϕ_{rep}, as explained in Sec. 6.1.2, the hypothesis of equality between the tangent of this angle and the internal friction coefficient μ_i is adopted.

To achieve this goal, 209 numerical simulations have been performed to have a sample of a finite size large enough to be representative. A heap formation of monosized spheres with a discharging method is simulated with the same procedure adopted by Zhou et al. (1999, 2001, 2002). Thus, the simulations are carried out considering the same geometrical framework and discharging method employed for the validation (Sec. 6.4) adopting particles with a diameter of 10 cm and static friction coefficient equal for particle-particle and wall-particle contacts. The angle of repose is then evaluated from the surface profile of the heap (Zhou et al., 2002).

The 209 numerical simulations are carried out combining static friction coefficients μ_s from 0.1 to 1.0 (-), with steps of 0.05, and rolling friction coefficients μ_r from 0.0 to 0.2 (-), with steps of 0.02. The range for the static coefficients is comprehensive of the real physical range for soil granular material. For the rolling friction coefficient, which represents a percentage of the rolling radius A_r, the range adopted includes also very high values, as it is used to represent also the effects of non-spherical shapes, as in real granular materials. The obtained results are shown in Fig. 6.9: the static sliding friction coefficients are plotted against the estimated angle of repose, changing the rolling friction coefficients. The choice of plotting the angle of repose instead of the tangent of this angle lies in allowing an easier fitting. Instead, the choice of a 2D plot rather than a 3D one allows to show that the sliding friction plays a major role in halting motion.
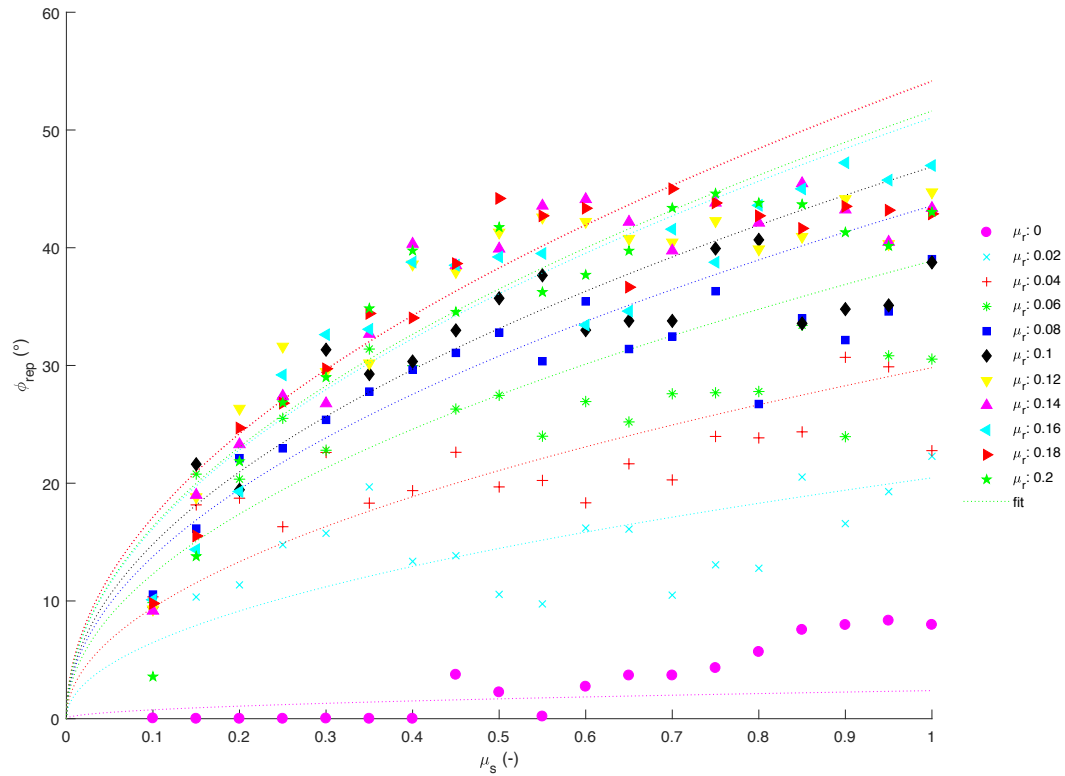
Fig. 6.9 Angle of repose versus sliding friction coefficient versus repose angle, changing the rolling friction coefficient.

As cited in Sec. 6.1.2, Zhou et al. (2002) formulated a predictive equation to compute the angle of repose in DEM numerical simulations (Eq. (6.7)). Despite the fact that the range of validity of this equation is upperly bounded by 10 mm particle diameter, an attempt to compare the results obtained in the DEM simulations with the angles derived from the law proposed by Zhou et al. (2002) has been done. Figure 6.10 reveals that a good agreement is observed only for value of $\mu_s \leq 0.3$ for every μ_r, or for $0.3 < \mu_s \leq 0.6$ for $\mu_s < 0.08$.

In order to overcome this problem, since Eq. (6.7) relates to lower particle sizes, a novel formulation is proposed. To find the best estimation of the correlation between μ_s, μ_r and ϕ_{rep}, the following steps are performed:

1. Search of the best fitting relation (model) for each curve $\phi_{rep} - \mu_s$, for each μ_r considered. The parameters of the model are estimated. It is assumed that the estimate varies depending on the value of μ_r. Among the possibile fitting models, single-parameters models (with parameter a) are adopted.
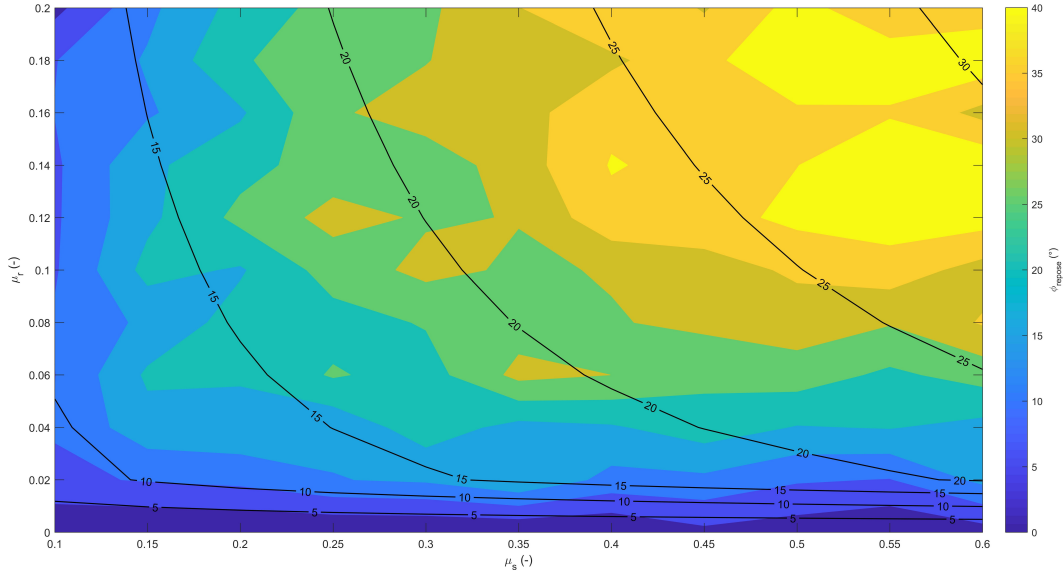
Fig. 6.10 Angle of repose obtained in the DEM simulations (coloured contour) in comparison with the law proposed by Zhou et al. (2002) (Eq. (6.7)) (black lines).

2. Search a model that describes the relationship between μ_r and parameter a.

3. The function found in step 2) is inserted in the one found in step 1), leading to a function of the type: $\phi_{rep} = f(\mu_s, \mu_r)$.

The choice of the best fitting curve is based on both a preliminary graphic observation and the consideration of the physical evidences since:

- The curve should intercept the origin: in absence of friction the angle of repose is 0.

- The relationship should be monotonically increasing.

The linear model is not appropriate, as the index of goodness of the linear fit R^2 is near 0. The parabolic fitting, with parabola-axis coincident with x axis and vertex in the origin, is found to give a better fit. The equation of this a parabola is $x = y^2/a$, with a the shape parameter of the model, i.e. $a = a(\mu_r)$. In the present problem, for a given μ_r, the model equation is:

$$\mu_s = \frac{\phi_{rep}^2}{a(\mu_r)}. \tag{6.31}$$
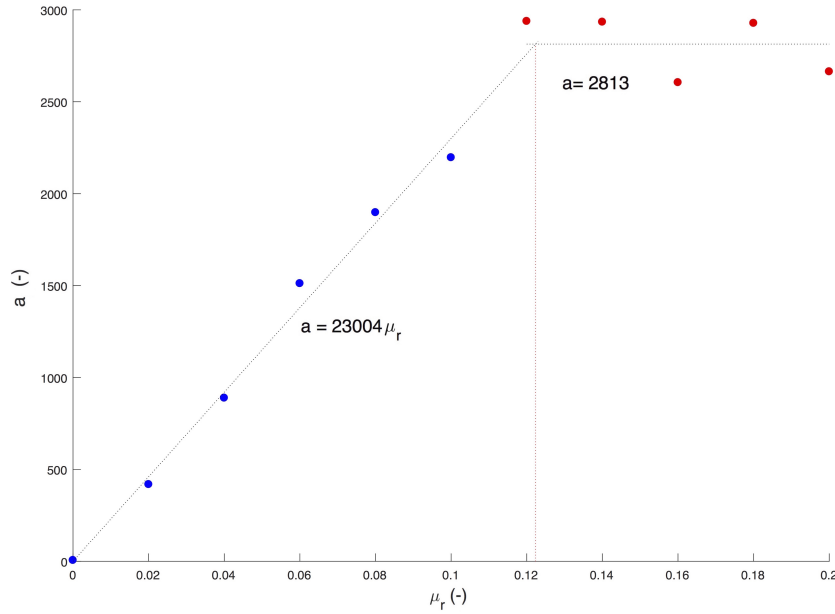
Fig. 6.11 Values of the shape parameter a against the rolling friction coefficient μ_r.

Considering only the positive quadrant of the Cartesian coordinate system, the equation simplifies as:

$$\phi_{rep} = \sqrt{\mu_s a(\mu_r)}. \tag{6.32}$$

Fig. 6.9 reveals a good fitting for μ_s smaller than 0.7, that is 35°. After this value, a flattening of the resulting couples $\mu_s - \phi_{rep}$ is observed. It is thus assumed that, for $\mu_s > 0.7$, the resulting ϕ_{rep} is independent from μ_s, thus, depends only on μ_r .

Figure 6.11 plots the values of the parameter a against μ_r. It emerges that the fitting law is not linear. Thus, the estimation of model parameters is led with the non-linear least squares method. A linear relationship in the range $\mu_r \leq 0.12$, while a constant value for larger μ_r seems to be a good interpolation. Thus, it result:

$$a(\mu_r) = \begin{cases} 23004\mu_r & \text{for } \mu_r \leq 0.12, \\ 2813 & \text{for } \mu_r > 0.12. \end{cases} \tag{6.33}$$

Inserting Eq. (6.33) into Eq. (6.32):

$$\mu_r = \frac{\phi_{rep}^2}{m\mu_s}. \tag{6.34}$$

In particular:

$$\phi_{\text{rep}} = \begin{cases} \sqrt{23004\mu_r\mu_s} = 151.7(\mu_r\mu_s)^{0.5} & \text{for } \mu_r \leq 0.12 \\ \sqrt{2813\mu_s} = 53.0\mu_s^{0.5} & \text{for } \mu_r > 0.12 \end{cases} \quad (^\circ). \qquad (6.35)$$

Consequently, once the internal friction angle is known, it is possible to draw a straight line parallel to the x-axis passing through the desired ϕ_i and define the (μ_s, μ_r) couple that satisfies the condition.

Nonetheless, a proper choice of the friction coefficients to choose as simulation inputs should take into account some important aspects, which emerge from Figs. 6.9 and 6.11. Only the curves with $\mu_r < 0.12$ show an upward trend of the parabolas amplitude. For $\mu_r \geq 0.12$ the fitting curves do not follow a specific order and have the same amplitude. A direct consequence of this behaviour is reported in the graph of Fig. 6.11: for $\mu_r \approx 0.12$, a assumes a constant value and a relationship between μ_r and μ_s can no longer be found. This results in a quasi-independence of the resulting ϕ_i for $\mu_r \geq 0.12$. Moreover, in the hypothesis that the rolling friction coefficients represent a percentage of the rolling radius A_r, a large value of μ_r implies a great deformability, not consistent with granular material, even considering the shape effects included in the coefficient. As a consequence of all these observations, the part of the graph of Fig. 6.9 in which the couples of $\mu_s - \mu_r$ are allowable is limited to $\mu_r < 0.12$ and $\mu_s < 0.7$.

In general, the internal friction angle, or the repose angle, is not equal to the sliding inter-particle friction angle, as it depends on both sliding and rolling friction of the grains and on the packing state of the material. Furthermore, sliding and rolling friction coefficients refer to the single particle and not to the material. In this situation, particle-particle friction is generally different from the internal friction of the material.

Since detailed information is not available, the arbitrary assumption $\mu_s = \tan \phi_i$ is considered. To find the corresponding μ_r the following formula is adopted:

$$\phi_{\text{rep}} = 151.7(\mu_r\mu_s)^{0.5},$$
$$\mu_r \leq 0.12, \qquad (6.36)$$
$$\mu_s \leq 0.7.$$
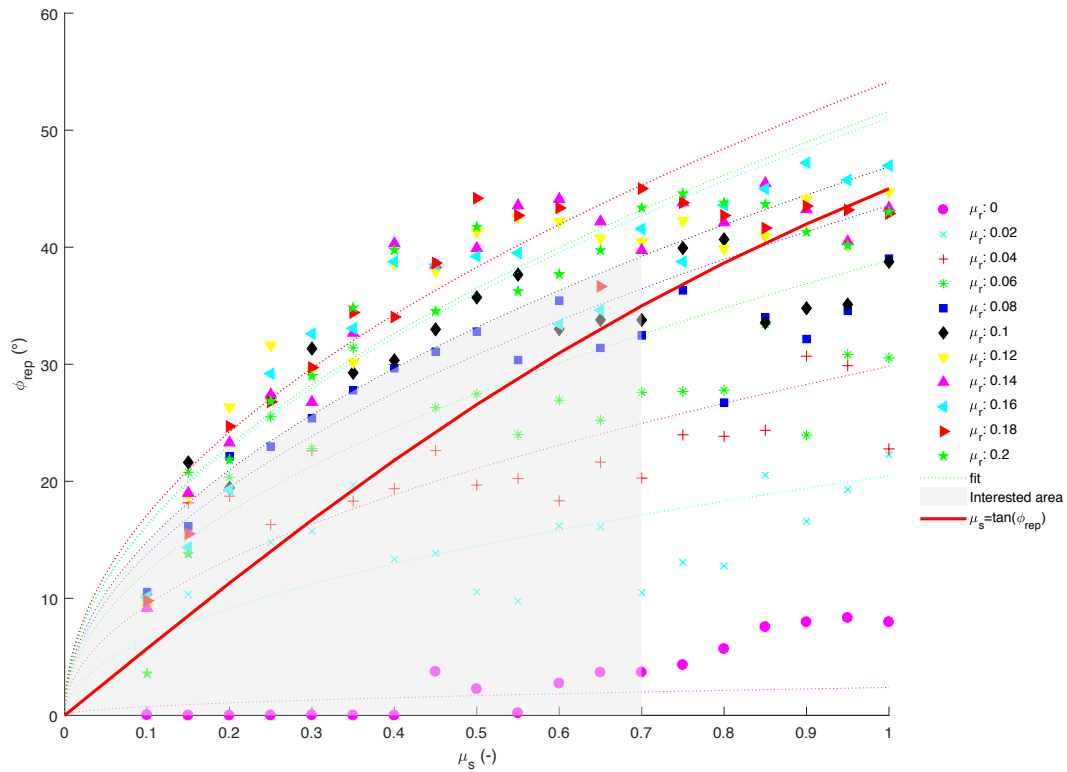
Fig. 6.12 Sliding friction coefficient versus repose angle, changing the rolling friction coefficient. The range of allowable friction coefficient couples is the gray shaded area. Red curve is the bisector $\phi_i = \arctan(\mu_s)$.

As a relation between the real physical measurements on material behaviour and input parameters for numerical modelling is found, simulating real granular material is now possible. This relation (Eq. (6.36)) will be adopted in the further chapters.

Chapter 7

Trapping efficiency and impact forces: the monophase model

This chapter deals with the numerical study of the interaction between a granular flow and an open rigid barrier. Both the dynamic and static forces arisen at the impact and the arching mechanisms are investigated. For engineering design purposes, consequently, the main goal of the results herein presented is to provide an enhancement both to the knowledge of the critical conditions beyond which no trapping occurs, and to the magnitude and the time-history distribution of the debris flow impact forces.

The leading idea for investigating the aforementioned phenomena is to start from the simplest case, i.e. of dry monosized flow against a single outlet barrier, in order to find the initial conditions that guarantee both the filtering and the energy breaker functions. Thus, the analyses herein presented have the double purpose of (1) understanding the mechanisms that lead to the formation of arching and clogging effects, and (2) defining the reference parameters for evaluating the mutual influence of multiple outlets in sectional barriers. The adoption of a monosized dry granular flow allows consideration of the phase representing the coarse grain (which has to be trapped by the barrier) alone. Consequently, both this hypothesis and the choice of single outlet barrier intend to limit the influence of other side-effects. The simulations analysed in this chapter make only use of the DEM module of the DEM-LBM code outlined in Ch. 5, and Secs. 6.2 and 6.3. From an engineering point of view, the limit setup here adopted can give interesting insights into the design of risk mitigation structures. Dry granular flows, due to the absence of a fluid phase, can have more

inter-particle contacts, and thus, force chains form more easily. This internal effects can produce high local forces against an obstacle or a barrier impacted by the flowing mass.

From a geometrical point of view, once the setting reference parameters for the simplest case are found, other more complex open barrier geometries are analysed, i.e. from the slit barrier case the performed simulations extend to the sectional barrier one. The results obtained will be used in Ch. 8 to progressively weaken the hypotheses herein made, considering a two-phase flowing mass, one representing the coarse material (which has to be trapped by the barrier), and one water and fine material.

The study cases are presented and discussed under a common framework (Sec. 7.1). Each simulation is analysed both in terms of trapping mechanism and interaction force, considering the influence of different parameters, e.g. the geometry of the barrier, the slope of the channel, and the impact angles of the flowing mass. The simulations here presented are subdivided in two main groups, according to the type of the open rigid barrier considered, i.e. slit or sectional. In particular, Section 7.2 relates to single open barriers, considering how the change of the impact angle, the slope, or the opening width can affect the results. Section 7.3 deals with the presence of a multiple outlets rigid structure, whose inter-distance and width can considerably affect the trapping efficiency of the barrier.

Some of the results presented in this chapter are part of two conference proceedings (Marchelli et al., 2017a,b) and one in-press article (Marchelli et al., 2018).

7.1   Release configuration

The geometrical properties of the channel, the initial condition of the discharged mass, and the position and modelling method of the rigid barrier are the same for all simulations. The adopted geometrical configuration aims to imitate a real case of a rigid sectional barrier in Saint-Vincent (Valle d'Aosta Region, Italy), on which a displacements monitoring system was installed (Fig. 7.1). In the perspective of future simulations of real recorded events, the investigated configuration considers a similar geometry. The width and height of the channel are chosen large enough not to have boundary effects, but, at the same time, sufficiently small not to require an unfeasible computational time. In addition, as explained below, the single outlet

Fig. 7.1 Sectional barrier in Saint-Vincent (Valle d'Aosta Region). It is realised with a 1 m high concrete basement and 2 m high steel piles (IPE 270), spacing 0.5 m from each others. The displacement monitoring system is installed at the base of each piles, downstream the flow. It consists in strain sensors (HBM SLB 700A).

studies allow to analyze the clogging mechanisms between two piles.

The domain, sketched in Fig. 7.2, is represented by a 20 m long, 1.9 m wide and 1.35 m deep channel, with variable slope θ. The boundaries of the domain are the rigid walls with frictional properties. A XYZ reference system linked to the local topography is used. The Z-axis is normal to the bottom wall and the X- and Y-coordinates are tangential to it, with the X-axis oriented in the down-slope direction (Fig. 7.2).

A barrier extends over the whole width of the domain in the Y direction. In the slit barrier case, the width S of the vertical outlet is varied, while, for the sectional barrier study (Fig. 7.2(c)) for equal domain size, both the width P and the number of piles are varied. To avoid numerical instabilities at the edge of the outlet, the barrier is modelled differently from the walls of the domain. It is constituted by an assembly of compacted spheres whose motion is prevented that allow small deformation and, thus, according to the DEM approach (Sec. 5.1), exchange of forces when impacted. This permits to know the forces on the center of each spheres of the barrier. The

spheres have a radius of 5 cm and their centers are one radius apart. This setting allows the forces exerted on each sphere to be evaluated. As a result, an estimation of the impact forces, from here defined as "local" $\mathbf{F}_\mathrm{L}$, is provided. This aspect is necessary to evaluate which part of the barrier is stressed the most.

The released mass is arranged in a regular structure extending 18 times the grain diameter d in Y-direction, so that the influence of the domain lateral boundary is minimised (Pournin et al., 2007; Zhou et al., 2002) (Fig. 7.2(a)). A dry mass, made of rigid monodisperse spheres of mean diameter d=10 cm, is modelled. The diameter is uniformly distributed between 9.5 and 10.5 cm, adopting a variation of size around the mean of 5%, as took up by Magalhães et al. (2015) and Holst et al. (1999), and of the same order of magnitude to what adopted by Pournin et al. (2007) and Ashour et al. (2017). This variation can lower the formation of crystalline packing structures, even though crystallisation is not completely avoided, similarly to the case reported by Holst et al. (1999). Geometrical and material parameters are collected in Tab. 7.1. The internal friction angle ϕ_i is set equal to 30° for both the wall-particle and the barrier-particle contacts. From a numerical point of view, the resulting sliding and rolling friction coefficients, μ_s and μ_r, are computed according to the expression in Sec. 6.5. The restitution coefficient ζ of the colliding particles is set equal to 0.2. The rheological parameters of the linear-dashpot model adopted for the particles (i.e. the normal stiffness coefficient k_n, the tangential stiffness coefficient k_t, and the tangential damping coefficient α_t) are chosen in order to respect the limit imposed by the numerical analysis efficiency, according to the criteria of Sec. 5.1.4. The initial velocity of the released mass is set equal to zero, that is, its discharge occurs under the force of gravity.

7.2   The slit barrier study

This section describes the simulations performed with the slit barrier. As explained earlier, the single outlet case, can be intended as a part of a hypothetical larger sectional barrier, made of large piles. With the purpose of finding the geometrical conditions which promote both arching and energy breaking effects, starting from the simplest situation, the influence of varying the impact angle, the slope of the channel, and the outlet width are investigated. In particular, Sec. 7.2.1 aims to investigate, comparing two different barrier incline configurations, the variation of

(a)

(b)

(c)
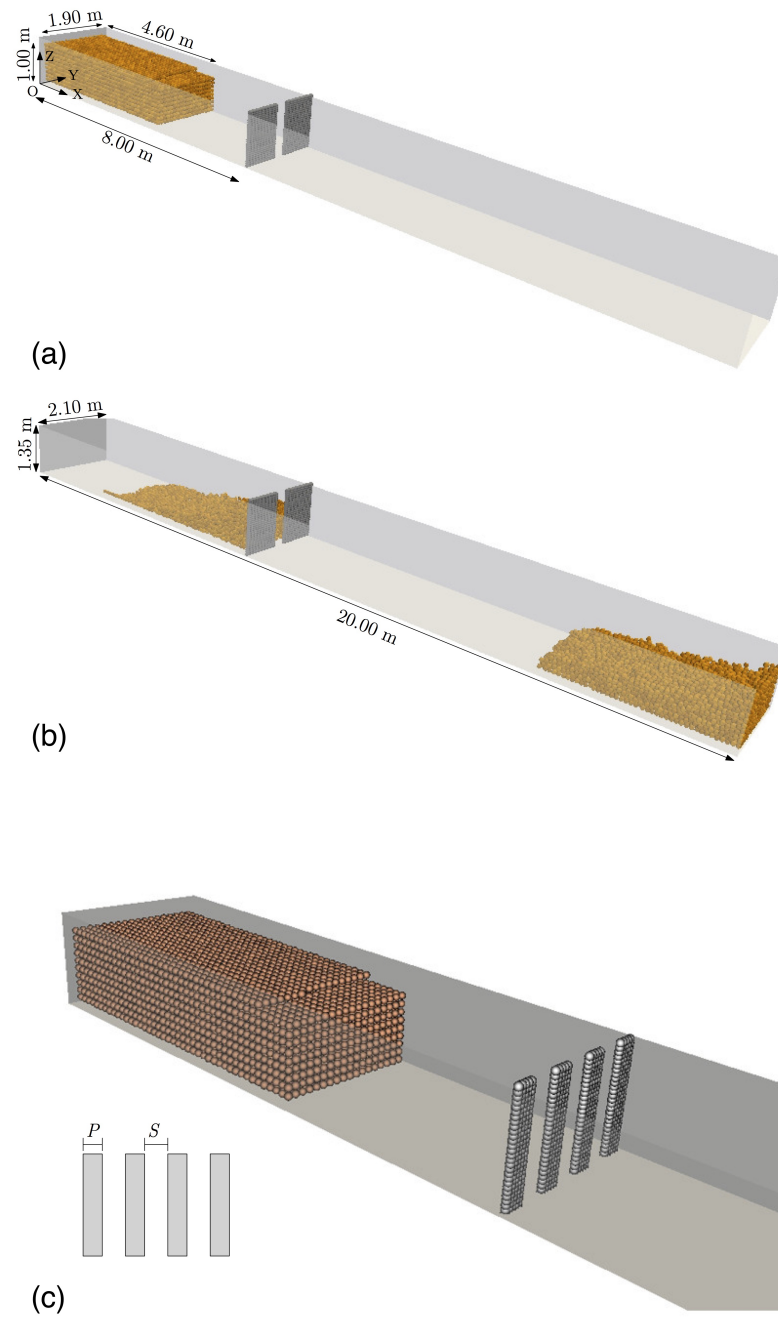
Fig. 7.2 Example of particle distribution at both (a) the initial and (b) the final stages of the carried out numerical analyses with a slit barrier. Panel (c) shows an example of the initial stage of a simulation with a sectional barrier.

Parameter Values	
Number of particles	7640
Released volume V (m^3)	4.03
Grain diameter d (cm)	10 ± 0.5
Grain density ρ (kg/m^3)	2500
Normal stiffness k_n (N/m)	10^6
Tangential stiffness k_t (N/m)	$\frac{2}{7}k_\mathrm{N}$
Tangential damping coefficient α_t (-)	1
Restitution coefficient ζ (-)	0.2
Static sliding friction coefficient $\mu_\mathrm{s,p\text{-}p}$, $\mu_\mathrm{s,p\text{-}w}$ (-)	0.577
Rolling friction coefficient $\mu_\mathrm{r,p\text{-}p}$ (-)	0.0678
$\mu_\mathrm{r,p\text{-}w}$ (-)	$2\mu_\mathrm{r,p\text{-}p}$
Domain size (XYZ) (m)	$20.00 \times 2.10 \times 1.35$
Mass discharge geometry (XYZ) (m)	$4.60 \times 1.90 \times 1.00$
Position of the front of the mass (X) (m)	4.725
Position of the barrier (X) (m)	8.00

Table 7.1 Geometry and characteristic parameters used in the carried out numerical analyses.

both the trapping efficiency and the impact forces as function of the impact angle. If the difference in results between the two barrier incline configurations is acceptable, indeed, a unique barrier setting can be adopted.

7.2.1 Influence of the impact angle

This section aims at evaluating the effects of the angle of impact of the flowing mass against the barrier. In the following simulations, two barrier configurations are evaluated: in the first case, a barrier parallel the Z-axis is considered (i.e. orthogonal to the channel bottom, from here on out called "OB"), while, in the second case a vertical barrier (i.e. parallel to the gravity vector) is defined (from here on out called "VB"), as shown in Fig. 7.3. A slope angle of $\theta = 35°$ is considered to simulate a real debris flow event in which the extra-mobility arisen from the presence of a fluid phase allows the moving mass to flow on less steep slope despite the presence of frictional forces. The simulated condition represents an inertial regime, in which the acting forces are governed by collisions and the frictional forces neither prevail nor halt the motion. Thus, particles can be retained and halted by the barrier itself. For this, this regime is essential for evaluating the barrier trapping efficiency. Both the trapping efficiency and the impact forces of the barrier are investigated for both the
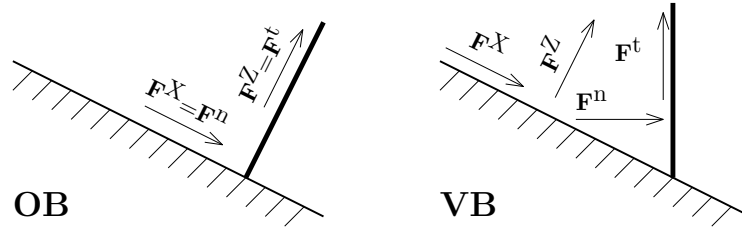
Fig. 7.3 The OB and VB schemes of the two barrier configurations; that is, parallel to Z-axis and to the gravity vector, respectively.

configurations, varying the outlet width S with respect to the mean radius r of the discharged mass. The simulations consider a normalised opening width S/r equal to 3,5,7,9, and 10. For this last value it is expected that clogging or a temporary jammed configuration does not occurs.

Analysis of the trapping efficiency

The clogging mechanisms is investigated considering, as a first aspect, the amount of material that passes through the outlet. Fig. 7.4 shows the amount of non-retained material with respect to the normalised opening width at a complete stop of the flowing mass. The non-retained material fraction is the ratio between the total mass and the mass that, at the end of the simulation, is beyond the barrier. A similar trend is observed. In both the cases, indeed, for $S/r \leq 4$ almost the whole material is trapped, then for larger ratios the amount of untrapped material progressively increases, until a value of 95%. However, it is evident that the VB configuration entraps a greater amount of particles.

Considering the entrapped material, Figure 7.5 represents an example of the stable arching formation. The height of the material deposited just behind the outlet is defined as "height of the arch" H_{arch}, despite the common definition of height of an arch. This height is normalised to the height of the barrier H_{bar}, equal to the height of the outlet. To compute H_{arch}, a volume behind the outlet extending $4r$ in X-direction is considered and subdivided in 10 intervals along H_{bar} (Fig. 7.5). The kinetic energy of the particles $E_{K,p}$ is computed for each interval. For each particle, it results:

$$E_{\text{K,p}} = \frac{1}{2}m_{\text{p}}\mathbf{v}_{\text{p}}^2 + \frac{1}{2}I_{\text{p}}\boldsymbol{\omega}_{\text{p}}^2,\tag{7.1}$$

where m_{p} is the mass, $\mathbf{v}_{\text{p}}$ the velocity, I_{p} the moment of inertia, and $\boldsymbol{\omega}_{\text{p}}$ the angular velocity of the particle p. If $\sum_{p=1}^{N} E_{K,p} < 10^{-5}$ J, where N is the number of particles
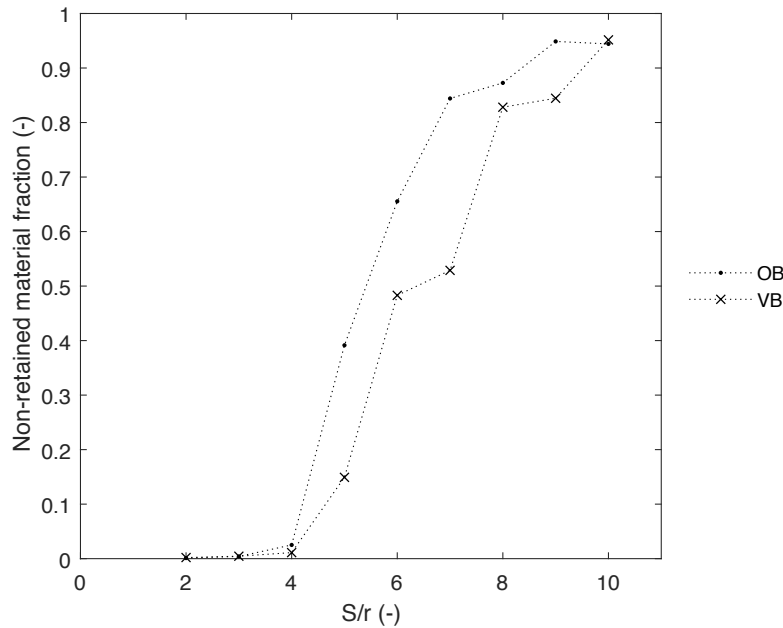
Fig. 7.4 Non-retained material fraction with respect to the S/r value at complete stop of the discharging mass for both the OB and the VB configurations.

in the interval, the particles are considered halted and the time of occurrence t_{stop} is evaluated. The time t_{stop} represents the time of arching, for each interval. The main goal of subdividing the outlet region in intervals is to consider that the flowing mass can stop at different times and at different heights. Particles on the bottom, indeed, can stop before the ones on top, due to both basal friction effects and stabilising weight of the mass pushing on them, as seen in Fig. 7.6. From here on, this effect is called "progressive clogging". This time has a crucial role for damages mitigation purposes. Figure 7.7 shows the trajectories of three different particles. Different behaviour are displayed: a particle can stop before reaching the barrier, alternatively it can pass through the outlet without decelerating, or it also can be partially clogged and deviated in direction in the outlet region, before passing through the outlet.

Figure 7.8 displays the ratio H_{arch}/H_{bar} as a function of the time of arching t_{stop}, related to the first arrival time t_0, for $S/r = 3, 5, 7, 9$ and 10 in the VB and the OB configurations. When no mass is trapped in an interval, no point is displayed. In this way a critical ratio S/r above which no clogging occurs is found. Spanning the whole results, four recurrent possible different clogging mechanisms appear, displayed qualitatively in Fig. 7.9(a). This figure shows a typical plot in which the
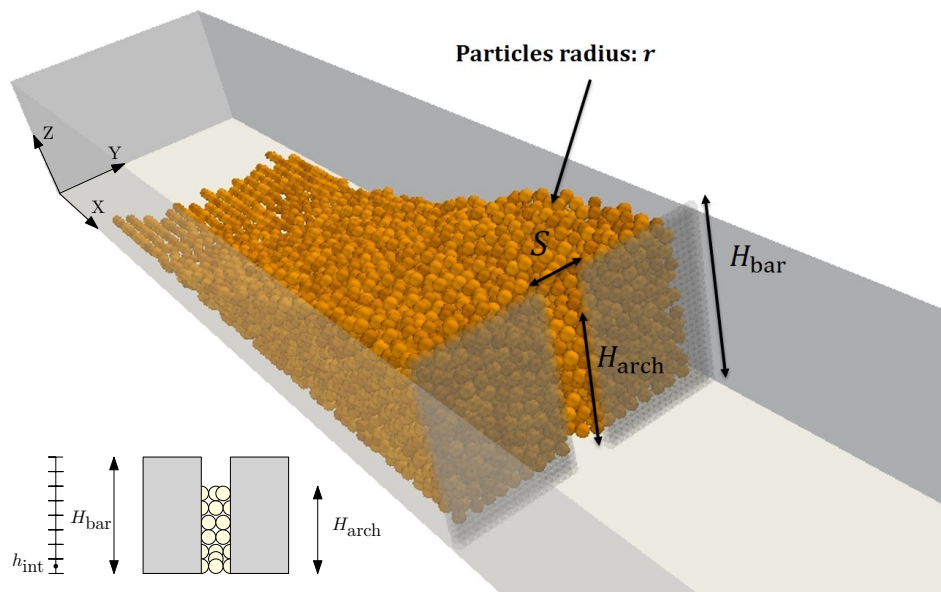
Fig. 7.5 Final typical configuration in the case of arch formation. The variation of size around the mean limits crystallization, especially in a 3D framework. However, some crystallization is observed in the basal layer of particles. This occurs in the rear part of the flow, i.e. in the 2D case of particles sliding on an inclined plane.

time when the particles at a given height stop is reported. Figure 7.9(b) summarise the results.

- The mass instantaneously clogs against the barrier at the very first seconds of the impact. Almost the whole mass is entrapped (H-A C S C in Fig. 7.9(b)).

- A progressive clogging situation occurs. The lower layers of the flowing mass start to clog, while the top part clogs later in time. In the time lag between the impact and the complete stop, particles flow through the outlet (P C in Fig. 7.9(b)).

- The mass starts to clog after a considerable time lag (with respect to the first impact). The height of the arch is small, involving few layers of particles. A noticeable amount of particles passes through the outlet before stable clogging occurs (L-A L C in Fig. 7.9(b)).

- No clogging occurs, thus, no mass deposits behind the barrier outlet (No C in Fig. 7.9(b)).
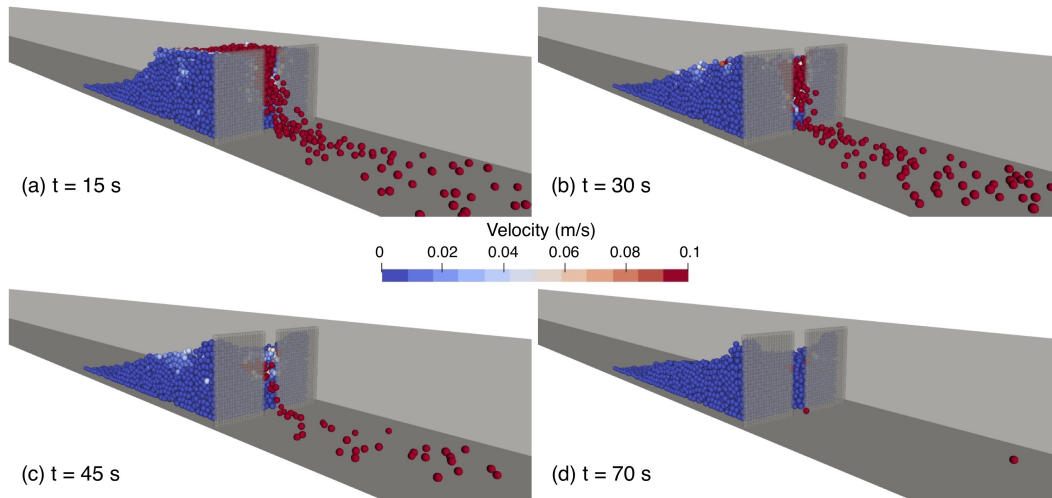
Fig. 7.6 Sketch of different times of a performed simulation (OB configuration, $S/r = 5$). Considering the region behind the outlet, it emerges that the flowing mass progressively stops at different times.

In the VB case, no arching occurs for $S/r = 10$. For $S/r = 3$, about the whole mass is stopped when it reaches the barrier and it is entrapped. For $S/r = 5$, the mass suddenly stops in the lower part, then a progressive clogging phenomenon occurs and a stable clogged configuration is reached within 10 s, with high arch height. For $S/r = 7$, a progressive clogging phenomenon occurs from 20 s to about 55 s, involving only few layers of particles. Finally, for $S/r = 9$, only a two layers high arch occurs at about 45 s. Considering the OB case, no arching occurs for $S/r = 9$. However, the same completely trapped situation is observed for $S/r = 3$, while for $S/r = 5$, a sudden stop occurs for the lower height subdivision and then a progressive clogging occurs until a stable situation is reached at about 70 s. Finally, for $S/r = 7$ a sudden stop happens, with a single layer arch, but late in time. Comparing the results for both the configurations, it emerges that increasing the normalised opening width, a decrease of H_{arch} and of t_{stop} occurs in both cases. Moreover, the same transition, i.e. from a suddenly-formed high arch to a late-formed low stable arch, which is observed in the VB configuration for $S/r \geq 7$, appears also in the OB case, but for $S/r \geq 5$. Thus, this change seems to be slightly decelerated as the boundary value between the two stages is shifted. Also the critical S/r ratio after which no clogging occurs is one S/r greater in the VB case than in the OB. In addition, considering t_{stop}, the halt of the material occurs earlier in the VB than in the OB case. Thus, it is seen that the VB configuration enhances to some extent the trapping efficiency of the
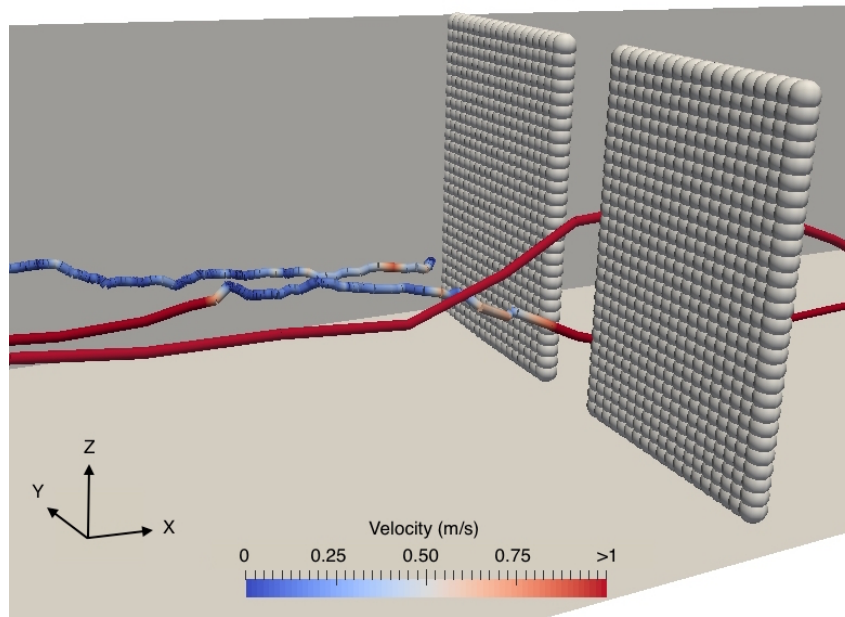
Fig. 7.7 Sketch of the trajectories of three particles: one stops behind the barrier, another one passes through the outlet without decelerating, and another one decelerates behind the barrier and then passes through the outlet.

barrier, in terms of both amount of material and stopping time. As a consequence, considering the OB rather than the VB configuration results in a slightly lower trapping efficiency.

Analysis of the impact forces

The dynamic and static forces exerted by the flowing mass on the barrier are evaluated in terms of both intensity and direction, with respect to time and point of application. For both the VB and the OB cases, the simulations with $S/r = 3, 7$ and 10 are analysed and compared. This choice allows the study of completely clogged, progressively-clogged, and no-clogged conditions. To evaluate the influence of the presence of an outlet, the situation of a closed barrier with equal geometrical setting and properties of an open one is analysed for both the configurations.

The intensity at each point of the barrier, that is the local force $\mathbf{F}_L$ (see Sec. 7.1), is calculated at each time step, and the global force $\mathbf{F}_G$ is computed by integrating the local forces over the whole barrier at a given time. The dynamics of motion is investigated with particular reference to the arrival times and the instants at which the maximum local impact and the maximum global impact occur. In order to better
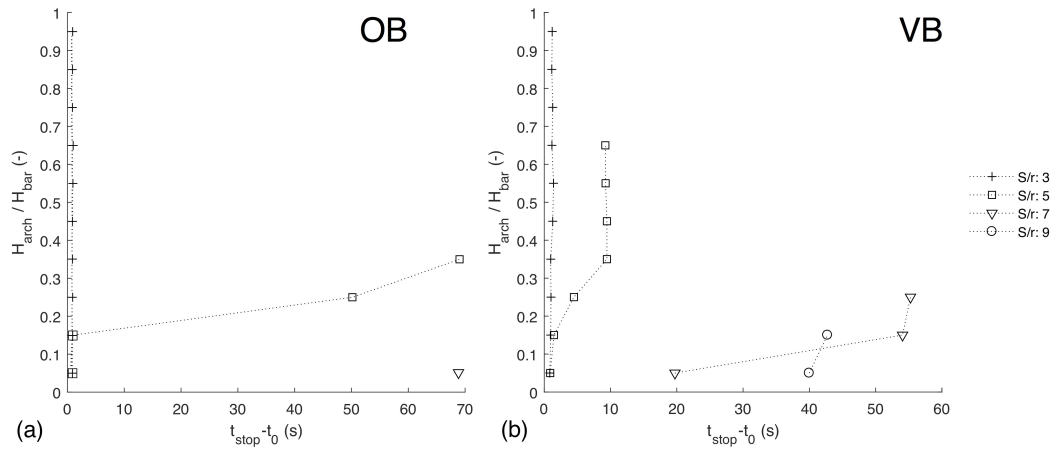
Fig. 7.8 Ratio between the height of the arch H_{arch} and the height of the barrier H_{bar} as a function of the time of arching t_{stop}, calculated with respect to the first arrival time t_0, for (a) the OB and (b) the VB configurations, for different S/r.

detail the results, also the envelope of the maximum local value observed in the dynamic phase is plotted (Fig. 7.15). In the following, the term "dynamic" phase relates to the first few seconds of the interaction between the flowing mass and the barrier. Generally the maximum impact values reside in this phase. These forces are the ones adopted for the design of the barrier. The forces on the barrier at complete stop, i.e. in the static condition, are also evaluated. These forces, exerted by the deposited mass, have to be properly considered as they persist in time until the material is removed.

The time-history of the global impact forces in terms of $\mathbf{F}_G^X$, $\mathbf{F}_G^Z$, as well as $\mathbf{F}_G^n$ and $\mathbf{F}_G^t$, i.e. in normal and tangential directions to the barrier, respectively, and the resultant force $\mathbf{F}_G^R$ are evaluated, for each S/r. In order to discuss the observed behaviour, $S/r = 7$ is chosen as a representative case Figure 7.10 shows the impact force time-history for $S/r = 7$.

Considering the general trend, it emerges that, at the very instant of the impact, the force arises abruptly and then it decreases until it settles in a final static value. The time to reach a stable configuration and the intensity of the final force depends on the occurrence of a stable clogging configuration and the amount of mass entrapped behind the barrier (Figs. 7.10 and 7.12). It is worth noting that in the OB configuration $\mathbf{F}_G^n$ coincides with $\mathbf{F}_G^X$ and $\mathbf{F}_G^t$ with $\mathbf{F}_G^Z$ (Fig. 7.3). In the OB configuration, the forces are mainly in the X-direction. After the impact, the material can freely run up the barrier and negligible forces act in the Z-direction, both in the dynamic and in the

(a)
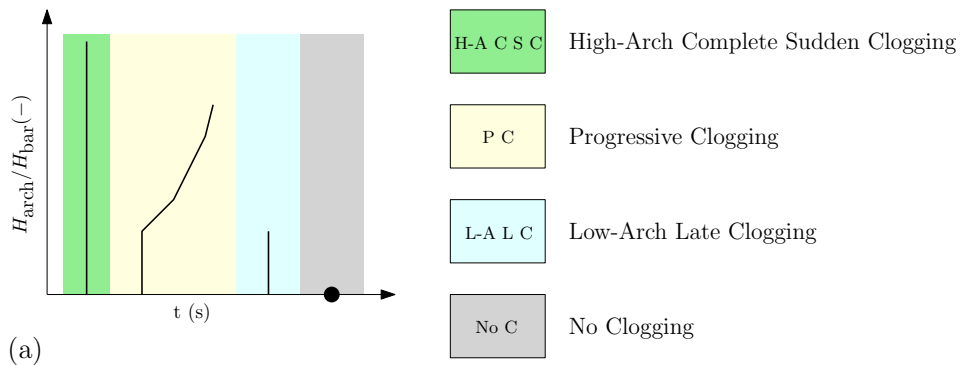
S/r (-) Type	2	3	4	5	6	7	8	9	10
OB	H-A C S C			P C	L-A L C			No C	
VB	H-A C S C				P C		L-A L C		No C

(b)

Fig. 7.9 (a) Four recurrent clogging mechanisms sketch and (b) individuation of them for the OB and the VB configurations.

final stage of the motion. Conversely, in the VB configuration, $\mathbf{F}_G^X$, $\mathbf{F}_G^Z$, $\mathbf{F}_G^n$ and $\mathbf{F}_G^t$ have comparable values, even if $\mathbf{F}_G^n > \mathbf{F}_G^t$. In this configuration, the non-orthogonal impact angle of the flowing front on the barrier causes a force with non negligible components both in *X*- and *Z*-directions (Figs. 7.10(a) and (b)).

Considering the first few seconds of interaction between the flowing mass and the barrier, Figures 7.10(c) and (d) evidence that $\mathbf{F}_G^R$ for the VB is higher than for the OB, while the opposite occurs for $\mathbf{F}_G^n$. These results, valid for all the investigated *S/r*, can be explained considering the dynamics of the flowing mass when it reaches the barrier. As sketched in Fig. 7.11, the mass impacts the barrier with an angle different from 90° (with respect to the barrier), thus the resulting impact force has both normal and tangential components.

After the impact, the run up of the flowing mass in the vertical direction is obstructed by the barrier itself. Frictional and compressive forces between the barrier and the impacted particles arise, altering the direction of motion. In this configuration, the upper particles are induced to invert the direction of their motion, compressing the particles at the bottom (Fig. 7.11). The behavior observed for the vertical barrier results in higher $\mathbf{F}_G^t$ and, consequently, also higher resultant forces
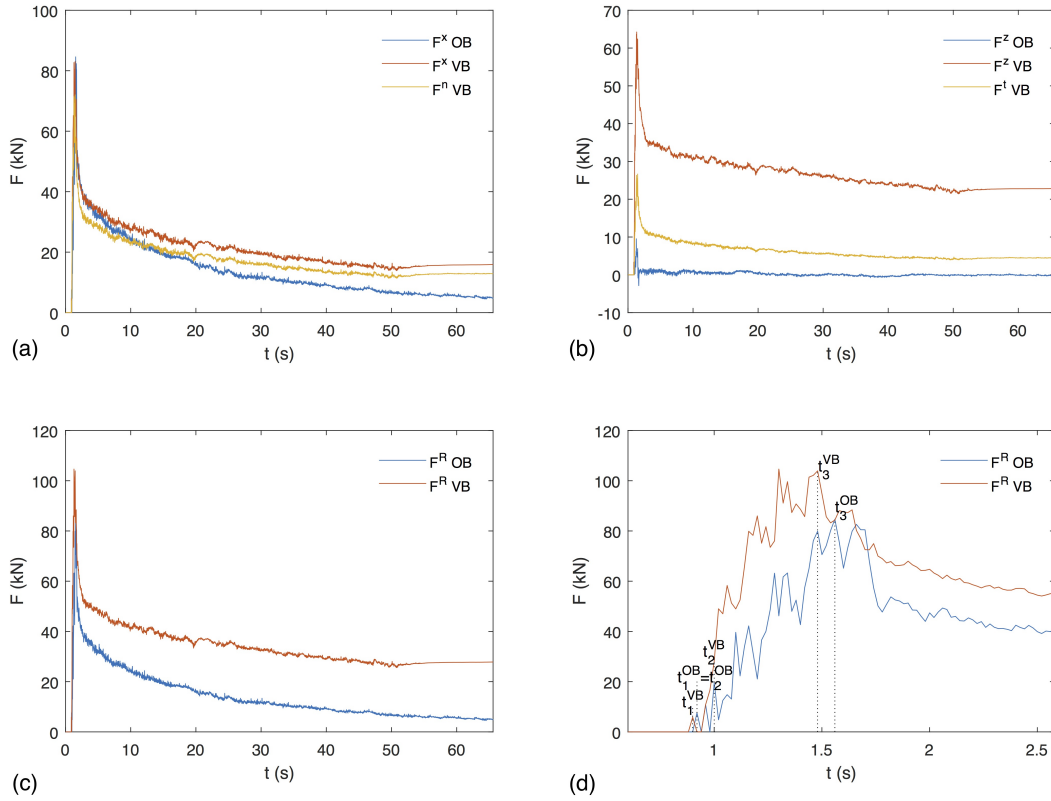
Fig. 7.10 Evolution of impact forces (a) $\mathbf{F}^X$ and $\mathbf{F}^n$, (b) $\mathbf{F}^Z$ and $\mathbf{F}^t$ and (c) $\mathbf{F}^R$ in time in the OB and the VB, for $S/r = 7$, (d) zoom of the dynamic phase of Figure (c): the time of the first impact (t_1), the time of the maximum local impact (t_2), the time of the maximum global impact (t_3). The time t_3 is used to the plot Figures 7.13 and 7.14.

$\mathbf{F}_G^R$ with respect of the OB configuration, even if lower normal components $\mathbf{F}_G^n$ are recorded.

Considering the temporal aspects and analysing some particular instants of the dynamic impact stage (Fig. 7.10(d)) i.e. the time of the first t_1, of the local maximum t_2, and of the global maximum impact t_3, the maximum impact in the OB coincides with the first impact of an isolate grain impact. Conversely, the local maximum impact in the VB occurs later in time and does not coincide with the first arrival of the grains in the front of the flow. Nevertheless, the time lag between the OB and VB is negligible, as well as the one observed for t_3. Also in this case, the global maximum impact force occurs earlier in the VB than in the OB case.

Table 7.2 reports relevant times and forces at different impact phases for closed barrier, OB and VB configurations. In the time following the impact, until a stable condition is reached, a consistent reduction of the global force is observed for both
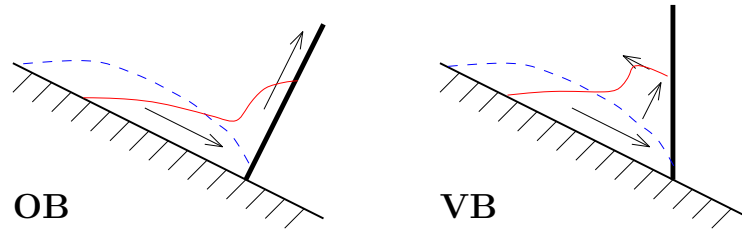
Fig. 7.11 The OB and VB schemes of the dynamic of impact of the flowing mass against the barrier.

(a)

(b)
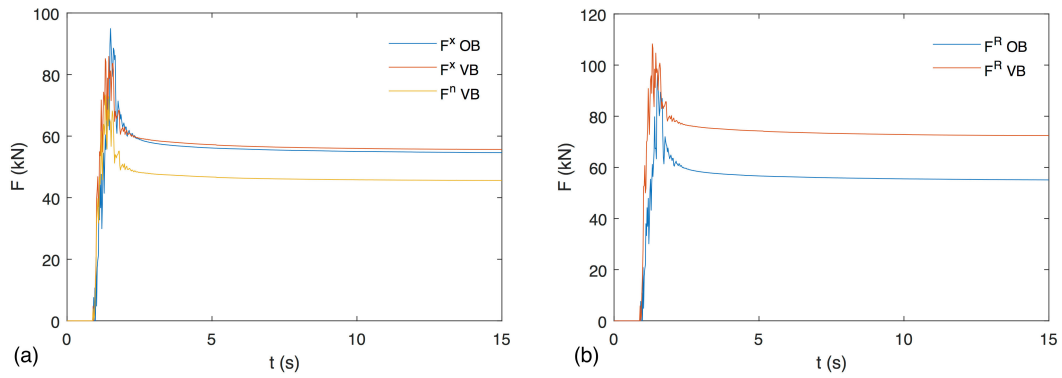
Fig. 7.12 Evolution of impact forces (a) $\mathbf{F}^{X}$ and $\mathbf{F}^{n}$ and (b) $\mathbf{F}^{R}$ in time in the OB and the VB, for $S/r = 3$.

the OB and the VB cases. Considering a completely clogged situation, that is $S/r = 3$ (Fig. 7.12), comparing columns 3 and 7 of Tab. 7.2, the reduction of the global force is about 40% and 30% in the OB and the VB, respectively. For $S/r \geq 7$, a partially clogged condition, the reduction increases up to 90% and 40%, in the OB and the VB, respectively. As expected, the increase of material deposited behind the barrier causes a decrease of the difference between static and dynamic forces. Comparing the OB and the VB in this period of time, as a general rule, $\mathbf{F}_{G}^{R}$ is greater for the VB than for the OB. On the contrary, the normal component $\mathbf{F}_{G}^{n}$ is greater in the OB in the only completely clogged condition, i.e. for $S/r = 3$. In the other cases, i.e. $S/r = 7$ and 10, due to the lower deposited material in the OB case, $\mathbf{F}_{G}^{n}$ is higher in the VB than in the OB. This implies that, when a static situation is reached, in the completely clogged condition the arches exert a noticeable compressive force against the barrier for the OB case, while, for the VB case the presence of barrier-particle friction reduces the normal component.   Considering the spatial distribution of the forces, Figure 7.13 shows the local resultant force distribution when the global maximum impact occurs. Numerical values of both times and forces are reported in

Simulation	t_3 (s)	$\mathbf{F}^R_{G,max}$ (kN)	$\mathbf{F}^R_{L,max}$ at t_3 (kN)	max $\mathbf{F}^R_{L,max}$ in the dynamic phase (kN)	$\mathbf{F}^R_{L,max}$ at t_{end} (kN)	$\mathbf{F}^R_G$ at t_{end} (kN)
Closed, OB	1.5	88.3	2.20	7.60	1.77	56.15
Closed, VB	1.4	107.15	4.02	6.66	4.08	79.29
$S/r = 3$, OB	1.5	88.99	1.71	7.60	1.39	56.43
$S/r = 3$, VB	1.4	109.74	3.93	662	4.02	80.33
$S/r = 7$, OB	1.6	78.47	3.09	7.60	0.41	4.07
$S/r = 7$, VB	1.5	100.47	4.06	6.62	4.07	35.48
$S/r = 10$, OB	1.6	74.52	1.93	7.60	0.32	3.28
$S/r = 10$, VB	1.3	82.51	3.72	6.70	3.77	16.18

Table 7.2 Time and force values in the instants when $\mathbf{F}^R_{G,max}$ is reached (t_3 in Fig. 7.10), during the dynamic phase, and when the static condition is reached (t_{end}), for all the simulations.

Table 7.2. It is evident that, for all the investigated S/r, the intensity of both local and global forces is greater in the VB than in the OB. This result can be associated with the different impact angle between the front of the flowing mass and the barrier. Due to its geometry, in the VB case both the top and the bottom parts of the front impact against the barrier approximately in the same instant. Thus, the number of contacts between the barrier and the particles at the impact time is larger than in the OB, with higher normal and tangential components, and, consequently, higher intensity. For both configurations, the largest magnitudes are in the lower part of the barrier, with the OB forces at a lower position with respect to the VB ones. The maximum local resultant force intensities remain approximately constant, increasing with S/r.

Regarding the maximum global resultant forces, instead, starting from the closed barrier case and progressively increasing the normalised opening width S/r, a decrease in terms of global force appears for both the OB and the VB cases. A decrease of 15% and 22% with respect to the closed barrier is observed for $S/r = 10$ in the OB and in the VB, respectively.

Figure 7.14 compares the OB and VB configurations with respect to the local impact on the barrier at the time at which the maximum global impact is recorded (i.e. t_3) in Fig. 7.10(d), in the open and in the closed barrier case. Red colour represents the areas in which the force in the open configuration are greater than in the closed. In the proximity of the outlet, and in the correspondent region for the closed case,
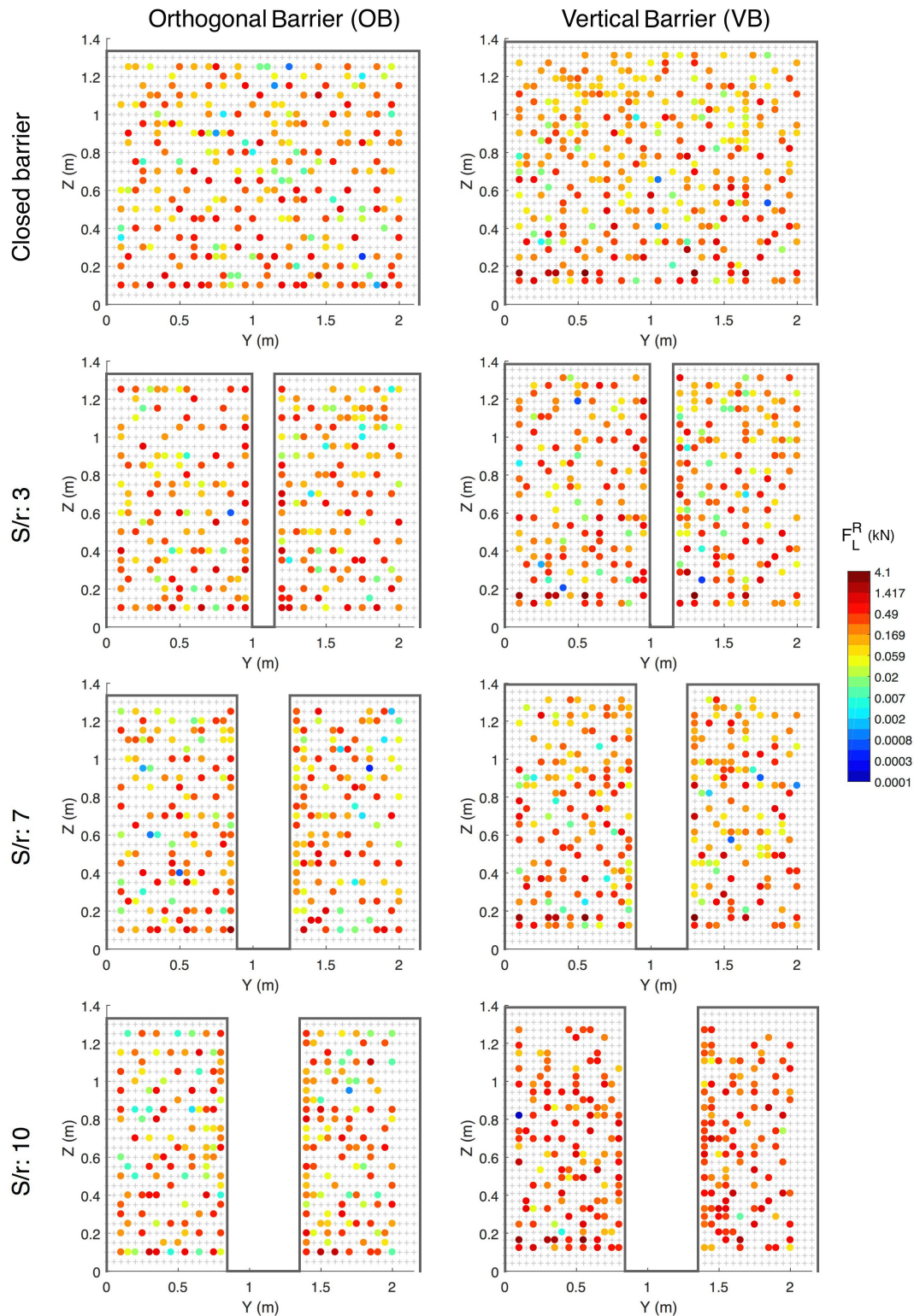
Fig. 7.13 Local impact forces when the maximum global impact occurs on the barrier face at time t_3, indicated in Figure 7.10(d), in OB and VB, for different S/r. The dimension of the coloured points is not representative of the dimension of the grains. The colorbar is in logarithmic scale. The time of occurence, the intensity of the maximum global resultant impact, and the maximum local impact force $\mathbf{F}^{R}_{L,max}$ in the same instant are reported in Table 7.2.

the forces are higher in the open case rather than in the closed one. In the other parts of the barrier face, an homogeneous distribution of the green and red areas emerges, in both configurations.

Evaluating the maximum forces occurred during the first few seconds of the impact, Figure 7.15 illustrates the distribution across the barrier of the maximum local values of the impact force. The areas where high forces concentrate are highlighted. Localised high forces are mainly in the lower part of the OB, while they are distributed over the whole VB. Increasing S/r, for both the OB and VB configurations, it appears that the maximum local values are reached in the outlet region. This phenomenon is a consequence of the dynamic impact forces exerted by the flowing mass passing through the outlet. In a suddenly clogged case, that is for $S/r \leq 5$, arching occurs almost at the time of first impact. Stable force chains arise among the grains and the arching effect in the outlet provoke forces on the outlet neighbourhood mainly in the normal direction. In contrast, for $S/r \geq 6$, the mass is not retained and passes through the outlet with a great kinetic energy, thus resulting in high forces in all directions. As highlighted by the presence of non impacted areas, arching also occurs along the barrier face. Nevertheless, this phenomenon can be enhanced by the modelling of the barrier as an assembly of compacted spheres and not with a smooth wall. This can promote interlocking among a particle of the moving mass and the spheres constituting the barrier. Thus, this phenomenon is only pointed out qualitatively.

Finally, the forces on the barrier at complete stop, i.e. in the static condition, are considered. Figure 7.16 shows the spatial distribution of local static resultant forces $\mathbf{F}_L^R$ on the barrier face. Table 7.2 reports in columns 2 and 3, the global $\mathbf{F}_G^R$ forces and maximum local $\mathbf{F}_L^R$, respectively, when the maximum global occurs. A substantial decrease of both these values is evident for both the OB and VB cases, shifting from a closed or completely clogged configuration (i.e. $S/r = 3$) to a partially clogged (i.e. $S/r = 7$) or unclogged barrier (i.e. $S/r = 10$). As expected, the higher amount of mass behind the barrier produces higher forces. Comparing the OB and the VB configurations, it emerges that both the $\mathbf{F}_{L,max}^R$ and the $\mathbf{F}_G^R$ are higher in the VB configuration and that the lower part of the barrier is the most stressed. In particular, $\mathbf{F}_{L,max}^R$ in the VB case is up to three times higher than in the OB for the closed or the completely clogged barrier ($S/r = 3$) and up to ten times higher for $S/r = 7$ and 10, that is the partially or unclogged condition. Considering the $\mathbf{F}_G^R$, the difference between the VB and the OB is about 40% for the closed barrier
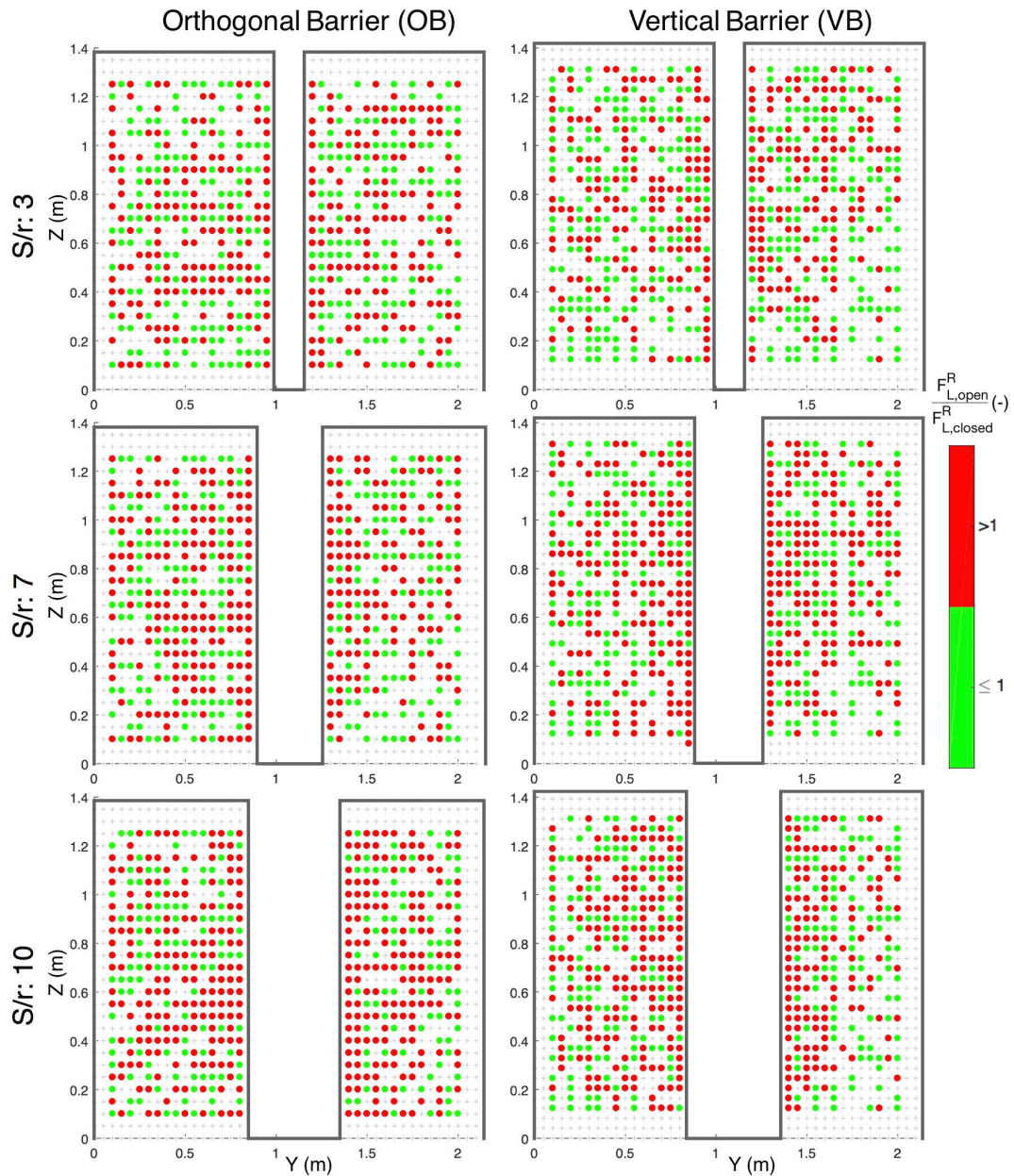
Fig. 7.14 Ratio between the local impact on the barrier face at time t_3, see Fig. 7.10(d), for the open ($\mathbf{F}^R_{L,open}$) and for the closed barrier ($\mathbf{F}^R_{L,close}$) cases, in OB and VB, for different S/r. Red points stands for $\mathbf{F}^R_{L,open}/\mathbf{F}^R_{L,close} > 1$, green in the opposite case.
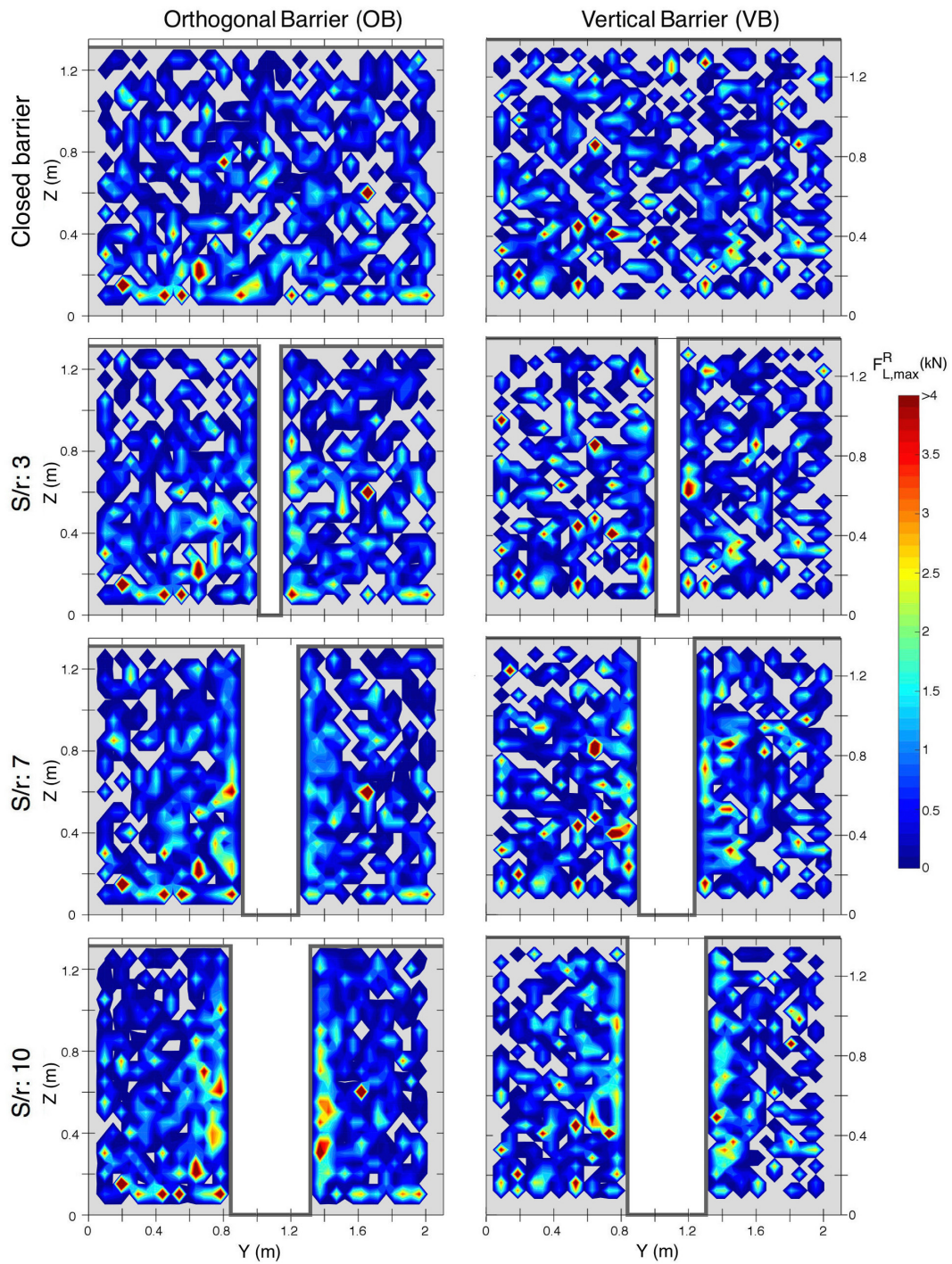
Fig. 7.15 Envelope of the maximum local resultant impact force $\mathbf{F}_L^R$ distribution during the dynamic phase of motion, in OB and VB configurations, for different S/r values. Grey areas in force distribution are due to gaps left by arching of particles against the barrier face. The maximum $\mathbf{F}_L^R$ occurred over the whole barrier is reported in Table 7.2.

($S/r = 3$). For the VB, for $S/r = 7$ and 10, $\mathbf{F}_G^R$ is up to six times higher than for the OB. The increase in the difference can be ascribed to the greater amount of trapped and deposited material as well as the higher tangential forces arisen in the VB case. The VB produces an interlock of the material at the bottom, thus enhancing the formation of the arches. Furthermore, due to this compression, the formed arches withstand a greater weight, resulting in forces on the barrier that are greater than those recorded in the OB. Showing the forces exerted by the mass at rest, Figure 7.16 allows some considerations on the shape of the deposit profile. A more pronounced notch is highlighted in the OB rather than in the VB: a "V" profile is observed in the OB, while the profile of the deposit is more curved ("U" profile) in the VB. This difference can be also ascribed to the higher quantity of entrapped material in the VB case.

As a consequence of these analyses, it appears that the VB configuration involves greater forces. Nevertheless, it is worth mentioning that the slope angle $\theta = 35°$ has been chosen as it guarantees a supercritical condition of motion allowing particles to reach high relative velocities at the impact. Consequently, this inclination does not represent the real typical inclination of the slope, as in general such barriers are located in proximity of the fan apex, where the slope is gentle. Furthermore, for this reason, both numerical simulations and laboratory experiments are usually carried out with the OB configuration (see Ch. 4 for references). This justifies the fact that, in the following section, all the simulations are performed with an orthogonal barrier (OB) configuration. However, in the hypothesis of a VB configuration, the expected global maximum impact force increases, while the local maximum values remain approximately the same. Furthermore, the expected trapping efficiency in the VB case is higher than in the OB case.

7.2.2   Influence of the channel slope

The simulations are performed varying both the slope of the channel θ and the outlet width S with respect to the mean radius r of the discharged mass. The considered slopes are: $10°, 20°, 30°, 35°$, and $40°$, with the intent to account for slope angles both lower and greater than the internal friction angle, that is $30°$. In this way, particles can be halted not only principally for the arisen of basal frictional forces but also for arching effects. The case in which the acting forces are governed by collisions, is of particular interest since it represents the so-called inertial regime, in
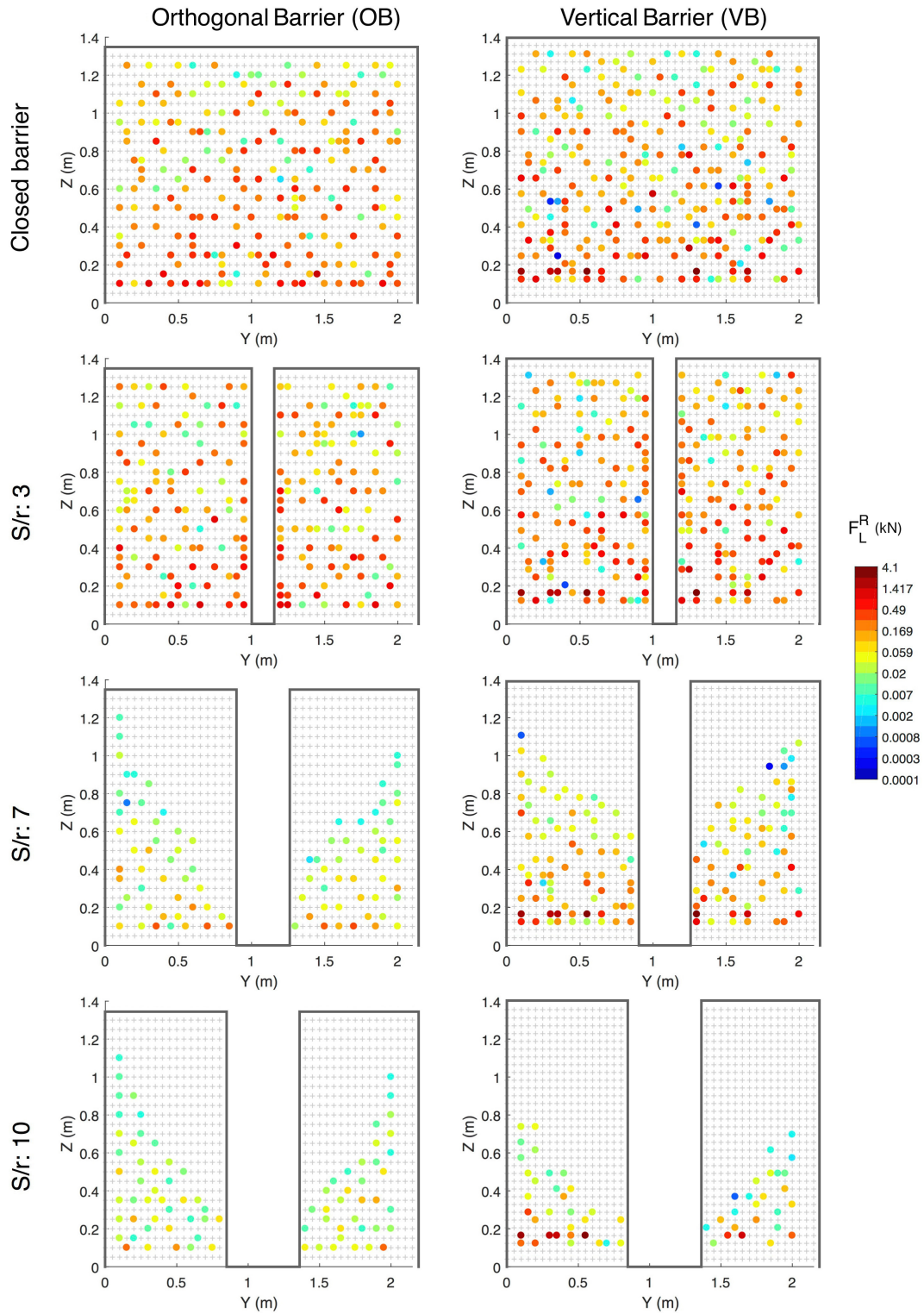
Fig. 7.16 Forces in static condition in OB and VB, for different S/r. The dimension of the coloured points is not representative of the dimension of the grains. The colorbar is in logarithmic scale. The maximum local resultant impact occurred in the whole barrier $\mathbf{F}_{L,max}^{R}$ and the global resultant force $\mathbf{F}_{G}^{R}$ values are reported in Table 7.2.

which frictional basal forces neither prevail nor halt the motion. Differently from what was performed in Sec. 7.2.1, the simulations consider a S/r ranging from 2 up to the critical condition in which no clogging occurs.

Figure 7.17 qualitatively represents the flowing mass when the first impact against the barrier t_0 occurs, for all the investigated channel slopes. Colour indicates the velocity of the grains. The frequency distribution of the velocity of the particles within the first meter behind the barrier is plotted in the 8-classes histogram. Despite the fact that the initial release configuration does not allow to consider the development of the flowing mass along a path, i.e. the transportation zone of a real event, the higher the channel slope is, the more the grains tend to reach the front and the higher the velocity of the impacting mass is.
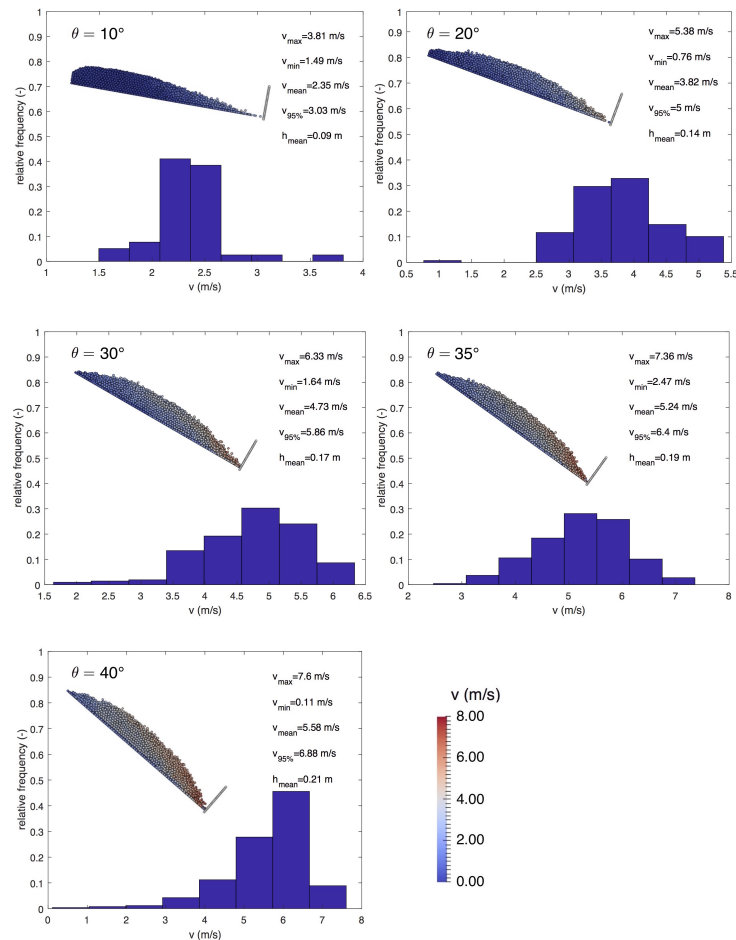
Fig. 7.17 Sketches of the flowing mass in the instant of the first arrival t_0, for all θ. The histograms show the relative frequencies of the velocity values of the the impacting mass in the first meter behind the barrier. Colour indicates the velocity of the grains.

Analysis of the trapping efficiency

The clogging mechanisms is investigated considering the amount of material that passes through the outlet of the barrier. Figure 7.18 shows the non-retained material fraction with respect to S/r at complete stop of the discharging mass, for all the investigated θ values.
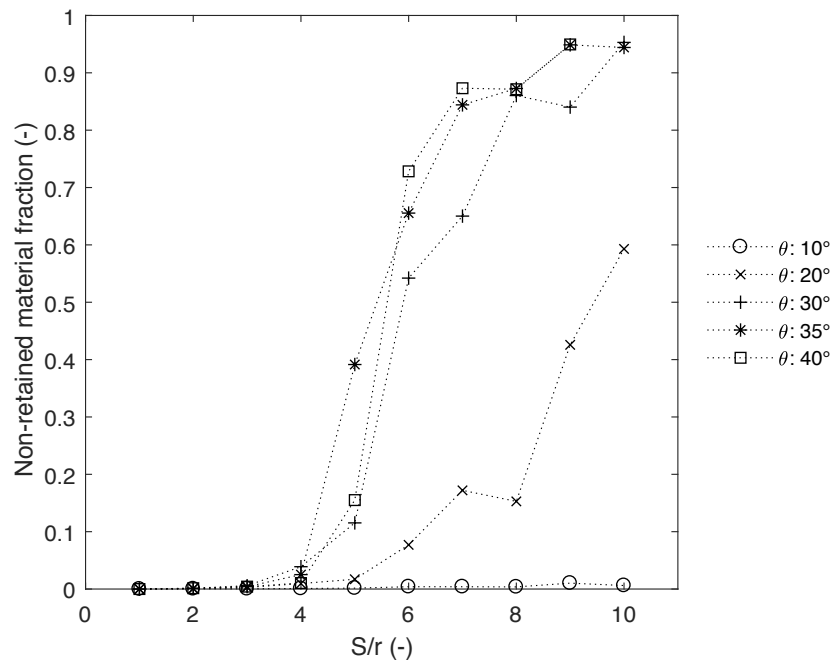
Fig. 7.18 Non-retained material fraction with respect to S/r value at complete stop of the discharging mass for all θ.

As expected, it is observed that increasing S/r, a smaller amount of material is trapped by the barrier. The same trend is observed by increasing θ. For $\theta = 10°$ about the whole flowing material is halted behind the barrier. For $\theta \geq 20°$ and $S/r > 4 - 5$, a transition emerges: the trapping efficiency reduces and the passing material progressively increases. This trend is more pronounced for $\theta \geq 30°$. In this last case, the curves are similar in magnitude and raise up to a constant value of 95% of non-retained material. The only different case at $\theta = 35°$ and $S/r = 5$, is a possible effect of the complexity of the model and of the interactions between the particles.

Figure 7.19 plots the ratios H_{arch}/H_{bar} as a function of the time of arching t_{stop},

calculated with respect to the first arrival time t_0, for each θ and for different values of S/r.

Considering the obtained results, they are presented for each value of θ.

- $\theta = 10°$: arching occurs for each investigated S/r, suddenly in time for $S/r \leq 8$, and later for $S/r = 9$ and 10. Part of the discharged mass stops along the channel before reaching the barrier. This results in a smaller H_{arch}, varying from two layers of particles for $S/r \leq 8$ to one for $S/r = 9$ and 10.

- $\theta = 20°$: arching occurs for each investigated S/r, suddenly in time for $S/r \leq 6$, and later for $S/r \geq 7$. Progressive clogging occurs for $S/r = 5$ and 6. H_{arch} decreases with S/r: from $H_{arch}/H_{bar} \simeq 0.70$ for $S/r = 2$ to an arch of only one layer of particles for $S/r = 10$. Also in this case part of the discharged mass stops along the channel before reaching the barrier.

- $\theta = 30°$: arching occurs for $S/r \leq 9$, suddenly in time for $S/r \leq 5$, and considerably later for $S/r \geq 6$, at around $60 - 80$ s after the first impact. A slight progressive clogging occurs for $S/r = 4$ and 5 and with a greater time lag for $S/r = 7$. H_{arch} decreases with S/r, from $H_{arch}/H_{bar} = 1.0$ for $S/r = 2 - 3$ to an arch of only one particle layer for $S/r = 8$. A considerable difference in term of both t_{stop} and H_{arch}/H_{bar} is observed in the transition from $S/r = 5$ to $S/r = 6$. With this incline, the whole mass reaches the barrier.

- $\theta = 35°$: arching occurs for $S/r \leq 8$, suddenly in time for $S/r \leq 4$, and considerably later for $S/r \geq 6$, around $45 - 70$ s after the first impact. For $S/r = 5$, a sudden stop occurs for the lower height subdivision and then a progressive clogging occurs with a considerable time lag, of about 70 s. For $S/r \geq 7$ a sudden stop happens. H_{arch} decreases with S/r, from $H_{arch}/H_{bar} = 1.0$ for $S/r = 2 - 3$ to an arch of only one particle height for $S/r = 7 - 8$. $S/r = 5$ represents a transition in term of both t_{stop} and H_{arch}/H_{bar}, from a sudden formed high arch to a low stable arch configuration.

- $\theta = 40°$: arching occurs for $S/r \leq 8$, suddenly in time for $S/r \leq 4$, and considerably later for $S/r \geq 6$, around $35 - 55$ s after the first impact. In the case of $S/r = 5$, a sudden stop happens for the lower subdivisions and then a progressive clogging occurs with a time lag of 20 s. H_{arch} decreases with S/r, from $H_{arch}/H_{bar} = 1.0$ for $S/r = 2 - 3$ to an arch of only one particle height
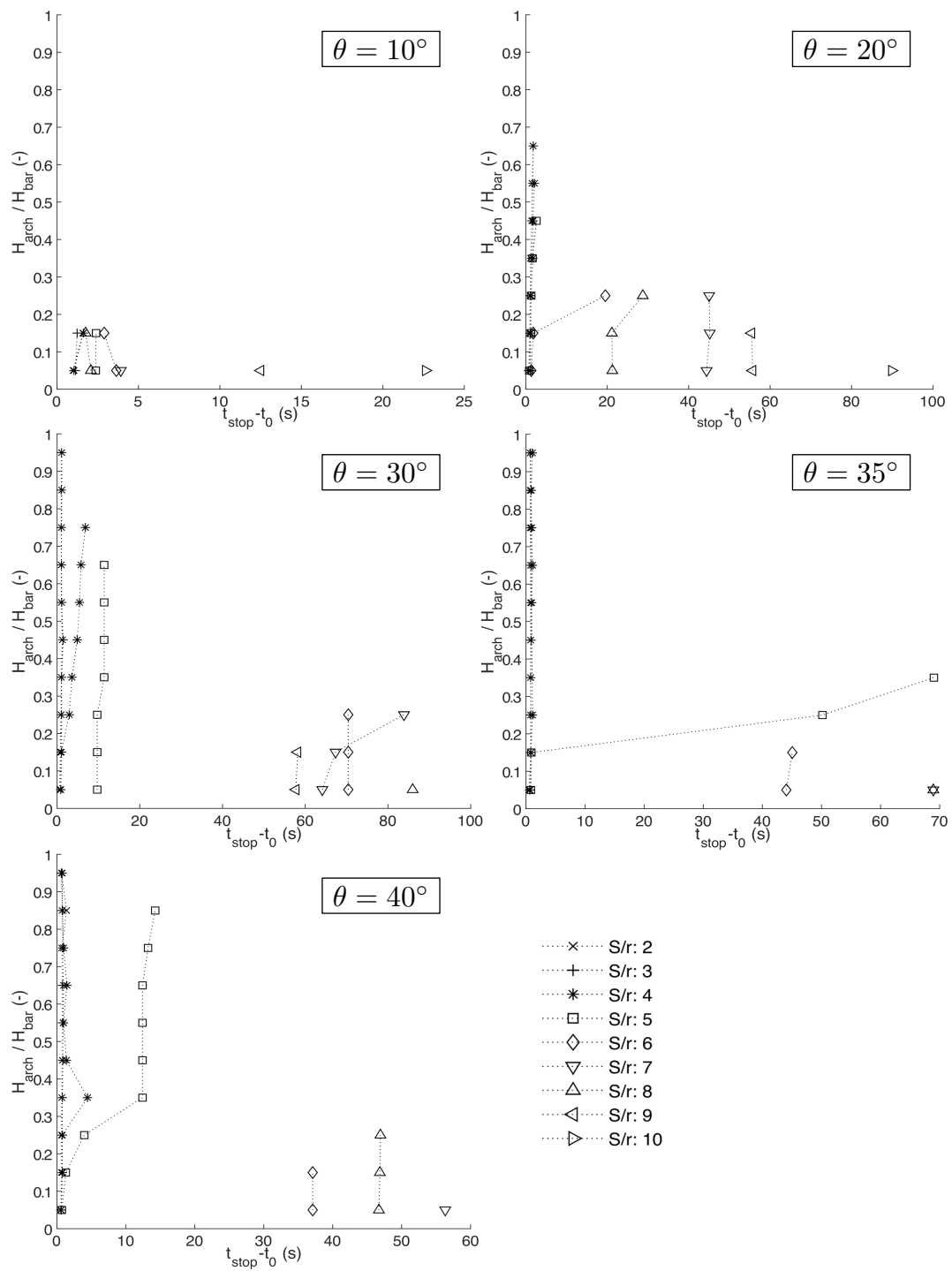
Fig. 7.19 Ratio between the height of the arch and the height of the barrier $H_{\text{arch}}/H_{\text{bar}}$ with respect to the time of arching t_{stop}, for different channel slope θ. Each marker is located at the center of the correspondent interval height.

for $S/r = 7$. A considerable difference in terms of both t_{stop} and H_{arch}/H_{bar} is observed in the transition from $S/r = 5$ to $S/r = 6$.

From these results, it emerges that the four possible clogging mechanisms individuated for $\theta = 35°$ (Sec. 7.2.1) reoccur also spanning the all investigated θ, as summarized in Fig. 7.20. It emerges a possible classification between "gentle slopes"

S/r (-) $\theta(°)$	2	3	4	5	6	7	8	9	10
10°	C S C							L-A L C	
20°	H-A C S C				P C		L-A L C		
30°	H-A C S C				L-A L C	P C	L-A L C		No C
35°	H-A C S C			P C	L-A L C			No C	
40°	H-A C S C			P C	L-A L C			No C	

H-A C S C	High-Arch Complete Sudden Clogging
P C	Progressive Clogging
L-A L C	Low-Arch Late Clogging
No C	No Clogging
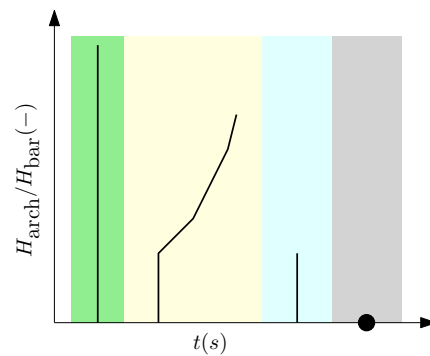
Fig. 7.20 Individuation of the four recurrent clogging mechanisms for different channel slope θ and dimensionless opening width S/r.

($\theta < 30°$) and "steep slopes" ($\theta \geq 30°$), where $30°$ exactly coincides with the internal friction angle value. In the former case, where $\theta < \phi_i$, the basal frictional forces play an important role in the stopping mechanism since the flowing mass stops before reaching the barrier. The trapping effect is anyway observed and its efficiency decreases when increasing the normalised opening width, considering both H_{arch} and t_{stop}. In the latter situation, instead, the forces arising from the collisions among grains constitute the leading contribution to the evolution of the mass motion. Thus, the arching effect is due mainly to the trapping effect of the barrier, rather than the

frictional forces. Increasing the normalised opening width, H_{arch} decreases and t_{stop} increases. The case $S/r \simeq 5$ constitutes a transitional condition from a suddenly formed high arch to a low stable arch, occurring late in time. This transition is abrupt for $\theta = 30°$, while, for $\theta = 35°$ and $40°$ ($S/r = 5$) progressive clogging occurs. In general, increasing θ, both H_{arch} and t_{stop} decrease. The steeper the slope is, indeed, the higher the velocities are, and this affects the duration of motion, as shown below.

Figure 7.21 shows the stopping time t_{stop} for different θ and S/r. In case of $\theta = 10°$ the flowing mass stops suddenly, for any normalised opening width. On the contrary, for $\theta = 20°$, increasing S/r, t_{stop} increases progressively. For steep slopes, the mass stops suddenly for $S/r \leq 4$. For opening widths larger than seven times the radius ($S/r > 7$), t_{stop} decreases by increasing θ, with a linear trend. For the intermediate values of S/r ($5 \leq S/r \leq 7$), t_{stop} increases progressively.

From these results, in the steep slope case, the existence of both a complete-clogging and a critical value emerges. For $S/r \leq 4$ almost the whole mass is trapped, while for $S/r \simeq 8 - 9$ no arching effect occurs. This critical value slightly decreases with θ. At $S/r = 5$ a transitional state verifies, which can lead to a progressive clogging mechanism. The result of a complete trapping condition, for $S/r \leq 4$, is in good agreement with the normalised opening width prescribed for a complete trapping by different Authors (Fig. 4.4), confirming the the goodness of the approach. These results are in line with what expressed by Arévalo and Zuriguel (2015), as explained in Sec. 4.3, even though the Authors found that no stable clogging occurs for a slightly higher value, i.e. $S/r > 10$.

For sake of completeness, it should be noticed that the behaviour of the flowing mass for steep slopes is influenced by the ceiling of the domain, i.e. $Z = 1.35$ m. H_{bar} spans the whole Z domain dimension, thus the material cannot overflow the barrier but can only pass through the outlet. Figure 7.22 shows that, for $\theta \geq 30°$, the maximum height reached by the mass during its motion is equal to H_{bar}. However, this does not occur for $\theta < 30°$, where the stopping mechanism is mainly governed by basal friction.

Analysis of the impact forces

The dynamics of flow impact is analysed in terms of both impact forces and basal bending moment exerted on the barrier. As a consequence, the results presented here are expressed as global forces (or moments), by summing the contributions
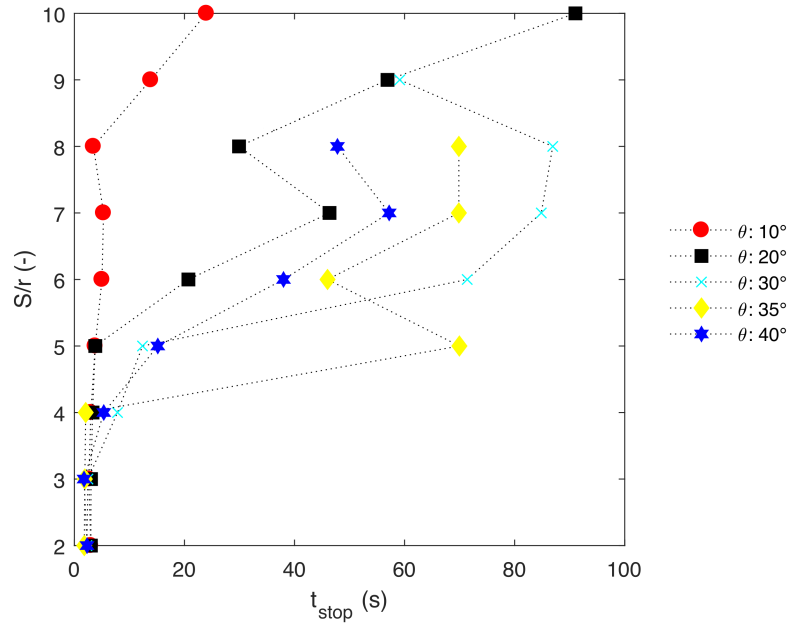
Fig. 7.21 Normalized opening width S/r with respect to the time of stop t_{stop} of the material, for different channel slope θ.

of the local forces (or moments) obtained at each point on the barrier. The study of the influence of the impact angle on the distribution of the forces, as well as force-time history analyses, have been already analysed in Sec. 7.2.1. Here the influence on the maximum global force of both the slope angle and the normalised opening width is evaluated, as the maximum global force generally constitutes the main input parameter for the structural design of a barrier. Unless otherwise stated, the considered impact values are related to the whole barrier, considering both piles.

Figure 7.23 contains the maximum value of the global force in the direction normal to the barrier F_{max}^{n}, with respect to the slope of the channel θ, for different S/r. In this plot, the values for a single pile are considered, taking the greatest value between the two. The analyses reveal that the values of the global forces for each of the two piles are very close (see e.g. Fig. 7.13), that is the presented results are representative of both piles. It is evident that an increment of the slope produces a significant increase in the intensity of the force, and the trend is almost a Y-axis symmetric concave parabola. In contrast, the normalised opening width seems not to affect the results. In particular, for $\theta = 10°$, all the values for each S/r converge to a unique point, as the maximum is due in all the cases to a single particle impact. For $\theta \geq 20°$, the curves tend to widen, but with marginal influence of S/r. The same
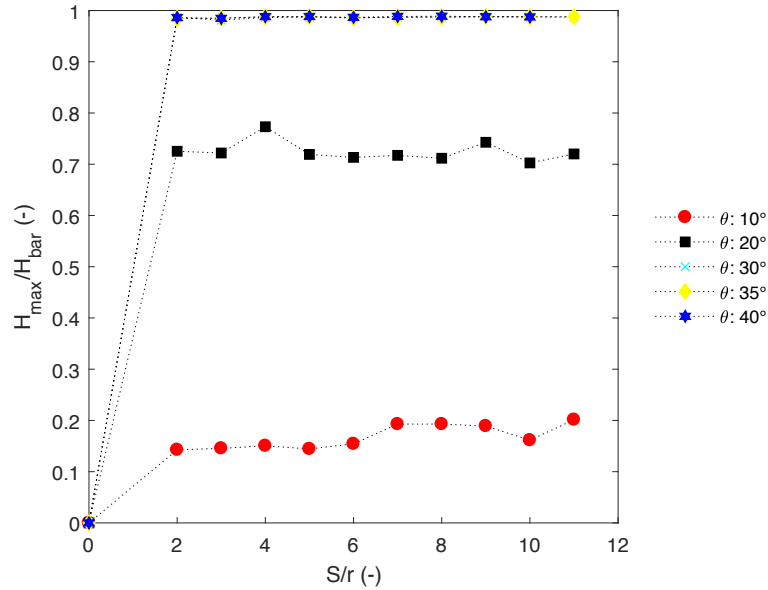
Fig. 7.22 Normalized opening width S/r with respect to the time of stop t_{stop} of the material, for different slopes of the channel θ.

trend can be observed for the moment M^X_{max}, computed at the base of the barrier. It should be noticed that for $\theta = 10°$, $M^X_{max} \simeq 0$ as the single impact occurs in the low part of the barrier (Fig. 7.23(b)).

Figure 7.24 displays F^n_{max} versus the time lag between the first arrival t_0 and the time at which the maximum force is recorded t_{max}. The case of a corresponding closed barrier is considered also. For $\theta = 10°$, all the results converge to the same value, apart for the closed barrier case. This is consistent with the fact that, for all the simulations with $\theta = 10°$, F^n_{max} is due to the same single particle impact. In the closed barrier case, the maximum value, even though due to a single grain impact as for the open barrier cases, occurs in the very center of the barrier, thus it is not recorded in the open cases. A consistent data scattering is evident for $\theta = 20°$, with no noticeable influence of S/r. For this slope, analysing the evolution of F^n in time, for $S/r = 9$ as an example (Fig. 7.25), the peak value of the force is not instantaneous, but several oscillations can be observed around this value. This can be ascribed to the fact that part of the flowing mass impacts the barrier progressively in time. For $\theta \geq 30°$, the time lag reduces as well as the data scattering. This trend is in good agreement with the one observed in Figure 7.21 for the clogging mechanism. The higher the slope is, the faster the motion is.

The force F^n_{max} on the whole barrier is then compared with the corresponding
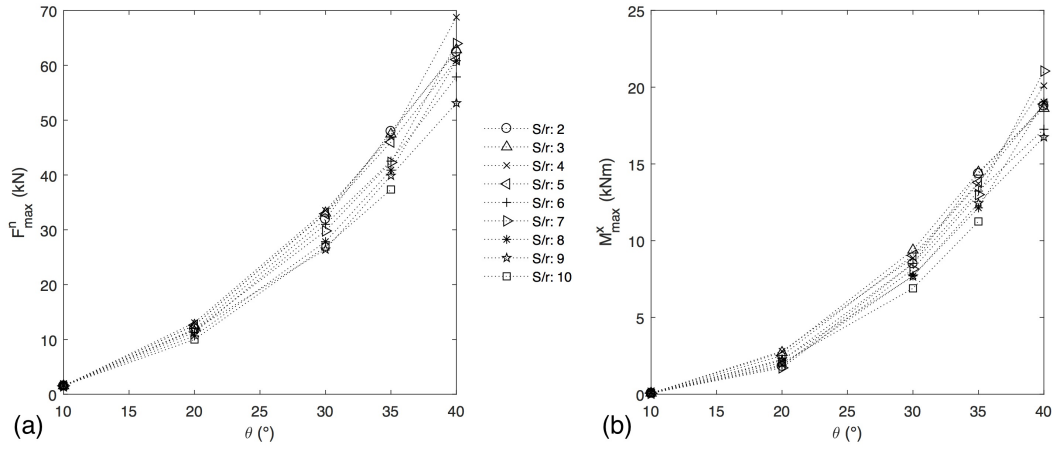
Fig. 7.23 (a) Maximum normal force $F_{\max}^n$ and (b) maximum momentum $M_{\max}^X$ in X direction exerted by the discharged mass to one pile of the barrier with respect to the inclination of the channel θ, for different S/r.

value obtained on a closed barrier F_0^n, set in the same position and with the characteristics of the open ones, as shown in Fig. 7.26(a). No appreciable influence of both S/r and θ is observed. Only a slight increase in the ratio $F_{\max}^n/F_0^n$ is produced increasing the slope. For $\theta = 10°$, all the results converge to one point for any value of S/r, $F_{\max}^n$ is the same for all simulations and is due to a single impact grain. The value of the ratio is slightly lower than one, as $F_{\max}^n$ is approximately equal for closed and open cases. The scatter of the data largely increases for steeper angles. Figure 7.26(b) illustrates the ratio between the maximum value of the force against the barrier $F_{\max}^n$ and its value in static condition F_{fin}^n for each S/r with respect to θ. All the results are grouped around the range 1 to 4, for $\theta = 10°$. This is consistent with the stopping dynamic of the mass, which partially halts before impacting the barrier. Thus, the force exerted in the final static condition is slightly lower than the forces in the dynamic phase.

For all the investigated θ, for $S/r \leq 5$, the ratio $F_{\max}^n/F_{\text{fin}}^n$ does not increase with θ and it is approximately equal to unity. This is ascribable to the fact that almost all the material is clogged behind the barrier, and exerts a static force against the barrier whose intensity is comparable with the dynamic one. A noticeable difference can be observed for $\theta = 35°$ and $S/r = 5$: in this configuration, a larger amount of grains flows through the outlet. On the contrary, for $\theta \geq 20°$ and $S/r \geq 6$, the ratio $F_{\max}^n/F_{\text{fin}}^n$ increases by increasing θ and S/r. This behaviour is more evident for steep slopes, since the clogging mechanism occurs late and involves a lower flow height. Moreover, only a small amount of mass is retained behind the barrier. As already
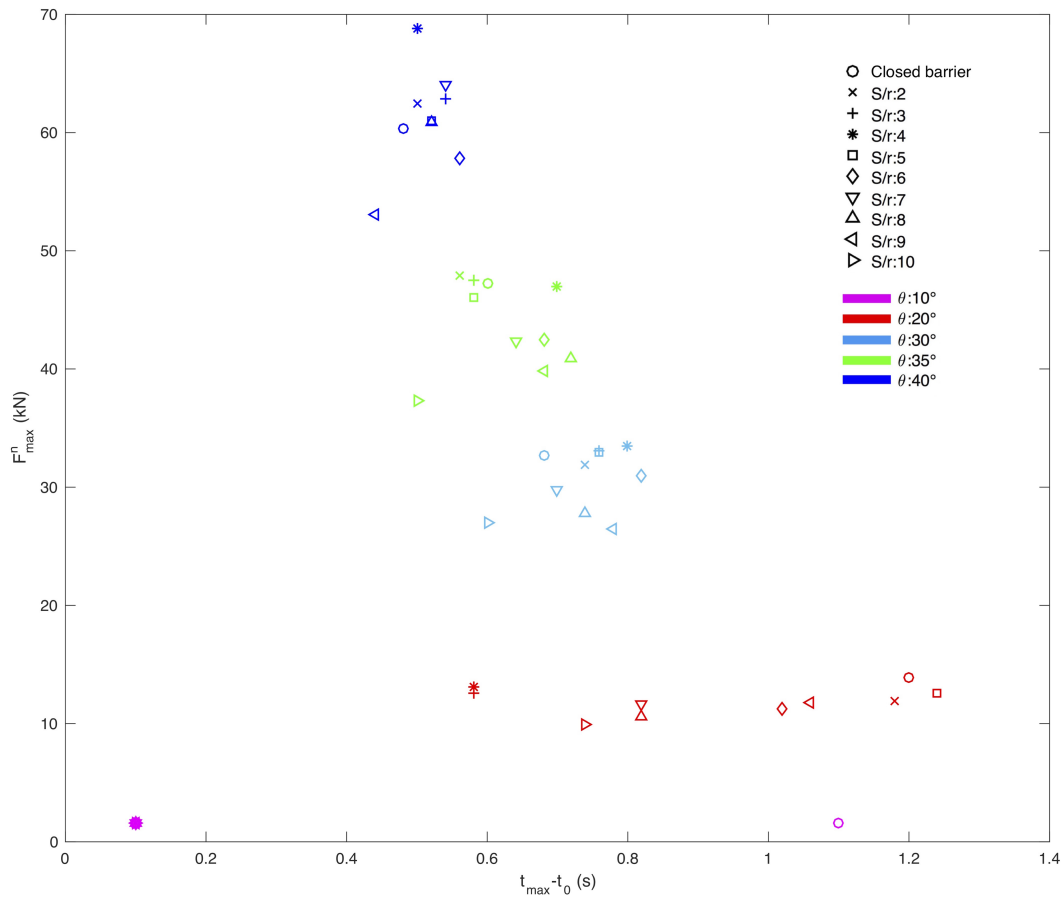
Fig. 7.24 Maximum normal force F_{max}^n exerted against one pile of the barrier versus time lag between the first arrival t_0 and the time at which the maximum force is registered t_{max}, for different θ and S/r.

explained, for $\theta = 20°$, although some of the released mass flows through the outlet, this tendency is less drastic. This is due to the basal friction, which slows down the mass, by reducing the amount of both the impacting mass and the non-retained mass.

Figure 7.27 shows an attempt to compare the results obtained in the numerical model with the correspondent forces calculated with the hydrostatic and hydrodynamic approaches previously detailed in Sec. 4.2. This allows, at a first approximation, to evaluate the validity of the general adopted empirical formulations relating to impact forces. In Figures 7.27(a) and 7.27(b), the maximum normal forces F_{max}^n, considering a 1 m-width pile of the barrier, i.e. in the case of $S/r = 3$, are compared with hydrostatic and hydrodynamic approaches, respectively, neglecting any dimensionless correcting coefficient, i.e. $k_{d,a}$ and $k_{d,b}$ of Eqs. (4.1) and (4.2). The ratio between the numerical and the calculated forces shows the range of $k_{d,a}$ and $k_{d,b}$ to
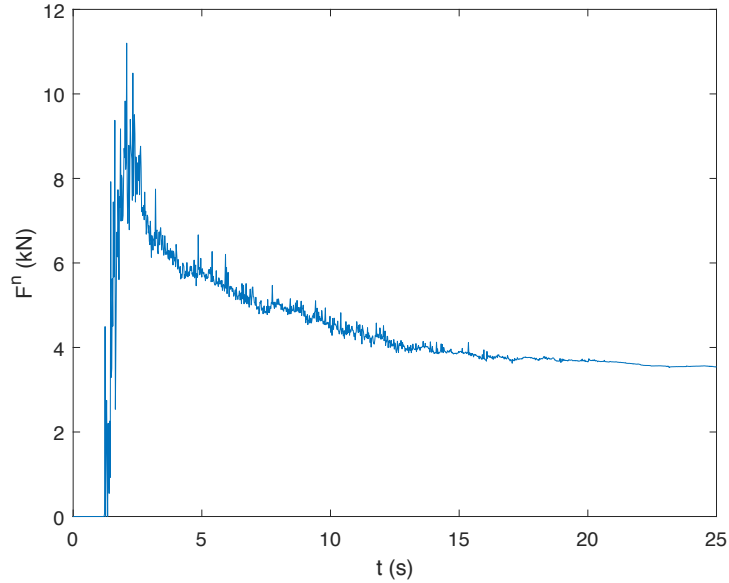
Fig. 7.25 Force in the direction orthogonal to the barrier $\mathbf{F}^n$ with respect to time, for $\theta = 20°$ and $S/r = 9$.

adopt. Calling $k_{d,a}$ as k_{st}, and $k_{d,b}$ as k_{dyn}, it results:

$$k_{st} = \frac{F_{max}^n}{\rho_d g h^2},$$
$$k_{dyn} = \frac{F_{max}^n}{\rho_d v_d^2 h}. \tag{7.2}$$

In order to take into account the non-complete development of the typical granular front due to the released initial geometry (Fig. 7.17), the mean height of the flow is the considered flow depth for both the hydrostatic and the hydrodynamic force computation. In fact, in all the performed numerical simulation, the mean height of the impacting mass is higher than the front height. Instead, in favour of safety, the considered flow velocity is the mean value within the first meter behind the barrier. In this region, grains reach higher velocities. Considering the debris flow density ρ_d, the same value adopted for the only grains is considered, i.e. 2500 kg/m^3. All these choices have been made in favour of safety and allow only some preliminary considerations. It emerges that the force obtained from the numerical simulations is much higher than the one computed through the hydrostatic approach, and that the corrective coefficient to adopt $k_{d,a}$ has values comparable with the ones generally used in literature (reported in Sec. 4.2 and highlighted in Fig. 7.27(a) with
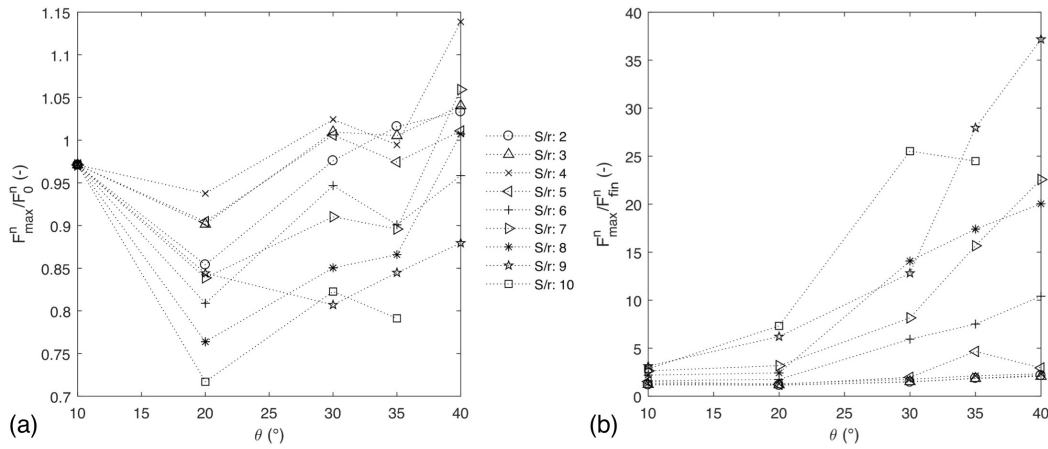
Fig. 7.26 (a) Ratio between F_{max}^n for each outlet size and the maximum value for a closed barrier with the same slope F_0^n is plotted with respect to θ and (b) ratio between maximum value of the force and its value in static condition F_{fin}^n for each S/r with respect to θ. The shadowed area in (a) represent the range generally adopted in literature for $k_{d,a}$.

a shadowed area). Furthermore, increasing the channel slope, this factor increases. In contrast, the force obtained from the numerical simulations is much lower than the one computed through the hydrodynamic approach. In this case, the value of the corrective coefficient to adopt $k_{d,b}$ is less than unity, while the generally adopted range is 2–5. Also in this case, however, increasing the channel slope, the value of the corrective coefficient increases. It results that, increasing the channel slope, the adoption of these formulations requires more precautionary coefficients.

7.3 The sectional barrier study

This section relates to barriers with multiple outlets, i.e. the sectional barriers. It is proved (Chevoir et al., 2007; Mondal and Sharma, 2014) that both clogging and impact forces occurring on the barrier are quite different if there are two or more adjacent outlets. Neighbouring outlets increase the frailness of the granular arches and, as a consequence, the exerted forces substantially differ from the single outlet case. Considering the sectional barrier, as an expansion towards a more realistic geometry of the single outlet barrier case, all the results obtained in Sec. 7.2 are used as reference parameters for analysing the influence of adjacent outlets both in terms of trapping and energy breaking efficiency for this barrier type. Two are the main goals: (1) individuating the critical pile width above which the clogging
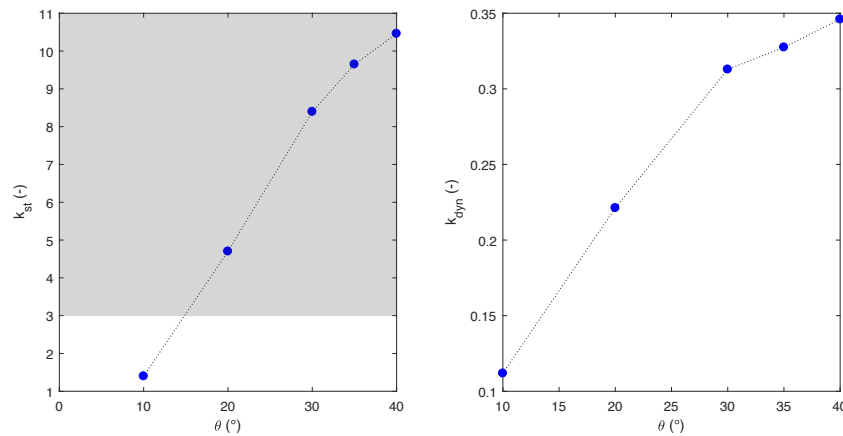
Fig. 7.27 Ratio between the maximum normal force for 1 m of barrier and (a) the correspondent hydrostatic force, in absence of the corrective coefficient $k_{d,a}$, and (b) the correspondent hydrodynamic force, in absence of the corrective coefficient $k_{d,b}$. The shadow area of (a) represents the general range of values adopted in literature for k_d, a (Sec. 4.2)

characteristics does not differ from those of a single outlet, (2) identifying the best configurations of widths for both outlets and piles with respect to the mean grain size. In this perspective, both outlet and pile widths, S and P respectively, are varied to study their effects in the interaction between flow and barrier. To achieve such goal, maintaining the domain size constant, numerical simulations are performed varying size and number of the piles. Figure 7.28 reports different barrier geometries, while the investigated number and dimension of the piles are listed in Table 7.3.

As previously done for the single outlet barrier, the outlet width S is varied as function of the particle mean radius r. In addition, the pile width P is also varied as function of r, i.e. the simulations consider a normalised pile width P/r. in order to find when particle arches on adjacent outlet start being mutually influenced thus becoming unstable. As the domain size is constant for all the simulations (Tab.

(a)   (b)   (c)
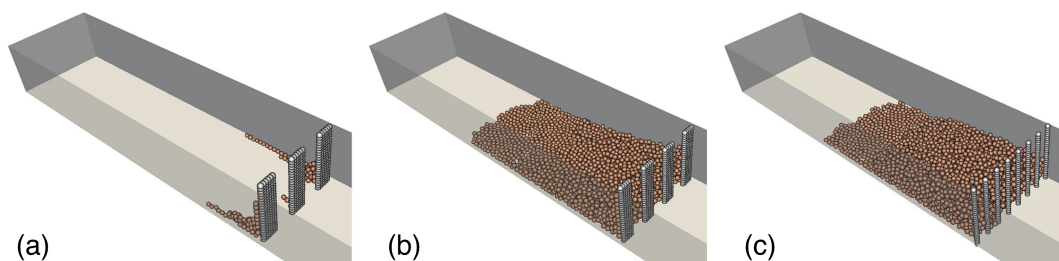
Fig. 7.28 Examples of multiple outlets rigid barrier: (a) $P/r = 8$, $S/r = 8$; (b) $P/r = 6$, $S/r = 5$; (c) $P/r = 2$, $S/r = 4$

Reference name	Number of piles	Pile width P (cm)	P/r	S/r
A	8	10	2	4
B	7	10	2	5
C	6	10	2	6
D	5	10	2	8
E	4	10	2	11
F	4	33	6	5
G	5	22	4	5
H	4	30	6	6
I	5	18	4	6
L	3	42	8	8

Table 7.3 Geometrical properties of the multiple outlets rigid barriers employed in the numerical simulations.

7.1), the variation of S and P in each configuration results in a different number of piles. Thus, it is assumed that simulating at least two consecutive openings is a good approximation to study the mutual influence of neighbouring outlets. Furthermore, as a consequence of the constant domain width limit, the boundary pile width is slightly adjusted in order to obtain outlets of constant width for each setting. In order to compare the results, the performed analyses are combined as described by Tab. 7.3:

- Five simulations with $P = 10$ cm, corresponding to $2r$, i.e. A, B, C, D, and E in Tab. 7.3;

- $P = 18$ cm and $P = 22$ cm, corresponding to $\sim 4r$, i.e. I and G in Tab. 7.3;

- $P = 30$ cm and $P = 33$ cm, corresponding to $\sim 6r$, i.e. H and F in Tab. 7.3;

- $P = 42$ cm, corresponding to $\sim 8r$, i.e. L in Tab. 7.3.

Analysis of the trapping efficiency

The trapping efficiency of the sectional barrier is investigated considering the amount of material flowing through the outlets. The barrier spans in the whole Y direction, independently from the number of outlets. Figure 7.29 depicts the non-retained material fraction with respect to time. The figure is subdivided into two plots, (a) considering a given P/r and varying S/r and (b) varying both P/r and S/r. The
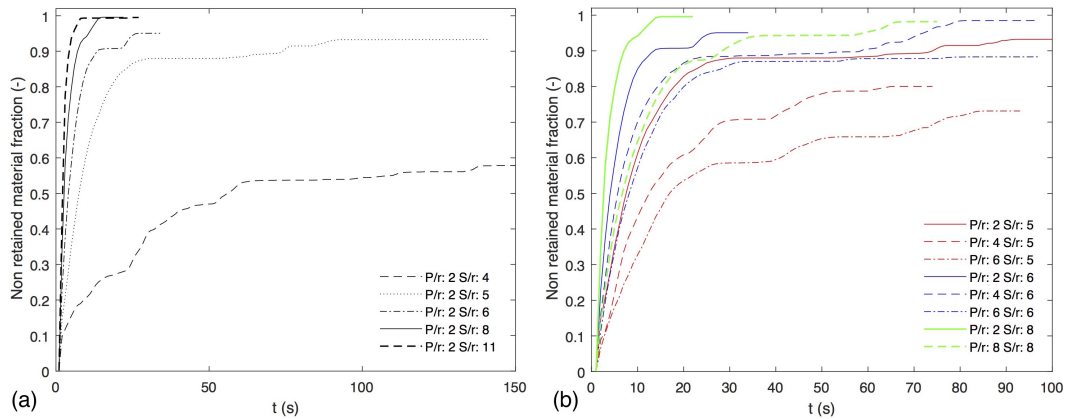
Fig. 7.29 Non-retained material fraction with respect to time, until a stable configuration of the mass is reached. (a) $P/r = 2$; (b) grouped by same S/r (color) and same P/r (line style).

colours are equal for each S/r value and the line styles for the P/r. This subdivision allows a first qualitative analysis of the influence of both S/r and P/r on the trapping efficiency of the barrier. Figure 7.29(a), where the only $P/r = 2$ is analysed, reveals that increasing the normalised opening width, the amount of the untrapped material increases, and this is particularly evident moving from $S/r = 4$ to $S/r = 5$, where a final stable clogged situation is reached. For $S/r \geq 6$, indeed, no trapping occurs, and the difference shifting to greater S/r is less evident. The time required to reach a stable configuration decreases as soon as S/r increases, notably moving from a clogged to an unclogged situation, i.e. from $S/r = 5$ to $S/r = 6$.

Figure 7.29(b) illustrates data for different P/r values. As already revealed by simulations displayed in Fig. 7.29(a), it results that the variation of S/r remarkably influences both the amount of non-retained material and the time to reach a stable configuration. Nevertheless, these effects are less evident as S/r increases. In contrast, the wider the pile is, i.e. the greater the P/r, the more the material is entrapped. Furthermore, it results that the influence of the variation of P/r affects less the amount of non-retained material than varying S/r. For low P/r values, progressive clogging occurs, as revealed from the humps in the curves (Fig. 7.29(b)). Furthermore, the progressive clogging duration increases in time as P/r decreases, while the dependence of this phenomenon on S/r is less evident.

Figure 7.30 shows the ratio between the height of the arch (H_{arch}) and the height of the barrier (H_{bar}) as a function of S/r and P/r for all the carried out simulations. To compare with the single outlet barrier case, the Figure 7.30 reports also the results obtained in Sec. 7.2.2. In the multiple outlet barrier cases, no stable arch occurs
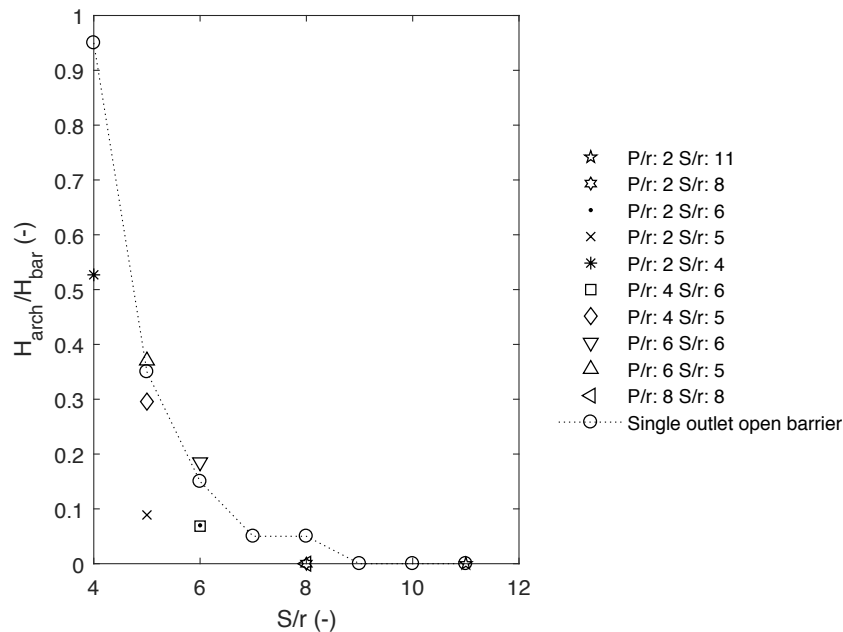
Fig. 7.30 Ratio between the height of the arch H_{arch} and the height of the barrier H_{bar} as a function of S/r and P/r for all the carried out simulations. The single outlet barrier case is also displayed for reference.

for $S/r \geq 8$, while the first clogged configuration appears for $S/r = 6$ with $P/r = 6$. Conversely, for the single outlet no arching is observed for $S/r \geq 9$. In agreement with the results previously obtained (Fig. 7.29), the height of the arches increases as soon as S/r decreases, also for small P/r (e.g. $P/r = 2$). It emerges that for $P/r \leq 5$, the height of the arches is lower than the height obtained in the single-outlet barrier with equal S/r. Conversely, for $P/r \geq 6$, the results are similar to those found for the single-outlet case. As a consequence, for $P/r \geq 6$ no mutual influence among two neighboring outlets is observed. In these cases, the slight difference observed among the results for equal S/r might be ascribed to modelling effects: the multiple outlets are scattered along the barrier width, while the single-outlet is centerd in the barrier.

Analysis of the impact forces

The performed simulations are analysed evaluating both the forces acting on the barrier and its efficiency in terms of energy dissipation. Also in this case, both the influence of S/r and of P/r are investigated. The forces are studied considering the maximum global force intensity found for the whole barrier. Also the spatial
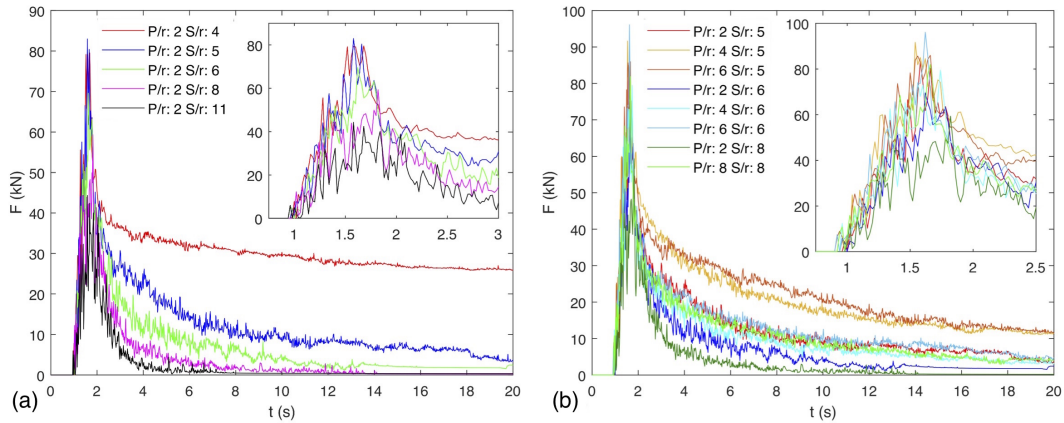
Fig. 7.31 Global resultant impact forces with respect to time, until a stable configuration of the mass is reached, and zoom of the dynamc phase: (a) $P/r = 2$, (b) grouped by same S/r (color range).

distribution of the forces is evaluated, both when the global maximum force occurs and when a stable static configuration is reached. Then, an envelope of the local maximum forces exerted during the dynamic phase is calculated. Moreover, since it is important for a hazard analysis purpose, the mean kinetic energy of the mass flowing through the outlets is evaluated and compared with the free-flow case.

Figure 7.31 plots the global resultant impact force exerted on the whole barrier $\mathbf{F}_G^R$ with respect to time for all the performed simulations. The intensity of the global forces refers to the whole barrier. As a consequence, for a constant domain width, the percentage of area covered by each barrier configurations is not the same. Thus, the forces in Fig. 7.31 cannot be directly compared in terms of magnitude, but only qualitatively. However, in the first few seconds of interaction (zooms in Fig. 7.31), the whole simulations sample reveals a common trend, with an instantaneous peak and a rapid decrease. Considering the decreasing part of the curves, instead, the trend depends on arching formation and on the amount of entrapped material. Table 7.4 reports the occurrence time t_{max}, the intensity of the maximum global impact, and the maximum local impact force $\mathbf{F}_{L,max}^R$ at the same instant, for all simulations. It emerges a good agreement in terms of both t_{max} and $\mathbf{F}_{L,max}^R$. In addition, analysing one by one the barrier configurations, it results that the values of $\mathbf{F}_G^{R,pile}$ of each pile of the considered barrier, obtained by summing up the local forces $\mathbf{F}_L^R$, divided by the area of the pile, i.e. the pressures on the piles, are substantially equal. This is not generally valid for the static case, in which forces are affected by the amount of deposited material. Comparing simulations with equal pile width, the $\mathbf{F}_G^{R,pile}$ (on a

single pile) have rather close value.

Figure 7.32(a) shows the distribution of the local forces when the global maximum force is reached. The cases with $S/r = 5$ are displayed, i.e. clogged situations, considering $P/r = 2$, 4 and 6, as representative cases, although all the results are commented. It emerges, indeed, that the overall response is quite similar in terms of distribution and intensity of the force for all the performed simulations with the same P/r. Similar trends are observed keeping constant the ratio S/r and increasing P/r, as reported in Fig. 7.32. From a qualitative point of view, for equal S/r, it appears that the larger the pile width is, the higher the forces in the neighbourhood of the outlet are. In addition, by increasing their width, a lower number of impacted areas is noted in the center of the piles. This can be explained by the fact that there is the possibility of creating arching configurations also behind the piles if their width is sufficiently large. The wider a pile is, the greater the number of possible grains involved in a arch is, and thus the forces exerted on the piles.

Considering the envelope of the maximum $\mathbf{F}_L^R$ observed during the dynamic phase (Fig. 7.33), the spatial distribution and the intensity are quite similar for all configurations. The local maximum values observed in the envelope, reported in column 5 of Table 7.4, are due to single grain collisions and are located in the lower half of the barrier, where the flowing mass firstly impacts.

Examining the situation when the mass is at rest, Figure 7.32(b) shows the spatial distribution of local static resultant forces $\mathbf{F}_L^R$ on the barrier. The numerical values of the global resultant force $\mathbf{F}_G^R$ and of the maximum local resultant impact forces occurring on the whole barrier $\mathbf{F}_{L,max}^R$ are reported in columns 4 and 3, respectively, of Table 7.4. In all the cases with equal S/r and varying P/r, an appreciable similarity is observed in the maximum $\mathbf{F}_L^R$ values. Nevertheless, as observed analysing the trapping efficiency, the amount of retained mass decreases as P/r decreases. Thus, $\mathbf{F}_G^R$ and the profile of the material deposited behind the barrier are different.

Analysis of the energy-breaking effect

In order to evaluate the reduction of the kinetic energy, the mean kinetic energy of the particles which have flown through the outlets (herein defined as "downstream of the barrier") is computed and compared with the values obtained in absence of barrier. Both translational and rotational kinetic energies are considered, according to Eq. (7.1), (Fig. 7.34). From Figure 7.34(a), which reports the simulation with the same
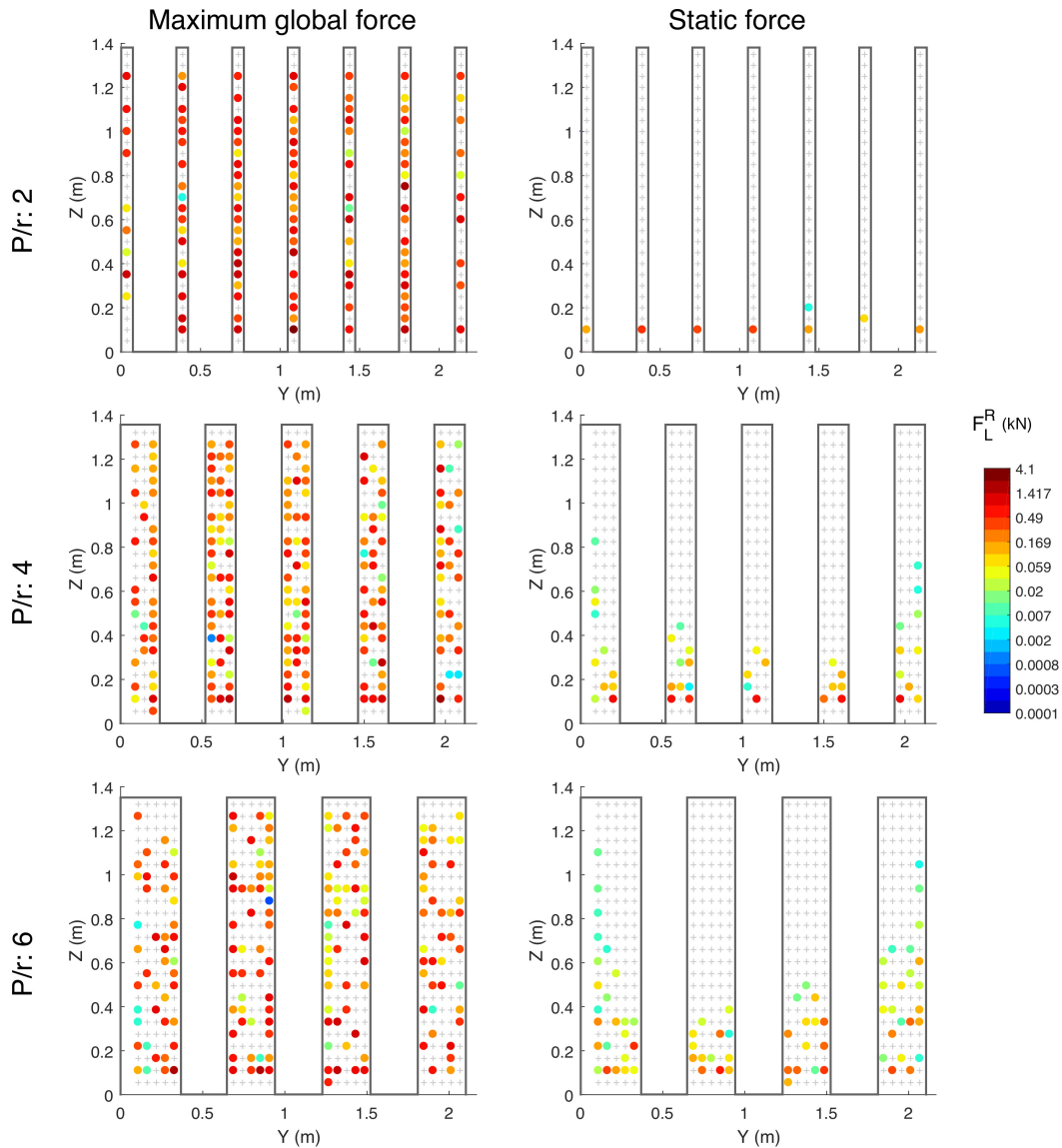
Fig. 7.32 Local forces on the barrier when (a) the maximum global impact occurs and (b) a stable static situation is reached, for $S/r = 5$ and different value of P/r. The dimension of the coloured points is not representative of the dimension of the grains. The colourbar is in logarithmic scale. The time of occurrence, the intensity of the maximum global resultant impact, and the maximum local impact force $\mathbf{F}^{R}_{L,max}$ in the same instant are reported in Table 7.4.
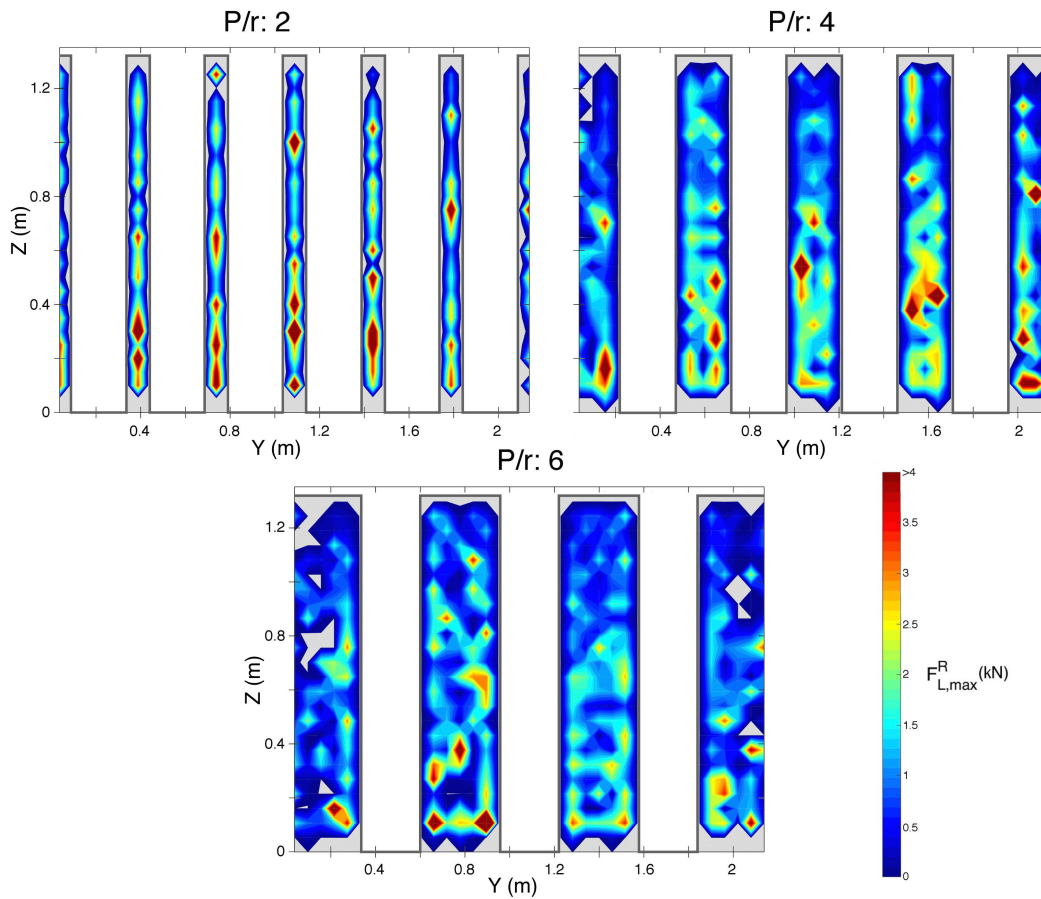
Fig. 7.33 Envelope of the maximum local resultant impact force $\mathbf{F}_{L,max}^{R}$ distribution during the dynamic phase of the motion, for $S/r = 5$ and different value of P/r. Grey areas in force distribution are due to arching of particles against the barrier face. The maximum $\mathbf{F}_{L,max}^{R}$ occurring in the whole barrier is reported in Table 7.4, as it constitutes an isolated case, over the limit of the colorbar.

Fig. 7.34 Mean kinetic energy downstream of the barrier with respect to time. (a) $P/r = 2$; (b) grouped by same S/r (color) and same P/r (line style).

Simulation	t_{max} (s)	$F^R_{G,max}$ (kN)	$F^R_{L,max}$ at t_{max} (kN)	max $F^R_{L,max}$ in the dynamic phase (kN)	$F^R_{L,max}$ at t_{end} (kN)	F^R_G at t_{end} (kN)
A	1.7	87.83	3.27	5.38	1.43	5.38
B	1.7	81.35	4.09	8.05	0.53	1.99
C	1.6	63.02	2.35	5.80	0.54	2.23
D	1.8	46.28	2.33	8.05	0.11	0.23
E	1.7	36.3	1.91	6.59	0.13	0.30
F	1.7	81.59	2.41	8.96	0.69	8.77
G	1.5	84.65	2.80	6.79	1.07	7.74
H	1.6	81.92	2.54	7.46	0.36	3.32
I	1.7	66.49	3.34	7.72	0.27	1.26
L	1.7	71.41	1.99	8.41	0.21	1.02

Table 7.4 Time and force values in the instants when $F^R_{G,max}$ is reached (t_{max}), during the dynamic phase, and when the static condition is reached (t_{end}), for each simulation (ref. to Tab. 7.3 for the simulation names).

$P/r = 2$, it emerges that the reduction of energy increases as soon as S/r decreases. This is confirmed also by other sectional barrier configurations (Fig. 7.34(b)). For $P/r = 2$, the curves are bell-shaped with an high peak value that lowers decreasing S/r. Considering the effects of P/r (Fig. 7.34(b)), it results that by increasing P/r the energy downstream of the barrier remarkably decreases. The curves tend to flatten, losing the marked bell shape and assuming a positive skew, i.e. with a long tail in the positive direction. Furthermore, in the limits of the performed simulations, a slightly greater influence of P/r rather than S/r in the flattening of the curve and energy reduction is highlighted. As an example, the configuration $S/r = 6$ and $P/r = 6$ lowers the kinetic energy peak value more than the one for $S/r = 5$ and $P/r = 2$. In the same way, for $S/r = 8$ and $P/r = 8$ the energy peak value is lower than with $S/r = 6$ and $P/r = 6$. It results that a variation of P/r has larger effects than a variation on S/r on the energy breaking downstream of the barrier. Trying to expand these observations to a wider range, at a channel slope scale, the mean kinetic energy downstream of the barrier is also analysed for $\theta = 30°$ and $\theta = 40°$ (small plots in Fig. 7.34(a) and (b)). All the results obtained for $\theta = 35°$, varying P/r and S/r, are evident also for $\theta = 30°$ and $\theta = 40°$. Furthermore, it emerges that increasing θ, the presence of a barrier enhances the temporal shifting of the peak value. In general, increasing θ, the scattering of the energy curves on the peak value

θ (°)	$\alpha(\theta)$ (-)	$\beta(\theta)$ (-)
30	0.95	-0.47
35	1.41	-0.85
40	1.91	-1.29

Table 7.5 Values of the α and β regression coefficients for the investigated slopes θ.

curve decreases and the positive skew of the curve is enhanced.

Since an influence of both S/r and P/r on the energy breaking effects is observed, an attempt to find a relationship between these two parameters and the mean kinetic energy downstream of the barrier is performed. A regression analysis is thus carried out. This can be considered as a preliminary analysis since the limited number of simulations might not constitute a representative sample for the problem. Among the possible interpolation functions that can suitably fit the problem, evaluating the goodness of fit indexes, a linear combination of the dependent parameters reveals to be the more appropriate for all the analysed θ values, i.e. $\theta = 30°$, $35°$ and $40°$. This results in a relation of the type:

$$\bar{E}_K = \alpha(\theta)\frac{S}{r} + \beta(\theta)\frac{P}{r} \tag{7.3}$$

Figure 7.35(a) displays the case of $\theta = 35°$. The value of α and β for each simulation are reported in Table 7.5. Fig. 7.35(b) plots the values of $\alpha(\theta)$ and $\beta(\theta)$ with respect to θ. An increasing linear trend is evident for α, while decreasing linear trend for β. In the limits of the available data, and of the range of θ investigated, two linear fitting relations are calculated for α and β, both as a function both θ.

$$\alpha(\theta) = 0.09\,\theta - 1.92 \tag{7.4}$$

$$\beta(\theta) = -0.08\,\theta + 2.01 \tag{7.5}$$

The proposed Eqs. (7.3), (7.4) and (7.5) are limited to the range $\theta = 30° - 40°$.

7.4   Concluding remarks

Considering the slit barrier case as the starting configuration for setting the reference parameters and analysing the influence of normalised pile width (P/r) and opening width (S/r) on both trapping and interaction forces in sectional barriers, it reveals
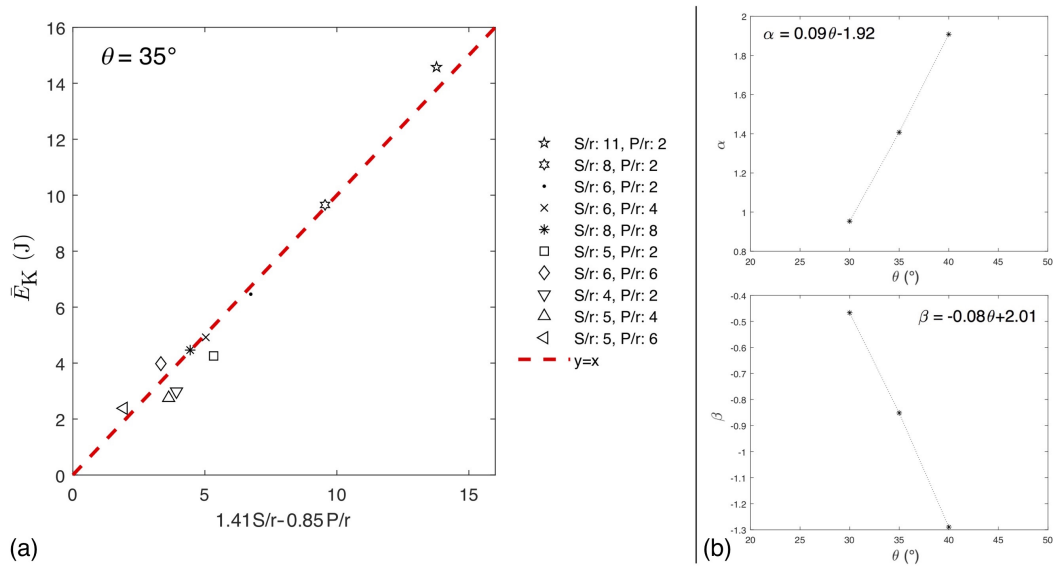
Fig. 7.35 (a) Regression analysis with a linear analytical function among the dependent parameter $\bar{E}_K$ and the independent parameters S/r and P/r for $\theta = 35°$.(b) The coefficients of the analytical function α and β are plotted with respect to the slope angle θ.

that the results on the two barriers configurations (slit and sectional) are consistent. In both cases, the influence of the opening size on the trapping efficiency is evident: the probability of clogging decreases increasing S/r. The shifting between a completely clogged to a no-clogged situation passes through a transition stage of progressive clogging. All these effects are enhanced by the presence of multiple outlets, which affects the probability of stable arching, lowering of about one radius the opening width boundary between a completely and progressively clogged situation and to an unclogged situation. However, increasing P/r up to ~ 6 no difference between the two configurations is observed. The results obtained are in good agreement with those found by Mondal and Sharma (2014), who simulated the discharge of a granular monodisperse mass into a vertical silos, whose rectangular base consists of two rectangular outlets, and found that arches do not influence each other anymore for $P/r \geq 6$. Nevertheless, their results related to a slope of $\theta = 90°$ and the only $S/r = 3$ and 4 were considered.

Comparing the forces, a common trend can be highlighted both for the slit and the sectional cases. The time-histories of the forces exerted by a flowing mass on the barrier shows a high peak value in the first instants of the impact and then a rapid decrease. A stable configuration is reached at different times, depending on the clogging capability of the barrier; the intensity of the forces on the static

condition depends on the amount of mass deposited behind the barrier. Concerning the spatial distribution of the forces at the impact, the local maximum values are in the lower half of the barrier, where the mass first impacts. Also in the neighbourhood of the outlets high magnitude forces are recorded; this effect is more noticeable when S/r increases, causing an increment of the mass passing through the outlets. The formation of stable arches is observed both on slit and sectional barriers. The presence of this equilibrium configuration depends on the ratio P/r, appearing for $P/r = 4$ in sectional barriers. Furthermore, it is noted that the energy breaker function is also guaranteed in sectional barriers too, depending on both S/r and P/r.

Chapter 8

Trapping efficiency and impact forces: more complex models

In chapter 7 the dynamics of interaction with an open barrier of a monosized dry granular material flowing along a channel was described. While some interesting insights on the clogging mechanisms and on the impact forces emerge, the adopted basic assumptions are far from being realistic.

As a consequence, this chapter presents an improved study by weakening the monosized dry granular assumption. In one case, from here on called "bidisperse case", a bidisperse dry granular material is considered; in the other, from here on called "solid-fluid case", an additional phase made either of fine grains or water is included. The results obtained in the previous chapter provide the geometrical setup, e.g. S/r, in which a monophase dry granular material of radius r is completely retained. Thus, the purpose of the simulations presented and discussed in the following is to evaluate the influence of either bidispersion or of a fluid on the trapping efficiency of the barrier and on the forces exerted on it. This two modelling approaches are to some extent complementary: even though the mechanisms differ, the effects of small particles in the bidisperse case are similar to the ones of the fluid in the solid-fluid case. Since, in the former case, the bidispersion is in terms of grain size, from here on, the terms bidisperse and bisized are alternatively used, as well as monodisperse and monosized.

Small particles, as well as the fluid phase, represent the material that should be filtered by the barrier. That is why, from here, it will be defined as "unretained material". Instead, the monosized dry granular of Ch. 7 represents the coarse material

that has to be trapped, i.e. from here "retained material". It is worth mentioning that the additional unretained material can also be trapped if the retained material clogs the barrier. In this case, the outlet of the barrier is totally or partially clogged by large particles and the voids among the particles are not large enough to allow small particles to pass through. This can occur for both bidisperse and, if a non-Newtonian rheology is adopted, fluid solutions. In real cases, this mechanisms induces the clog of progressively finer sediments behind the barrier, while water leaks out during time. Thus, due to this complex interaction process, the behaviour of the mixture is investigated instead of the behaviour of the two phases, independently.

Considering the results obtained in the previous chapter, the adopted slope angle and ratio between retained phase mean radius and outlet size S/r are such as to provide a complete trapping of the considered retained material in absence of bidispersion of a fluid phase. Thus, the influence of the additional material on both trapping efficiency and impact forces is evaluated. The geometry of the domain and numerical parameters of the simulations presented in the following are equal to the ones adopted in the previous chapter (Tabs. 7.1 and 7.3).

The bidisperse case is illustrated in Sec. 8.1, both with the slit (Sec. 8.1.1) and the sectional (Sec. 8.1.2) barrier configurations. Sec. 8.2 deals with the solid-fluid case, only in the slit barrier configuration. Modelling the fluid, two different rheologies are adopted: Newtonian and Bingham.

8.1   The bidisperse case

This section deals with the presence of bidispersion in grain size, simulated by means of a dry granular material smaller than the primary phase, i.e. the retained phase. This results in a bidispersion in terms of grain size in the granular mass. The radius of the large particles is R, while the radius of the small particles is r. The total volume of the small particles is $V_{s,small}$, while $V_{s,tot}$ is the total solid volume, which is kept constant across all the simulations and equal to the one adopted for the monosized analyses presented in the previous chapter. The density and the numerical inputs parameters of the two phases are the same. In this way, maintaining an equal discharged weight, it is possible to compare the results with the monosized case. Different small-to-large volume fractions, identified in terms of the ratio $\Phi_{small} = V_{s,small}/V_{s,tot}$, are investigated. Using this notation, $\Phi_{small} = 0$ denotes simulations with only large
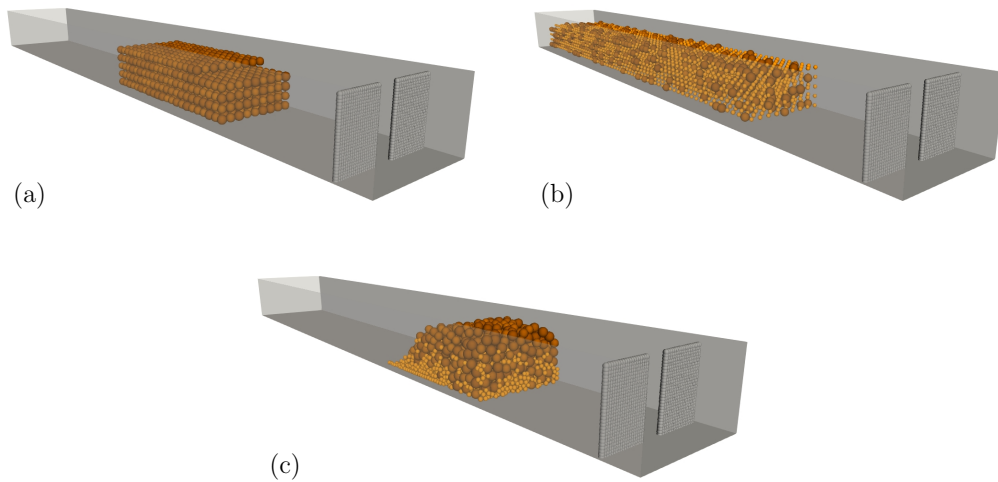
Fig. 8.1 Example of particle initial distribution at the low-compacted situation for (a) $\Phi_{small} = 0$, (b) $\Phi_{small} = 0.3$, and (c) the highly-compacted situation with $\Phi_{small} = 0.3$ of the carried out numerical analyses with a slit barrier. In the last case the particles segregated.

particles, while $\Phi_{small} = 1$ simulations with only small particles. That is, these configurations represent monosized cases. The outlet width S is normalised with R, in order to maintain the geometrical reference parameters found for the monosized grains. The considered channel slope angle θ is $35°$.

The initial configuration of the released mass is constituted by a regular assembly of grains, in which the distance between the centers of two adjacent particles is equal to a large particle diameter (adding a deviation of $5\%R$) as illustrated in Fig. 8.1(a) and (b). This results in a lower compaction with respect to the initial configuration of the monosized case, Fig. 8.1(a), where the whole assembly has mean radius equal to R. The distance between the front of the released mass and the barrier is equal to the one adopted for the monosized case (Fig. 7.2).

These preliminary analyses constitutes an attempt to generalise the obtained results and to numerically model the variability of real debris flow events. As a consequence, the influence of the variability of various important parameters, e.g. the particles size, the ratio between large and small particle radii R/r, the initial discharging configuration, and the small particles volume fraction Φ_{small} is considered albeit only qualitatively. As shown in the following, various different configurations, in term of particle radii, initial compaction degree, and amount of small particles are simulated.

8.1.1   Slit barriers

For the slit barrier cases, three different configurations are considered accounting
for the variability of the R/r ratio and for the initial configuration of the discharged
mass. As the time step of the simulations is proportional to the minimum radius (Eq.
(5.14)), to reduce the computing efforts, the adopted radius of the large particles R is
either 10 cm or 12.5 cm and the radius of the small particles r is either 5 cm or 7.5
cm, respectively. Thus, the ratio R/r is not constant.

   For the configuration R/r=(10cm/5cm)= 2, two initial arrangements are con-
sidered. Besides the regular assembly described above (Fig. 8.1(a) and (b)), from
here named as "low-compacted", an additional and more compacted initial condi-
tion is considered, namely "highly-compacted" (Fig. 8.1(c)). In order to model the
highly-compacted configuration, a preliminary simulation with a low-compacted
configuration discharged against a closed barrier is performed. The closed barrier
has the same geometry of the open one, and it is positioned upstream the open one,
just in front of the released mass. Simulations end when a stable configuration is
reached. The obtained deposited mass behind the closed barrier, removing then the
closed barrier, is adopted as the initial configuration for the simulations with the
only open barrier. The distance between the front of the discharged mass and the
open barrier is equal to the one of the low-compacted case. The highly-compacted
initial situation reveals the presence of a kinetic sieving mode of segregation, i.e.
separation of particles occurs according to size. As a result of local fluctuations, in
the porosity of the flowing mass internal voids are produced, which are in turn filled
with particles under the influence of gravity (Marks and Einav, 2011); the degree of
segregation is a function of the degree of agitation of the flow. According to Marks
et al. (2012), this can increase the destructive power of the flow, i.e. the impact forces
expected in the highly-compacted case are greater then in the low-compacted case.
Nevertheless, a deep investigation on the influence of segregation on the results is
beyond the purposes of this study.

   In summary, three configuration are considered:

- $R = 12.5$ cm, $r = 7.5$ cm, $R/r = 1.67$, low-compacted.

- $R = 10$ cm, $r = 5$ cm, $R/r = 2$ low-compacted.

- $R = 10$ cm, $r = 5$ cm, $R/r = 2$, highly-compacted.

For ease of reference $R_{12.5}/r_{7.5}$ denotes the case with $R = 12.5$ cm and $r = 7.5$ cm, while R_{10}/r_5 the one with $R = 10$ cm and $r = 5$ cm. The barrier has a normalised opening width S/R equal to 4. In the monosized case this value guarantees a complete clogged condition, retaining almost the whole mass by the barrier.

For all these three configurations, the simulations are performed with different percentage of small particles, i.e. with a small-particle volume fraction Φ_{small} ranging from 0 to 1, with steps of 0.1. As already stated, the total solid volume is preserved and kept equal to the monosized analyses.

In the following, the results are discussed with reference to the trapping efficiency of the barrier and the forces exerted on it by the flow.

Analysis of the trapping efficiency

The effects of bi-dispersion on the trapping efficiency are evaluated considering the amount of non-retained material with respect of the solid volume fraction of small particles Φ_{small}.

Figure 8.2 resumes the results for the three configurations, differing for initial conditions and R/r. A general trend can be observed: for $0.0 \leq \Phi_{small} \leq 0.7$, the non-retained material fraction is ≤ 0.4, and a considerable amount of material is retained by the barrier. For $\Phi_{small} > 0.7$ the non-retained material fraction arises abruptly. It results that $\Phi_{small} = 0.7$ represents the threshold value from a high-trapping condition to a low-trapping one. The differences between results obtained in different initial configurations are marginal and can be attributed to the random variability associated with the problem. Due to the limited number of simulations, a quantitative parametric analysis cannot be performed. Due to the lack of a representative comparative sample, the effects due to the variation of the grain sizes and of R/r cannot be separated and properly considered in the two low-compacted cases, which, despite these variables, reveal a common trend. In addition, for all analyses, the variability of the initial conditions seems not to affect the results in terms of trapping efficiency. Nonetheless, the main difference among these results lies in the fact that only in R_{10}/r_5 low-compacted case no clogging is observed for $\Phi_{small} = 0.9$ and 1. However, for $\Phi_{small} = 1$ the normalised outlet width S/r is equal to 8 for the R_{10}/r_5 case and 6.6 for the $R_{12.5}/r_{7.5}$ case. Considering the results of Ch. 7 on monodisperse cases, with this S/r, i.e. $S/r = 8$ and 6.6 respectively, the former situation does not clog, while for the second a low arch forms late in time. Consequently, the results obtained are
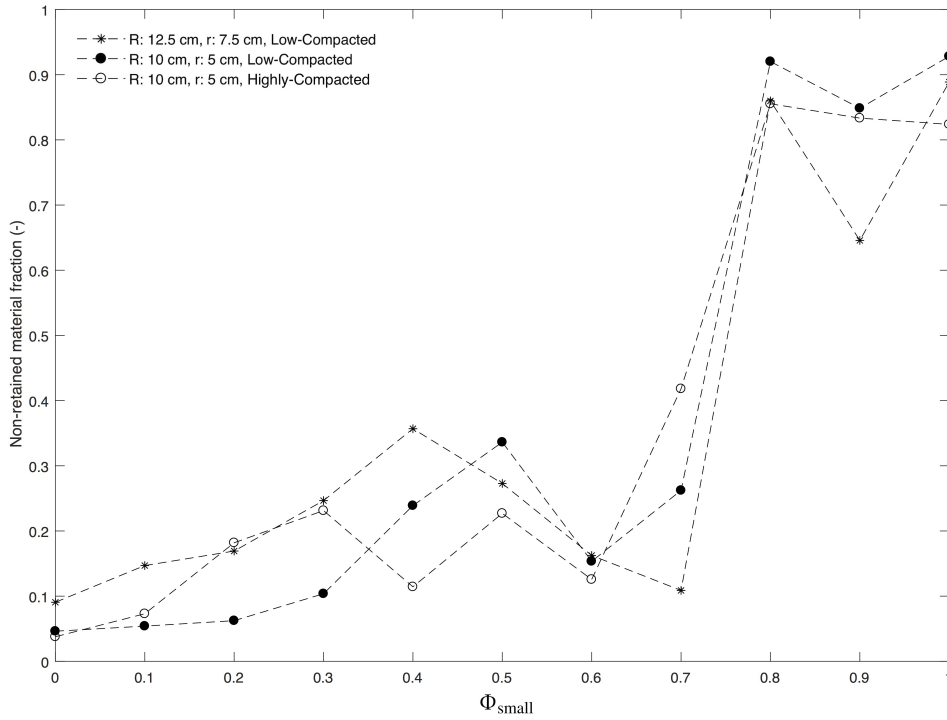
Fig. 8.2 Non-retained material fraction with respect to the solid volume fraction of small particles Φ_{small}, for the different simulated configurations.

consistent with the previous findings. On the contrary, a clogged condition occurs for R_{10}/r_5 highly-compacted case. Although differing from the monosized condition, this result seems to be ascribed mainly to random variability or to segregation history. However, the performed simulations are not enough in number to investigate this aspect.

With the main goal to compare the results with the monodisperse case, Figure 8.3 displays the non-retained material fraction with respect to an "equivalent radius" r^*, which stands for the radius that would have an equivalent monosized mass with same volume. As the total volume is preserved in all the simulations regardless of Φ_{small}, the equivalent radius is calculated by averaging R and r weighed to the volume fractions $\Phi_{\text{large}} = V_{\text{s,large}}/V_{\text{s,tot}}$ and Φ_{small}, respectively, that is:

$$r^* = \sqrt[3]{\Phi_{\text{large}}R^3 + \Phi_{\text{small}}r^3},\qquad(8.1)$$

where $\Phi_{\text{large}} = 1 - \Phi_{\text{small}}$. The plot demonstrates that the transition from a high-trapping to a low-trapping configuration occurs for $S/r^* \simeq 5$. Interestingly, the value
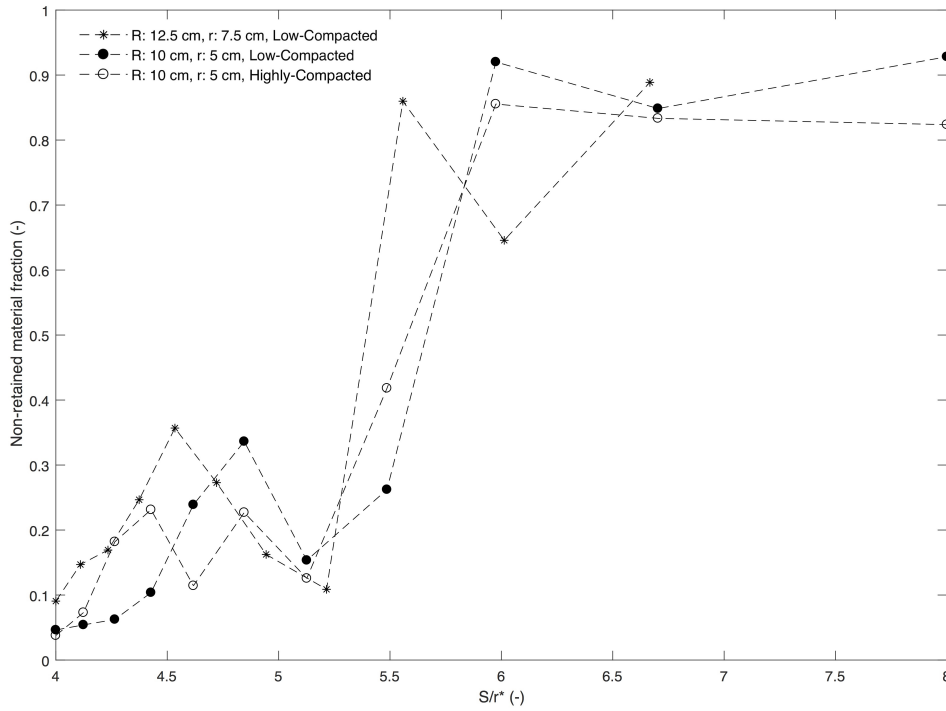
Fig. 8.3 Non-retained material fraction with respect to the equivalent radius r^*, for the different simulated configurations.

$S/r \simeq 5$ represents the threshold value from a high- to a low-trapping configuration also in a "true" monodisperse case, as discussed in Ch. 7. For $S/r \simeq 5$, indeed, in the steep slope cases, i.e. $\theta \geq 30°$, a progressive clogging phenomenon is observed.

Analysis of the impact forces

The evaluation of the effects of the bidispersion on the impact force is performed by comparison with the global force obtained in the monosized case. The influence of a progressively increasing fraction of small particles is investigated.

Figure 8.4 illustrates the global resultant force as a function of time, related to the first arrival time t_0, for Φ_{small} ranging from 0 to 1. It reveals that the bidispersion lowers the maximum value of the impact force for all the performed simulations. This tendency appears for the whole range $0.1 \leq \Phi_{small} \leq 0.9$, i.e. with no apparent influence of the amount of small particles. Considering the case R_{10}/r_5 highly-compacted configuration, the maximum force value occurs almost at the same time across all the performed simulations at different small-to-large fractions. Figure 8.5 represents the impacting mass at time $t = 1$ s, for $\Phi_{small} = 0.2$, 0.5, and 0.8

(Fig. 8.5(a), (b), and (c), respectively). The picture evidences similar trend for all the different small-to-large fractions, with comparable velocities of the front and flow height. On the contrary, for both the low-compacted cases, for $\Phi_{small} \geq 0.1$, the maximum force value occurs after a considerable time lag in comparison with $\Phi_{small} = 0$. Furthermore, this time lag increases by increasing Φ_{small}. This is due to the way adopted for creating the initial configuration in the low-compacted case: for larger Φ_{small}, the distance between the barrier and the rear of the initial assembly increases, and this affects the arrival time of the flowing mass against the barrier. Thus, despite the lack of a representative comparative sample of simulations, it emerges that the initial particles compaction and disposition affect the results.

Figure 8.6(a) shows the global resultant maximum force as function of Φ_{small}, for the different simulated configurations. As observed in Fig. 8.4, it results that the presence of bidispersion lowers the global force maximum value, independently from the percentage in volume of small grains. Compared to the monosized situation $\Phi_{small} = 0$, this reduction is much more evident for the low-compacted cases, while in the highly-compacted case the force reduction is less pronounced. Considering the highly-compacted case for $\Phi_{small} = 0$, the maximum value is considerably lower than in the low-compacted cases, while in both low-compacted simulations, the maximum values are quite similar. This can be explained by considering that, in the low-compacted condition, the center of gravity of the discharged mass is higher than in the highly-compacted, as well as the potential energy of the initial mass. For $\Phi_{small} \geq 0.1$, this tendency also occurs, but it is less pronounced. Even if the center of gravity of the released mass is higher for the low-compacted case rather than in the highly-compacted one, in fact, the presence of small particles (that are placed more distant one to the other) promotes, at the discharge, the fall on the basal surface rather than collisional forces between grains. It results in a thin and long flowing mass. By consequence, it results that in the monosized case the influence of the initial compaction condition considerably affects the global maximum value of the force. On the contrary, results show that the influence of the size of the particles is less pronounced: for $\Phi_{small} = 0.0$ similar maximum force value are obtained for both $R_{12.5}/r_{7.5}$ and R_{10}/r_5. In the bidisperse case, i.e. $0.1 \leq \Phi_{small} \leq 0.9$, this aspect cannot be properly evaluated as the R/r value differs between the two cases.

The effects of Φ_{small} on the time when the global maximum force is recorded are considered. With reference to Fig. 8.6(b) for the low-compacted case, the time lag between the first contact and the maximum impact force increases by increasing
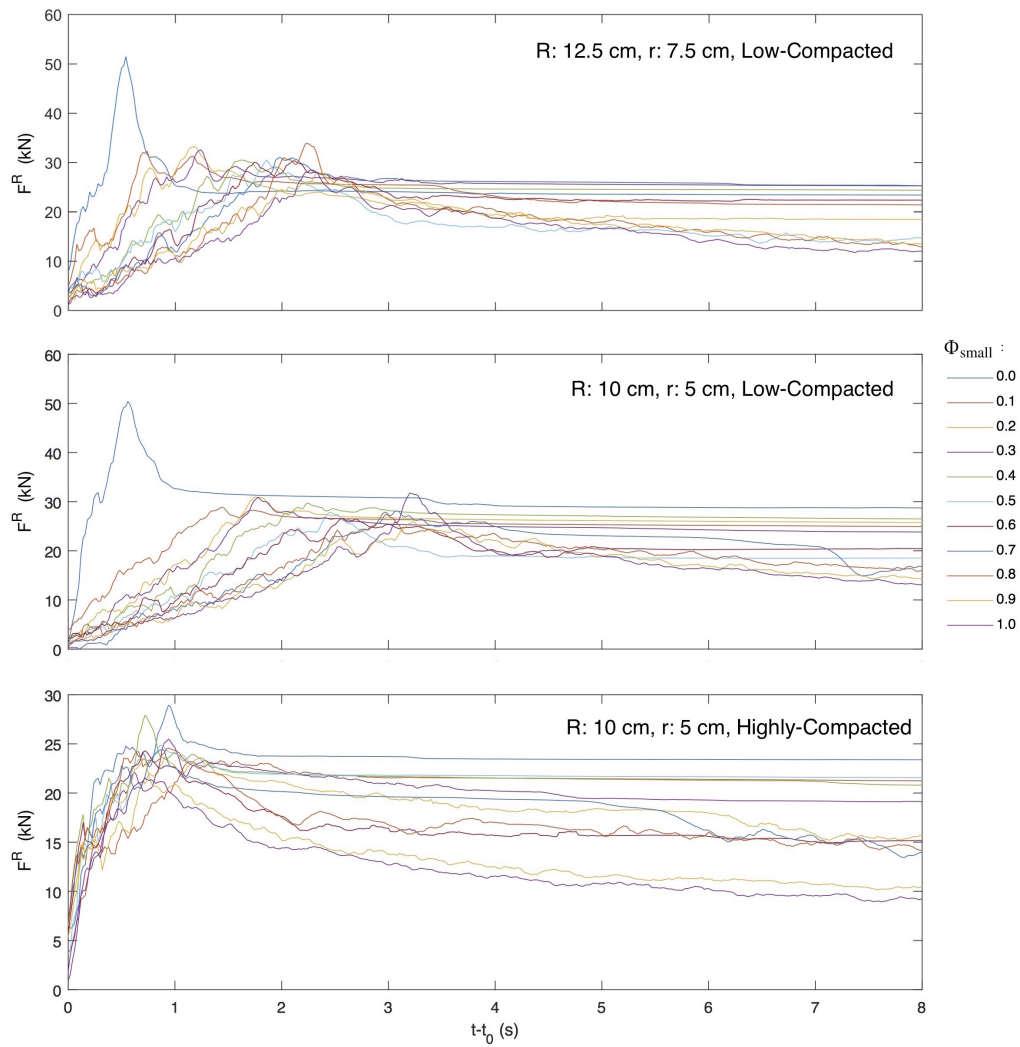
Fig. 8.4 Global resultant force as a function of time, calculated with respect to the first arrival time t_0, for Φ_{small} for the different simulated configurations.
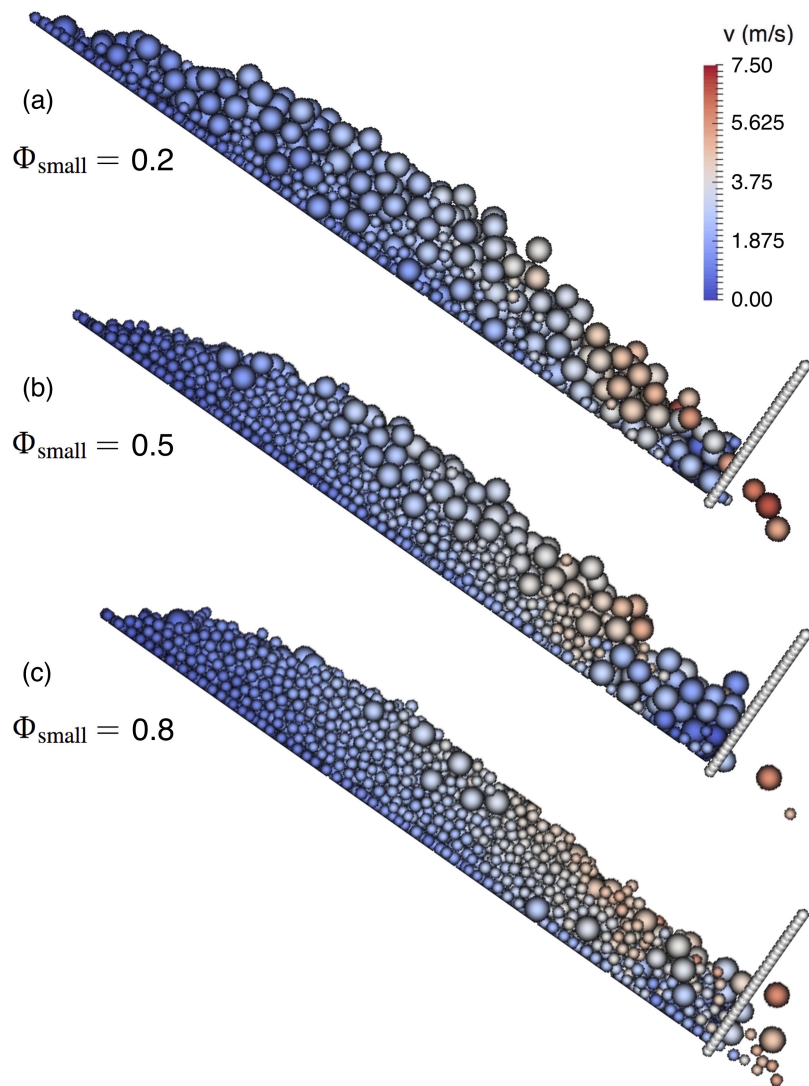
Fig. 8.5 Sketch of the flowing mass impacting against the barrier at time $t = 1$ s, for (a) $\Phi_{\text{small}} = 0.2$, (b) $\Phi_{\text{small}} = 0.5$, and (c) $\Phi_{\text{small}} = 0.8$, with $R = 10$ cm, $r = 5$ cm in the highly-compacted case. A colour scale as function of velocity is adopted.

Φ_{small}. Conversely, in the highly-compacted case, the time at which the maximum occurs are quite close to each other. Comparing the two low-compacted cases, a higher lag occurs for $R_{12.5}/r_{7.5}$. Considering the monosized case, it results that small particles impact later in time with respect to large particles. Finally, Figure 8.6(c) displays the value of the global force when a stable configuration is reached. As expected, the observed trend of the forces is opposite to the one illustrated in Fig. 8.2: the higher Φ_{small} is, the lower the clogging probability is and thus the amount of mass deposited behind the barrier. The only difference appears for $\Phi_{\text{small}} = 0$. While the non-retained material fraction does not depend on the initial configuration, the value of force in the static condition is lower for the highly-compacted case, as already observed for the global maximum force value.

From all these results, it results that, compared to the monosize case, the presence of bidispersion decreases the maximum impact force, almost independently from the amount of small particles. Furthermore, in the monosized case, the influence of the initial configuration is relevant: the higher the center of gravity of the released mass, the higher the potential energy that turns into kinetic energy.

8.1.2   Sectional barriers

The here discussed configurations extend the already performed simulations to the case of sectional barriers. The three considered barrier configurations are those already adopted in Sec. 7.3; normalising the parameters with respect to the particles with radius equal to 5 cm (indicated with r_5), it results:

- $S/r_5 = 4$ and $P/r_5 = 2$ (A in Tab. 7.3).

- $S/r_5 = 5$ and $P/r_5 = 6$ (F in Tab. 7.3).

- $S/r_5 = 8$ and $P/r_5 = 8$ (L in Tab. 7.3).

These configurations correspond to a completely trapped, a partially trapped, and a no-trapped configurations in the monosized case, respectively. Three different R/r and Φ_{small} are considered and compared to the monosized case (named "M"):

- 80% $R = 5$ cm and 20% $r = 2.5$ cm (named "B1").

- 50% $R = 10$ cm and 50% $r = 5$ cm (named "B2").

(a)

(b)

(c)

Legend:
- – * – R: 12.5 cm, r: 7.5 cm, Low-Compacted
- – ● – R: 10 cm, r: 5 cm, Low-Compacted
- – ⊖ – R: 10 cm, r: 5 cm, Highly-Compacted
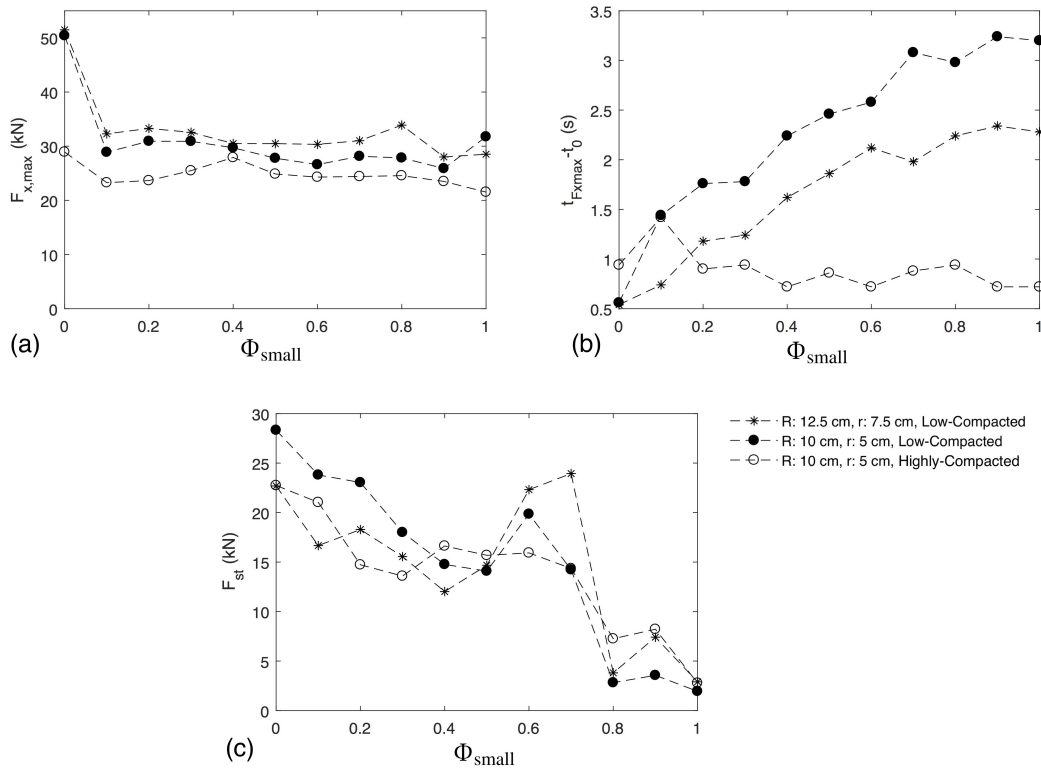
Fig. 8.6 (a) Global maximum force, (b) time of occurrence, and (c) global force in the static situation, as function of Φ_{small}, for the different simulated configurations.

- 20% $R = 10$ cm and 80% $r = 5$ cm (named "B3").

Table 8.1, in the first column, reports the complete lists of the performed simulations. A low-compacted initial configuration is adopted for sectional barrier simulations, detailed in Secs. 8.1 and 8.1.1. For all the different variables introduced (i.e. solid volume fraction, R, r, and sectional barrier configurations) the trapping efficiency and the impact forces are discussed, only from a preliminary point of view.

Analysis of the trapping efficiency

The trapping efficiency in the bidisperse case with a sectional barrier configuration is here evaluated in terms of non-retained material fraction. Table 8.1 lists the geometrical parameters as well as the resulting non-retained material fraction for all the considered cases. Also the monosized cases are reported. For example, configuration A-B1 is a $S/r_5 = 4$, $P/r_5 = 2$ sectional barrier impacted by a 80%

Config.	S/r_5 (-)	P/r_5 (-)	R (cm)	r (cm)	Φ_{small} (-)	Non-retained material fraction (-)
A-B1	4	2	5	2.5	20%	0.99
A-M	4	2	-	5	100%	0.54
A-B2	4	2	10	5	50%	0.09
A-B3	4	2	10	5	80%	0.19
F-B1	5	6	5	2.5	20%	0.99
F-M	5	6	-	5	100%	0.73
F-B2	5	6	10	5	50%	0.06
F-B3	5	6	10	5	80%	0.08
L-B1	8	8	5	2.5	20%	0.99
L-M	8	8	-	5	100%	0.98
L-B2	8	8	10	5	50%	0.94
L-B3	8	8	10	5	80%	0.97

Table 8.1 Geometrical, initial parameters and non-retained material fractions for all the performed simulations.

$R = 5$ cm and 20% $r = 2.5$ cm mass. Figure 8.7 displays the final configurations for all the performed simulations. This picture permits to qualitatively assess if clogging occurs or is promoted by large or small particles. Considering the B1 mixture, only in the barrier types A and F a low-arch late clogging occurs, and only few particles are retained. In the A-B1 configuration, arching occurs in 5 of the 7 outlets, involving only one layer of small particles, while in the F-B1 a layer of large particles clogs the central outlet. In the L-B1 configuration, no arching occurs. As a consequence, a slight inverse grading phenomenon can be observed in the A-B1 configuration: the clogging particles are the ones that compose the tail of the flow, i.e. the small ones. Referring to the B2 mixture, it results that for the A-B2 and F-B2 configurations, the presence of particles with $R = 10$ cm considerably increases the amount of retained material. In these configurations, almost the whole mass clogs with a ratio $H_{arch}/H_{bar} \simeq 1$. This effect is due to the inverse grading phenomenon (Sec. 2.3.2): large particles reach the front and clog the barrier, as the relative outlet size S is very low (i.e. 1 and 1.5 times the diameter of the large particles, respectively). In the L-B2 configuration a low-arch late clogging occurs, involving only small particles and retaining only a small amount of particles. This result is similar to the A-B1 configuration, where, a single layer arch involving small particles clogging verifies.
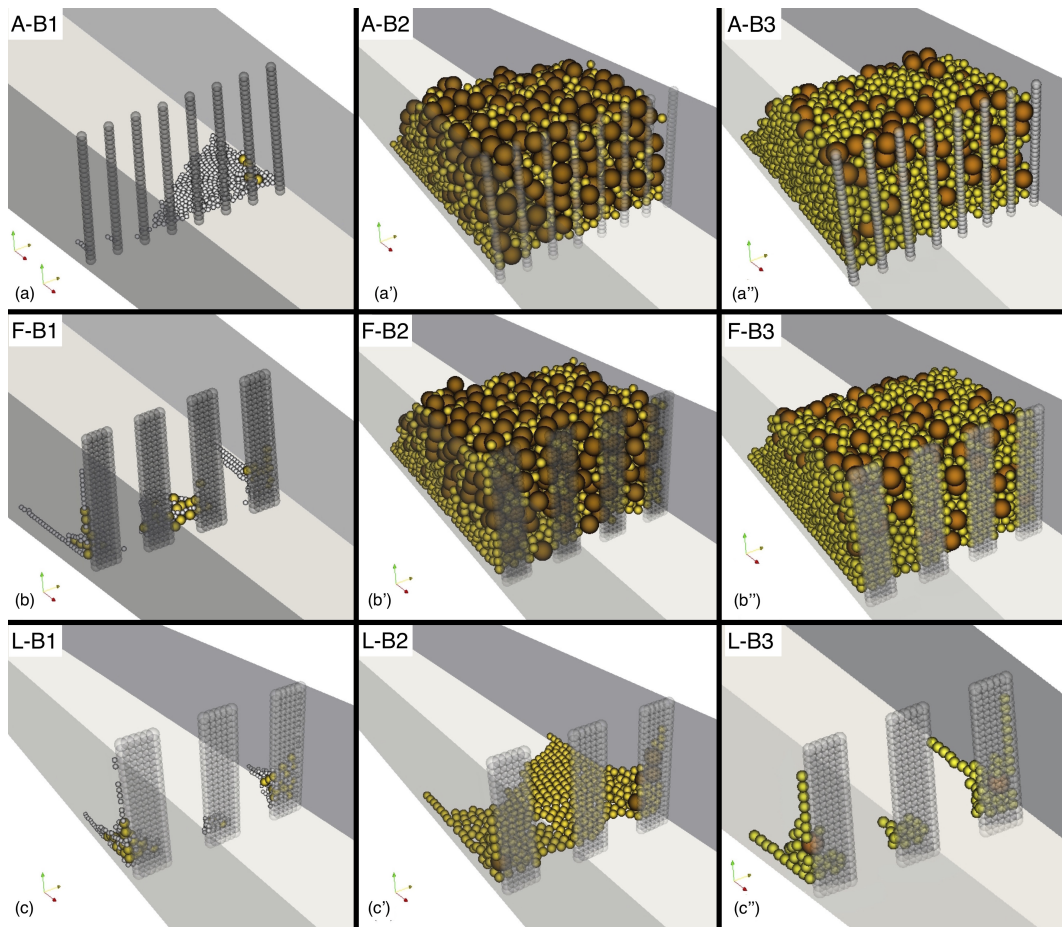
Fig. 8.7 Final configurations for all the bidispersed simulations.

Referring to the B3 mixture, the trend is very similar to what observed for the B2 mixture. In the A-B3 and F-B3 configurations, the amount of retained material is very close to the one of the correspondent barrier configurations with B2 mixture, i.e. almost the whole mass is retained. Despite the fact that an inverse grading phenomenon is observed also for the B3 mixture, the retained situation involves both small and large particles. It emerges that, for these outlets sizes, the presence of large grains promotes the clogging of the mass, almost irrespective of their amount. This is in line with what observed in Sec. 8.1.1. Considering the equivalent radius r^* defined in the silt barrier case (Sec. 8.1.1, Fig. 8.3), the outlet size of the A barrier configuration corresponds to an $S/r^* \simeq 2.5$ or 3 for the B2 and the B3 mixtures, respectively. In the case of the F barrier configuration, the outlets size corresponds to an $S/r^* \simeq 3$ or 4 for the B2 and the B3 mixtures, respectively. In the slit barrier case, for these $S/r*$ values, the impacting mass is almost completely retained. In the L-B3 configuration, no arching occurs; however, the amount of retained mass is similar to the one related to the other mixtures. For A-B1, L-B2, and L-B3 it results that $S/R = 4$ and $S/r = 8$. By comparison, in the monosized case, where only r appears, for $S/r = 4$, a higher arching effects is observed. Considering all the results, it emerges that when small particles are added (i.e. A-B1, L-B2, L-B3), the trapping capacity reduces. It has to be noted that, in the monosized case and in the specific case of barrier type L, i.e. $P/r = 8 \geq 6$, no differences in terms of trapping efficiency between slit and sectional barriers are observed. In the bidisperse case, the slit barrier with R_{10}/r_5 and $\Phi_{small} = 0.5$ and 0.8 can be compared with the L-B2 and L-B3 configurations, respectively. Considering the trapping efficiency (Fig. 8.2 for the slit barrier and Fig. 8.7 and Tab. 8.1 for the sectional barrier), a considerably lower amount of material is retained in the sectional barrier case rather than in the slit barrier one. It results that the combination of both bidispersion and sectional barrier geometry lowers the clogging probability.

The inverse grading phenomenon, qualitatively observed on Fig. 8.7, is an important aspect in the clogging mechanisms and, thus, for the trapping efficiency, Figure 8.9 displays, for the B2 mixtures, the volume fraction $V_{s,large}/V_{s,tot}$ with respect to the X-direction of the deposited mass. This ratio is evaluated in the three different sub-volumes (Fig. 8.8), that is the Z-direction is subdivided in three intervals, i.e. $0 \leq Z \leq 0.45$, $0.45 < Z \leq 0.9$, and $0.9 < Z \leq 1.35$, spanning the whole domain in the Y-direction. The amount of large particles is evaluated at intervals of 25 cm (at a distance slightly grater than one particle size) in the X-direction. Given
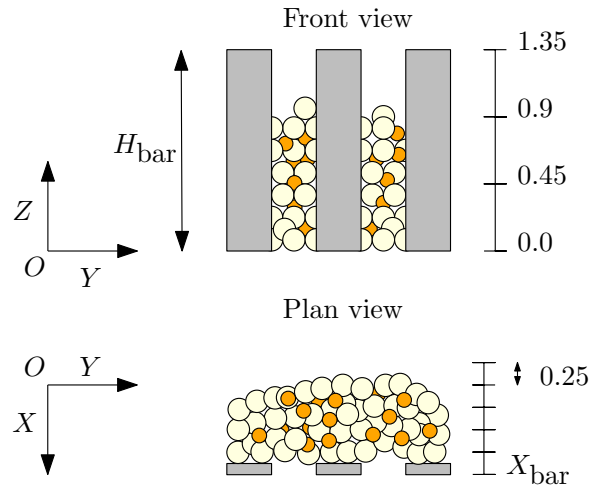
Fig. 8.8 Sketch of volume subdivision for computing the amount of large particles with respect to the total volume.

a Z range and a position behind the barrier, a volume (of about $0.25 \times 2.10 \times 0.45$ m^3 in X-, Y and Z-directions) is identified. $V_{s,large}$ and $V_{s,tot}$ are the volume of large particles and the total volume, respectively, computed only in the considered sub-volume. As a consequence, it results $V_{s,large}/V_{s,tot} = 1$ if in the identified volume large particles only are present. In the A-B2 case the barrier is clogged. In the $0 \leq Z \leq 0.45$ interval, near the barrier, $V_{s,large}/V_{s,tot} = 0.5$, while it increase to 0.75 and 0.80 for $0.45 < Z \leq 0.9$ and $0.9 < Z \leq 1.35$, respectively. This means that, just behind the barrier, the largest part of the mass is made of around 80% in volume of large grains, i.e. $V_{s,large}/V_{s,tot} \simeq 0.8$. A similar trend is observed for the F-B2 case (Fig. 8.9), with 0.45, 0.85 and 0.75 $V_{s,large}/V_{s,tot}$, for increasing Z-intervals. On the contrary, for the L-B2 case, where only a low arch clogging verifies, for the lowest Z-interval almost only small particles stops behind the barrier. In the second Z-interval, the greater $V_{s,large}/V_{s,tot}$ value, equal to 0.75, refers to the large grains deposited behind the piles and no arching verifies (Fig. 8.9).

During the flow, small particles are pushed in the lower part and in the tail of the flowing mass. Thus, the basal friction plays an important role in the stopping mechanisms of such particles, while large particles flow through the outlets. Despite the number of parameters involved in the simulations being large, the present results give interesting insights into the possibility of numerically reproducing debris-flow phenomena.
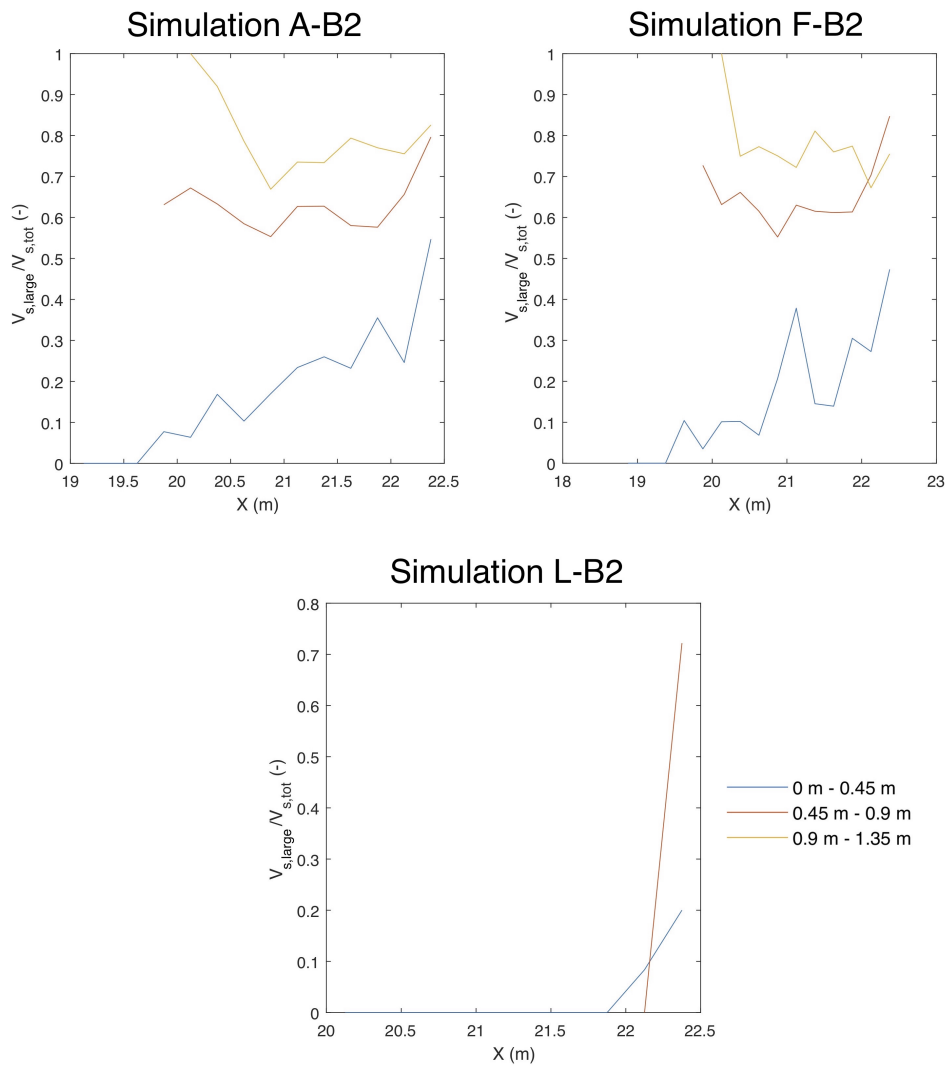
Fig. 8.9 Simulations with 50% $R = 10$ cm and 50% $r = 5$ cm (B2). Amount of large particles (in volume) with respect to the total solid volume on each subsection. The barrier is set at X=22.5 m.
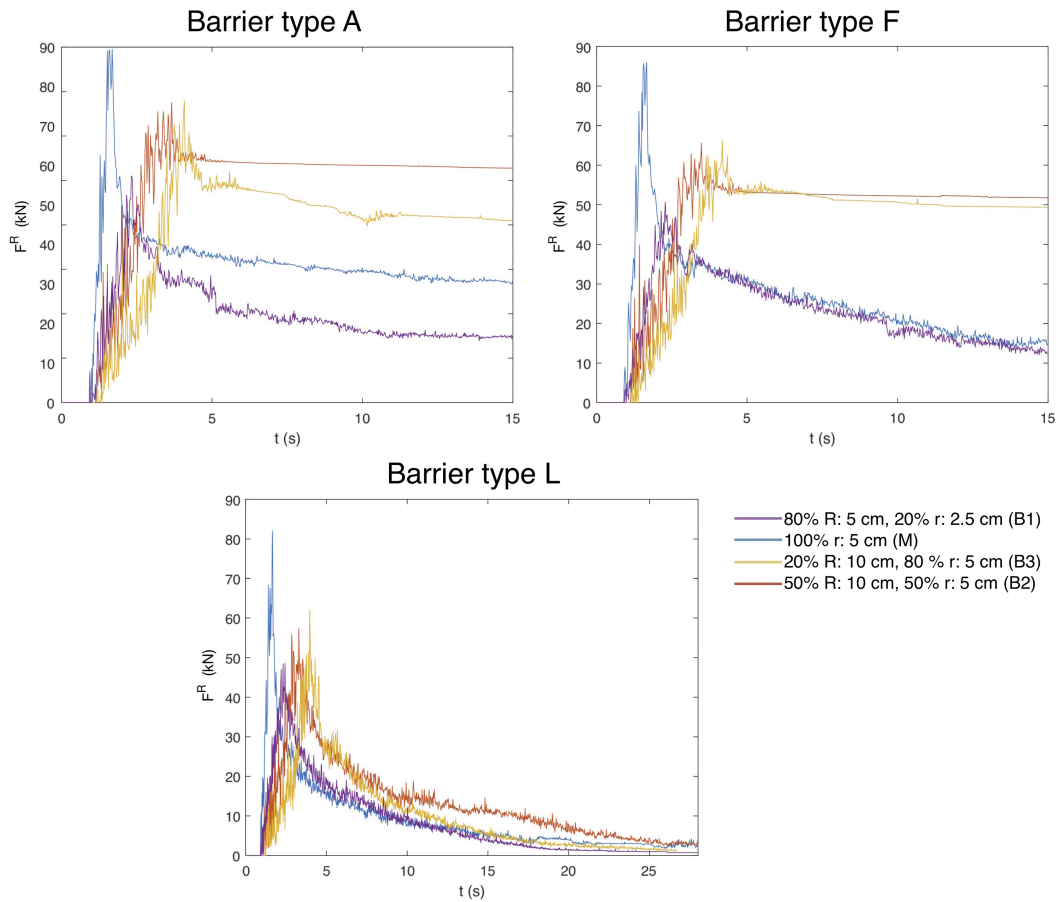
Fig. 8.10 Global force as function of time for the barrier types A, F, and L, for the different simulated mixtures.

Analysis of the impact forces

Referring to the impact forces, both the evolution in time of the global resultant force $\mathbf{F}_G^R$ and the spatial distribution of the local resultant forces $\mathbf{F}_L^R$ are considered. Figure 8.10 displays time history of the global force: the plots are grouped according to the different barrier configurations. The three configurations B1, B2, and B3 are compared with the monosized (M) case. In particular, Figure 8.10 refers to barrier types A, F, and L. Observing the plots, it emerges that the introduction of bidispersion lowers the global maximum value with respect to the monosized case, almost independently from the other parameters Φ_{small}, R, and r. The maximum values in the bidispersed cases are reached later in time than in the monodisperse one, but this can be ascribed to the low-compacted initial configuration, as for the slit barrier case (Sec. 8.1.1). Considering the descending part of the curves, until

a stable configuration is reached, a similar trend is observed for both B1 and M, independently from the barrier type. Furthermore, for mixtures B1 and M, the same value in magnitude is observed for the barrier types F and L, i.e. when partial clogging or no clogging verifies. On the contrary, in the barrier type A, the forces in the monosized case (M) are higher than for the B1 mixture, as the amount of trapped material is higher. No differences emerge for barrier type F. Considering configuration B2, the magnitude of the force in the descending part of the curve is higher than in the other cases. In particular, for the barrier types A and F, arching verifies and almost the whole material is trapped, exerting a high static force. In these configurations, the static stable situation is reached early in time, almost instantaneously after the impact. This does not happens in the L barrier case, where only a low arching occurs, late in time. The trend observed for the B3 mixture is similar to that observed for the B2 mixture for all the barrier types. For the types A and F, arching verifies, resulting in high static forces, even slightly lower than those for the B2 mixtures. This is due to the fact that B2 mixture has a greater amount of big particles, thus impacting with a greater inertia. In the L barrier type no arching occurs, resulting in a low static force. The maximum values are reached slightly later for the B3 mixture for all the barrier types. This is due to the initial configuration, which is for the B3 mixture significantly low-compacted.

Figure 8.11 shows the local forces exerted on the barrier face when the maximum global force occurs. Only the barrier type F is displayed as representative of the whole cases. Table 8.2 reports the time t_{max} at which the maximum force is recorded and the intensity of the maximum global resultant impact force, and the maximum local impact force $\mathbf{F}_{\text{L,max}}^{\text{R}}$ (referring all to the same instant), for all the simulations. It reveals that the local force magnitude decreases, while the number of contacts increases as soon as the grain size decreases, or the the amount of small particles increases. This last aspect is particularly evident for the barrier types F and L, where the barrier face is large enough to make the arch formation possible, and local forces can be due to both single impacts or potential force-chains. For barrier type A, i.e. $P/r = 2$, the greater forces are due to impacts of single grains. It is worth mentioning that, despite the fact that grains size affects the local forces, the global maximum force decreases in the bidisperse case, independently from the grains size.

Considering the envelope of the maximum $\mathbf{F}_{\text{L}}^{\text{R}}$ observed during the dynamic phase (Fig. 8.12) the spatial distribution in the bidisperse cases is compared with the monosized case. The local maximum values observed in the envelope are reported in
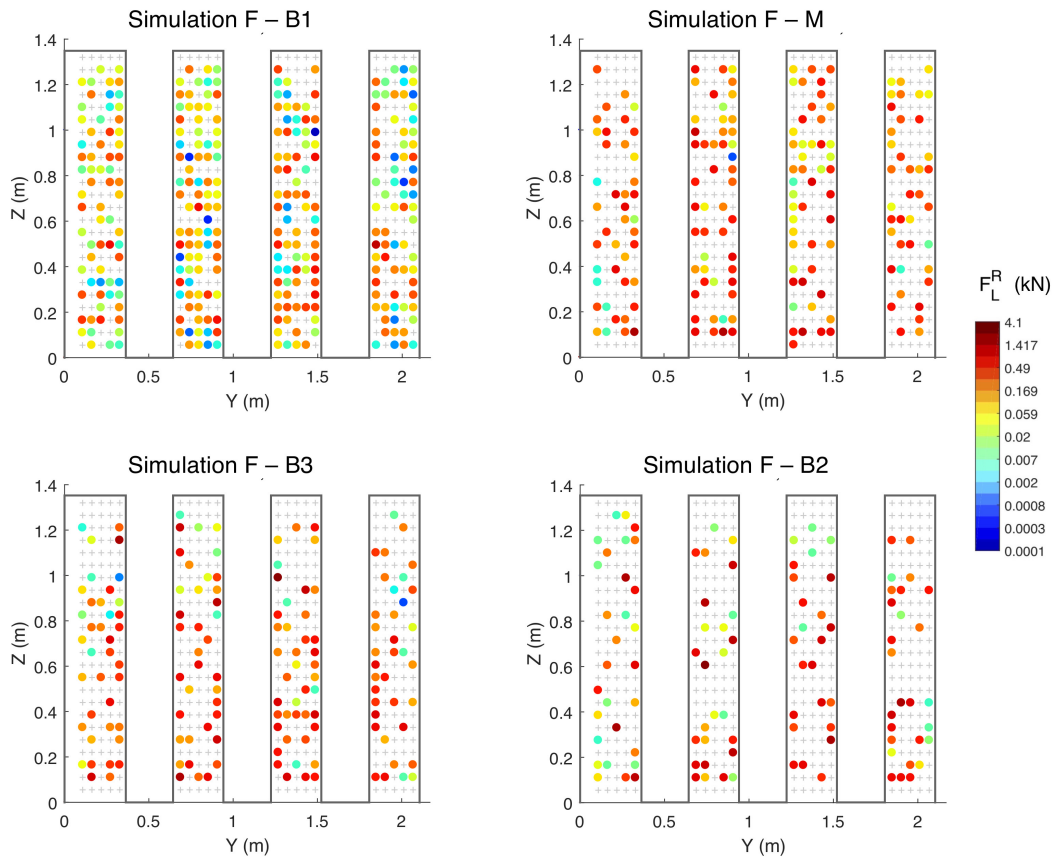
Fig. 8.11 Local forces at the time in which the maximum global impact verifies for barrier type F, for the different simulated mixtures. The colormap is in logarithmic scale.

column 5 of Table 8.2. It emerges that, increasing the grain size, the local maximum forces increases in magnitude. This is explained by the fact that these forces are due to single-grain impacts: thus, big grains generally have higher kinetic energy. Increasing grains size, high forces progressively verify not only in the bottom half of the barrier but also in the top part. This aspect is due to the occurrence of the inverse grading phenomenon: the large grains reach the front and the highest part of the flow, increasing their kinetic energy and consequently exerting large forces against the barrier. Another interesting aspect emerges. The amount of large particles affects the results similarly to the grain size: increasing the amount of large particles, the local maximum forces increases and the high impacts happens also in the top part. The high maximum local force value occurred for the A-B1 simulation is due to a single grain impact and can be ascribed to the stochastic variability of the simulations.

Examining the effects on the barrier when the mass is at rest, Figure 8.13 shows

Simulation	$t_{\max}$ (s)	$F_{G,\max}^R$ (kN)	$F_{L,\max}^R$ at $t_{\max}$ (kN)	max $F_{L,\max}^R$ in the dynamic phase (kN)	$F_{L,\max}^R$ at t_{end} (kN)	F_G^R at t_{end} (kN)
A-B1	2.32	55.35	2.08	7.03	0.49	2.92
A-M	1.68	87.83	3.27	5.38	1.43	19.52
A-B2	3.66	78.11	3.60	12.07	3.36	71
A-B3	4.08	72.1	2.55	16.88	2.15	49.9
F-B1	2.28	52.13	1.92	3.98	0.19	1.48
F-M	1.66	81.59	2.41	8.96	0.69	8.77
F-B2	3.48	69.83	3.69	19.29	3.20	59.64
F-B3	4.18	78.56	3.59	9.97	3.06	65.86
L-B1	2.20	42.44	1.29	3.11	0.08	0.9
L-M	1.66	71.47	1.99	8.41	0.21	1.02
L-B2	3.30	52.38	2.93	9.54	0.35	2.79
L-B3	3.98	53.99	2.06	8.24	0.49	1.61

Table 8.2 Time and force values in the instants when $F_{G,\max}^R$ is reached ($t_{\max}$), during the dynamic phase, and when the static condition is reached (t_{end}), for each simulation (ref. to Tab. 8.1 for simulation names).

the spatial distribution of local static resultant forces F_L^R acting on the barrier types F an L. The numerical values of the global resultant force F_G^R and of the maximum local resultant impact forces occurring on the whole barrier $F_{L,\max}^R$ are reported in columns 4 and 3, respectively, of Table 8.2. A similar trend is observed for barrier types A and F. Increasing the grains size, trapping is enhanced and thus the mass deposited behind the barrier increases. The local forces magnitude increases with grains size, due to force chains formation on the barrier face. However, increasing the amount of large particles, the number of contacts observed on the barrier face decreases. This results to the higher number of arches formed by large particles, and thus with a lower number of particles involved. In barrier type L, similar local forces verify for mixtures, as no clogging occurs in all cases.

In conclusion, it is observed that the presence of bidispersion decreases the global maximum forces exerted on the whole barrier, almost independently of the grains size in the mixture. In contrast, increasing grains size, the local force magnitude increases, and the maximum values location progressively moves from the bottom to the top part of the barrier. When the pile width is large enough, force chains

arise also on the pile face and resulting in high contact forces. The modified spatial distribution of local forces, compared with the monosized case, has to be properly considered in the design process.
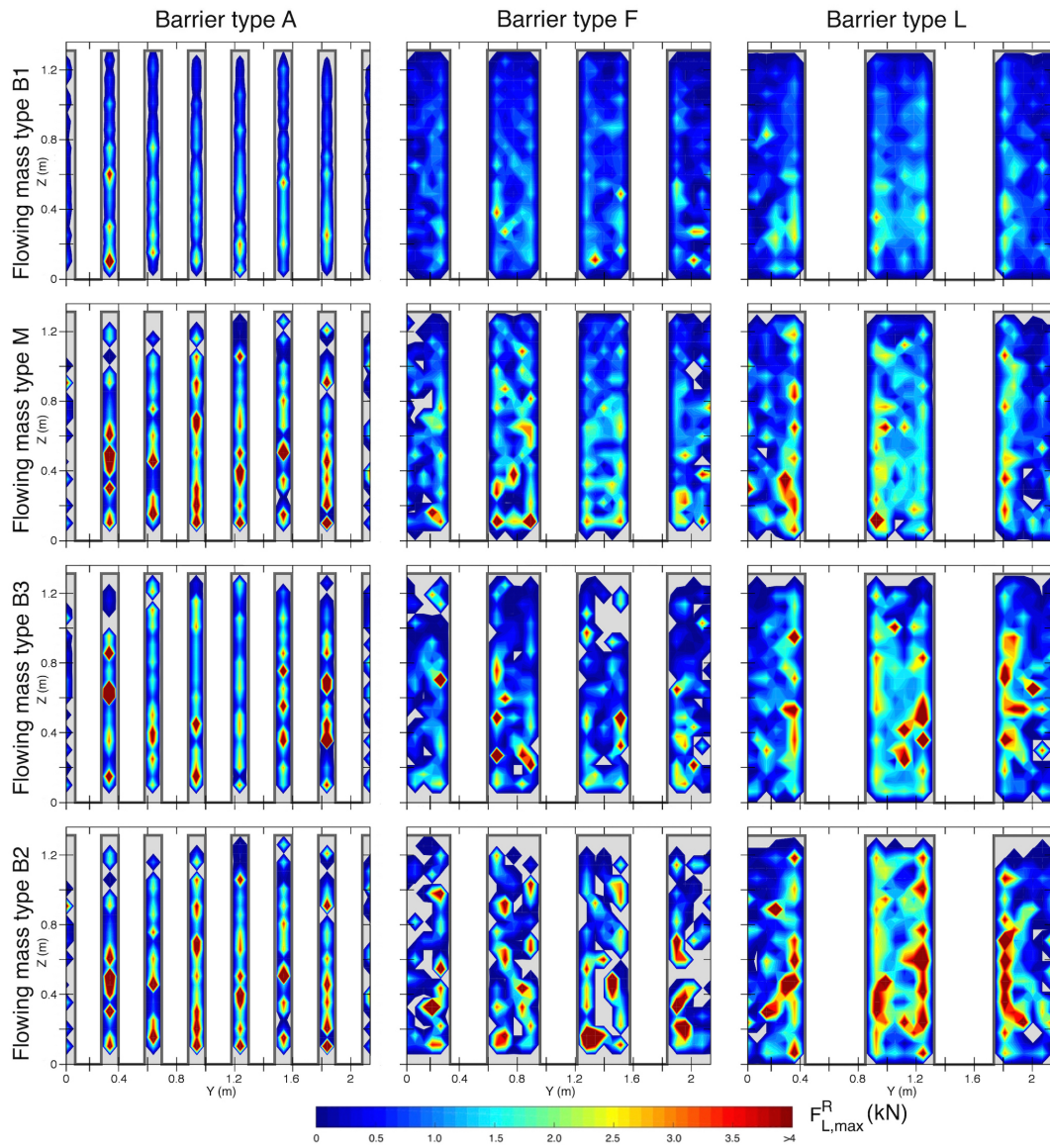
Fig. 8.12 Envelope of the maximum local resultant impact force $\mathbf{F}_L^R$ distribution during the dynamic phase of the motion, for all the performed simulations. White areas in force distribution are due to arching of particles against the barrier face. The maximum $\mathbf{F}_L^R$ occurred over the whole barrier is reported in Table 8.2.
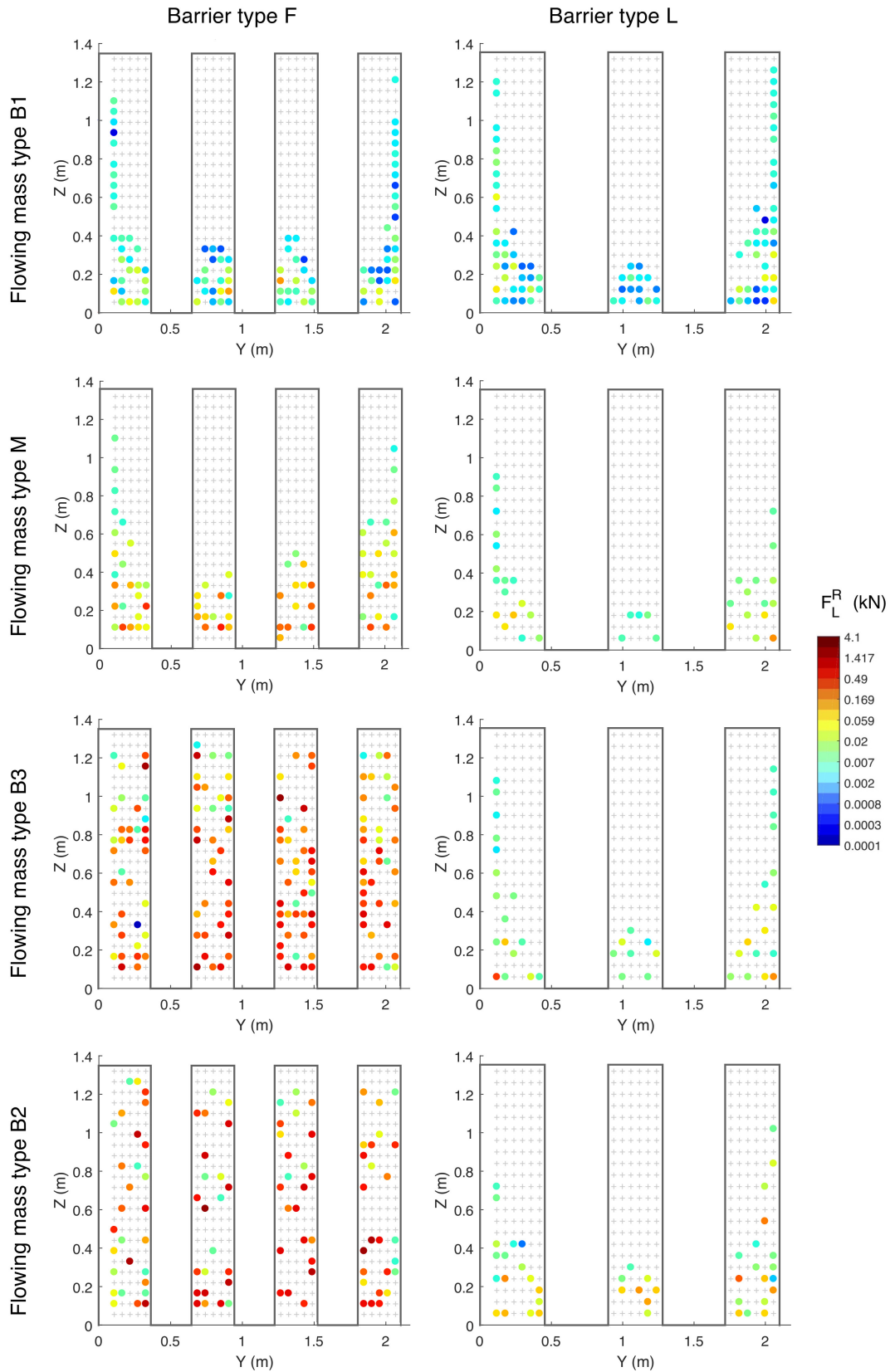
Fig. 8.13 Local forces when the static situation is reached for barrier type F and L, for the different simulated mixtures. The colormap is in logarithmic scale.

8.2   The solid-fluid case

This section deals with the presence of a fluid phase in addition to the a monodisperse granular phase. The introduction of this phase in the simulations is performed with the LBM modulus of the code (Sec. 5.2). The mechanisms of forces exchange between the solid and the fluid components can affect the probability of stable force chains among particles and, thus, the clogging probability. Moreover, the total resulting force exerted on the barrier is the sum of two contributions, the solid and the fluid ones, whose influences vary in time and intensity. Also the mechanisms of force transfer is influenced by the presence of two different components, a discrete and a continuum ones. Both these aspects need clarifications.

In this section, only the slit barrier case is studied. All the simulations are performed twice, adopting two different rheologies for the fluid phase: Newtonian and Bingham (Sec. 5.2.1). For the Newtonian rheology, in which the viscous stresses arising during motion are linearly proportional to the local strain rate, the fluid phase cannot be trapped in the inter-particles spaces but filters through them. In the hypothesis that the coarse particles clog, also the fine particles of the water-fine mixture can be trapped, as shown during real debris flow events. In this perspective, the Bingham rheology is considered. Due to its capacity to sustain stress at rest, the Bingham fluid phase can be trapped by the coarser particles. In fact, the Bingham fluid, once its motion is halted can be conceptually seen as a solid.

As the fluid phase considers both water and fines particles, in the performed numerical simulations, the density of the fluid is set equal to $\rho = 1500$ kg/m^3. The adopted rheological parameters are consistent with the ones proposed in the literature (Iverson, 2003; Jeong, 2014; Kaitna et al., 2007, e.g.) in the field of numerical simulations of debris flows. Furthermore, among the suggested values, the ones adopted are within the bounds required by the numerical constraints (Sec. 5.2.5). For the Newtonian rheology, the viscosity η is equal to 20 Pa·s. In order to qualitatively evaluate the influence of plasticity, for the Bingham case the plastic viscosity η_0 is set equal to 20 Pa·s, as in the Newtonian case. In the hypothesis of high shear rate, indeed, the apparent viscosity η_{app} of the Bingham fluid converges toward η_0. The yield stress τ_0 is estimated in order to guarantee the possibility that fine grains are trapped if coarse particles clog behind the barrier creating voids of about 12 cm wide, i.e. greater than a particle size. To this aim, a simple calculus is proposed. A shear stress field develops in a Bingham fluid flowing on an inclined channel

(a)   (b)
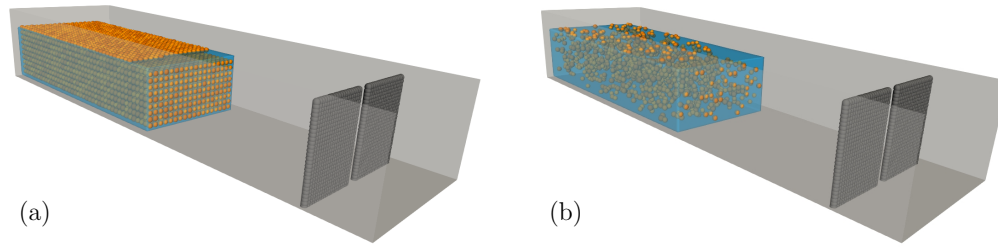
Fig. 8.14 Example of the initial distribution for (a) $V_s/V_{box} = 0.35$, and (b) $V_s/V_{box} = 0.10$ of the numerical analyses with a slit barrier.

of height $h_0 = 12$ cm. The idea is to compute the minimum yield stress necessary to prevent the fluid to flow through the outlet. In this case it is supposed that the value of the shear stress at the edges of the outlet is equal to the yield stress τ_0. By equilibrium condition, the acting force, i.e. the weight of the flow in the direction normal to the outlet, has to be equal to the maximum resisting force due to τ_0, that is $h_0 \rho g \sin \theta = 2\tau_0$. Rearranging the expression results in $\tau_0 \approx 500$ Pa. To guarantee a complete trapping of the fine material, 12 cm is chosen as the maximum value of void size, even though this value is greater than the particle diameter d, while generally, at least in static packings, void sizes are of the order of $d/5$ (Alonso et al., 1995). However, Reboul et al. (2008), considering a polydisperse system of spheres, defining the "equivalent radius" of the void as the radius of the disc whose area is equal to the area of void within the face, found also values slightly greater than the mean radius of the particles.

The numerical simulations are performed considering a slope angle $\theta = 35°$ with a slit barrier with $S/r = 3$. In the monodisperse dry granular condition, such configuration represents a complete trapping condition. In the absence of the solid phase, the released fluid occupies a $4.75 \times 2.10 \times 1.1$ m^3 parallelepiped, in $X-$, $Y-$, and $Z-$directions respectively. This volume (11 m^3) represents the total volume of a rectangular box V_{box} that perfectly circumscribes the particle assembly.

From a numerical point of view, in the simulations performed some approximations are made in order to limit computational time and to obtain preliminary results highlighting the general trend of the flow rather than a complete parametric study. Thus, the three requirements explained in Ch. 5 (the limits in the relaxation time and the number of lattice nodes, and the need to have a Mach number smaller than 1) are only partially fulfilled. In particular, the length of the cubic lattice edge is taken only 1/4th of the minimum diameter of the particles, i.e. 2.5 cm for 10 cm-diameter

particles. With this discretisation, the number of lattice nodes is 3.9×10^6, thus below the suggested threshold value. However, this sub-optimal lattice allows to highlight the main features of a two-phase flow. Considering the other two requirements, the adopted lattice time step, 0.0005 s, the density, and the plastic viscosity guarantee a relaxation time of $\tau_{\text{coll}} = 0.532$. This high value of viscosity lowers the probability of turbulence. As a consequence, the requirement on the length of the lattice is less stringent. The adopted density takes into account the presence of fine particles inside the fluid. Referring to the third requirement, considering a mean fluid velocity of about 10 m/s, Ma is about 0.75, assessing that the chosen lattice time step is sufficiently small.

It can be expected that, with the only fluid phase all the released material passes through the opening of the slit barrier. In order to study the transition between this trapping condition to a fully-clogged situation and the effects on the barrier, various solid concentrations are considered. This is implemented introducing an increasing volume fraction of granular material in the volume, requiring that an equal amount (in volume) of fluid is removed keeping the total volume constant. In this way the total volume is preserved, decreasing the fluid volume fraction. This process is described through solid-to-total volume ratio $V_{\text{s}}/V_{\text{box}}$, ranging from 0.0 to 0.35, with 0.05 incremental steps. This process allows to simulate, to a first approximation, different types of flow behaviour, i.e. from a streamflow to a debris flow, or, in the frame of the only debris flow type, the different parts of its head-and-tail morphology (Sec. 2.3.2). Nevertheless, the total weight of solid and fluid phases varies in each simulation. All the added particles have mean radius $r = 5$ cm, as in the monodisperse case of Ch. 7, in such a way that, for $V_{\text{s}}/V_{\text{box}} = 0.35$, the solid discharged mass is equal to the one adopted for the monodisperse dry granular material simulations (Fig. 8.14(a)). In the other $V_{\text{s}}/V_{\text{box}}$ ratios, particles positions are randomly generated with a minimum distance between two adjacent particle centers larger than $2r$, i.e. one particle diameter (Fig. 8.14(b)).

The influence of the fluid phase is analysed in terms of both trapping efficiency and forces exerted on the barrier, highlighting the contribution of both solid and fluid phases.

For computational convenience, the simulations are stopped at 30 s. At this time the fluid phase has not reached a completed stable configuration yet, i.e. for the Newtonian case a slight percolation is observed through the clogged particles.
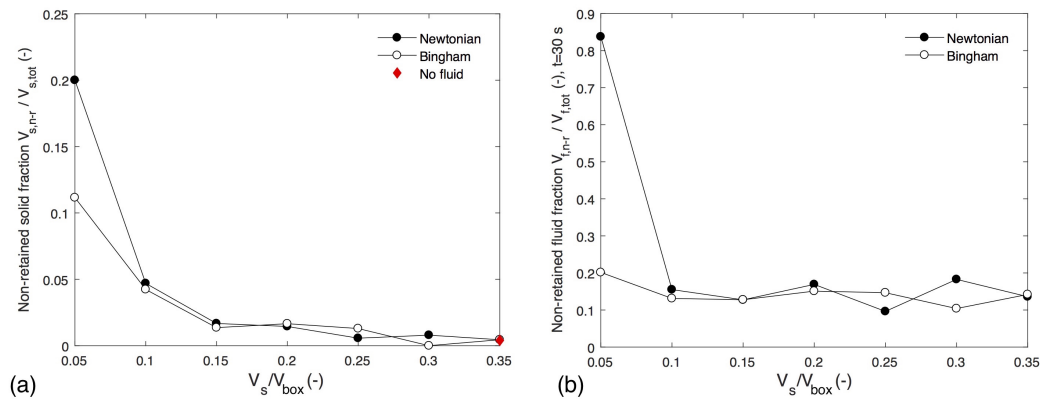
Fig. 8.15 (a) Non-retained solid fraction with respect to the solid volume fraction V_s/V_{box}, for both the Newtonian and Bingham rheologies. The red diamond shows the dry monodisperse case, i.e. in absence of fluid. (b) Non-retained fluid fraction with respect to the solid volume fraction V_s/V_{box}, for both the Newtonian and Bingham rheologies at 30 s.

However, the main features of the evolution of the forces in time, as well as the trapping efficiency for both the phases, are evident within this timeframe.

Analysis of the trapping efficiency

The effects of a fluid phase on the trapping efficiency are evaluated comparing the non-retained material fraction for the dry monodisperse case reported in Ch. 7 with the one obtained in simulations in which a fluid phase is added. It has to be remembered that, in the dry simulations, with the same geometrical setting, a complete clogging occurs (Ch. 7). Relating to the notation adopted in this section, the dry monodisperse case can be intended as a simulation in which the fluid is substituted by air, thus, with volume fraction $V_s/V_{box} = 0.35$, where V_{box} is the total volume of a rectangular box that perfectly circumscribes the discharged mass.

Figure 8.15(a) displays the non-retained solid fraction with respect to the solid volume fraction V_s/V_{box}, for both the Newtonian and the Bingham rheologies. The solid material is entrapped and reaches a stable configuration even before the fluid phase completely passes through the outlet (or reaches a stable configuration). It appears that, for $V_s/V_{box} = 0.05$, i.e. a very diluted flow, the Newtonian rheology enhances the flowing of the particles through the outlet more than in the Bingham case. However, a consistent trapping occurs in both cases, as the non-retained solid fraction is around 0.2 and 0.12 for the Newtonian and Bingham cases, respectively.

From $0.1 \leq V_s/V_{box} \leq 0.35$, a completely trapped situation occurs irrespective of the rheology adopted. For $V_s/V_{box} = 0.35$, the red diamond mark shows the value found in the dry case, finding a perfect correspondence.

In order to give an estimation of the amount of fluid phase that has passed through the outlet when the solid phase reaches a static condition, Figure 8.15(b) shows the non-retained fluid fraction 30 s after the release of the fluid/solid mass. The plot reveals that for $V_s/V_{box} = 0.05$ almost all the fluid passes through the outlets in the Newtonian case, while for the Bingham fluid almost 80% of the fluid phase has not passed yet. For $V_s/V_{box} \geq 0.10$, conversely, for both rheologies, the non-retained fluid phase is less than 20%. In the Newtonian case the fluid mass is consistently decelerated, while it has stopped in the Bingham case. A Newtonian fluid cannot stop, while its deceleration is a function of its viscosity. The non-retained fluid fraction tends to zero as soon as the observation time window enlarges. All the simulations are performed with a unique viscosity, thus a parametric study on the influence of this parameter on the velocity of the fluid cannot be done. However, it is known that decreasing the viscosity, the retained volume fraction substantially decreases. It results that the influence of the rheology is only evident for small amount of solid fraction, when the plasticity of the Bingham fluid plays an important role in the clogging mechanisms. Furthermore, the effects of rheology are only observed on the trapping of the fluid phase for $V_s/V_{box} = 0.05$. In this simulation it is observed that, when the fluid reaches the barrier there is no complete trapping (of the solid phase) and, thus, the fluid can flow through the outlet. For $V_s/V_{box} \geq 0.1$, the fluid phase is filtered through the voids of the solid mass entrapped behind the barrier.

The total amount of non-retained material, at 30 s, is also represented (Fig. 8.16). A trend similar to the one discussed for the only-fluid phase is observed. From these preliminary results, it may be concluded that, for $V_s/V_{box} \geq 0.10$, the trapping efficiency seems to be preserved independently from the presence (or not) of the fluid phase, and from the adopted rheology. Nevertheless, these results can only be considered valid in the range of the viscosity value adopted. Furthermore, for $V_s/V_{box} \geq 0.10$, the fluid phase is also consistently decelerated, in the Newtonian case, or stopped, in the Bingham case. Solid and fluid phases approach the barrier with comparable velocity, then the solid material is retained and the fluid phase separates from the solid one. During the motion, the surface layer of the flowing mass is only fluid. This layer has higher velocity. Figure 8.17 qualitatively shows the above detailed results: at $t = 30$ s, only for $V_s/V_{box} = 0.05$, in the Newtonian case, almost
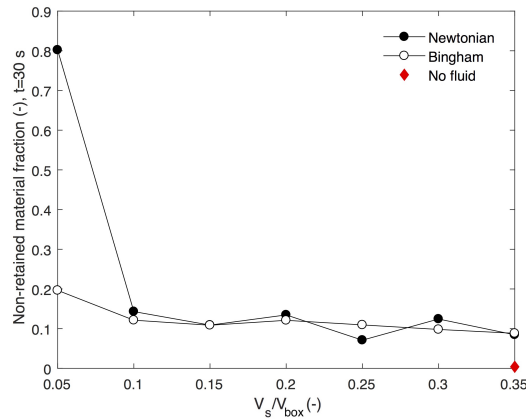
Fig. 8.16 Total amount of non-retained material (solid and fluid) with respect to the solid volume fraction V_s/V_{box}, for both Newtonian and Bingham rheologies, at 30 s.

the whole fluid and solid material pass through the outlets. For $V_s/V_{box} \geq 0.05$, for both the Newtonian and the Bingham rheologies, the trapping efficiency is preserved. As previously observed, in the $V_s/V_{box} = 0.05$-Newtonian case, the fluid phase can flow through the outlet separately from the solid. This is why only in this case the maximum velocity of the fluid phase is higher than those for all the other V_s/V_{box} values. Despite the fact that the number of simulations is not representative, the obtained results provide interesting inputs for further parametric analyses.

Analysis of the impact forces

The study of the impact forces is performed considering the global resultant forces acting on the barrier. The forces exerted by the fluid phase on the barrier are calculated with the dry coupling scheme (Sec. 5.2.3), considering the barrier as a rigid wall. It is worth mentioning that the term "dynamic phase" refers to the initial interaction between the moving mass and the barrier, i.e. a few seconds time window following the first contact with the barrier, while "transitional phase" denotes the following period, up to the end of the simulation at 30 s. The forces, for both solid and fluid phases, are first evaluated in terms of presence or absence of the fluid phase. In this sense, considering a solid volume fraction $V_s/V_{box} = 0.35$, the results discussed in Ch. 7 related to a monosized dry granular impact are compared with those obtained with the inter-particles voids filled with fluid. In this way, the dynamics of the phenomenon are investigated. After that, the influence of different amount of solid volume fraction is investigated.
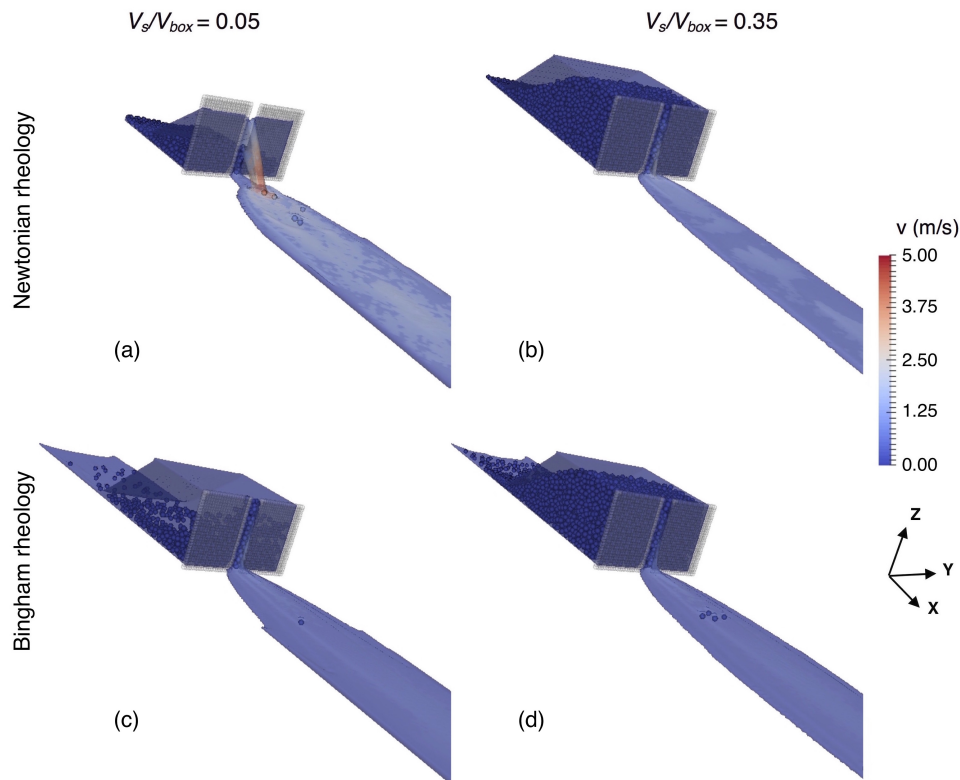
Fig. 8.17 Sketches of the flowing mass (solid and fluid) at 30 s, for $V_s/V_{box} = 0.05$ and 0.35 for both Newtonian and Bingham rheologies.

Figures 8.18(a) and 8.19(a) show the global resultant force time-history, considering both the contribution of single phases, $\mathbf{F}_{s,Wet}$ and $\mathbf{F}_{f,Wet}$, and the total force, $\mathbf{F}_{tot,Wet}$, for Newtonian (Fig. 8.18) and Bingham (Fig. 8.19) fluids (the ^{R} is suppressed in the symbols for simplicity). "Wet" and "Dry" relate to the presence or the absence of the fluid phase, respectively. The results obtained in the "Wet" case, represented by blue curves in both the plots, are compared with the correspondent monosized dry simulation, represented by the red curves. The effects of the fluid phase on the resulting forces on the barrier is computed in terms of the difference between the forces exerted by the solid phase with the different initial configurations (with and without fluid), $\mathbf{F}_{s,Wet} - \mathbf{F}_{s,Dry}$ (Figs. 8.18(b) and 8.19(b)). A quite similar trend is observed for both rheologies.

Observing the plots, it results that, for both rheologies, the solid phase impacts the barrier before the fluid one. During the whole dynamic phase, it clearly emerges that fluid phase considerably affects both the total and the solid forces exerted against the barrier. Considering the dynamic phase of the wet case, fluid forces are greater

than the solid ones. The contribution of the fluid phase in the maximum global resultant force is substantial: the fluid phase is predominant and the maximum total force occurs when the maximum fluid contribution is recorded. The force exerted by the solid phase is markedly lower than the fluid one, and contributes in the first initial contacts, when the fluid phase has not reached the barrier yet. Considering the transitional phase, the fluid contribution decreases while the solid one increases, keeping the total value near constant. This is explained by the dynamics of motion. The solid phase reaches the barrier earlier than the fluid and clogs almost instantaneously. When the fluid phase arrives at the barrier location it encounters the solid phase clogging behind the barrier. In the transitional phase, the fluid impacts mainly against the trapped and deposited grains and in a low part directly against the barrier. Thus, its dynamic effect is transferred to the barrier through the solid phase. Because of that, the solid forces on the barrier increase and the total ones remain constant. This process is much more evident in the Newtonian case, where, a few seconds after impact, the solid force is greater than the fluid one. For the Bingham case, the same phenomenon occurs later, that is, in the final stage of the motion. Comparing the forces exerted by the solids in the wet and in the dry cases reported in Figs. 8.18(b) and 8.19(b), it emerges that the solid phase is accelerated by the presence of the fluid. Being released at the same distance from the barrier, the particles of the wet cases impact against the barrier earlier in time than those in the dry case. Nevertheless, the presence of the fluid slightly decreases the maximum force value since the fluid phase makes the collisions of grain less frequent. As a lower amount of collisions happens in the same instant, the force is reduced. Figure 8.20 represents a pictographic time series of the front approaching and impacting the barrier for the dry and wet cases (both Newtonian and Bingham rheologies). The colour displays the velocity values of the flow. In the wet case, for $t = 0.8$ and 1 s, the superficial layer is almost characterised by the fluid phase only. The fluid, not decelerated by the presence of solid, reaches higher velocities. As a general trend, solid and fluid phases are characterised by comparable values of velocities.

Having highlighted the main aspects of the presence/absence of a fluid phase, the concentration of the solid fraction is now investigated. Figure 8.21 represents the time-histories of the forces exerted by the fluid phase $\mathbf{F}_f^*$, the solid phase $\mathbf{F}_s^*$, and the total contribution $\mathbf{F}_{tot}^*$ for both investigated rheologies, for all the investigated V_s/V_{box}. The absence of solid fraction is considered ($V_s/V_{box} = 0.0$). As the total weight is not preserved across the simulations, all the force values are normalised by
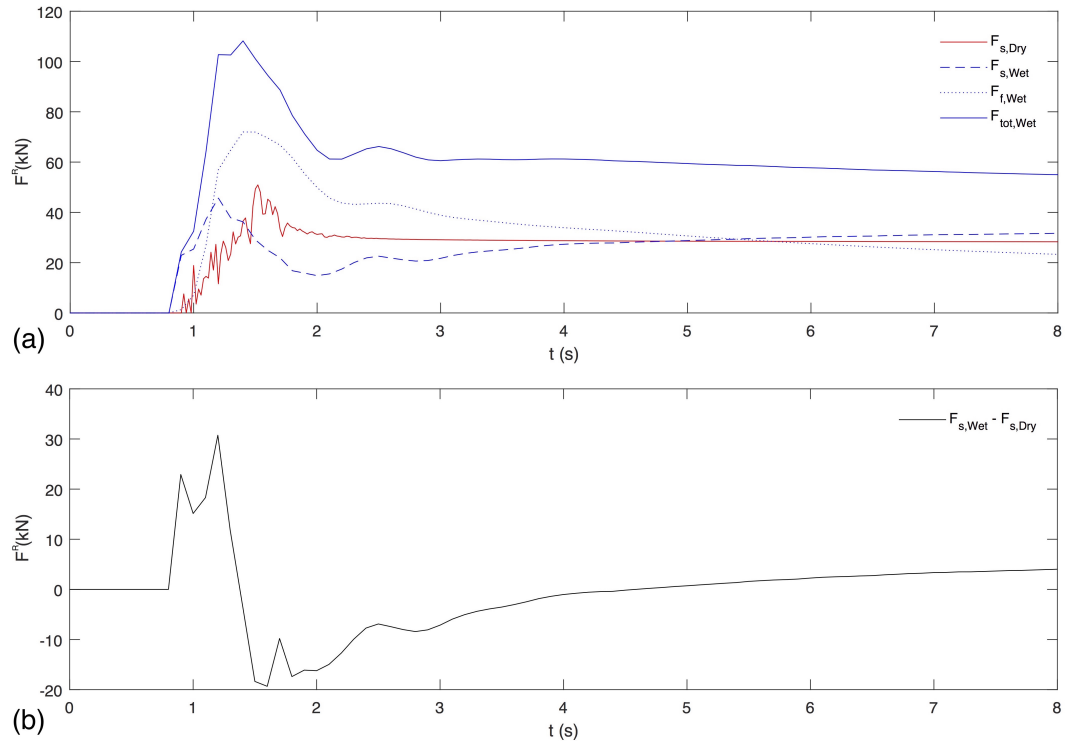
Fig. 8.18 Newtonian rheology case: (a) global resultant forces in time exerted by the fluid and the solid phases, together and separately. Also the dry case is considered. (b) Difference between the force exerted by the solid phase in the wet and in the dry cases.

the initial total weight W_{tot} in the direction normal to the barrier, resulting in:

$$\mathbf{F}^*_{\text{tot,s,f}} = \frac{\mathbf{F}_{\text{tot,s,f}}}{W_{\text{tot}} \sin \theta}. \tag{8.2}$$

In this way it is possible to compare the observed trends, which are similar for both rheologies.

Considering the fluid phase (Fig. 8.21(a) and (d)), it emerges that the solid concentration does not affect the normalised forces exerted by the fluid on the barrier. As already commented, the contribution $\mathbf{F}^*_{\text{f}}$ reduces as soon as $V_{\text{s}}/V_{\text{box}}$ increases. This is particularly evident for $V_{\text{s}}/V_{\text{box}} = 0.35$, both in the peak and in the decreasing parts of the curve. In contrast, referring to the solid phase (Fig. 8.21(b) and (e)), the maximum impact force $\mathbf{F}^*_{\text{s}}$ is reached for $V_{\text{s}}/V_{\text{box}} = 0.35$. After the impact, the forces decrease and then they increases again because of the effect of the fluid phase, as previously described. For $V_{\text{s}}/V_{\text{box}} < 0.35$ the peak value tends to decrease in magnitude and to occurs later in time as soon as $V_{\text{s}}/V_{\text{box}}$ decreases. The limit
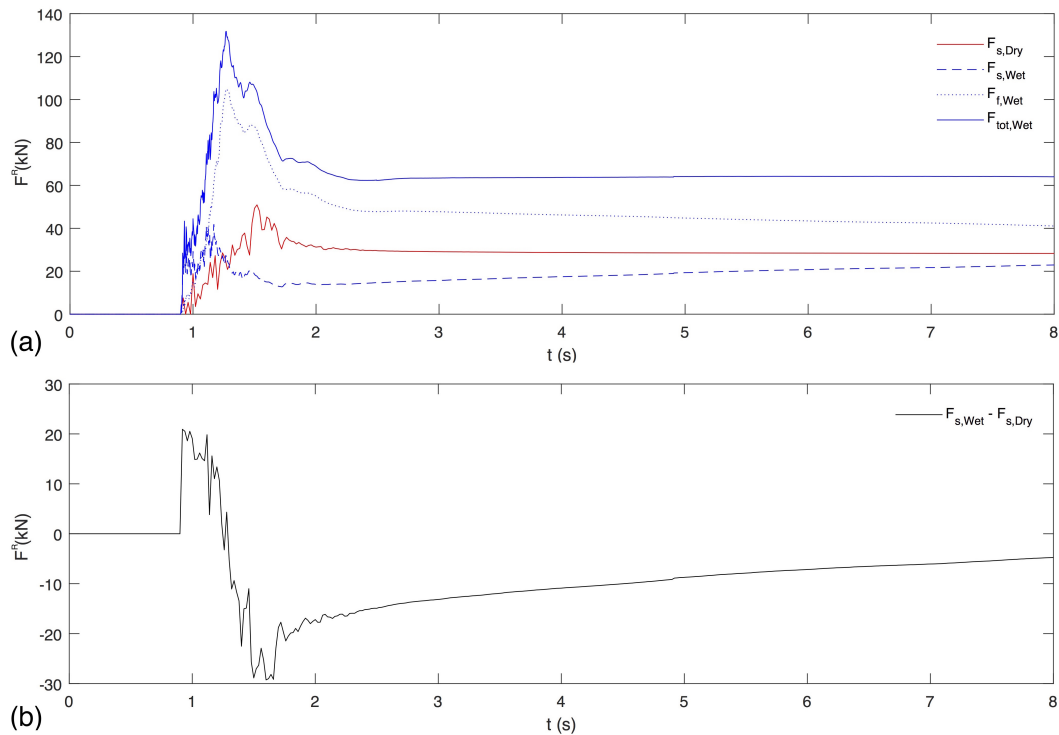
Fig. 8.19 Bingham rheology case: (a) global resultant forces in time exerted by the fluid and the solid phases, together and separately. Also the dry case is considered. (b) Difference between the force exerted by the solid phase in the wet and in the dry cases.

condition is represented by the fluid-only simulations, where the solid contribution is null. The highlighted trend is particularly evident in the Newtonian case, where the effect of plasticity is absent. Conversely, the effects on the solid phase due to the fluid are more noticeable for high V_s/V_{box}. Considering the total normalised forces (Fig. 8.21(c) and (f)), the trend in the dynamic phase is dominated by the fluid component and then the force settles to a constant value.

Figure 8.22 displays the maximum total normalised force, the time of occurrence and the solid and fluid forces in the same instant, for increasing V_s/V_{box}, for both rheologies. It emerges that the total maximum force grows by increasing V_s/V_{box} up to 0.20. Then, for $V_s/V_{box} \geq 0.20$, it reaches a constant value (1.35 for Newtonian fluid and 1.23 for Bingham fluid). Considering the time lag between the maximum force and the first impact, it emerges that, in all cases, the maximum force occurs almost at the same time (the slight difference is negligible). Considering the solid and fluid components of the maximum total normalised force separately, it emerges that the fluid force is higher than the solid one. In particular, the difference between
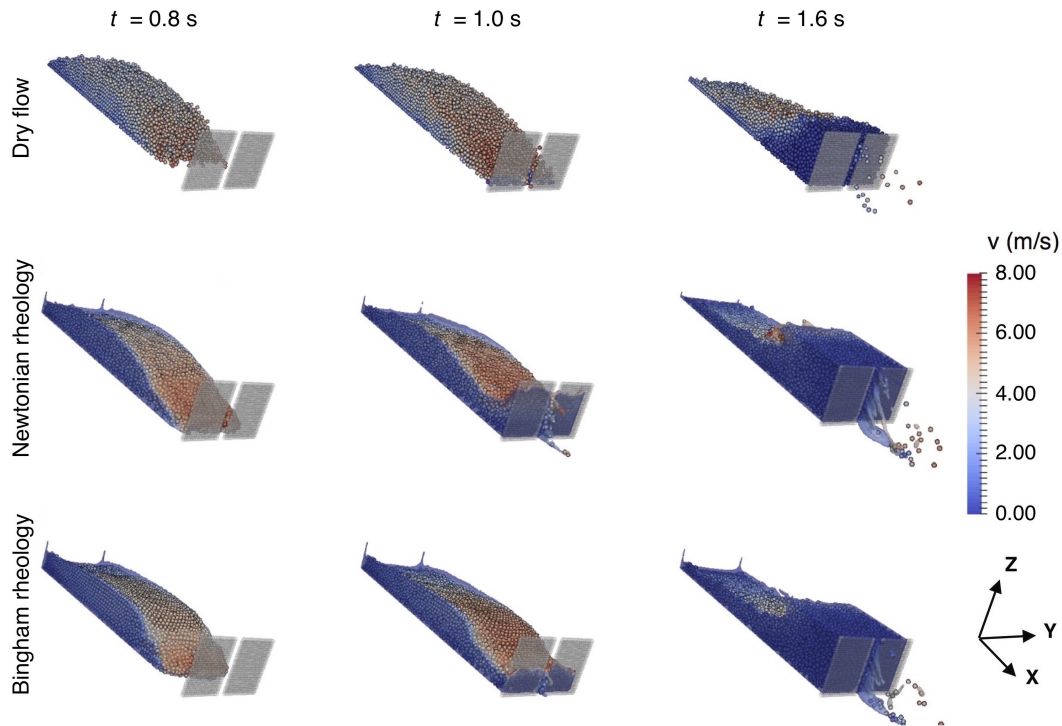
Fig. 8.20 Sketches pictographic Time series sketches of the flow front approaching and impacting the barrier for the dry and wet cases (both Newtonian and Bingham rheologies). Colour refers to the magnitude of the velocities.

solid and fluid force increases until $V_s/V_{box} = 0.20$ and 0.25 for Bingham and Newtonian rheologies, respectively, then it decreases. In contrast, the solid phase force monotonically increases by increasing V_s/V_{box}. As a general rule, fluid and total forces are higher in the Newtonian case. This is due to the fact that plasticity in the Bingham case decelerates the flow. These trends are consistent with what is observed in Figs. 8.21: generally the fluid phase plays the main role, although its force value slightly decreases when the amount of the solid phase becomes marked (for $V_s/V_{box} \approx 0.20$).

Figure 8.23 illustrates both the maximum normalised forces exerted by the solid and fluid phases and their time of occurrence with respect to the solid volume fraction V_s/V_{box}, for both the rheologies. It has to be noted that the maximum force value can occur at different instants, as detailed in Fig. 8.23(b) and (d). Considering the fluid phase and comparing the Fig. 8.23(b) with Fig. 8.22(b), it emerges that the maximum fluid impact forces are recorded at the same instant of the maximum total forces. As a consequence, this fact supports the evidence of a greater contribution
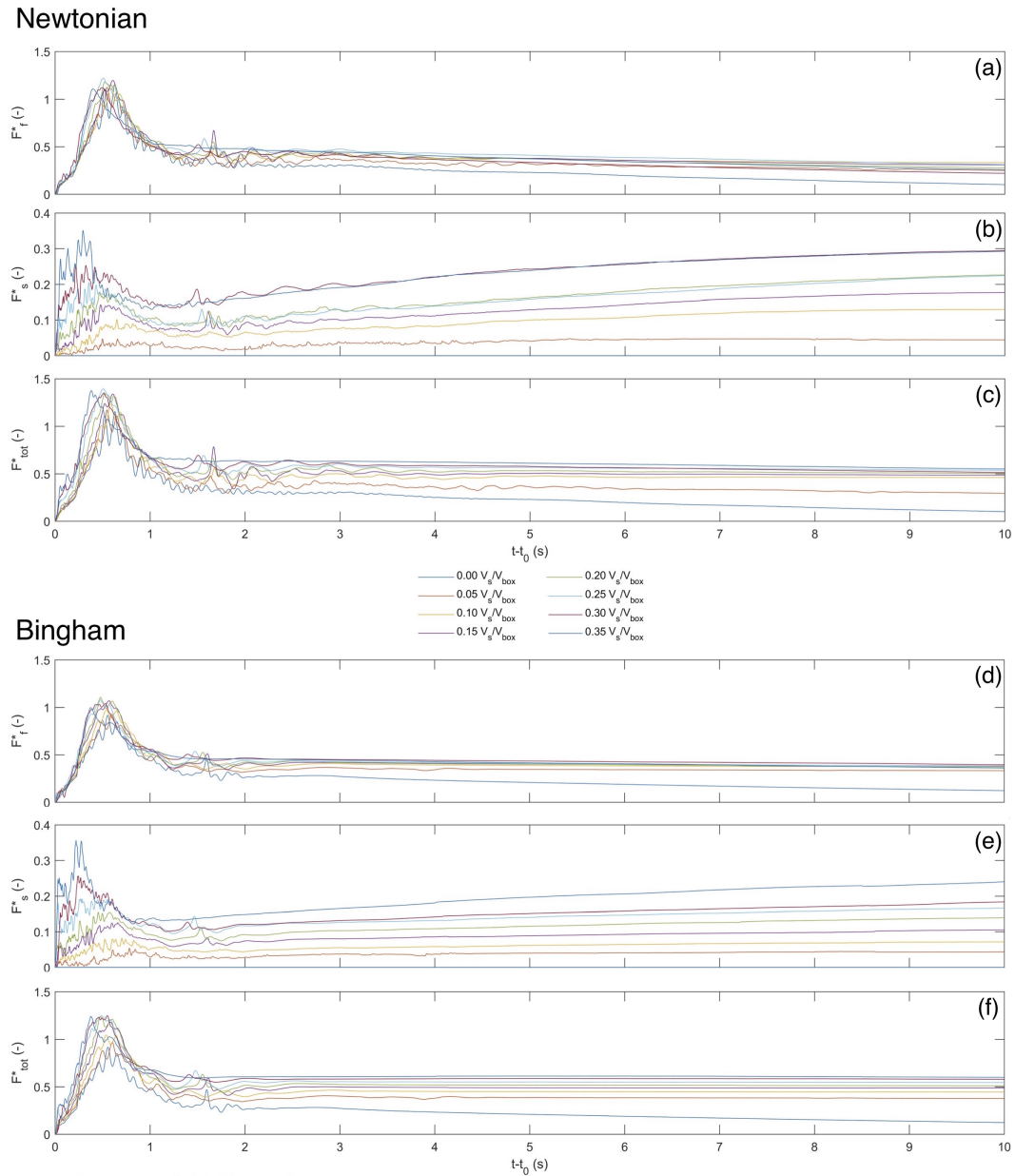
Fig. 8.21 Time-histories of the normalised forces exerted by the (a) fluid and (b) solid phases, and (c) the total force for $0 \le V_\mathrm{s}/V_\mathrm{box} \le 0.35$ for the Newtonian rheology. Time-histories of the forces exerted by the (d) fluid and (e) solid phases, and (f) the total force for $0 \le V_\mathrm{s}/V_\mathrm{box} \le 0.35$ for the Bingham rheology.
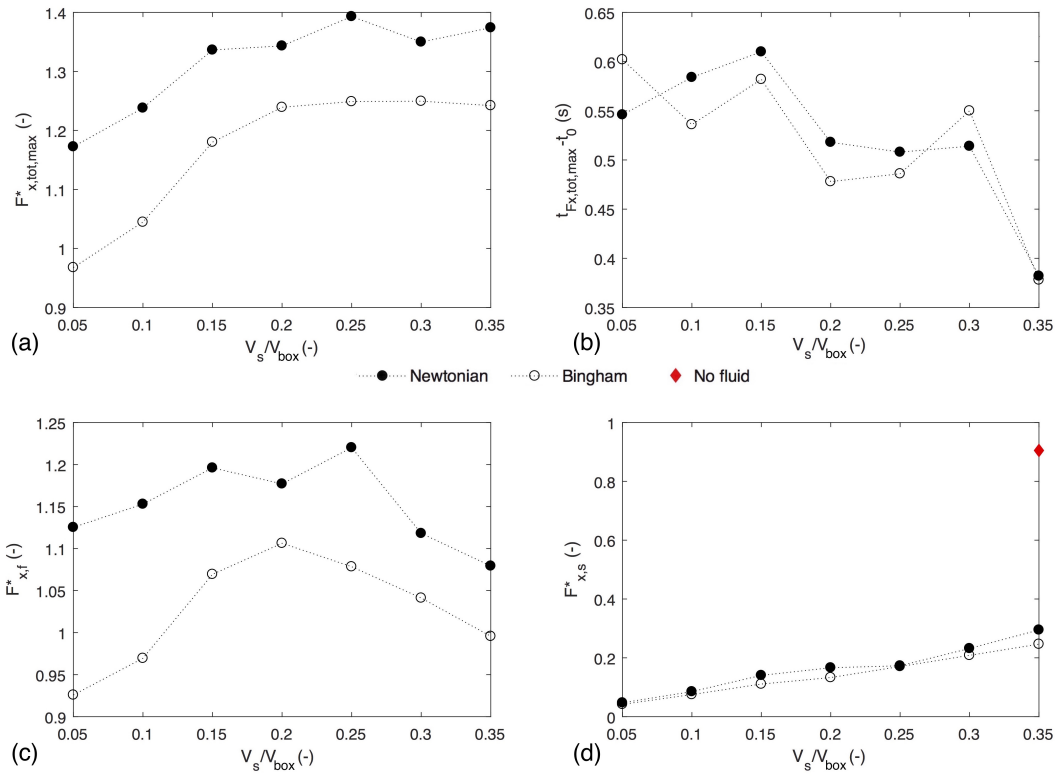
Fig. 8.22 (a) Maximum total force, (b) time of occurrence and (c) fluid and (d) solid forces at the time at which the maximum total force is recorded, as function of V_s/V_{box}, for both Newtonian and Bingham rheologies.

of the fluid phase to the dynamic phase of the force, with respect to the solid one. In contrast, the maximum forces for the solid phase occur at different times, even though with a maximum lag of less than half a second. The maximum force value increases as soon as V_s/V_{box} increases. This is due to the fact that the higher the amount of solid volume fraction is, the less the fluid phase affects the solid and, thus, the probability of collisions among grains increases. Considering the dry case, as already observed in Figs. 8.18 and 8.19, the plots confirm that the presence of the fluid phase lowers the maximum force value and accelerates the motion of the particles.

Finally, the forces at the end of the simulations are evaluated. Figure 8.24 reports the value of the fluid, solid, and total forces at 30 s, with respect to the solid volume fraction, for both rheologies. It emerges that the contribution of the solid phase on the total value increases, by increasing V_s/V_{box}. As can be observed cross-comparing the three plots, as the amount of solid increases the solid force increases, while
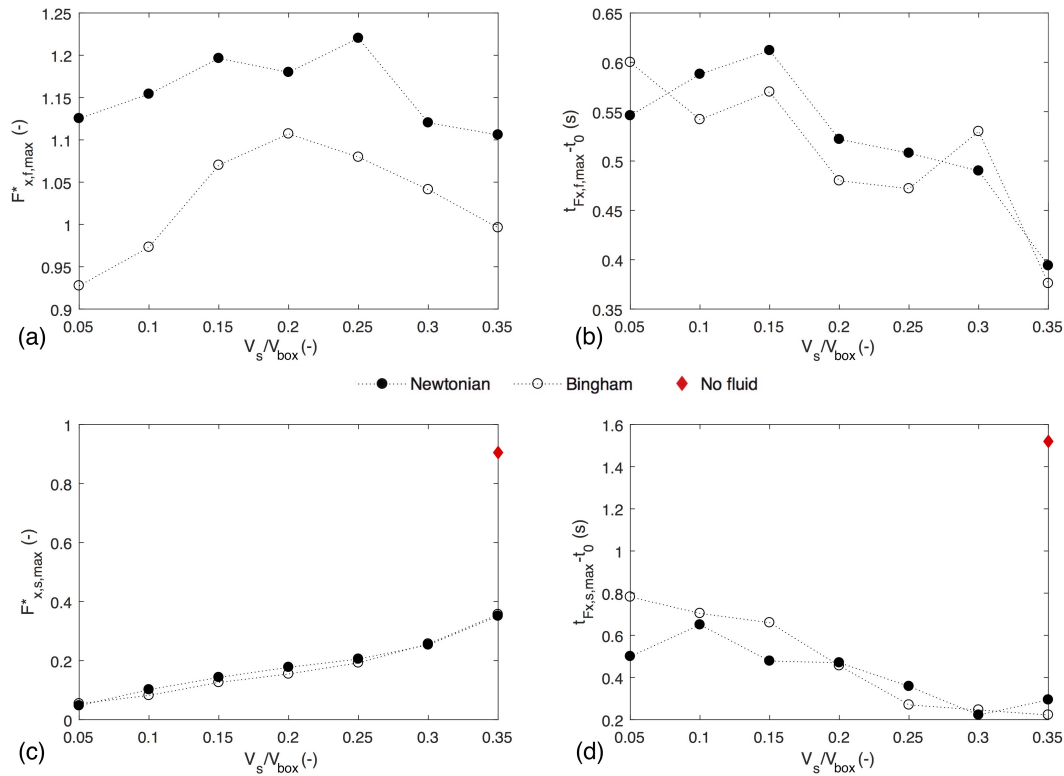
Fig. 8.23 (a) Maximum total force exerted by the fluid and (b) its time of occurrence, and (c) maximum total force exerted by the solid and (d) its time of occurrence with respect to the solid volume fraction V_s/V_{box}, for both the Newtonian and the Bingham rheologies.

the fluid component decreases, keeping the total force constant. This trend is quite similar for both rheologies, differing only for $V_s/V_{box} = 0.05$, where the fluid force is remarkably lower in the Newtonian fluid compared to the Bingham case. In Newtonian case, indeed, almost the whole fluid phase has passed through the outlet, as it reaches the barrier before the solid phase impacts and clogs behind the barrier, differently from what was observed for case $V_s/V_{box} = 0.35$ previously described in detail.

From all these results, a remarkable influence of the fluid phase emerges for all the investigated V_s/V_{box}. In the dynamic phase, the fluid phase constitutes the main contribution to the total force, in terms of both magnitude and time at which the maximum force is recorded. Furthermore, the fluid affects the solid phase, accelerating its motion and lowering its peak values. The presence of the fluid phase makes the collisions between grains less frequent in time. Thus, at a given instant, the total force exerted by the solid phase is lower than in the correspondent dry case,
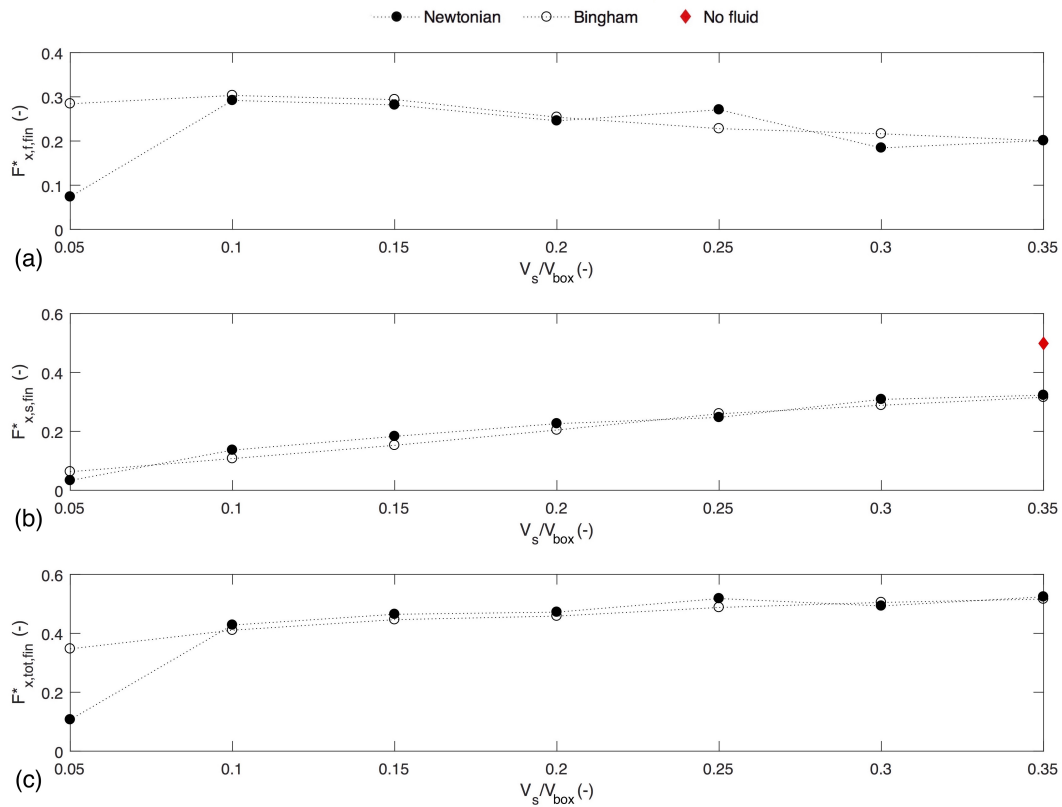
Fig. 8.24 (a) Fluid, (b) solid and (c) total normalised forces at 30 s simulation time, with respect to the solid volume fraction, for both Newtonian and Bingham rheologies.

even though the force of each individual particle is greater. This effect increases as soon as the solid concentration (V_s/V_{box}) decreases. However, for $V_s/V_{box} \geq 0.20$, the contribution of the solid phase becomes significant and the peak force settles to a constant value, almost independently from the solid concentration. Conversely, considering the transitional phase, the contribution of the fluid phase is essentially indirect since it hits the solid entrapped behind the barrier, thus enhancing the forces exerted on the barrier by the solid phase. Figure 8.20 qualitatively highlights this behaviour. After the impact, at $t = 1.6$ s, the fluid phase transfers part of its force to the solid phase, which in turn increases its force against the barrier.

8.3   Concluding remarks

All these results allow a first evaluation of the influence of an "unretained phase" in the dry monodisperse case. Considering the trapping efficiency of a bidispersed mixture, an equivalent radius r^* of a correspondent monosized simulation has been determined. It emerges that the introduction of a bidispersion lowers the probability of clogging, and thus the trapping efficiency, for a large amount of fine particles, that is for $\Phi_{small} > 0.7$. In the limits of the performed simulations, this value corresponds to a ratio $S/r^* \sim 5$. For the monosized case, $S/r = 5$ corresponds to the transitional value from a high trapped to a partial or low trapped condition. In addition, considering a sectional barrier, the presence of both bidispersion and multiple outlets remarkably lowers the probability of clogging.

The introduction of a fluid phase does not affect the trapping efficiency, also for small amount of solid fraction, i.e. $V_s/V_{box} \geq 0.05$. This result evidences a good correspondence between the results obtained in the bidisperse and in the solid-fluid cases in terms of trapping efficiency. However, it is worth mentioning that the presence of a mixture promotes the clogging also of the "unretained phase". This has to be correctly taken into account in the design perspective. Evaluating the influence on the impact forces, the results reveal an opposite trend between the bidisperse and the solid-fluid case, considering the total forces. The presence of a bidispersion lowers the global impact forces, almost independently from the amount of small particles (Fig. 8.6(a)). The normalised maximum impact forces are obtained by dividing the forces reported in Fig. 8.6(a) by the total discharged mass weight projected along X-direction, that is $W_{s,tot} \sin \theta$=5.7 kN, with $W_{s,tot} = V_{s,tot}\rho_s$. It results that the normalised global maximum force is approximatively 31/5.7=5.4. This normalisation allows to qualitatively compare the bidispersed cases with the the solid-fluid simulations, where the total weight differs from one concentration to the other (Fig. 8.22). The maximum normalised total force for $V_s/V_{box} = 0.35$ (i.e. with equal solid weight and volume of the bidispersed case) is approximately equal to 1.38. Comparing the bidispersed and the solid-fluid simulations with equal solid weight and volume, it results that in the latter case the maximum normalised impact force is 75% lower than in the former configuration.

Considering the solid-fluid case alone, it emerges from Figs. 8.18 and 8.19 that the presence of the fluid phase slightly lowers the solid force with respect to a dry case only during the dynamic phase of the impact. When the solid clogs against the

barrier, the fluid does not impact directly on the barrier but transfers parts of its force through the solid phase, increasing its value. This phenomenon cannot be observed in the bidispersed case.

Chapter 9

Conclusions and further developments

The present thesis focuses on the numerical study of the interaction between a debris flow and an open rigid barrier. As emerged from the literature, the knowledge on barrier trapping efficiency coupled with the forces exerted on the barrier is still incomplete. Due to the complexity of debris-flow phenomena, an appropriate numerical modelling needs a numerical code able to catch in three dimensions the behaviour of granular materials, the influence of a fluid, and their effects when they impact on the barrier. To tackle this problem, an existing DEM-LBM code (Leonardi et al., 2015) has been enhanced with a complete friction model, implementing both static sliding and rolling friction. This development allows the creation of stable structures among grains, and, thus, the possibility that particles clog behind the barrier. These stable structures are generally defined as arches. The new code has been validated by comparison between both experimental results and numerical setups.

Referring to the clogging, the mechanisms and the geometry of the outlet that promote it have been investigated at first. The evaluation in time of the clogged material, i.e. entrapped by the barrier, has been performed in the perspective of studying the barrier trapping efficiency. A monosized dry granular mass has been released under the effect of gravity in an inclined channel, at the end of which the barrier is set. A complete parametric study on a slit barrier has been used as the basis for further simulations on sectional barriers. The influence of the impact angle, of the channel slope, and of the normalized outlet width on both the trapping efficiency

and the impact force time-history have been evaluated and critically discussed. On the basis of the results on a dry monodisperse mass, a more realistic configuration has been analyzed by assuming, on one side, a bidisperse granular mass, accounting for the presence of fine particles, and, on the other side, a fluid phase to be added to the monosized dry granular mass, standing for water and fine particles. Interesting results have been obtained in the frame of trapping efficiency and impact forces.

Considering the trapping efficiency, as a first step the clogging mechanisms have been investigated, revealing the recurrent presence of four different possible clogging scenarios:

- The mass instantaneously clogs and almost the whole mass is entrapped.

- A progressive clogging condition, in which the lower layers of the flowing mass start to clog, while the top part clogs later in time.

- The mass starts to clog after a considerable time lag and the height of the arch is small.

- No clogging occurs.

Starting from the dry monosized material impacting against a slit barrier, the afore-mentioned carried parametric analyses reveal that for the normalized opening width $S/r \leq 4$ an almost complete trapping occurs, while for $4 < S/r \leq 8 - 9$ only a partial trapping verifies and $S/r \simeq 8 - 9$ reveals to be the critical value above which no clogging occurs. Extending to the sectional barrier case, it emerges that all these results are valid if the normalized pile width P/r is at least equal to 6. For smaller pile width, trapping efficiency lowers and, thus, the results have to be slightly adjusted, by decreasing of about a unit S/r. These results provide, in the first instance, a geometrical setting that guarantees a complete trapping for a given characteristic grain size.

Introducing an additional phase representing the material that has to be filtered by the barrier, i.e. considering a bisized granular material, the influence of the small particle volume fraction Φ_{small} is investigated. Interestingly, the high trapping efficiency found in the monosized case is almost preserved for $\Phi_{small} \leq 0.7$. Furthermore, considering an equivalent radius r^*, standing for the radius that would have an equivalent monosized mass with same volume of the bisized, it emerges that $S/r \simeq 5$ is the threshold value from a high- to a low-trapping configuration, similarly

to the "true" monodisperse case. This result is in line with what prescribed by several Authors and technical guidelines, which suggest to adopt $3 \leq S/r \leq 6$.

Finally, adding a fluid phase to the dry monosized granular material, the influence of different solid volume fraction for equal total volume of the mixture $V_{\mathrm{s}}/V_{\mathrm{box}}$, is analyzed. It reveals that for $V_{\mathrm{s}}/V_{\mathrm{box}} \geq 0.05$ the barrier trapping efficiency of the dry material alone is preserved. Both in the bidisperse and in the solid fluid cases (i.e. when a second phase is introduced) the clogging of the primary phase (i.e. the coarse particles) causes the clogging also of the fine material. Fine particles, in fact, must pass through the voids among large particles entrapped behind the barrier.

Impact forces are evaluated analyzing both magnitude and time-history. Starting from a closed barrier and increasing progressively the outlet width, in a slit barrier case, forces near the outlets increase increasing the outlet width. If a complete trapping occurs, a condition similar to the closed barrier case occurs. Furthermore, in all the investigated cases high impact forces are in the lower part of the barrier. On the contrary, the opening width does not affect the intensity of the total impact force exerted on the barrier. Finally, when a stable condition is reached, i.e. a static situation occurs, the magnitude of the forces is a function of the material deposited behind the barrier, and thus depends on the height of the arching. Coupling the study of the impact force with that of arching occurrence, both in the slit barrier and in the sectional barrier cases, the higher the arch H_{arch}, the higher the deposit and the static forces behind the barrier. In addition, high H_{arch} means an instantaneous clog and thus the dynamic phase duration lasts only few instants. Furthermore, both in the slit and the sectional case with $P/r \geq 4$, stable arches structures create also on the barrier face, by generating localised pressure and letting the net span of the arch free of forces.

Interesting considerations emerge considering the introduction of an additional particle size. The bidispersion lowers the global impact forces, almost independently from the amount of smaller particles, while the fluid phase only slightly lowers the solid force with respect to a dry case and only during the dynamic phase of the impact. When the solid clogs against the barrier, the fluid, not directly impacting against the barrier, transfers a part of its force through the solid phase. Comparing the bidispersed and the solid-fluid simulations with equal solid weight and volume, it results that in the solid-fluid case the maximum normalized impact force, i.e. the force normalized by the initial total weight force, is much lower than in the former configuration (with bidispersion).

Further developments of the research can concern investigations both in the mono-phase and two-phase cases. The adoption of a fixed geometrical domain setup can be relaxed. Grain size can be also varied to evidence possible size effects. One aspect that has not been investigated in this thesis is the effect of pore pressure on the global dynamics of the flowing mass. Local variation of the fluid matrix pressure are a major candidate for explaining the large mobility of debris flow. The coupled DEM-LBM method could possibly contribute to understand this phenomenon. It is however not clear whether these vanishing pressure peaks could be captured with the typical employed discretizations. In alternative, extra mobility induced by excess pore pressure could be obtained by enriching the contact law with a lubrication correction. Furthermore, as the present research focuses on the debris-flow barrier interaction, all the simulations start from a dam-break condition in the proximity of the barrier, not considering the mass flowing along the channel. The simulation of debris flow events along the whole path with a coupled continuum-discrete method requires non-affordable computational efforts. An interesting and profitable solution can be simulating with a two-phase continuum depth-averaged model the transportation phase of a debris flow and adapting the obtained velocities and heights upstream of the barrier as inputs for a DEM-LBM analysis of the flow in the barrier proximity.

From the performed analyses it emerges that, for a given S/r, the clogging of large particles, i.e. coarse grains with mean radius r, affects the motion of small particles. Thus, starting from the obtained results, investigating the possible clogging scenarios for the finer fraction (i.e. with a radius smaller than r) is important for the barrier design, in terms both of entrapped materials and impact forces. Different small-to-big radius ratios and volume fractions can be evaluated. Results can influence the choice of the value of r to consider for the filter size. Furthermore, the present research work provides a starting point also for studying the influence of a fluid phase, standing for both water and fine particles. The role of water and the amount of fine particles inside the flow (i.e. its plasticity) can be investigated, performing a wide parametric studies by varying the rheological parameters of the fluid phase.

References

Ai, J., Chen, J.-f., Rotter, J. M., and Ooi, J. Y. (2011). Assessment of rolling resistance models in discrete element simulations. *Powder Technology*, 206(3):269–282.

Albaba, A., Lambert, S., Nicot, F., and Chareyre, B. (2015). Relation between microstructure and loading applied by a granular flow to a rigid wall using DEM modeling. *Granular Matter*, 17(5):603–616.

Albert, R., Albert, I., Hornbaker, D., Schiffer, P., and Barabási, A.-L. (1997). Maximum angle of stability in wet and dry spherical granular media. *Physical Review E*, 56(6):R6271–R6274.

Alonso, M., Sainz, E., Lopez, F. A., and Shinohara, K. (1995). Void-size probability distribution in random packings of equal-sized spheres. *Chemical Engineering Science*, 50(12):1983–1988.

Ancey, C. (2001). Debris flows and related phenomena. In Balmforth, N. J. and Provenzale, A., editors, *Geomorphological Fluid Mechanics*, pages 528–547. Springer Berlin Heidelberg, Berlin, Heidelberg.

Antypov, D. and Elliott, J. A. (2011). On an analytical solution for the damped Hertzian spring. *EPL (Europhysics Letters)*, 94(5):50004.

Arattano, M. and Franzi, L. (2003). On the evaluation of debris flows dynamics by means of mathematical models. *Natural Hazards and Earth System Science*, 3(6):539–544.

Arévalo, R. and Zuriguel, I. (2015). Clogging of granular materials in silos: effect of gravity and outlet size. *Soft Matter*, 12:123–130.

Armanini, A. (1997). On the dynamic impact of debris flows. *Recent Development on Debris Flows*, Lecture No:208–226.

Armanini, A., Claudio, D., and Larcher, M. (2006). Slit-Check Dams for Controlling Debris Flow and Mudflow Effect of a width contraction in a debris / mud channel flow. *Disaster Mitigation of Debris Flows, Slope Failures and Landslides*, pages 141–148.

Armanini, A., Dellagiacoma, F., and Ferrari, L. (1991). From the check dam to the development of functional check dams. In *Fluvial Hydraulics of Mountain Regions*, pages 331–344.

Armanini, A., Fraccarollo, L., and Rosatti, G. (2009). Two-dimensional simulation of debris flows in erodible channels. *Computers & Geosciences*, 35(5):993–1006.

Armanini, A. and Larcher, M. (2001). Rational criterion for designing opening of slit-check dam. *Journal of Hydraulic Engineering*, 127(2):94–104.

Armanini, A. and Scotton, P. (1993). On the dynamic impact of a debris flow on structures. In *Proceedings of XXV IAHR Congress, Tokyo (Tech. Sess. B, III)*, pages 203–210.

Ashour, A., Wegner, S., Trittel, T., Börzsönyi, T., and Stannarius, R. (2017). Outflow and clogging of shape-anisotropic grains in hoppers with small apertures. *Soft Matter*, 13(2):402–414.

Bagnold, R. A. (1971). *The Physics of Blown Sand and Desert Dunes*. Springer Netherlands, Dordrecht, 1971 edition.

Balevičius, R., Kačianauskas, R., Mróz, Z., and Sielamowicz, I. (2008). Discrete-particle investigation of friction effect in filling and unsteady/steady discharge in three-dimensional wedge-shaped hopper. *Powder Technology*, 187(2):159–174.

Balevičius, R., Kačianauskas, R., Mróz, Z., and Sielamowicz, I. (2011). Analysis and DEM simulation of granular material flow patterns in hopper models of different shapes. *Advanced Powder Technology*, 22(2):226–235.

Bardou, E., Ancey, C., Bonnard, C., and Vuillet, L. (2003). Classification of debris-flow deposits for hazard assessment in alpine areas. In *Proceedings of the 3rd International Conference on debris flow hazards mitigation*, pages 799–808.

Beer, F. and Johnson, E. (1976). *Mechanics for Engineers – Statics and Dynamics*. MacGraw-Hill, New York, 1976 edition.

Bhatnagar, P. L., Gross, E. P., and Krook, M. (1954). A Model for Collision Processes in Gases. I. Small Amplitude Processes in Charged and Neutral One-Component Systems. *Physical Review*, 94(3):511–525.

Braun, O. M. and Peyrard, M. (2011). Dependence of kinetic friction on velocity: Master equation approach. *Physical Review E*, 83(4):046129.

Brilliantov, N. and Pöschel, T. (2003). *Kinetic Theory of Granular Gases*. Oxford University Press, Oxford, oxford uni edition.

Brilliantov, N. V. and Pöschel, T. (1998). Rolling friction of a viscous sphere on a hard plane. *EPL (Europhysics Letters)*, 42(5):511.

Bugnion, L., McArdell, B. W., Bartelt, P., and Wendeler, C. (2012). Measurements of hillslope debris flow impact pressure on obstacles. *Landslides*, 9(2):197–187.

Calvetti, F., di Prisco, C., and Vairaktaris, E. (2015). Impact of dry granular masses on rigid barriers. *IOP Conference Series: Earth and Environmental Science*, 26:012036.

Calvetti, F., di Prisco, C., and Vairaktaris, E. (2016). Dry Granular Flows Impacts on Rigid Obstacles: DEM Evaluation of a Design Formula for the Impact Force. *Procedia Engineering*, 158:290–295.

Calvetti, F., di Prisco, C. G., and Vairaktaris, E. (2017). DEM assessment of impact forces of dry granular masses on rigid barriers. *Acta Geotechnica*, 12(1):129–144.

Calvetti, F. and Vairaktaris, E. G. (2016). Debris flow impact forces on rigid barriers: existing practice versus DEM numerical results. In *1st International Conference on Natural Hazard & Infrastructure, 28-30 June, 2016, Chania, Greece*, pages 1–14.

Carrigy, M. A. (1970). Experiments on the angles of repose of granular materials. *Sedimentology*, 14(474):147–158.

Carstensen, J. and Chan, P.-C. (1976). Relation between particle size and repose angles of powders. *Powder Technology*, 15(1):129–131.

Ceccato, F. and Simonini, P. (2016). Granular Flow Impact Forces on Protection Structures: MPM Numerical Simulations with Different Constitutive Models. *Procedia Engineering*, 158:164–169.

Ceccato, F., Simonini, P., di Prisco, C., and Redaelli, I. (2017). The effect of the front inclination on the impact forces transmitted by granular flows to rigid structures. In *World Landslides Forum: Advancing Culture of Living with Landslides*, pages 593–599.

Chevoir, F., Gaulard, F., and Roussel, N. (2007). Flow and jamming of granular mixtures through obstacles. *Europhysics Letters (EPL)*, 79(1):14001.

Choi, C., Goodwin, G., Ng, C., Cheung, D., Kwan, J., and Pun, W. (2016). Coarse granular flow interaction with slit structures. *Geotechnique Letters*, 4(4):1–8.

Choi, C., Ng, C., Song, D., Kwan, J., Shiu, H., Ho, K., and Koo, R. (2014). Flume investigation of landslide debris-resisting baffles. *Canadian Geotechnical Journal*, 51(5):540–553.

Choi, S.-K., Lee, J.-M., and Kwon, T.-H. (2018). Effect of slit-type barrier on characteristics of water-dominant debris flows: small-scale physical modeling. *Landslides*, 15:111–122.

Cleary, P. W. and Sawley, M. L. (2002). DEM modelling of industrial granular flows: 3D case studies and the effect of particle shape on hopper discharge. *Applied Mathematical Modelling*, 26(2):89–111.

Costa, J. E. (1984). Physical geomorphology of debris flow. In Costa JE, F. P., editor, *Developments and Applications in Geomorphology*, pages 268–317. Springer, Berlin, Heidelberg.

Coussot, P. and Meunier, M. (1996). Recognition, classification and mechanical description of debris flows. *Earth-Science Reviews*, 40:209–227.

Cruden, D. and Varnes, D. (1996). Landslide types and processes. In Turner AK, S. R., editor, *Landslides investigation and mitigation. Special Report 247*, pages 36–75. Transportation research board, US National Research Council, Washington DC.

Cundall, P. and Strack, O. (1979). A discrete numerical model for granular assemblies. *Géotechnique*, 29(1):47–65.

D'Agostino, V. and Bertoldi, G. (2014). On the assessment of the management priority of sediment source areas in a debris-flow catchment. *Earth Surface Processes and Landforms*, 39(5):656–668.

Daido, A. (1993). Impact force of mud debris flow on structures. In *Proceedings of XXV IAHR Congress, Tokyo (Tech. Sess. B, III)*, pages 211–218.

Di Maio, F. P. and Di Renzo, A. (2004). Analytical solution for the problem of frictional-elastic collisions of spherical particles using the linear model. *Chemical Engineering Science*, 59(16):3461–3475.

Du, R., Kang, Z., Chen, X., and Zhu, P. (1987). A comprehensive investigation and control planning for debris flow in the xiaojiang river basin of yunnan province. *Science Press*, page 287.

Egli, T. (2000). Objektschutz: Angepasste bauweise reuziert das personen und sachrisiko bei gabauden. Technical report, Interpravent 2000.

El Shourbagy, S. and Matuttis, H.-G. (2005). *Proc. Powders and Grains*. Balkema, Leiden.

Elperin, T. and Golshtein, E. (1997). Comparison of different models for tangential forces using the particle dynamics method. *Physica A: Statistical Mechanics and its Applications*, 242(3-4):332–340.

Fannin, R. J. and Wise, M. P. (2001). An empirical-statistical model for debris flow travel distance. *Canadian Geotechnical Journal*, 38(5):982–994.

FEMA P-259 (2012). Engineering Principles and Practices for Retrofitting Flood-Prone Residential Structures (Third Edition).

FEMA P-55 (2011). Coastal Construction Manual, Principles and Practices of Planning, Siting, Designing, Constructing, and Maintaining Residential Buildings in Coastal Areas (Fourth Edition).

Feng, Z. G. and Michaelides, E. E. (2004). The immersed boundary-lattice Boltzmann method for solving fluid-particles interaction problems. *Journal of Computational Physics*, 195(2):602–628.

Frankowski, P. and Morgeneyer, M. (2013). Calibration and validation of DEM rolling and sliding friction coefficients in angle of repose and shear measurements. *AIP Conference Proceedings*, 1542:851–854.

Fukawa, G., Katsuki, S., Ishikawa, N., and Yamada, T. (2002). Simulation and stochastic evaluation of the open type steel check dam for damming up performance. In *International Congress INTERPRAEVENT 2002 in the Pacific Rim - Matsumoto (JP)*, pages 751–760.

Gabrieli, F. and Ceccato, F. (2016). Impact of Dry Granular Flows on a Rigid Wall: Discrete and Continuum Approach. *Procedia Engineering*, 158:152–157.

Garcimartín, A., Zuriguel, I., Pugnaloni, L. A., and Janda, A. (2010). Shape of jamming arches in two-dimensional deposits of granular materials. *Physical Review E*, 82(3):031306.

Ghazavi, M., Hosseini, M., and Mollanouri, M. (2008). A comparison between angle of repose and friction angle of sand. *Proceedings of the 12th International Association for Computer Methods and Advances in Geomechanics (IACMAG)*, pages 1272–1275.

Girolami, L., Hergault, V., Vinay, G., and Wachs, A. (2012). A three-dimensional discrete-grain model for the simulation of dam-break rectangular collapses: Comparison between numerical results and experiments. *Granular Matter*, 14(3):381–392.

Gracia, F., Villard, P., and Richefeu, V. (2017). A comparison between DEM and MPM for the modeling of unsteady flow. *EPJ Web of Conferences*, 140:11011.

Haff, P. K. and Werner, B. T. (1986). Computer Simulation of the Sorting of Grains. *Poweder Techn.*, 48(3):239–245.

Han, W. and Ou, G. (2006). Efficiency of slit dam prevention against non-viscous debris flow. *Wuhan University Journal of Natural Sciences*, 11(4):865–869.

Hertz, H. (1882). Ueber die Berührung fester elastischer Körper. *Journal für die reine und angewandte Mathematik (Crelle's Journal)*, 1882(92).

Hidalgo, R. C., Lozano, C., Zuriguel, I., and Garcimartín, A. (2013). Force analysis of clogging arches in a silo. *Granular Matter*, 15(6):841–848.

Hill, K. M. and Tan, D. S. (2014). Segregation in dense sheared flows: gravity, temperature gradients, and stress partitioning. *J. Fluid Mech.*, 756:54–88.

Holst, J. M. F. G., Rotter, J. M., Ooi, J. Y., and Rong, G. H. (1999). Numerical modeling of silo filling - Part 2: discrete element analyses and comparison. *Journal of Engineering Mechanics ASCE*, 125(1):104–110.

Huang, H.-p., Yang, K.-c., and Lai, S.-w. (2007). Impact force of debris flow on filter dam. *European Geosciences Union General Assembly*, 9:1–32.

Hübl, J. and Fiebiger, G. (2005). *Debris-flow mitigation measures*, pages 445–487. Springer Berlin Heidelberg, Berlin, Heidelberg.

Hübl, J. and Holzinger, G. (2003). Entwicklung von Grundlagen zur Dimensionierung kronenoffener Bauwerke für die Geschiebebewi rtschaftung in Wildbächen: Kleinmaßstabliche. WLS Report 50-3. Technical report, Institute for Forest and Mountain Risk Engineering, BOKU. University of Natural Resources and Applied Life Sciences, Vienna, Modellversuche zur Wirkung von Murbrechern.

Hübl, J., Nagl, G., Suda, J., and Rudolf-Miklau, F. (2017). Standardized Stress Model for Design of Torrential Barriers under Impact by Debris Flow (According to Austrian Standard Regulation 24801). *International Journal of Erosion Control Engineering*, 10(1):47–55.

Hübl, J., Strauss, A., Holub, M., and Suda, J. (2005). Structural mitigation measures. In *3rd Probabilistic Workshop: Technical Systems + Natural Hazards, 24.- 25. Nov. 2005, Wien*.

Hübl, J., Suda, J., Proske, D., Kaitna, R., and Scheidl, C. (2009). Debris Flow Impact Estimation. In *International Symposium on Water Management and Hydraulic Engineering*, pages 137–148.

Hungr, O. (1995). A model for the runout analysis of rapid flow slides, debris flows, and avalanches. *Canadian Geotechnical Journal*, 32(4):610–623.

Hungr, O., Corominas, J., and Eberhardt, E. (2005). Estimating landslide motion mechanism, travel distance and velocity. In *International Conference on Landslide Risk Management*, pages 99–128.

Hungr, O., Evans, S., Bovis, M., and Hutchinson, J. (2001). Review of the classification of landslides of the flow type. *Environmental and Engineering Geosciences*, VII:221–238.

Hungr, O., Leroueil, S., and Picarelli, L. (2014). The Varnes classification of landslide types, an update. *Landslides*, 11(2):167–194.

Hungr, O., Morgan, G. C., and Kellerhals, R. (1984). Quantitative analysis of debris torrent hazards for design of remedial measures. *Canadian Geotechnical Journal*, 21:663–677.

Hutchinson, J. (1988). General report: morphological and geotechnical parameters of landslides in relation to geology and hydrogeology. In *Proceedings of the 5th International Symposium on Landslides*, pages 3–35, Lausanne.

Hutter, K., Svendsen, B., and Rickenmann, D. (1996). Debris flow modeling: A review. *Continuum Mechanics and Thermodynamics*, 8(1):1–35.

Ikeya, H. (1989). Debris flow and its countermeasures in Japan. *Bulletin of the International Association of Engineering Geology*, 40(1):15–33.

Ishikawa, N., Shima, J., Matsubara, T., Tatesawa, H., Horiguchi, T., and Mizuyama, T. (2014). Trapping mechanism of debris flow by steel open dams. INTERPRAEVENT 2014 in the Pacific Rim, O-23, 1-6, Nov. 25-28, 2014, Nara, Japan.

Itoh, T., Horiuchi, S., Akanuma, J.-i., Kaitsuka, K., Kuraoka, S., Morita, T., Sugiyama, M., and Mizuyama, T. (2011). Fundamental Hydraulic Flume Tests Focused on Sediment Control Function using a Grid-Type High Dam. In *5th International Conference on Debris-Flow Hazards Mitigation: Mechanics, Prediction and Assessment*, pages 1051–1061.

Iverson, R. (1997). The physics of debris flows. *Reviews of Geophysics*, 35(3):245–296.

Iverson, R. (2003). The debris-flow rheology myth. *3rd International Conference on Debris-Flow Hazards Mitigation: Mechanics, Prediction, and Assessment*, pages 303–314.

Iverson, R. M. (2014). Debris flows: behaviour and hazard assessment. *Geology Today*, 30(1):15–20.

Iverson, R. M., Reid, M. E., and LaHusen, R. G. (1997). Debris-Flow Mobilization From Landslides 1. *Annual Review of Earth and Planetary Sciences*, 25(1):85–138.

Jakob, C. and Konietzky, H. (2005). Particle methods. *International Journal for Numerical Methods in Fluids*, 47:693–705.

Janda, a., Zuriguel, I., Garcimartín, A., Pugnaloni, L. a., and Maza, D. (2008). Jamming and critical outlet size in the discharge of a two-dimensional silo. *EPL (Europhysics Letters)*, 84(4):44002.

Jeong, S. W. (2014). The effect of grain size on the viscosity and yield stress of fine-grained sediments. *Journal of Mountain Science*, 11(1):31–40.

Jiang, M. J., Yu, H.-S., and Harris, D. (2005). A novel discrete model for granular material incorporating rolling resistance. *Computers and Geotechnics*, 32(5):340–357.

Jiang, Y.-J., Zhao, Y., Towhata, I., and Liu, D.-X. (2015). Influence of particle characteristics on impact event of dry granular flow. *Powder Technology*, 270:53–67.

Johannesson, T., Gauer, P., Issler, P., and Leid, K. (2009). The design of avalanche protection dams. Technical report, European Commision, Climate Change and Natural Hazard Research - Series 2 Project report, 2009.

Johnson, C. G., Kokelaar, B. P., Iverson, R. M., Logan, M., Lahusen, R. G., and Gray, J. M. N. T. (2012). Grain-size segregation and levee formation in geophysical mass flows. *Journal of Geophysical Research: Earth Surface*, 117(1):1–23.

Kaitna, R., Proske, D., König, U., Hübl, J., and Holzinger, G. (2007). On design impact forces for torrential barrier structures. *Proceedings of the European Safety and Reliability Conference 2007, ESREL 2007 - Risk, Reliability and Societal Safety*, 3:2209–2217.

Khan, K. M. and Bushell, G. (2005). Comment on "Rolling friction in the dynamic simulation of sandpile formation". *Physica A: Statistical Mechanics and its Applications*, 352:522–524.

Kherkheulidze, I. I. (1967). Estimation of basic characteristics of mud flows. Technical report, International Association of Scientific Hydrology (IAHS) Studies and Reports in Hydrology.

Koo, R. C. H., Kwan, J. S. H., Ng, C. W. W., Lam, C., Choi, C. E., Song, D., and Pun, W. K. (2017). Velocity attenuation of debris flows and a new momentum-based load model for rigid barriers. *Landslides*, 14(2):617–629.

Körner, C., Thies, M., Hofmann, T., Thürey, N., and Rüde, U. (2005). Lattice Boltzmann model for free surface flow for modeling foaming. *Journal of Statistical Physics*, 121(1-2):179–196.

Kuwabara, G. and Kono, K. (1987). Restitution coefficient in a collision between two spheres. *Japanese Journal of Applied Physics*, 26(8R):1219–1223.

Kwan, J. (2012). Supplementary Technical Guidance on Design of Rigid Debris-resisting Barriers. GEO Report No. 270. Technical Report No. 270, Geotechnical Engineering Office Civil Engineering and Development Department The Government of the Hong Kong Special Administrative Region, Hong Kong.

Ladd, A. J. C. (1994). Numerical simulations of particulate suspensions via a discretized Boltzmann equation. Part I. Theoretical foundation. *Journal of Fluid Mechanics*, 271(1):285–309.

Larcher, M. and Armanini, A. (2000). Design criteria of slit check dams and downstream channels for debris flows. In *International Workshop on the debris flow disaster of December 1999 in Venezuela*, pages 1–12.

Lee, J. and Herrmann, H. J. (1993). Angle of repose and angle of marginal stability: molecular dynamics of granular particles. *Journal of Physics A: Mathematical and General*, 26(2):373–383.

Leonardi, A. (2015). *Numerical simulation of debris flow and interaction between flow and obstacle via DEM*. PhD thesis, ETH Zurich.

Leonardi, A., Cabrera, M., Wittel, F. K., Kaitna, R., Mendoza, M., Wu, W., and Herrmann, H. J. (2015). Granular-front formation in free-surface flow of concentrated suspensions. *Physical Review E - Statistical, Nonlinear, and Soft Matter Physics*, 92(5):1–10.

Leonardi, A., Wittel, F. K., Mendoza, M., and Herrmann, H. J. (2014). Coupled DEM-LBM method for the free-surface simulation of heterogeneous suspensions. *Computational Particle Mechanics*, 1(1):3–13.

Leonardi, A., Wittel, F. K., Mendoza, M., Vetter, R., and Herrmann, H. J. (2016). Particle-Fluid-Structure Interaction for Debris Flow Impact on Flexible Barriers. *Computer-Aided Civil and Infrastructure Engineering*, 31(5):323–333.

Leonardi, C. R., Owen, D. R. J., and Feng, Y. T. (2011). Numerical rheometry of bulk materials using a power law fluid and the lattice Boltzmann method. *Journal of Non-Newtonian Fluid Mechanics*, 166(12-13):628–638.

Li, S., Yao, Q., Chen, B., Zhang, X., and Yl, D. (2007). Molecular dynamics simulation and continuum modelling of granular surface flow in rotating drums. *Chinese Science Bulletin*, 52(5):692–700.

Li, X., He, S., Luo, Y., and Wu, Y. (2010). Discrete element modeling of debris avalanche impact on retaining walls. *Journal of Mountain Science*, 7(3):276–281.

Li, Y., Xu, Y., and Thornton, C. (2005). A comparison of discrete element simulations and experiments for 'sandpiles' composed of spherical particles. *Powder Technology*, 160(3):219–228.

Lichtenhahn, C. (1973). Die Berechnung von Sperren in Beton und Eisenbeton. *Kolloquium über Wildbachsperren, Mitteilungen der forstlichen Bundesversuchsanstal*, 102:91–127.

Lien, H. (2002). Study on treatments of debris flow (ii). Technical report, Soil and Water Conservation Bureau, Council of Agriculture (COA), Taiwan.

Lin, H. (1994). The study of impact force of debris flow upon model dams of different types. Master's thesis, National Chung Hsing University, Taichung, Taiwan.

Liu, J. and Zhou, J. (2008). Numerical Study on Sandpile Formation of Granular Materials with Different Grain Size Distributions. In Liu, H., Deng, A., and Chu, J., editors, *Geotechnical Engineering for Disaster Mitigation and Rehabilitation: Proceedings of the 2nd International Conference GEDMAR08, Nanjing, China 30 May – 2 June, 2008*, pages 374–380. Springer Berlin Heidelberg, Berlin, Heidelberg.

Lo, D. (2000). Review of natural terrain landslide debris-resisting barrier design. GEO Report no. 104. Technical report, Geotechnical Engineering Office Civil Engineering and Development Department The Government of the Hong Kong Special Administrative Region.

Lötstedt, P. (1981). Coulomb Friction in Two-Dimensional Rigid Body Systems. *ZAMM - Zeitschrift für Angewandte Mathematik und Mechanik*, 61(12):605–615.

Luding, S. (2005). Molecular Dynamics Simulations of Granular Materials. In *The Physics of Granular Media*, pages 297–324. Wiley-VCH Verlag GmbH & Co. KGaA, Weinheim, FRG.

Luding, S. (2008). Introduction to discrete element methods: Basic of contact force models and how to perform the micro-macro transition to continuum theory. *European Journal of Environmental and Civil Engineering*, 12(7–8):785–826.

Magalhães, C. F. M., Moreira, J. G., and Atman, A. P. F. (2010). Catastrophic regime in the discharge of a granular pile. *Physical Review E - Statistical, Nonlinear, and Soft Matter Physics*, 82(5):1–4.

Magalhães, C. F. M., Moreira, J. G., and Atman, A. P. F. (2012). Segregation in arch formation. *The European Physical Journal E*, 35(5):38.

Magalhães, F. G. R., Atman, a. P. F., Moreira, J. G., and Herrmann, H. J. (2015). Analysis of the velocity field of granular hopper flow. *Granular Matter*, 18(2):1–11.

Management), N. N. I. f. L. and Infrastructure (2007). Manual of technical standards for designing sabo facilities against debris flow and Driftwood, Technical Note of NILIM No. 365. Tsukuba, Japan:(in Japanese).

Marchelli, M., Leonardi, A., and Pirulli, M. (2017a). Modellazione numerica dem dell'interazione di flussi granulari secchi con barriere a singola apertura: analisi dell'effetto arco e della dinamica di impatto. In *IARG 2017 Incontro Annuale dei Ricercatori di Geotecnica*, pages 1–6.

Marchelli, M., Leonardi, A., and Pirulli, M. (2017b). Numerical analysis of debris-flow interaction with open barriers. In *PARTICLES 2017. V International Conference on Particle-based Methods - Fundamentals and Applications*, pages 837–848.

Marchelli, M., Leonardi, A., and Pirulli, M. (2018). The clogging mechanism of debris-flow material in the multiple-outlets of sectional barriers. *GEAM Geoingegneria Ambientale e Mineraria* (in Press).

Marks, B. and Einav, I. (2011). A cellular automaton for segregation during granular avalanches. *Granular Matter*, 13(3):211–214.

Marks, B., Rognon, P. G., and Einav, I. (2012). Grainsize dynamics of polydisperse granular segregation down inclined planes. *J. Fluid Mech.*, 690:499–511.

Matuttis, H. G., Luding, S., and Herrmann, H. J. (2001). Discrete element simulations of dense packing and heaps made of spherical and non-spherical particles. *Powder Technology*, 109(1-3):278–292.

Metcalf, J. (1966). Angle of repose and internal friction. *International Journal of Rock Mechanics and Mining Sciences & Geomechanics Abstracts*, 3(2):155–161.

Mitarai, N. and Nakanishi, H. (2003). Hard-sphere limit of soft-sphere model for granular materials: Stiffness dependence of steady granular flow. *Physical Review E*, 67(2):021301.

Miura, K., Maeda, K., and Toki, S. (1997). Method of measurement for the angle of repose of sands. In Japanese Geotechnical Society, editor, *Soils and Fundations*, volume 37, pages 89–96. NTT-Electronic Library Service, 1997 edition.

Mizuyama, T. (1979). Computational method and some consideration on impulsive force of debris flow acting on sabo dams. 11(2):40–43.

Mizuyama, T., Kobashi, S., and Mizuno, H. (1995). Control of Passing Sediment with Grid-type Dams. *Sabo Gakkaishi*, 47(5):8–13.

MLR (2004). Design standards for debris flow hazard mitigation measures (DZ/T0239-2004). Beijing, China: (in Chinese).

Mohamad, A. A. (2011). *Lattice Boltzmann Method*, volume 1. Springer London, London.

Mondal, S. and Sharma, M. M. (2014). Role of flying buttresses in the jamming of granular matter through multiple rectangular outlets. *Granular Matter*, 16(1):125–132.

Mondal, S., Sharma, M. M., Chanpura, R. A., Parlar, M., and Ayoub, J. A. (2011). Numerical Simulations of Sand-Screen Performance in Standalone Applications. *SPE Drilling & Completion*, 26(04):472–483.

Nagel, S. R. (1992). Instabilities in a sandpile. *Reviews of Modern Physics*, 64(1):321–325.

Nakano, K. and Ukon, S. (1986). Experiments of impact of sand avalanches. *Journal of Japan Society of Erosion Control Engineering*, 39(1):17–23.

Navarro, H. A. and Braun, M. P. D. S. (2013). Determination of the normal spring stiffness coefficient in the linear spring-dashpot contact model of discrete element method. *Powder Technology*, 246:707–722.

Nikitin, K. D., Olshanskii, M. A., Terekhov, K. M., and Vassilevski, Y. V. (2012). Numerical Modelling of Viscoplastic Free Surface Flows in Complex 3D Geometries. In *European Congress on Computational Methods in Applied Sciences and Engineering*, pages 1–14.

Norouzi, H. R., Zarghami, R., Sotudeh-Gharebagh, R., and Mostoufi, N. (2016). *Coupled CFD-DEM Modeling*. John Wiley & Sons, Ltd, Chichester, UK, 2016 edition.

ONR 24800 (2009). Protection works for torrent control - Terms, definitions and classification. Technical report, Austrian Standards.

ONR 24801 (2013). Protection works for torrent control - Actions on structures. Technical report, Austrian Standards.

ONR 24802 (2010). Protection works for torrent control - Design of structures. Technical report, Austrian Standards.

ONR 24803 (2008). Protection works for torrent control - Operation, monitoring, maintenance. Technical report, Austrian Standards.

Pailha, M. and Pouliquen, O. (2009). A two-phase flow description of the initiation of underwater granular avalanches. *Journal of Fluid Mechanics*, 633:115.

Pierson, T. (1986). Flow behavior of channelized debris flows Mount St. Helens Washington. In *Hillslope Processes*, pages 269–296. Boston, Allen & Unwin.

Pierson, T. C. and Costa, J. E. (1987). A rheological classification of subaerial sediment-water flows. *Geological Society of America: Reviews in Engineering Geology*, VII:1–14.

Pirulli, M. (2010). Continuum description of flow-like landslide dynamics. In *Continuum mechanics*, pages 105–146. Nova Science Publishers, New York.

Pirulli, M., Scavia, C., and Tararbra, M. (2015). On the Use of Numerical Models for Flow-like Landslide Simulation. In Lollino, G., Giordan, D., Crosta, G. B., Corominas, J., Azzam, R., Wasowski, J., and Sciarra, N., editors, *Engineering Geology for Society and Territory - Volume 2: Landslide Processes*, pages 1625–1628. Springer International Publishing, Cham.

Pitman, E. B. and Le, L. (2005). A two-fluid model for avalanche and debris flows. *Philosophical transactions. Series A, Mathematical, physical, and engineering sciences*, 363(1832):1573–1601.

Piton, G. and Recking, A. (2016). Design of sediment traps with open check dams. I: Hydraulic and deposition processes. *Journal of Hydraulic Engineering*, 142(2):04015045.

Pöschel, T. (2005). *Computational Granular Dynamics*. Springer-Verlag, Berlin/Heidelberg.

Pöschel, T. and Buchholtz, V. (1993). Static friction phenomena in granular materials: Coulomb law versus particle geometry. *Physical Review Letters*, 71(24):3963–3966.

Pournin, L., Ramaioli, M., Folly, P., and Liebling, T. M. (2007). About the influence of friction and polydispersity on the jamming behavior of bead assemblies. *European Physical Journal E*, 23(2):229–235.

Pudasaini, S. P. (2012). A general two-phase debris flow model. *Journal of Geophysical Research: Earth Surface*, 117(3):1–28.

Reboul, N., Vincens, E., and Cambou, B. (2008). A statistical analysis of void size distribution in a simulated narrowly graded packing of spheres. *Granular Matter*, 10(6):457–468.

Sadrekarimi, a. and Olson, S. (2011). Critical state friction angle of sands. *Géotechnique*, 61(9):771–783.

Salciarini, D., Tamagnini, C., and Conversini, P. (2010). Discrete element modeling of debris-avalanche impact on earthfill barriers. *Physics and Chemistry of the Earth*, 35(3-5):172–181.

Savage, S. B. and Hutter, K. (1989). The motion of a finite mass of granular material down a rough incline. *Journal of Fluid Mechanics*, 199:177–215.

Scotton, P. and Deganutti, A. M. (1997). Phreatic line and dynamic impact in laboratory debris flow experiments. In *1st International Conference on Debris-Flow Hazards: Mitigation, Mechanics, Prediction and Assessment, San Francisco*.

Senetakis, K., Coop, M. R., and Todisco, M. C. (2013). The inter-particle coefficient of friction at the contacts of Leighton Buzzard sand quartz minerals. *Soils and Foundations*, 53(5):746–755.

Shafer, J., Dippel, S., and Wolf, D. E. (1996). Force Schemes in Simulations of Granular Materials. *Journal de Physique I*, 6(1):5–20.

Sharpe, C. F. (1938). *Landslides and related phenomena.* Columbia University Press, New York.

Sheldon, H. G. and Durian, D. J. (2010). Granular discharge and clogging for tilted hoppers. *Granular Matter*, 12(6):579–585.

Shima, J., Moriyama, H., Kokuryo, H., Ishikawa, N., and Mizuyama, T. (2016). Prevention and Mitigation of Debris Flow Hazards by Using Steel Open-Type Sabo Dams. *International Journal of Erosion Control Engineering*, 9(3):135–144.

Shrestha, Badri Bhakta Nakagawa, H., Kawaike, K., and Baba, Y. (2007). Study on Debris-Flow Deposition and Erosion Processes Upstream of a Check Dam.

Silva, M., Costa, S., Canelas, R., Pinheiro, A., and Cardoso, A. (2016). Experimental and numerical study of slit-check dams. *International Journal of Sustainable Development and Planning*, 11(2):107–118.

Silva, M., Costa, S., and Cardoso, a. H. (2015). Effect of plan layout on the sediment control efficiency of slit-check dams for stony type debris flows mitigation. In *River Basin Management VIII*, volume 197, pages 259–270.

Song, Y. (1994). A study of impact of debris flow. Master's thesis, National Chung Hsing University, Taichung, Taiwan.

Stini, J. (1910). *Die Muren.* Verlag der Wagner'shen Universitätsbuchhandlung, Innsbruck, 1910 edition.

Succi, S., Benzi, R., and Higuera, F. (1991). The Lattice Boltzmann Equation: a new tool for computational fluid-dynamics. *Physica D*, 47:219–230.

Suda, J., Hübl, J., and Bergmeister, K. (2010). Design and construction of high stressed concrete structures as protection works for torrent control in the Austrian alps. In *Proceedings of the Third International fib Congress*, pages 1–12.

Suda, J., Strauss, A., Rudolf-Miklau, F., and Hübl, J. (2009). Safety assessment of barrier structures. *Structure and Infrastructure Engineering*, 5(4):311–324.

Švec, O., Skoček, J., Stang, H., Geiker, M. R., and Roussel, N. (2012). Free surface flow of a suspension of rigid particles in a non-Newtonian fluid: A lattice Boltzmann approach. *Journal of Non-Newtonian Fluid Mechanics*, 179-180:32–42.

SWCB (Soil and Water Conservation Bureau) (2005). Soil and water conservation handbook. Nantou, Taiwan: Soil and Water Conservation (in Chinese).

Szarf, K., Combe, G., and Villard, P. (2011). Polygons vs. clumps of discs: A numerical study of the influence of grain shape on the mechanical behaviour of granular materials. *Powder Technology*, 208(2):279 – 288. Special Issue: Papers presented to the Symposium STPMF 2009,Science and Technology of Powders and Sintered Materials.

Takahashi, T. (1978). Mechanical characteristics of debris flow. *Journal of Hydraulic Engineering*, 104:1153–1169.

Takahashi, T. (2007). *Debris flow. Mechanics, Prediction and Countermeasures*. Taylor & Francis/Balkema, London, 2007 edition.

Teufelsbauer, H., Wang, Y., Chiou, M. C., and Wu, W. (2009). Flow-obstacle interaction in rapid granular avalanches: DEM simulation and comparison with experiment. *Granular Matter*, 11(4):209–220.

Teufelsbauer, H., Wang, Y., Pudasaini, S. P., Borja, R. I., and Wu, W. (2011). DEM simulation of impact force exerted by granular flow on rigid structures. *Acta Geotechnica*, 6(3):119–133.

Thomas, C. C. and Durian, D. J. (2013). Geometry dependence of the clogging transition in tilted hoppers. *Physical Review E - Statistical, Nonlinear, and Soft Matter Physics*, 87(5):1–8.

Thürey, N. and Rüde, U. (2009). Stable free surface flows with the lattice Boltzmann method on adaptively coarsened grids. *Computing and Visualization in Science*, 12(5):247–263.

To, K. (2005). Jamming transition in two-dimensional hoppers and silos. *Physical Review E - Statistical, Nonlinear, and Soft Matter Physics*, 71(6):1–4.

To, K. and Lai, P. Y. (2002). Jamming pattern in a two-dimensional hopper. *Physical Review E - Statistical, Nonlinear, and Soft Matter Physics*, 66(1):1–8.

To, K., Lai, P. Y., and Pak, H. K. (2001). Jamming of granular flow in a two-dimensional hopper. *Physical Review Letters*, 86(1):71–74.

Tsuji, Y., Tanaka, T., and Ishida, T. (1992). Lagrangian numerical simulation of plug flow of cohesionless particles in a horizontal pipe. *Powder Technology*, 71(3):239–250.

Tsukahara, M. (2009). *Jamming in Granular Media: Modeling of Experimental Data*. PhD thesis, EPFL Lausanne.

Turnbull, B., Bowman, E. T., and McElwaine, J. N. (2015). Debris flows: Experiments and modelling. *Comptes Rendus Physique*, 16(1):86 – 96. Granular physics / Physique des milieux granulaires.

Vagnon, F. and Segalini, A. (2016). Debris flow impact estimation on a rigid barrier. *Natural Hazards and Earth System Sciences*, 16(7):1691–1697.

Vallance, J. W. (2005). *Volcanic debris flows*, pages 247–274. Springer Berlin Heidelberg, Berlin, Heidelberg.

Van Burkalow, A. (1945). Angle of repose and angle of sliding friction: an experimental study. *Bulletin of the Geological Society of America*, 56(6):669–707.

Van Dine, D. (1996). Debris flow control structures for forest engineering. Technical report, B.C. Ministry of Forests.

Varnes, D. (1954). Landslide types and processes. In Schuster RL, K. R., editor, *Landslides and engineering practice, special report 28*, pages 20–47. Highway research board. National Academy of Sciences, Washington DC.

Varnes, D. (1978). Slope movement types and processes. In: Schuster RL, Krizek RJ (eds) Landslides, analysis and control, special report 176. Technical report, Transportation research board, National Academy of Sciences, Washington DC.

Vikhansky, A. (2008). Lattice-Boltzmann method for yield-stress liquids. *Journal of Non-Newtonian Fluid Mechanics*, 155(3):95–100.

Wang, C., Chen, S.-c., and Lu, S.-j. (2014). Sediment trapping efficiency of adjustable check dam in laboratory and field experiment. Technical Report 1.

Watanabe, M. and Ikeya, H. (1981). Investigation and analysis of volcanic mud flows on mout sakurajima. *International Association of Hydrological Sciences Publ. Florence*, (133):245–256.

Watanabe, M., Mizuyama, T., and Uehara, S. (1980). Review of debris flow countermeasure facilities. *Journal of Japanese Erosion Control Engineering Society*, 115:40–45.

Wehrmann, H. and Johannes, H. (2006). Classification of Dams in Torrential Watersheds. In *Disaster Mitigation of Debris Flows, Slope Failures and Landslides*, pages 829–838.

Wendeler, C. (2008). Murgangrukhalt in wildbachen - grundlagen zur planung und berechnung von fflexible barrieren. Master's thesis, Eidgenössische Technische Hochschule, Zürich.

Wendeler, C., Volkwein, A., Roth, A., Denk, M., and Wartmann, S. (2007). Field measurements and numerical modelling of flexible debris flow barriers. In *Debris-Flow Hazards Mitigation. Mechanics, Prediction, and Assessment*, pages 681–687.

Wu, F., Fan, Y., Liang, L., and Wang, C. (2016a). Numerical Simulation of Dry Granular Flow Impacting a Rigid Wall Using the Discrete Element Method. *Plos One*, 11(8):e0160756.

Wu, K., Yang, D., and Wright, N. (2016b). A coupled SPH-DEM model for fluid-structure interaction problems with free-surface flow and structural failure. *Computers & Structures*, 177:141–161.

Yamaguchi, I. (1985). *Erosion Control Engineering*.

Yu, F. (1992). A study on the impact force of debris-flow. In *roceedings of the national science council, part A: Physical Science and Engineering,Taipei,Taiwan*, pages 32–39, Taipei, Taiwan.

Yuu, S., Abe, T., Saitoh, T., and Umekage, T. (1995). Three-dimensional numerical simulation of the motion of particles discharging from a rectangular hopper using distinct element method and comparison with experimental data (effects of time steps and material properties). *Advanced Powder Technology*, 6(4):259–269.

Zanuttigh, B. and Lamberti, A. (2006). Experimental analysis of the impact of dry avalanches on structures and implication for debris flows. *Journal of Hydraulic Research*, 44(4):522–534.

Zhang, C., Chen, S., Sun, Q., and Jin, F. (2016). Free-surface Simulations of Newtonian and Non-Newtonian Fluids with the Lattice Boltzmann Method. *Acta Geologica Sinica*, 90(3):999–1010.

Zhang, J., Hu, Z., Ge, W., Zhang, Y., Li, T., and Li, J. (2004). Application of the Discrete Approach to the Simulation of Size Segregation in Granular Chute Flow. *Industrial & Engineering Chemistry Research*, 43(18):5521–5528.

Zhang, S. (1993). A comprehensive approach oto the observation and prevention of debris flow in china. *Natural Hazards*, 7:1–23.

Zhang, S., Hungr, O., and Slaymaker, O. (1996). The calculation of impact force of boulders in debris flow. In Du, R., editor, *Debris Flow Observation and Research*, pages 67–72. Science Press, 1996 edition.

Zhou, C. and Ooi, J. Y. (2009). Numerical investigation of progressive development of granular pile with spherical and non-spherical particles. *Mechanics of Materials*, 41(6):707–714.

Zhou, Y., Xu, B. H., Zou, R. P., Yu, a. B., and Zulli, P. (2003). Stress distribution in a sandpile formed on a deflected base. *Advanced Powder Technology*, 14(4):401–410.

Zhou, Y. C., Wright, B. D., Yang, R. Y., Xu, B. H., and Yu, A. B. (1999). Rolling friction in the dynamic simulation of sandpile formation. *Physica A*, 269:536–553.

Zhou, Y. C., Xu, B. H., Yu, A. B., and Zulli, P. (2001). Numerical investigation of the angle of repose of monosized spheres. *Physical review. E*, 64(2):021301.

Zhou, Y. C., Xu, B. H., Yu, a. B., and Zulli, P. (2002). A numerical and experimental study of the angle of repose of granular particles. *Powder Technol*, 125:45–54+.

Zhou, Z. Y., Liu, S. D., Zou, R. P., Yu, A. B., Pinson, D., and Zulli, P. (2011). Numerical investigation of piling and hopper flow of ellipsoidal particles. *Chemeca 2011: Engineering a Better World*, pages 2890–2899.

Zhou, Z. Y., Zou, R. P., Pinson, D., and Yu, A. B. (2014). Angle of repose and stress distribution of sandpiles formed with ellipsoidal particles. *Granular Matter*, 16(5):695–709.

Zhu, H. P. and Yu, A. B. (2003). The effects of wall and rolling resistance on the couple stress of granular materials in vertical flow. *Physica A: Statistical Mechanics and its Applications*, 325(3-4):347–360.

Zhu, H. P., Zhou, Z. Y., Yang, R. Y., and Yu, A. B. (2007). Discrete particle simulation of particulate systems: Theoretical developments. *Chemical Engineering Science*, 62(13):3378–3396.

Zuriguel, I., Garcimartín, A., Maza, D., Pugnaloni, L. A., and Pastor, J. M. (2005). Jamming during the discharge of granular matter from a silo. *Physical Review E - Statistical, Nonlinear, and Soft Matter Physics*, 71(5):1–9.

Zuriguel, I., Pugnaloni, L. a., Garcimartín, A., and Maza, D. (2003). Jamming during the discharge of grains from a silo described as a percolating transition. *Physical review. E, Statistical, nonlinear, and soft matter physics*, 68:030301.